



**HAL**  
open science

# Dynamical thermalization in heavy-ion collisions

Mahbobeh Jafarpour

► **To cite this version:**

Mahbobeh Jafarpour. Dynamical thermalization in heavy-ion collisions. Physics [physics]. Nantes Université, 2022. English. NNT : 2022NANU4072 . tel-04026310v2

**HAL Id: tel-04026310**

**<https://hal.science/tel-04026310v2>**

Submitted on 31 Mar 2023

**HAL** is a multi-disciplinary open access archive for the deposit and dissemination of scientific research documents, whether they are published or not. The documents may come from teaching and research institutions in France or abroad, or from public or private research centers.

L'archive ouverte pluridisciplinaire **HAL**, est destinée au dépôt et à la diffusion de documents scientifiques de niveau recherche, publiés ou non, émanant des établissements d'enseignement et de recherche français ou étrangers, des laboratoires publics ou privés.

# THESE DE DOCTORAT DE

NANTES UNIVERSITÉ

ECOLE DOCTORALE N° 596

*Matière, Molécules, Matériaux*

Spécialité : Physique théorique, physique hadronique

Par

**Mahbobeh JAFARPOUR**

**Thermalisation dynamique dans les collisions d'ions lourds**

Thèse présentée et soutenue à Nantes, le 3 Juin 2022

Unité de recherche : SUBATECH UMR6457

## Rapporteurs avant soutenance :

Hanna Zbroszczyk

Taesoo Song

Professeure d'université, Université de Technologie de Warsaw

Chercheur Scientifique, GSI Darmstadt

## Composition du Jury :

Président : Elena Bratkovskaya

Examineurs : Marlene Nahrgang

Elena Bratkovskaya

Hanna Zbroszczyk

Taesoo Song

Dir. de thèse : Klaus Werner

Professeure d'université, Université de Goethe et GSI Darmstadt

Professeure Associée, IMT Atlantique, SUBATECH

Professeure d'université, Université de Goethe et GSI Darmstadt

Professeure d'université, Université de Technologie de Warsaw

Chercheur Scientifique, GSI Darmstadt

Professeur d'université, Université de Nantes

**Titre :** Thermalisation dynamique dans les collisions d'ions lourds

**Mots clés :** Collisions d'ions lourds, Générateur d'événements, EPOS, PHSD, EPOSi+PHSDe, Plasma de Quarks et de Gluons

**Résumé :** Les collisions d'ions lourds ultra-relativistes au Collisionneur d'Ions Lourds Relativistes (RHIC) et au Grand Collisionneur de Hadrons (LHC) créent une forme de matière chaude et ultra-dense de quarks et gluons déconfinés, appelée Plasma de Quarks et de Gluons (PQG). Différents modèles, tels que EPOS et PHSD, permettent d'étudier l'évolution spatio-temporelle de ces collisions. La dynamique de ces collisions étant très sophistiquée, différentes étapes doivent être considérées. La première correspond aux interactions primaires, qui définit en grande partie la distribution de matière dans l'espace des phases. La deuxième étape est appelée phase partonique, durant laquelle le système évolue jusqu'à être assez dilué pour hadroniser.

L'approche EPOSi+PHSDe est introduite dans cette thèse, dans laquelle la distribution initiale de matière (partons/hadrons) est déterminée

grâce à EPOS, étape désignée par EPOSi. Puis, PHSD est employé pour simuler l'évolution de la matière par une approche hors-équilibre, ce à quoi réfère PHSDe. Le couplage non-trivial de ces deux approches est discuté en détail dans ce manuscrit. En comparant les trois modèles EPOS, EPOSi+PHSDe et PHSD, des résultats intéressants ont déjà été obtenus concernant les évolutions spatio-temporelles qu'ils utilisent respectivement. Nous présentons l'étude d'observables de la "matière brute" (spectres  $p_T / m_T$ , distributions en  $y / \eta$ ,  $v_{2/3/4}$ ), ainsi que des sondes électromagnétiques, pour des collisions Au-Au à 200 GeV/A. La comparaison des résultats obtenus pour ces observables clés, entre les trois modèles, reflète notamment des comportements considérablement différents en terme d'expansion radiale, en particulier pour l'expansion asymétrique.

**Title :** Dynamical Thermalization in Heavy-ion Collisions

**Keywords :** Heavy-ion Collisions, Event generator, EPOS, PHSD, EPOSi+PHSDe, Quark-Gluon Plasma

**Abstract :** Ultrarelativistic heavy-ion collisions at the Relativistic Heavy-Ion Collider (RHIC) and the Large Hadron Collider (LHC) provide a hot and ultra-dense form of matter composed of deconfined quarks and gluons, named Quark-Gluon Plasma (QGP). Different models like EPOS and PHSD allow to study the space-time evolution of such heavy-ion collisions. Their dynamics is complicated; hence, various stages should be considered. The first is the primary scattering which defines to a large extent the matter distribution in the phase-space. The second stage concerns the evolution of the partonic system until the system is sufficiently dilute to hadronize. The EPOSi+PHSDe approach is introduced in this thesis, in which the EPOS model is used to determine the initial distribution of matter (partons/hadrons). This part is referred to as EPOSi.

Then PHSD is employed to simulate the evolution of the matter in a non-equilibrium transport approach, referred to as PHSDe. The coupling of the two approaches is non-trivial and not straight-forward, and is discussed in detail in this manuscript. Comparing the three models, EPOS, EPOSi+PHSDe, and PHSD, interesting results find concerning their respective space-time evolutions. The results demonstrate considerably different behavior in terms of radial expansion, especially asymmetric expansion, indicating that these three models will provide different results concerning key observables. To confirm this, we study the "bulk matter observables" ( $p_T/m_T$  spectra,  $y/\eta$  distribution,  $v_{2/3/4}$ ) for Au-Au collisions at 200 GeV/A. We also investigate the Electromagnetic probes compared to the PHSD approach.



# Dynamical Thermalization in Heavy Ion Collisions



## *Thermalisation dynamique dans les collisions d'ions lourds*

Mahbobeh JAFARPOUR

SUBATECH – Nantes (France) – 2022



<b>Acknowledgement</b>	<b>1</b>
<b>Introduction</b>	<b>3</b>
<b>1 General aspects</b>	<b>5</b>
1.1 Standard Model in Particle Physics . . . . .	5
1.1.1 The fundamental particles and forces . . . . .	5
1.1.2 The Higgs boson . . . . .	7
1.1.3 Open questions in particle physics . . . . .	8
1.1.4 Units in particle physics . . . . .	8
1.2 From QCD to QGP . . . . .	9
1.3 Heavy-ion collisions . . . . .	11
1.3.1 Geometric relation between centrality and the impact parameter in relativistic heavy-ion collisions . . . . .	13
1.4 Signatures of QGP in experiment . . . . .	15
1.4.1 Jet-quenching . . . . .	15
1.4.2 Heavy flavours and quarkonia suppression . . . . .	16
1.4.3 Anisotropic flow . . . . .	18
1.4.4 Strangeness enhancement . . . . .	22
1.4.5 Photons . . . . .	22
1.4.6 Dilepton production . . . . .	25
1.5 Monte Carlo event generators . . . . .	26
1.6 Summary and conclusion . . . . .	28
<b>2 EPOS</b>	<b>31</b>
2.1 A brief history of EPOS . . . . .	31
2.2 The theoretical foundation of EPOS . . . . .	32
2.2.1 Parton Model . . . . .	33
2.2.2 Gribov-Regge Theory . . . . .	36
2.2.3 Parton Based Gribov Regge Theory . . . . .	38
2.3 How does the EPOS event generator work? . . . . .	41
2.3.1 Initial conditions (EPOS <sub>i</sub> ) . . . . .	41
2.3.2 Core-Corona separation (EPOS <sub>e</sub> ) . . . . .	42
2.3.3 Hydrodynamic expansion (EPOS <sub>e</sub> ) . . . . .	44
2.3.4 Statistical hadronization (EPOS <sub>e</sub> ) . . . . .	44
2.3.5 Final state rescattering (EPOS <sub>e</sub> ) . . . . .	45
2.4 Summary and conclusion . . . . .	45

<b>3</b>	<b>Parton-Hadron-String Dynamics Transport approach</b>	<b>47</b>
3.1	Non-equilibrium QFT . . . . .	47
3.1.1	Dyson series on the Keldysh contour . . . . .	48
3.1.2	Green's functions . . . . .	49
3.1.3	Kadanoff-Baym equations . . . . .	50
3.1.4	Spectral function and transport equation . . . . .	51
3.2	Heavy-ion collisions in PHSD . . . . .	53
3.2.1	Initialization (PHSDi) . . . . .	53
3.2.2	String production in primary scatterings (PHSDi) . . . . .	54
3.2.3	Quark-gluon plasma (PHSDe) . . . . .	55
3.2.4	Hadronization and hadronic scattering (PHSDe) . . . . .	59
3.3	Summary and conclusion . . . . .	60
<b>4</b>	<b>The combination of EPOS and PHSD</b>	<b>61</b>
4.1	Initial condition in EPOSi+PHSDe . . . . .	61
4.1.1	Wood-Saxon distribution . . . . .	61
4.1.2	How are particles identified in EPOS? . . . . .	62
4.1.3	From core-corona separation to pre-hadrons . . . . .	66
4.2	Inserting pre-hadrons from EPOS to PHSD . . . . .	69
4.3	Space-time evolution of particles in EPOSi+PHSDe . . . . .	74
4.4	Summary and conclusion . . . . .	77
<b>5</b>	<b>Comparing results in three different approaches</b>	<b>79</b>
5.1	Energy density evolutions . . . . .	80
5.2	Bulk matter observables . . . . .	84
5.2.1	Transverse mass spectra . . . . .	84
5.2.2	Rapidity and pseudorapidity spectra . . . . .	88
5.2.3	Transverse momentum spectra . . . . .	91
5.2.4	Anisotropic flow . . . . .	99
5.3	Summary and conclusion . . . . .	108
<b>6</b>	<b>Electromagnetic probes</b>	<b>111</b>
6.1	Dileptons enhancement . . . . .	111
6.1.1	Cocktail in Au-Au collisions . . . . .	113
6.1.2	Invariant mass spectrum . . . . .	114
6.1.3	Transverse momentum and rapidity spectra . . . . .	118
6.2	Summary and conclusion . . . . .	122
	<b>Conclusion and outlook</b>	<b>125</b>
	<b>Résumé en français</b>	<b>129</b>
	<b>Appendices</b>	
	<b>Appendix A Kinematics in accelerators and coordinate systems</b>	<b>135</b>
A.1	Kinematics in accelerators . . . . .	135
A.1.1	Light Cone dynamics . . . . .	135
A.1.2	Hyperbola definition . . . . .	137
A.1.3	Transverse momentum and transverse mass . . . . .	137
A.2	Milne coordinates definition . . . . .	138

<b>Appendix B Required code in EPOSi+PHSDe approach</b>	<b>141</b>
B.1 Input file . . . . .	141
B.2 Relationship between centrality classes and impact parameters . . . . .	143
B.3 Construction of the color flow diagram in EPOS code . . . . .	143
<b>Glossary</b>	<b>171</b>
<b>Acronyms</b>	<b>173</b>



## ACKNOWLEDGEMENT

I would like to use this small space to express my appreciation to a number of persons whose support was important to the achievement of my thesis.

First of all, I would like to express my gratitude to my supervisor, Prof. Klaus Werner, for his guidance, recommendations, corrections, remarks, and sometimes contradicting criticisms that have aided in my progress as a scientist and as a person in general. In particular, I would like to thank Prof. Elena Bratkovskaya and Dr. Vadim Voronyuk for their contributions and insightful assessment which helped in the development of the framework that constitutes the basis of my thesis. I would also want to thank my jury members, Prof. Hanna Zbroszczyk, Dr. Marlène Nahrgang, and Dr. Taesoo Song, for their time, feedback and advice. Additionally, I want to thank my "Committee de Suivi de thèse" members, Dr. Yuri Sinyukov and Dr. Richard Lednicky, for monitoring my work and offering beneficial advice to improve my performance. I also want to express my gratitude to Prof. Pol-Bernard Gossiaux, Taklit Sami, Marcus Bluhm, Francois Arleo, Stephane Peigne, and Jacopo Ghiglieri for their continuous encouragement and assistance.

I want to thank all the Subatech staff, my fellow Ph.D. students (Johannes, Grégoire, Denys, Roland (M. SBF), Maria, Michael, Eamonn, Rita, Stephane, Gabriel, David, Nathan), secretaries (Farah, Servine, Sophie, Stephanie, Isabelle, Tanja) for making my stay in the laboratory a pleasant period of my life. I will never forget how much your support and encouragement helped me change the trajectory of my life by learning French.

I cannot miss my Iranian friends that make lots of pleasing moments for me during these four years. Khalil Aghoo, Shirin Khanom, Sima, Hamidreza, Ehsan, Parisa, Sohrab, Darya Joon, Erfan, Haed, Sayeh, Faezeh, Yousef, Pouya, Meryam, Amin, Maryam, Parmida, Ahmad, Atiyeh, Aron, Ali, Mahsa, Houra, Mahdiyeh, Parastoo, Mercedeh, Mohsen, Nouchin, Kiyam, thank you for making my stay in Nantes enjoyable and for always being there for me!

I want to thank my dear family, you supported me from the beginning in executing all my crazy ideas. Thanks to you, I was able to go to Kerman and Shiraz to study and continue my scientific activities in France. My dear mom, you showed me that patience, effort, and trust in God are necessary for success. My dear father, thanks for your support and grace, I know that you will never leave me, I have become a hardworking person and I have improved both in terms of personality and social status. What makes me happy is that you learned me what adventure and activity are. I am proud to be

## ACKNOWLEDGEMENT

---

your daughter. For sure, I cannot forget the rest of my family members for their ongoing support and encouragement, especially my dear little brother, Mohsen. THANKS A LOT FOR EVERYTHING. I achieved my goals thanks to you, my family, and I will undoubtedly improve with your help.

**I dedicate this thesis to my family and friends because without them, I would not have been capable of following this winding path.**

The title of this thesis is "Dynamical Thermalization in Heavy Ion Collisions (HICs)", which studies the role of the initial stage concerning the dynamics of HICs using models, EPOS and PHSD. Ultrarelativistic HICs at the RHIC and the LHC provide a hot and ultra-dense form of matter composed of deconfined quarks and gluons, named QGP. The goal of measurements is to investigate this state of the matter and understand how it is produced, evolves, and impacts measurements. To study HICs, we usually employ some approaches for the initial phase (for  $t < 1$  fm/c) followed by the modeling of the second phase, covering expansion and hadronization.

Although using HICs we have learned many things both on theoretical and phenomenological aspects, there is still a large amount of uncertainty in particular concerning the thermalization of the system. The dynamics is complicated; hence, various stages should be considered. The first is the primary scattering which defines to a large extent the matter distribution in the phase-space. The second stage concerns the evolution of the partonic system until the system is sufficiently dilute to hadronize. Therefore, we need models with different degrees of sophistication concerning the various stages (initial, evolution, and hadronization). In this context, we find out that EPOS and PHSD models can be seen as suitable alternatives, and they are among the successful models to investigate the space-time evolution of such HICs.

As indicated in Fig. 1, the initial phase of EPOS (EPOS<sub>i</sub>) amounts to multiple scatterings based on Parton-Based-Gribov-Regge Theory (PBGRT), whereas the following dynamics has been realized so far by assuming that a fast equilibration occurs followed by a hydrodynamical evolution (EPOS<sub>e</sub>).

PHSD is a microscopic covariant dynamical approach for the strongly interacting systems formulated based on the Kadanoff-Baym equations. This approach consistently describes the full evolution of a relativistic HICs, including (1) the initial hard scatterings and the string formation based on the LUND string model using Pythia event generator (PHSD<sub>i</sub>), and (2) the dynamical deconfinement phase transition to the strongly-interacting QGP and the hadronization and the subsequent interactions in the expanding hadronic phase (PHSD<sub>e</sub>). The theoretical transport description of the quarks and the gluons in PHSD is based on the DQPM for partons that has been constructed to reproduce lattice Quantum Chromodynamics (QCD) for the QGP thermodynamics.

When comparing two models, like EPOS and PHSD, looking at numerous observables, is not always clear to what extent the two parts, the initial phase (i) and the

<b>Models Steps</b>	<b>EPOS</b>	<b>PHSD</b>
<b>Initial Conditions (i)</b>	<b>PBGRT</b>	<b>PYTHIA</b>
<b>Evolutions (e)</b>	Core-Corona Separation Viscous Hydrodynamic Expansion Statistical Hadronization Final State Hadronic Cascade	<b>QGP Formation</b> <b>Non-Equilibrium Parton/Hadron Evolution</b>

Figure 1: The EPOS and PHSD stages to investigate the entire space-time evolution of matter in HICs. The new approach is called EPOS+PHSDe since it integrates the initial conditions of EPOS (EPOS<sub>i</sub>) with the evolution of matter in a non-equilibrium transport approach (PHSD<sub>e</sub>).

expansion (e), contribute to the final results. Therefore, the idea to combine the initial EPOS phase (EPOS<sub>i</sub>) and the evolution from PHSD (PHSD<sub>e</sub>), giving rise to the EPOS+PHSDe model. In this way, comparing EPOS+PHSDe and pure EPOS, we compare two models with the identical initial condition but different evolution. However, when comparing EPOS+PHSDe and pure PHSD, we compare two models with different initial conditions but the same evolution. So we can clearly separate "initial" and "evolution" effects.

The following is the outline of this manuscript: in chapter 1, I will briefly describe how we obtain the QGP theoretically from QCD in the Standard Model and how we can produce it in the laboratory using HICs. Then, concerning the experiments, the main signatures of the QGP will be presented. Finally, because we will be using event generators, I will go over the various event generators using the Monte Carlo technique. The theory inside EPOS and PHSD models is summarized in the second and third chapters, respectively. The new approach, EPOS+PHSDe, will be covered in more detail in the fourth chapter. The findings of these three alternative approaches, EPOS, EPOS+PHSDe, and PHSD, for various observables of Au-Au collisions at RHIC energy, such as bulk matter observables, anisotropic flow, and electromagnetic probes, are presented and compared in the last two chapters. Finally, we have one more small chapter to wrap up our results and outlook for this manuscript.

As the title of this thesis reveals, we would like to investigate dynamical properties of [Heavy Ion Collisions \(HICs\)](#) and its consequences such as the [Quark Gluon Plasma \(QGP\)](#). In the following, I will provide some background of this research field. I will first review the [Standard Model \(SM\)](#)'s basic particles and forces. Then I will describe how the [QGP](#) can be obtained in the [SM](#). In the third section, I will briefly explain how a [QGP](#) may be created in the laboratory via colliding heavy nuclei, and I consider the various stages of such collisions. In the following, I will introduce some theoretical tools to investigate the [QGP](#), referred to as "soft", "hard", and "electromagnetic probes". Finally, I will discuss various [Monte Carlo \(MC\)](#) event generators that are commonly employed by experimentalists in analyses, and by many theorists in order to make predictions for collider experiments.

## 1.1 Standard Model in Particle Physics

One of the successes of modern physics is the [SM](#) of particle physics [1]. All of the particles in [SM](#) have now been observed, thanks to the discovery of the Higgs boson at the [Large Hadron Collider \(LHC\)](#) in 2012 [2]. Particle physics is crucial to our understanding of natural laws. It is concerned with the Universe's fundamental constituents, the elementary particles, and associated interactions or forces. The [SM](#) of particle physics incorporates our current understanding, providing a picture that the interactions between particles are themselves explained by particle exchange. The [SM](#) successfully describes all current experimental data, and this is considered as one of modern physics' achievements.

### 1.1.1 The fundamental particles and forces

The basic components of matter, fundamental particles, make up everything around us. Quarks and leptons are the two primary kinds of these particles. Each group is made up of six particles that are linked together in pairs, or "generations", as seen in table 1.1. The first generation has the lightest and most stable particles, whereas the second and third generations include the heavier and less stable particles. All stable matter in the universe comprises first-generation particles; heavier particles decay quickly to more stable ones. The six quarks are coupled in three generations: the "up quark" and "down quark" are the first, followed by the "charm quark" and "strange quark", and finally the "top quark" and "bottom (or beauty) quark".

Quarks are also available in three different "colors", which only combine to make colorless things. The six leptons – the "electron" and "electron neutrino", the "muon" and "muon neutrino", and the "tau" and "tau neutrino" – are similarly grouped in three generations. The electron, muon, and tau all have an electric charge and a considerable mass, but neutrinos are electrically neutral and have a negligible mass.

Table 1.1: List of leptons and quarks in Standard Model [1].

	Leptons			Quarks		
	Particle	Q	mass(GeV/c <sup>2</sup> )	Particle	Q	mass(GeV/c <sup>2</sup> )
First generation	electron ( $e^-$ )	-1	0.0005	down (d)	-1/3	0.003
	neutrino ( $\nu_e$ )	0	$< 10^{-9}$	up (u)	+2/3	0.005
Second generation	muon ( $\mu^-$ )	-1	0.106	strange (s)	-1/3	0.1
	neutrino ( $\nu_\mu$ )	0	$< 10^{-9}$	charm (c)	+2/3	1.3
Third generation	tau ( $\tau^-$ )	-1	1.78	bottom (b)	-1/3	4.5
	neutrino ( $\nu_\tau$ )	0	$< 10^{-9}$	top (t)	+2/3	174

The Dirac equation of relativistic quantum mechanics describes the dynamics of each of the twelve fundamental fermions. One of the most fundamental consequences of the Dirac equation is that each of the twelve fermions has an antiparticle state with the same mass but the opposite charge. Antiparticles are indicated by a bar over the associated particle symbol or their charge. The anti-electron (known as a positron) is represented by  $e^+$ , and the anti-up-quark is represented by  $\bar{u}$ .

In addition to the fermions presented in table 1.1, bosons are one of the other fundamental kinds of subatomic particles whose spin quantum number has an integer value (0,1,2,...). In particle physics, the elementary bosons play a unique role. They may either behave as force carriers, causing forces between other particles, or they can cause mass phenomena. There are five elementary bosons in the SM of particle physics: one scalar boson (spin=0) which named  $H^0$  Higgs boson. It gives rise to the phenomenon of mass via the Higgs mechanism. I will explain more about this mechanism in the next subsection. Additionally, there are four vector bosons (spin=1) that act as force carriers, and they categorize as gauge bosons, as shown in table 1.2.

Each of the three relevant forces in particle physics is represented by [Quantum Field Theory \(QFT\)](#) corresponding to the exchange of a gauge boson, a spin-1 force-carrying particle. The [Quantum ElectroDynamics \(QED\)](#)'s gauge boson is the spin-1 photon. The force-carrying particle in the strong interaction is called gluon, which like the photon, has no mass. The charged  $W^+$  and  $W^-$  bosons, which are about eighty times heavier than the proton, mediate the weak charged-current interaction. The electrically neutral Z boson mediates a weak neutral-current interaction closely related to the charged current. Gravity is assumed to be carried by a tensor boson (spin=2) termed the graviton ( $G$ ), but all attempts to include gravity into the SM so far have failed. Bose-Einstein statistics explain the behavior of many bosons at high densities as quantum particles.

Table 1.2: The four known forces of nature [1].

Force	Strength	Gauge Boson	Spin	Mass(GeV/c <sup>2</sup> )
Strong	1	gluon (g)	1	0
Electromagnetism	$10^{-3}$	photon ( $\gamma$ )	1	0
Weak	$10^{-8}$	W boson ( $W^\pm$ )	1	80.4
Weak	$10^{-8}$	Z boson (Z)	1	91.2

The forces work in a variety of ranges and have different strengths. The weakest is gravity, although it has an infinite range. The electromagnetic force can be felt from an infinite distance like gravity, but it is stronger. The weak and strong forces are only effective over a very small distance and dominate at the subatomic particle level. The weak force, despite its name, is much stronger than gravity, although it is the weakest of the three. As its name indicates, the strong force is the most powerful of the four fundamental interactions.

Table 1.3 summarizes how the properties of the twelve fundamental fermions are classified based on the types of interactions they face. The weak force impacts all twelve fundamental particles, creating weak interactions. The other nine particles, except for electrically neutral neutrinos, are electrically charged and participate in the electromagnetic interaction of QED. Only quarks have the color charge, which is Quantum Chromodynamics (QCD) version of electric charge. As a result, only the quarks are affected by the strong force. Because of a phenomenon known as color confinement, quarks are never found in isolation; they can be found only within hadrons, which include baryons (such as protons and neutrons) and mesons, or in QGP. In the following, I will explain these states of matter in more detail. The properties of quarks are very different from leptons because quarks sense the strong force.

Table 1.3: The forces experienced by leptons and quarks.

					strong	electromagnetic	weak
Quarks	down-type	$d$	$s$	$b$	✓	✓	✓
	up-type	$u$	$c$	$t$	✓	✓	✓
Leptons	charged	$e^-$	$\mu^-$	$\tau^-$		✓	✓
	neutrinos	$\nu_e$	$\nu_\mu$	$\nu_\tau$			✓

### 1.1.2 The Higgs boson

The Higgs boson, the last ingredient of the SM, was discovered in 2012 by the A Toroidal LHC Apparatus (ATLAS) [3] and Compact Muon Solenoid (CMS) [4] experiments. All other the SM particles differ from the Higgs boson. The Higgs boson mass is  $m_H \approx 125$  GeV. The Higgs boson is a spin-0 scalar particle, unlike the fundamental fermions and gauge bosons, both spin-half and spin-1 particles. The Higgs boson is the only fundamental scalar found so far, as predicted by the SM. The observation of a Higgs-like particle at LHC was a crucial confirmation of the SM's theoretical concepts.

In the SM, the Higgs boson plays a key role: it supplies the process by which all other particles gain mass. The universe would be significantly different if it did not exist; all particles would be massless and propagate at the speed of light. In QFT, all elementary particles are possibly excited states (or quanta) of some field. This includes the Higgs boson, which is the Higgs field's quanta, the photon, which is the electromagnetic field's quanta, the electron, which is the electron field's quanta, etc. At all points in time and space, all fields exist. Fields can couple with other fields, and the fields are assumed to be interacting in this respect.

The Higgs field is coupled to some fields. The Higgs field is broken into two components after a process known as spontaneous symmetry breaking. The Higgs bosons are the quanta of the first component, which is still a dynamic field. The second part is a constant, called the vacuum expectation value, and the equations describing the Higgs field's coupling to other fields become equations describing other fields coupling to themselves, which is understood as providing mass to a field in QFT. As a result, the Higgs

field's vacuum expectation value is proportional to the mass of each field. The particles that are quanta of fields that couple to the Higgs field acquire mass due to spontaneous symmetry breaking, which is the nature of the Higgs mechanism [5,6]. Except for photon, gluon, and probably the three generations of neutrinos, it contains all known particles or fields.

### 1.1.3 Open questions in particle physics

The achievement of particle physics' SM in describing a wide range of accurate experimental data is a remarkable realization. The SM, however, is just a model, and there are many unanswered questions. The SM is not the final theory of particle physics. On the other hand, there are many possibilities for the nature of physics Beyond the Standard Model (BSM), including supersymmetry, large-scale extra dimensions, and possibly even string theory. Only a brief overview of a few of the current issues with the SM is provided here. They are based on all active areas of the current experimental study.

- What is the dark matter?
- Does supersymmetry exist?
- Can the forces be unified?
- What is the nature of the Higgs boson?
- Flavour and the origin of CP violation.
- Are neutrinos Majorana particles?

### 1.1.4 Units in particle physics

The S.I. units system [ $kg, m, s$ ] provides a natural basis for measuring macroscopic objects' mass, length, and time. However, when particles have very small amounts, such as the mass of an electron, it is not a natural choice for describing their properties. The mass of an electron is  $9.1 \times 10^{-31}$  kg in S.I. units. We use other units based on the S.I. units to avoid large exponents. Natural units are a set of units used in particle physics. It is based on the fundamental constants of quantum mechanics and special relativity. [ $kg, m, s$ ] are replaced by [ $\hbar, c, \text{GeV}$ ] in natural units, where  $\hbar = 1.055 \times 10^{-34}$  Js is the quantum mechanics unit of action,  $c = 2.998 \times 10^8$  ms<sup>-1</sup> is the speed of light in vacuum, and  $1 \text{ GeV} = 10^9 \text{ eV} = 1.602 \times 10^{-10}$  J is the rest mass energy of proton. Table 1.4 represents the relationship between S.I. and natural units. In the natural units, one can simplify the quantities by choosing  $\hbar = c = 1$ . For instance, the Einstein energy-momentum relation

$$E^2 = p^2 c^2 + m^2 c^4, \quad (1.1.1)$$

becomes

$$E^2 = p^2 + m^2. \quad (1.1.2)$$

The variables  $\hbar$  and  $c$  have not simply disappeared; they are still found in quantity dimensions. To convert the quantity from natural units to S.I. units, depending on the variables, the appropriate dimensions are obtained by multiplying by  $\hbar c = 0.197 \text{ GeV fm}$  or  $c$ , where one femtometre (fm) is  $10^{-15}$  m.

Table 1.4: Relationship between S.I. and natural units.

Quantity	[kg, m, s]	$[\hbar, c, \text{GeV}]$	$\hbar = c = 1$
Energy	$\text{kg m}^2 \text{s}^{-2}$	GeV	GeV
Momentum	$\text{kg m s}^{-1}$	$\text{GeV}/c$	GeV
Mass	kg	$\text{GeV}/c^2$	GeV
Time	s	$(\text{GeV}/\hbar)^{-1}$	$\text{GeV}^{-1}$
Length	m	$(\text{GeV}/\hbar c)^{-1}$	$\text{GeV}^{-1}$
Area	$\text{m}^2$	$(\text{GeV}/\hbar c)^{-2}$	$\text{GeV}^{-2}$

The quantities in this thesis are represented using the S.I. units system.

## 1.2 From QCD to QGP

The theory of the strong interaction between quarks and gluons, which forms compound hadrons like the proton, neutron, and pion, is known as **QCD**. This is an essential part of the **SM** in particle physics. **QCD** is a non-abelian gauge theory with the symmetry group  $\text{SU}(3)$ , which is a kind of **QFT**. Gluons are the force transporters of this theory, exactly as photons are in **QED** for the electromagnetic force. In **QCD**,  $\alpha_s$  is a fundamental coupling that determines the strength of the quarks and gluons interactions. The underlying dynamics of hadron physics – from color confinement to asymptotic freedom at short distances – are represented by  $\alpha_s(Q^2)$  dependence on momentum transfer  $Q$ , as seen in Fig. 1.1. Based on different  $\alpha_s$  values, **QCD** has three remarkable features:

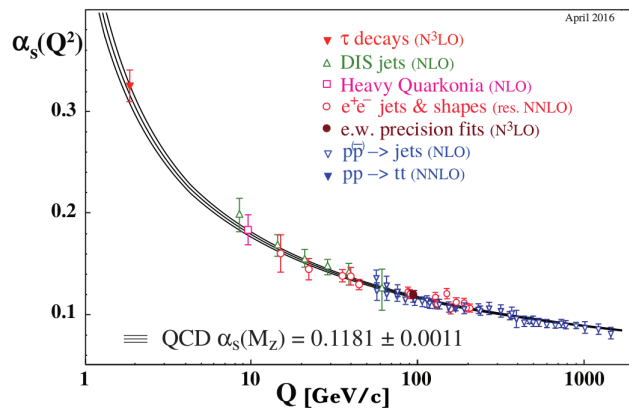


Figure 1.1: Summary of measurements of  $\alpha_s$  as a function of the momentum transfer  $Q$ . The respective degree of **QCD** perturbation theory used in the extraction of  $\alpha_s$  is indicated in brackets (NLO: next-to-leading order; NNLO: next-to-next-to leading order; res. NNLO: NNLO matched with resummed next-to-leading logs;  $\text{N}^3\text{LO}$ : next-to-NNLO) [7].

- **Color confinement.** Two or more quarks close to each other rapidly exchange gluons, creating a very strong "color force field" binding the quarks together. There are three color charges, and three corresponding anti-color (complementary color) charges. Quarks constantly change their color charge as they exchange gluons with other quarks. Each quark has one of the three color charges, and each antiquark has one of the three complementary color charges. Gluons carry color/anti-color pairs (they do not necessarily have to be the same color; i.e. red/anti-blue gluons are legal). While there are 9 possible combinations of color/anti-color pairs, due to symmetry considerations one

of these combinations is eliminated. A gluon can effectively carry one of eight possible color/anti-color combinations. Color-charged particles cannot be found individually because they must maintain a color-force field with other quarks. For this reason, the color-charged quarks are confined in groups (hadrons) with other quarks at low energies, with  $\alpha_s \sim O(1)$ . These composites are color neutral. The mesons (one quark, one anti-quark) and baryons (three quarks) are the two main types of hadrons.

Colorless particles made fully of gluons are also consistent with confinement, although they are difficult to recognize in the experiment. Without creating new hadrons, quarks and gluons can not be separated from their parent hadrons [8]. The energy grows until a quark–antiquark pair is spontaneously generated. Then the original hadron convert into a pair of hadrons instead of separating a color charge. Color confinement is well confirmed by [lattice Quantum ChromoDynamics \(lQCD\)](#) calculations and decades of experiments, while still being unproven theoretically [9]. The gluon field produces a narrow flux tube (or string) between two color charges. Because of the nature of the gluon field, the strong force between the particles remains unchanged despite their separation.

- **Chiral symmetry breaking.** Spontaneous symmetry breaking is a symmetry breaking process that occurs when a physical system in a symmetric state becomes asymmetric [10]. It can explain systems in which the equations of motion or the Lagrangian obey symmetries but the lowest-energy vacuum solutions do not. The chiral symmetry breaking is the spontaneous breaking of an essential global symmetry of quarks. The spontaneous symmetry breaking resulting in hadrons with masses considerably greater than the masses of the quarks and very light pseudoscalar mesons. The mass formation of nucleons from more fundamental light quarks, which accounts for around 99% of their combined mass as a baryon, is where chiral symmetry breaking is most visible. Therefore, it makes up the majority of the mass of all visible objects. For instance, the valence quarks, two up quarks with  $m_u = 2.3$  MeV and one down quark with  $m_d = 4.8$  MeV, only contribute roughly 9.4 MeV (= 1%) to the mass of the proton, which has a mass of  $m_p = 938$  MeV. Quantum chromodynamics binding energy, which results from QCD chiral symmetry breaking, is the main source of the proton’s mass. For describing the phenomena, Yoichiro Nambu was awarded the Nobel Prize in Physics in 2008 [11]. All of his general predictions have been validated by lattice simulations.

- **Asymptotic freedom.** As the energy scale increases and the corresponding length scale drops, it is a property of some gauge theories that causes particle interactions to become asymptotically weaker. At high energies, quarks interact weakly and  $\alpha_s$  becomes sufficiently small, see Fig. 1.1. This condition is known asymptotic freedom which quarks and gluons can be free. David Gross, H. David Politzer [12], and Frank Wilczek [13] were awarded the Nobel Prize in Physics in 2004 [14] for discovering the asymptotic freedom in the theory of the nuclear matter. This result was (and still is) very significant for both its physical meaning and calculational applicability. From a calculational standpoint, it says that at high energies we can perform perturbative QCD calculations, while at low energies QCD calculations will be very difficult. Physically, it means that at low energies one cannot find deconfined quarks, but must always find pairs or trios of quarks coupled together by gluons. However, at high energies, one can essentially neglect these gluonic interactions and consider quarks “free” [15].

Free quarks are never detected at normal length and energy scales, therefore this prediction of free quarks is basically a prediction of an entire different type of matter. Free color charges exist for these free quarks, just as they do for the particles in a nor-

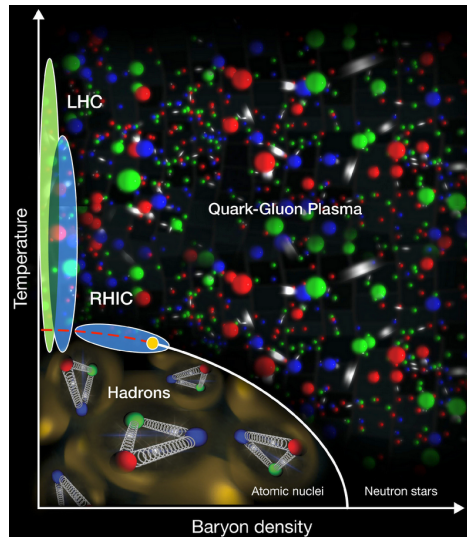


Figure 1.2: Phase diagram of nuclear matter.

mal plasma. As a result, as much as charged particles screen the Coulomb interaction in normal plasma, free color charges screen the strong interaction. As a result of the comparison with ordinary plasma, the new state of matter is known the **QGP** [16, 17]. These perturbative calculations were expected to explain the quark gluon plasma, at least qualitatively, beginning from the critical temperature [18]. Before matter was formed, a plasma of quarks and gluons covered the entire Universe.

In 1974, the idea of predicting the formation of the **QGP** was proposed [19]. The experiment proposal to create artificial **QGP** using **Relativistic Heavy Ion Collider (RHIC)** was presented at BNL in 1983 [20]. Additionally, experiments at **Conseil Européen pour la Recherche Nucléaire (CERN)** to produce quark matter began in 1986/7, with the first claims reported in 1991 [21]. It took several years for the concept to gain traction among particle and nuclear scientists. The formation of a new state of matter in Pb-Pb collisions was officially announced at **CERN** in 1999 [22, 23] in view of the convincing experimental results provided by the **CERN Super Proton Synchrotron (SPS)** WA97 experiment, **LHC**.

Quark matter takes various forms in the **SPS**, **RHIC**, and **LHC** experiments, depending on the temperature  $T$  (MeV) and baryon chemical potential  $\mu_B$ , as seen in Fig. 1.2. At high temperature  $T \gg \mu_B$ , where it is more than the critical one,  $T > T_c \approx 175 \text{ MeV}$ , the hadrons are deconfined into free quarks and gluons. This condition happen based on the asymptotic freedom and called the **QGP**. It is defined as a phase of highly interacting matter with no spontaneous symmetry breaking that filled the Universe for the first microseconds after the big bang. At low temperatures and densities, the quarks and gluons are confined into hadrons, and the matter is known as hadronic gas. At low temperature and high baryon density  $T \ll \mu_B$ , the matter is as a gas of neutron star, where we find a rich variety of spontaneous symmetry breaking phases [24].

### 1.3 Heavy-ion collisions

**HICs** at **RHIC**, and **LHC** can probably produce the **QGP**. It is an expansive medium of deconfined nuclear matter in which the degrees of freedom are quarks and gluons [25, 26]. **Brookhaven National Lab (BNL)**'s **RHIC**, where heavy ions are collided up to a center-of-mass energy per nucleon-nucleon collision of 3 to 200 GeV for gold (Au), uranium

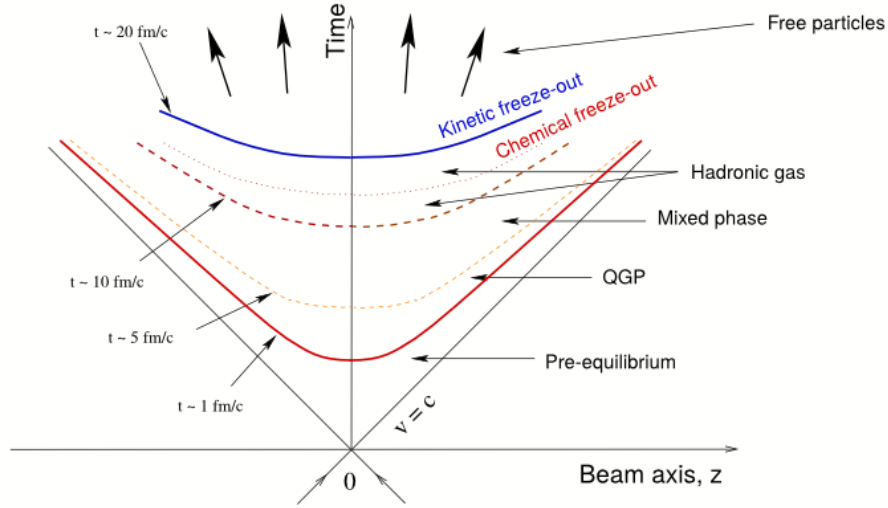


Figure 1.3: Exposition of QGP space-time evolution.

(Ur), and copper (Cu) ions collisions, have been performed since 2000. The [Alternating Gradient Synchrotron \(AGS\)](#) at BNL can also collide Au-Au at 11.5 GeV center of mass energy colliding [27,28]. Some [HICs](#), collisions with the center of mass energies less than 20 GeV/c, do not form [QGP](#), and the system's evolution is different. Only primary scattering and particle production are possible in this situation. The various stages of [HICs](#) will be shown in the following paragraphs. [HICs](#) were successfully performed at [CERN](#) using [LHC](#) between Lead-Lead (Pb-Pb) at  $\sqrt{s_{NN}}=2.76$  TeV in RUN I [29] and  $\sqrt{s_{NN}}=5.02$  TeV in RUN II [30].

Due to the sensitivity of various probes to the various stages of the collision, the produced system passes through different phases in [HICs](#). Fig. 1.3 depicts these steps in space and time, which can be summarized as follows [31]:

- **Pre-equilibrium** ( $0 < \tau < 1 \text{ fm/c}$ ): The produced particles in the collision region achieve thermal equilibrium after colliding two nuclei. In theoretical relativistic hydrodynamical models, this is supposed to be extremely fast, although a precise mechanism for this is yet unknown. Hard parton scattering occurs quickly after primary collisions,  $\tau < 0.1 \text{ fm/c}$ , resulting in high  $p_T$  probes such direct photons, heavy quarks, and jets. Hard particles with either a big mass or a large transverse momenta  $p_T \gg 1 \text{ GeV/c}$  are produced in this stage before the majority of the elementary particles, which are created from the fraction of the beam energy lost in the collision, have time to rescatter.

- **QGP or hydrodynamic phase** ( $1 < \tau < 10 \text{ fm/c}$ ): Quickly after pre-equilibrium, a fireball (collection of particles with a lower energy and transverse momentum) is formed, with thermal and chemical equilibrium developing, depending on the initial conditions. A high concentration of high-energy nucleus-nucleus collisions concentrated in a small volume that can generate billions of degrees produces the [QGP](#)-like phase. We will need to use magnets to accelerate particles to extremely high speeds before colliding them, which will produce a large amount of heat. This is why, unlike high-energy lepton-lepton or single hadron-nucleus interactions, we can use [HICs](#) to recreate matter as in the early universe. [Equation of State \(EoS\)](#) can be used to describe the thermodynamic properties of this fluid, such as pressure, volume, and temperature. The transition from a hadronic matter to a [QGP](#) state potentially occurs when the temperature of the system reaches up to about 155 MeV predicted by [lQCD](#) [32]. After reaching local thermal equilibrium, the

system expands due to the huge pressure gradient compared to the surrounding vacuum. In this stage, the produced partons can rescatter both elastically and inelastically. Only inelastic collisions affect the relative abundances of gluons, light, and strange quarks, but both types of collisions lead to equal sharing of the injected energy.

- **Hadronization** ( $10 < \tau < 20$  fm/c): Thermal pressure in a thermalized system causes the collision fireball to expand collectively or hydrodynamically. Then, the fireball cools and loses its energy density from before to after a mixed phase. Therefore, the system hadronizes and partons confined into hadrons. The entropy density reduces dramatically over a short temperature range during the phase transition. Since the volume of the fireball increases slightly, the fireball spends some times around critical temperature. Furthermore, while the matter hadronizes, its sound speed  $c_s = \sqrt{\partial p / \partial e}$  is low, resulting in inefficient acceleration and no rise in the collective flow during this time [33].

- **Freeze-out** ( $\tau > 20$  fm/c): Following the hadronization process, the system continues to expand and cool like a hot hadron gas. Produced particles interact with one another via inelastic and elastic collisions. The inelastic collisions cease first for the smaller cross-section during the additional expansion procedure, this condition is called "chemical Freeze-out". Then, the system maintains a combined expansion via hadron-hadron elastic collisions until the particles have sufficient energy. When the particles no more have adequate energy to rescatter, all elastic collisions will be stopped, and the particles fly to the detector to be observed. This is referred to as "kinetic freeze-out".

Relativistic hydrodynamics has been used successfully in high-energy HICs. Hydrodynamics may be used to link the conservation laws with the EoS, viscosity, and heat conductivity of the fluid. Relativistic hydrodynamics shows the space-time evolution of the hot or dense volume produced in the central rapidity area of relativistic AA collision. The Bjorken approach [34] and Energy conserving quantum mechanical approach, based on Partons, parton ladders, strings, Off-shell remnants, and Saturation of parton ladders (EPOS) model [35] are among the successful hydrodynamical models which employ to explain the space-time evolution of high-energy HICs. In the next chapter, I will explain the EPOS model, which I used in my Ph.D. thesis.

### 1.3.1 Geometric relation between centrality and the impact parameter in relativistic heavy-ion collisions

Experimental data from relativistic heavy-ion collisions (SPS, RHIC) are typically categorized by introducing centrality,  $c$ , defined as the percentile of events with the largest number of produced particles (as registered in detectors), or the largest number of participants. Results of measurements, such as multiplicities,  $p_T$  spectra, the elliptic flow coefficient  $v_2$ , etc., are then presented for various centralities. From the experimental viewpoint the centrality is a good, unambiguous criterion allowing to divide the data [36].

On the other hand, theoreticians need to assign an impact parameter,  $b$ , to a given centrality. The impact parameter is more basic since it determines the initial geometry of the collision and appears across the formalism. Theoretical calculations in heavy-ion physics input  $b$  to obtain predictions. After the calculation, the question arises as to which centrality data the model results should be compared.

Depending on the overlap of nuclei, entirely or partially, the strongly-coupled QGP created will be completely different. The geometric degree of overlap can be quantified with the impact parameter  $b$ , shown in Fig. 1.4.

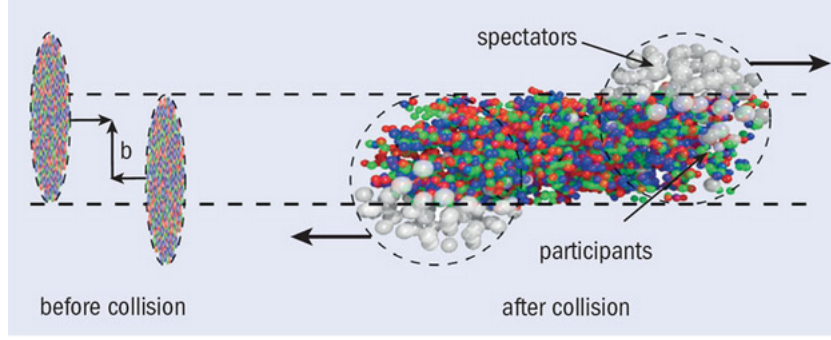


Figure 1.4: Two heavy ions before the collision with impact parameter  $b$  (l.h.s). The spectator nucleons remain unaffected while particle production takes place in the participants' zone (r.h.s) [37].

The geometric picture, in Fig. 1.4, is a very intuitive way of picturing HICs. At small  $b$ , one has a big overlap zone, which will lead to a large-volume plasma, whereas large  $b$  corresponds to a small overlap, creating a small and short-lived plasma. The nucleons that interact in the overlapping region are known as "participants", and the rest are "spectators". It is essential to remember that the impact parameter is not a quantity extracted from HICs data. It can be preferable to think of it as a model parameter, not a measurable quantity. The impact parameter is the vector  $(b_x, b_y) = (b, 0)$  in a transverse plane, and the overlapping of two spheres gives an elongation along the  $y$ -axis.

A highly simplified picture, the "hard sphere approach", allows to understand some purely geometric aspect of HICs (although real particle production is much more complex). In this approach, two nuclei "interact", whenever their transverse distance is closer than  $b_{max}$ . This corresponds to  $\sigma_{inel} = \pi b_{max}^2$ . Therefore, a "centrality measure  $c(b)$ " is given by:

$$\frac{d\sigma}{db} \approx \begin{cases} 2\pi b, & b \leq b_{max} \\ 0, & b > b_{max}, \end{cases} \quad (1.3.1)$$

for  $b < b_{max}$ ,

$$c(b) = \frac{\pi b^2}{\sigma_{inel}}. \quad (1.3.2)$$

If we assume that the maximum impact parameter in a Au-Au collision is 13.5 fm, one can define the centrality classes for different amounts of impact parameters less than 13.5 fm. For instance, based on Eq. 1.3.2, we get  $c(2) = 2.2\%$  for  $b=2$ fm, which is the most central collisions.

The centrality of a collision cannot be determined clearly from the data collected by a detector. One can estimate the centrality based on how many particles come out and how strongly they are scattered. The charged particle multiplicity may be taken as a measure of the centrality: with decreasing impact parameter, we expect increasing multiplicity. Therefore rather than defining percentiles (like 0-5%) based on  $d\sigma/db$ , one defines them based on  $dN/dN_{ch}$ , as shown in Fig. 1.5.

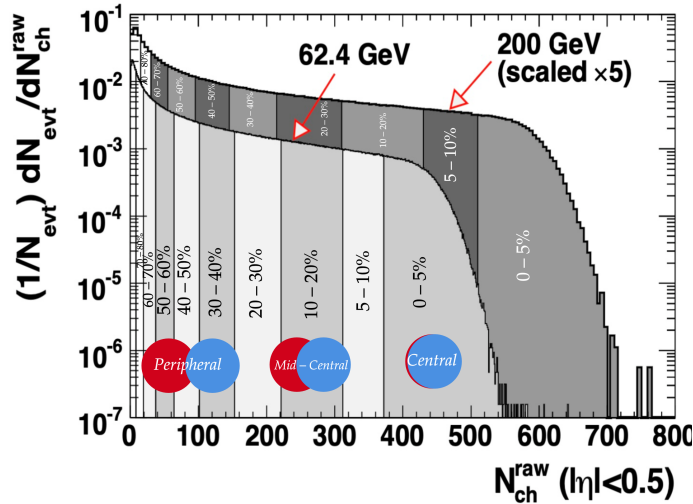


Figure 1.5: The measured charged-particle multiplicity distribution in the [Solenoidal Tracker At RHIC \(STAR\)](#) experiment in  $|\eta| < 0.5$  for [Au-Au](#) collisions at 62.4 GeV and 200 GeV [38]. The shaded regions indicate the centrality bins used in the analysis. The 200 GeV data are scaled by a factor 5 for clarity.

I will introduce some of the diagnostic tools that have been used to investigate the [QGP](#) in the next section.

## 1.4 Signatures of QGP in experiment

One of the most difficult aspects of [HICs](#) investigations is identifying and diagnosing the [QGP](#) features. Because the [QGP](#) cannot be observed in actual time, theoretical models must predict which aspects of the final state of the interactions will be useful in determining the [QGP](#) formation. They must predict which properties will differ depending on whether the [QGP](#) is created or not in colliding systems. These features must then be experimentally validated before being used as the [QGP](#) signatures.

The signatures can be divided into three types: hard, soft, and electromagnetic probes depending on the collision phase. The interaction of high momentum partons in the early stages of a collision, the pre-equilibrium, produces hard probes like production of heavy flavour quarks, quarkonia, and jets. Soft probes are related to later-produced collision signals such as hadron spectra, and anisotropy. The strangeness enhancement can be part of soft or hard probes, depending on its transverse momentum. In the early stages of collisions, electromagnetic probes, such as direct photons and dileptons, are produced, either by first hard collisions or by high temperature. The electromagnetic probes carry information deep inside the [QGP](#) since they have less interaction with the [QGP](#) or hadronic particles [39]. In the following, some of these probes will be discussed, although not in more details.

### 1.4.1 Jet-quenching

When a parton of one hadron collides with a parton of another hadron from the opposite direction in a relativistic heavy ion collision, various partons with very high transverse momenta are produced. Then, they move in all possible directions from the collision positions and subsequently fragment into thin cones of hadrons named jets. They are produced as pairs back to back. In principle, these highly energetic secondary quarks,

antiquarks, and gluons are known as jet partons. When one of the jet parton pairs interacts with the medium particles, they lose energy and momenta before hadronizing.

The interaction between hard partons and the colored medium leads to "jet quenching" [40]. It is important in understanding the thermodynamical or transport properties of the QGP in energetic collisions. The precise procedures for the interaction of energetic partons with the hot and dense nuclear medium, as well as the expression of medium modification of jets in the final state observables, are the key topics of jet quenching in HICs. The formation and the interaction of jets with dense nuclear matter can be investigated via the perturbative Quantum ChromoDynamics (pQCD) on a large scale.

The nuclear modification factor,  $R_{AA}$ , is employed to estimate the number of particles suppressed by the jet quenching process. The value of  $R_{AA}$  is determined by [39, 41]

$$R_{AA}(p_t) = \frac{\frac{dN_{AA}}{dp_t}}{N_{coll} \times \frac{dN_{pp}}{dp_t}}, \quad (1.4.1)$$

where  $\frac{dN_{AA}}{dp_t}$  and  $\frac{dN_{pp}}{dp_t}$  are the transverse momentum distribution for AA and pp collisions, respectively. The  $N_{coll}$  is the average number of nucleon-nucleon interactions in AA collisions. If we assume that no jet quenching has occurred, the ratio for all jet momenta must equal unity  $R_{AA} \approx 1$ . If the ratio is less than unity  $R_{AA} < 1$ , however, it can be used as a specific measure of jet suppression in the medium.

For various types of collisions, the jet quenching probe has been studied in both RHIC and LHC. Figs. 1.6 and 1.7 indicate the nuclear modification factor  $R_{AA}$  as a function of transverse momentum  $p_T$  for charged hadrons and other identified particles. Fig. 1.6 shows Pioneering High Energy Nuclear Interaction eXperiment (PHENIX) measurement for most central Au+Au collisions at  $\sqrt{s_{NN}} = 200$  GeV, and Fig. 1.7 reveals CMS and A Large Ion Collider Experiment (ALICE) measurements for most central Pb+Pb and p-Pb collisions at  $\sqrt{s_{NN}} = 5.02$  TeV. In comparison to pp collisions, the yields of high  $p_T$  charged hadrons are strongly suppressed in AA collisions.

In Fig. 1.6, for high  $p_T$  photons, the nuclear modification factor  $R_{AA}$  is consistent with unity. Photons do not have a color charge, therefore they only interact with matter electromagnetically. Due to the fact that photons' mean free paths are significantly larger than the medium size, they will fly to the detectors without additional rescattering. This demonstrates that the strong suppression seen for high  $p_T$  hadron production is related to the final state effect. For instance, the interaction of partonic jets with the colored medium usually causes jets to lose a portion of their energy. As illustrated in Fig. 1.7, for all ranges of transverse momentum, we have more suppression or less  $R_{AA}$  in the case of Pb-Pb than the p-Pb collision. We can claim we have a dense soup of quarks and gluons when we have a large suppression with  $R_{AA} < 1$  or jet quenching. There are further effects that have an impact on the proton-nucleus collisions'  $R_{AA}$ , such as the Cronin effect. Based on this effect, the high  $p_T$  hadrons are not suppressed, like p-Pb collisions in Fig. 1.7, but they have a reasonably large production rate. James Cronin presented this effect [42], which demonstrates how bound nuclei help to produce high  $p_T$  particles.

### 1.4.2 Heavy flavours and quarkonia suppression

Heavy quarks are effective probes of the medium. Charm and beauty quarks (heavy quarks) are typically produced in hard-scattering processes between partons of colliding

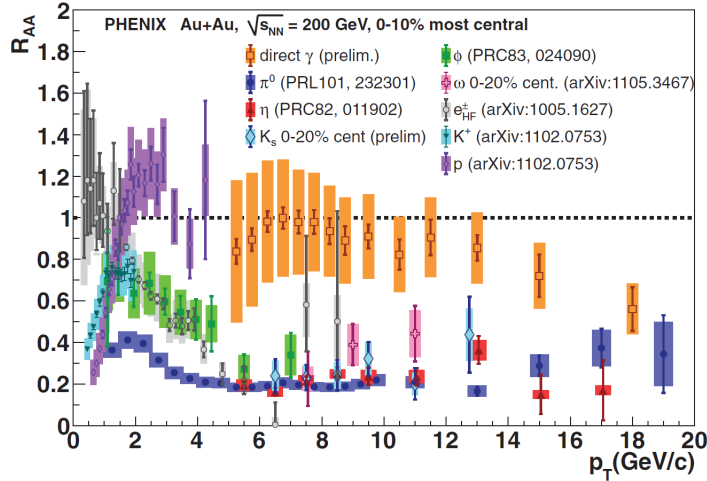


Figure 1.6: Nuclear modification factor of several mesons in the central (0–20%) Au–Au collisions [43] in the PHENIX experiment.

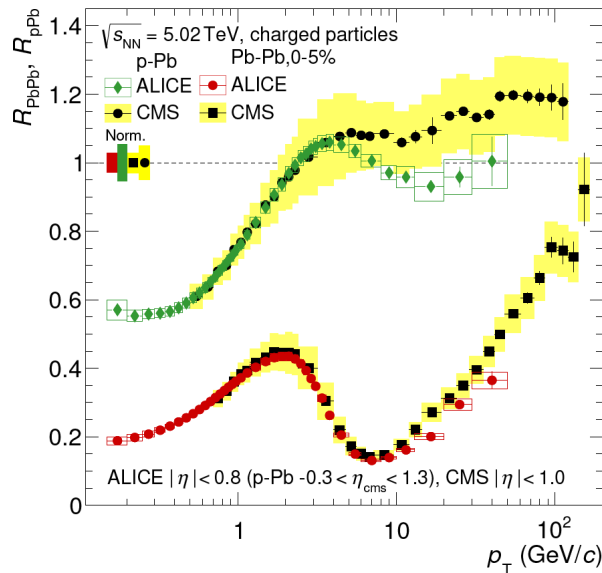


Figure 1.7: A comparison of the nuclear modification factors for central (0–5%) Pb–Pb and p–Pb collisions measured by ALICE and CMS [44].

nucleons because of their large masses. The pQCD calculations down to zero transverse momentum can be used to describe their production. Heavy quarks are created in the early stages of the nucleus–nucleus collision, before the QGP is formed. Then, they go through the entire system’s evolution while traveling across the medium and interacting with the QGP constituents.

Recent ALICE results on heavy flavour hadron production in pp, p–Pb, and Pb–Pb collisions at various energies are discussed in [45]. The heavy flavour hadrons might be open or closed. Charged heavy hadrons are known as open, such as D mesons ( $D^+(\bar{d}c)$ ,  $D^-(d\bar{c})$ ,  $D_s^+(\bar{s}c)$ ,  $D_s^-(s\bar{c})$ ). The neutral heavy hadrons are referred to closed or quarkonia, like  $J/\psi$  ( $c\bar{c}$ ), and  $\Upsilon$  ( $b\bar{b}$ ).

$c\bar{c}$  pairs are the "hardest" particles that can be produced at SPS energy ( $\sqrt{s_{NN}} < 450$  GeV [46]) and are easily identifiable by their unique decay pattern. These charmed quarks

and antiquarks form either a bound charmonium state ( $J/\psi$ ,  $\psi'$ , or  $\chi$ , "hidden charm" production) or they find light quark partners to hadronize into "open charm" states ( $D$  and  $\bar{D}$  mesons or charmed baryons).

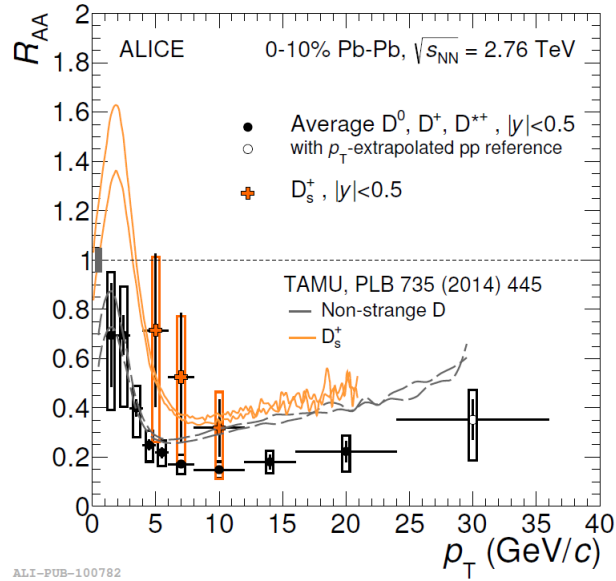


Figure 1.8:  $R_{AA}$  of prompt  $D_s^+$  and non-strange  $D$  mesons (average of  $D^0$ ,  $D^+$  and  $D^{*+}$ ) in the 0-10% centrality class, compared to TAMU model predictions [47].

The  $R_{AA}$  of open heavy flavour measured with ALICE for  $D^0$ ,  $D^+$ ,  $D^{*+}$ , and  $D_s^+$  in Pb-Pb collisions shows a substantial decrease of yields at large transverse momenta ( $p_T > 5$  GeV/c) in the most central collisions compared to a pp reference, see Fig. 1.8. Charm quark in-medium energy loss is considered to be the cause of this suppression.

When the  $c\bar{c}$  pair is created in HICs, the two heavy quarks must travel through a dense medium of soft particles, which interferes with their aim to hadronize and modifies their branching ratios into open and hidden charm states, similar to what happens with the jets. If the soft medium thermalizes into a QGP, the colored quarks and gluons in the plasma screen the color interaction between the  $c$  and  $\bar{c}$ , preventing their usual binding into one of the charmonium states. " $J/\psi$  suppression" should occur as a result of this [48].

Fig. 1.9 illustrates the nuclear modification factor  $R_{AA}$  of  $J/\psi$  as a function of the number of participants  $N_{part}$  in central Au-Au collisions. Open circles represent data in the midrapidity ( $|y| < 0.35$ ) and full circles indicate data in the forward and backward rapidities ( $1.2 < |y| < 2.2$ ). As  $N_{part}$  is raised, the suppression becomes stronger. This behavior is compatible with theoretical predictions that  $J/\psi$  should melt in the QGP since the initial temperature and size of the QGP are increased for larger  $N_{part}$ .

### 1.4.3 Anisotropic flow

The strong anisotropic collective flow in the plane transverse to the beam is one of the consequences of the hydrodynamical behavior and interesting observable to study the QGP formation in HICs. The collective properties concern soft bulk matter consisting of more than 99 percent of particles produced in collisions. Due to the intrinsic collision geometry and fluctuations of the initial states, the produced QGP matter in a AA collision is anisotropic in the transverse plane [50–53]. The beam direction ( $z$ ) and the impact

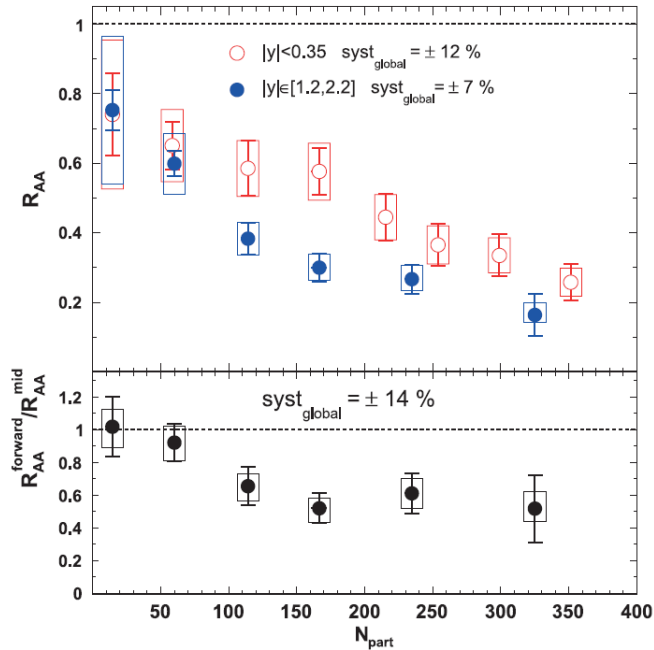


Figure 1.9: Nuclear modification factor  $R_{AA}$  of  $J/\psi$  as a function of the number of participant nucleons  $N_{part}$  in the central (0–10%) Au-Au collisions at  $\sqrt{s_{NN}} = 200$  GeV [49].

parameter direction ( $x$ ) define the reaction plane. The transverse plane is defined by the impact parameter direction and the third orthogonal direction ( $y$ ), see Fig 1.10.

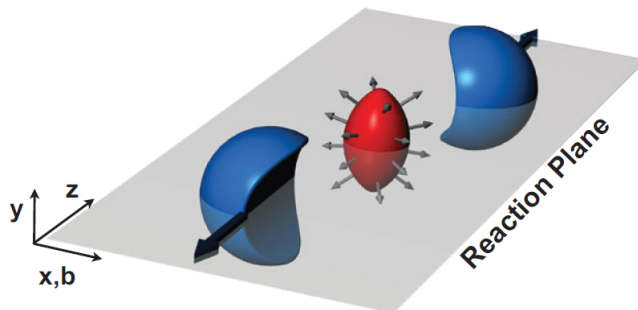


Figure 1.10: Almond shaped interaction volume after a non-central collision of two nuclei. The spatial anisotropy with respect to the  $x$ - $z$  plane (reaction plane) translates into a momentum anisotropy of the produced particles [54].

The anisotropies in the initial geometry of the collisions are transformed via pressure gradients to the anisotropies in the final state momentum distribution. The particle momentum distribution anisotropy can be calculated as follows using the Fourier expansion of the spectrum [54],

$$E \frac{d^3 N}{d^3 \mathbf{p}} = \frac{1}{2\pi} \frac{d^2 N}{p_t dp_t dy} \left[ 1 + 2 \sum_{n=1}^{\infty} v_n \cos [n(\phi - \Psi_{RP})] \right], \quad (1.4.2)$$

where  $E$  is the energy of the particle,  $\mathbf{p}$  the momentum,  $p_t$  the transverse momentum,  $\phi$  the azimuthal angle,  $y$  the rapidity, and  $\psi_{RP}$  the reaction plane angle. Because of the reflection symmetry with respect to the reaction plane, the sine terms in such an

expansion vanish. Eq. 5.2.1 is an idealized formula. In reality, one uses the event plane angle ( $\psi_{EP}$ ) instead of the reaction plane angle ( $\psi_{RP}$ ) because the  $\psi_{RP}$  cannot be observed. I will explain more about the event plane method in chapter 5. The Fourier coefficients concerning the event plane, which are dependent on  $p_t$  and  $y$ , are given by

$$v_n(p_t, y) = \langle \cos [n(\phi - \psi_{EP})] \rangle, \quad (1.4.3)$$

in the  $(p_t, y)$  bin under research, the angular brackets denote an average over the particles, sum over all events. The directed and elliptic flows are the first two coefficients of the Fourier expansion. The  $v_1 = \langle \cos \phi \rangle$  corresponds to the strength of the directed flow and  $v_2 = \langle \cos 2\phi \rangle$  quantifies the strength of the elliptic flow. Elliptic flow is a measure of how the flow is not uniform in all directions when viewed along the beam-line ( $z$  direction). The magnitude of  $v_2$  is sensitive to the initial conditions, fluctuation and geometry, and the [EoS](#) of the hot and dense fireball.

The higher order flow harmonics, such as  $v_3$ ,  $v_4$ ,  $v_5$ , etc., are sensitive parameters for studying initial state fluctuations and to obtain  $\eta/s$  ratio, where  $\eta$  is shear viscosity over entropy density  $s$  of the fluid produced in a collision. The original asymmetry in the configuration space (non-central collisions) and rescatterings are the two causes of anisotropic flow [55].

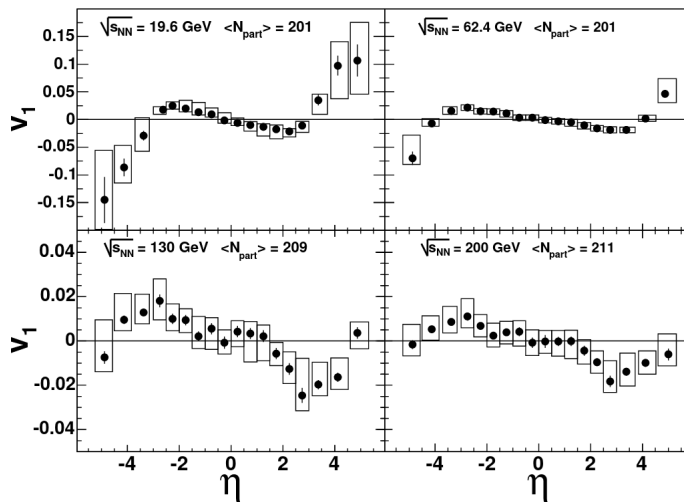


Figure 1.11: Measured directed flow as a function of space-time rapidity  $\eta$  of [Au-Au](#) collisions at  $\sqrt{s_{NN}} = 19.6, 62.4, 130,$  and  $200$  GeV averaged over centrality (0 – 40%) from the [PHOBOS](#) experiment [56].

The directed flow is mostly formed at an early stage of the collisions and hence is sensitive to early pressure gradients in the developing nuclear matter [57]. Stronger pressure develops when the [EoS](#) gets harder. As a result, the directed flow investigates the stiffness of the nuclear [EoS](#) at the early stages of nuclear collisions, which is crucial for heavy-ion research and astrophysics [58]. The initial conditions of the medium are very important for directed flow. The  $v_1$  is supposed to be produced by the spectator matter deflecting at high pseudorapidity. Because the deflection anisotropy is small at mid-rapidity,  $v_1$  goes to zero very quickly as can be seen in Fig. 1.11. The deflection perpendicular to the beam appears to be smaller as the beam energy increases.

In the case of elliptic flow, the eccentricity defines the initial "ellipticity" of the overlap zone, assuming the reaction plane is the  $xz$ -plane. The spatial anisotropy decreases

as the system expands. This is the cause for elliptic flow's great sensitivity to system evolution at very early times, 2–5 fm/c, on the scale of the system's size [57].

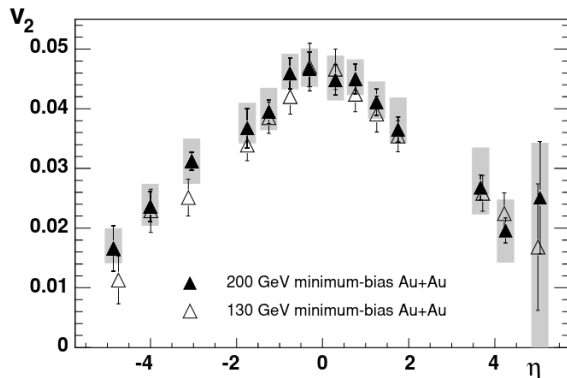


Figure 1.12: Elliptic flow as a function of pseudorapidity  $\eta$  for charged hadrons in minimum-bias Au-Au collisions at  $\sqrt{s_{NN}}=130$  GeV (open triangles) and 200 GeV (closed triangles). One sigma statistical errors are shown as the error bars. Systematic errors (90% C.L.) are shown as gray boxes only for the 200 GeV data [59].

The minimum-bias result using the hit-based approach for Au+Au collisions at 200 GeV and 130 GeV data are shown in Fig. 1.12. The results show a steady decrease in  $v_2$  as  $|\eta|$  increases, comparable to what is seen at lower energies such as  $\sqrt{s_{NN}}=130$  GeV. Within the systematic errors, there is no noticeable difference in shape or magnitude. In the mid-rapidity region, the elliptic flow is particularly remarkable.

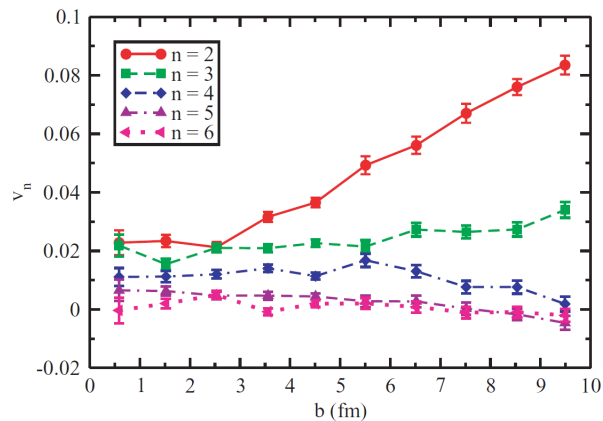


Figure 1.13: (Color online) The final-flow coefficients  $v_n$  as a function of impact parameter  $b$  [60] in Au-Au collisions at 200 GeV.

The impact parameter (or centrality) dependence of the final state flow coefficients can be studied as shown in Fig. 1.13. For all impact parameters, the splitting of  $v_n$  is clearly visible: lower  $v_n$  are bigger than higher  $v_n$ , at least for the first few  $v_n$  (for  $n \geq 5$ ,  $v_n$  are so small that their splitting is difficult to resolve). To distinguish between various curves for the most central collisions, sufficient statistics are required. Even if the splitting may be smaller, one would predict the same ranking. As a result, it should reflect the fact that the lowest  $v_n$  has the highest centrality dependence.

### 1.4.4 Strangeness enhancement

One of the initial signatures proposed for the possible observation of a QGP is strangeness enhancement [61]. The strangeness production would be as soft or hard hadronic probes depending on the transverse momentum. Nucleons containing up ( $u$ ) and down ( $d$ ) quarks collide in pp or HICs. However, hadrons made up of  $u$ ,  $d$ , and other heavy quark flavors can be seen in the final state. Strange ( $s$ ) quarks are the lightest among the rest of the quarks with the strangeness quantum number.

In all scenarios (statistical hadronization and string decay), strange hadrons are suppressed compared to those composed of  $u$  and  $d$  quarks, but this "strangeness suppression" is stronger in string decay compared to statistical production. The suppression is even more pronounced in the case of multi-strange baryons. They are very much suppressed in string decay compared to statistical decay.

In EPOS model [62], there are both: the core represents statistical hadronization, and the corona part string decay. I will explain more about core and corona in the next chapter. In Fig. 1.14, the omega ( $\Omega$ ) and kaon ( $K$ ) to pion ratio versus multiplicity per  $\eta$  interval  $\langle dn/d\eta(0) \rangle$  at central pseudorapidity ( $\eta=0$ ) have been shown for both statistical hadronization, and string decay contributions. Look at the caption of Fig. 1.14 to see different contributions made in this simulation.

One can see that the corona curves are way below the core ones in both  $K$  and  $\Omega$  productions. The core-corona method provides a mixture of core and corona contributions, the corona weight increases with multiplicity. So comparing pp (small  $dn/d\eta(0)$ ) and central Pb-Pb, we compare "string decay" with "statistical decay", showing a huge (not-huge) increase concerning  $\Omega$  ( $K$ ) over  $\pi$  production. So what is usually referred to as "strangeness enhancement" is essentially the fact that particles, especially multi-strange particles like  $\Omega$ , are much more frequent in statistical particle production compared to string decay. The full curve (including core, corona, and hadronic cascade contributions) for  $\Omega$  is slightly reduced at high multiplicity than co+co due to hadronic final state interactions (baryon-baryon annihilation).

Strangeness enhancement has been experimentally observed in experiments at the CERN SPS [69], RHIC [70], and LHC [67] energies in HICs. In chapter 5, we will show some results for various types of strange/multi-strange particles.

### 1.4.5 Photons

One of the electromagnetic probes produced in pp, pA, and AA collisions is the inclusive photon yield. Direct photons and indirect photons are two types of inclusive photons. In the following, I will classify these two types of photons.

#### Indirect photons

Indirect photons are also known as decay photons. The decay photons make up the majority of the inclusive photon spectrum. They are created by the photonic decay of hadrons (mesons and baryons) which are produced during the reaction. Since these decays occur at later times and outside of the active reaction zone (maybe in a mixed state or hadronization), they provide only relatively little information about the initial high-energy state. As a result, researchers have tried to remove the decay photons from the inclusive yield (preferably using experimental methods) and investigate the remaining

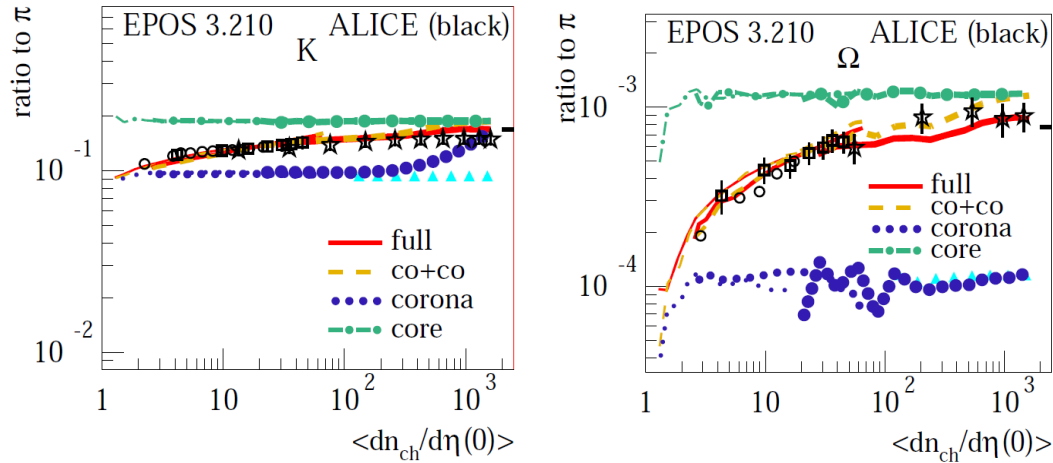


Figure 1.14: (Color online) Strange particles (Kaon  $K$  (l.h.s), and Omega  $\Omega$  (r.h.s)) yields to pion ratio versus multiplicity  $\langle dn_{ch}/d\eta(0) \rangle$ , for different contributions from the EPOS 3 simulations [62], and different systems (pp, p-Pb, and Pb-Pb). The green dashed-dotted, blue dotted, yellow dashed, red full, and blue triangles are related to particles from the core only (core), particles from corona only (corona), particles from core and corona (co-co), all particles with hadronic cascade (full), and particles from pure string decay, respectively. The thin, intermediate, and thick lines refer to pp, p-Pb, and Pb-Pb collisions. The results compared to the ALICE data with open circles (pp), open squares (p-Pb), and open stars (Pb-Pb) from [63–68].

photons as direct photons.

Different definitions of decay photons are used by the various collaborations depending on the particular experimental set-up. The decays of  $\pi^0$ - and  $\eta$ -mesons are removed from the inclusive photons by all groups. Some groups, however, also include decays of the less common and short-lived particles  $\eta'$ ,  $\omega$ ,  $\phi$ ,  $a_1$  and the  $\Delta$ -resonance in their calculations such as Parton Hadron String Dynamics (PHSD) group [71]. Because of photon emission during multiple absorption and formation in the initial interaction phase, experimental approaches for determining the  $a_1$  and  $\Delta$  are problematic. The photon production from the following hadronic decays is predicted using PHSD:

$$\pi^0 \rightarrow \gamma + \gamma, \quad \eta \rightarrow \gamma + \gamma, \quad \eta' \rightarrow \rho + \gamma, \quad \omega \rightarrow \pi^0 + \gamma, \quad \phi \rightarrow \eta + \gamma, \quad a_1 \rightarrow \pi + \gamma, \quad \Delta \rightarrow \gamma + N,$$

where the parent hadrons can be generated in baryon–baryon (BB), meson–baryon (mB), or meson–meson (mm) collisions, or they can come via hadronization. The decay probabilities are derived using the appropriate branching ratios from the Particle Data Group’s latest collection [72].

### Direct photons

The direct photons are derived by removing the decay-photon contributions from the inclusive (total) spectra observed experimentally, as I explained in the previous paragraph. The direct photons include the prompt and thermal photons.

The photons with large transverse momentum  $p_T$ , also known as prompt or pQCD photons, are produced in the early stages via hard nucleon-nucleon collisions, and they come from jet fragmentation. The pQCD models their contributions effectively. Contributions from the produced jet- $\gamma$ —conversion in the QGP may also be present in AA

collisions at high  $p_T$ , and photons from the scattering of hard partons by thermalized partons,  $q_{hard} + q(g)_{QGP} \rightarrow \gamma + q(g)$ .

There is a significant remaining photon yield for  $p_T < 3$  GeV/c after the prompt photons are subtracted from the direct photon spectra, which are defined as thermal photons. These kind of photons can be emitted by different partonic and hadronic sources as:

1. Photons that are radiated by quarks in the interaction with antiquarks and gluons,  $q + \bar{q} \rightarrow g + \gamma$ , and  $q/\bar{q} + g \rightarrow q/\bar{q} + \gamma$ . Additionally, photon production in the bremsstrahlung reactions,  $q + q/g \rightarrow q + q/g + \gamma$ , is possible [73].

2. All colliding hadronic charges (meson, baryons) can also radiate photons by the bremsstrahlung processes,  $m + m \rightarrow m + m + \gamma$ , and  $m + B \rightarrow m + B + \gamma$  [74].

3. Binary meson + meson and meson + baryon collisions can produce photons. The following  $2 \rightarrow 2$  scattering mechanisms can predict direct photon production within PHSD:

$$\pi + \pi \rightarrow \rho + \gamma, \quad \pi + \rho \rightarrow \pi + \gamma, \quad V + N \rightarrow \gamma + N,$$

where  $V$  is the vector mesons such as  $\rho, \phi, \omega$ , and  $N = n, p$  [75].

On the left side of Fig. 1.15, the results for the inclusive photon spectrum as a sum of all the considered partonic and hadronic sources for photons produced in minimal bias Au+Au collisions at  $\sqrt{s_{NN}} = 200$  GeV as a function of the transverse momentum  $p_T$  at midrapidity  $|y| < 0.35$  are shown. The simulations have been done in PHSD framework. From the results, it is clear that indirect photons are produced in larger abundance than other types of photons.

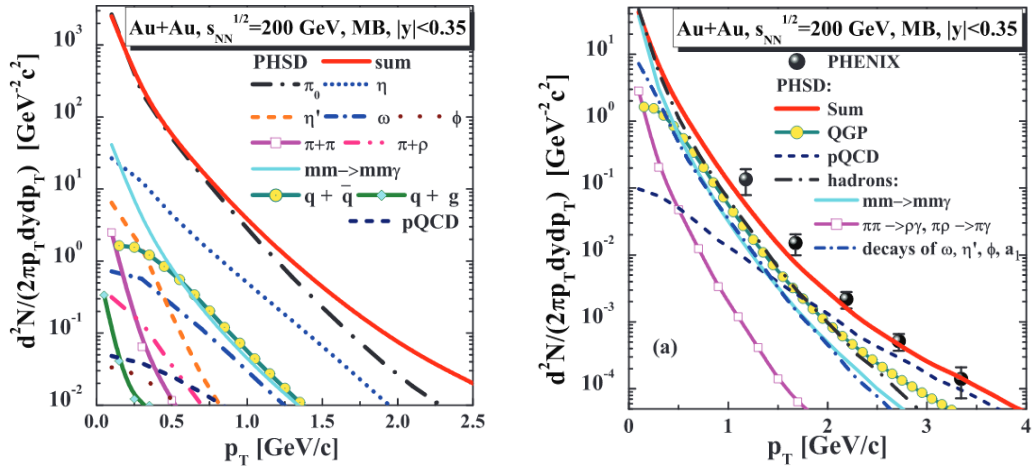


Figure 1.15: Photon production as a function of transverse momentum  $p_T$  spectrum from PHSD for minimal bias Au-Au collisions at  $\sqrt{s_{NN}} = 200$  GeV at midrapidity  $|y| < 0.35$  [74]. Left: (color online) the channel decomposition of the inclusive photon  $p_T$  spectrum. Right: (color online) direct photons (sum of all photon production channels except the  $\pi^-$  and  $\eta$ -mesons decays) from PHSD approach (red solid line) in comparison to the PHENIX experiments [76]. The channel description is given in the legend.

These indirect photons, are subtracted experimentally to access the direct photons spectrum because they are less sensitive to the formation of the hot and dense medium and its properties. As illustrated on the right side of the Fig. 1.15, the sum over direct photon production is near to the real data from PHENIX experiment. If the partonic and hadronic sources are added together (red solid line), the observed transverse

momentum spectrum  $dN/dp_T$  can be reproduced. The photons emitted by the strongly QGP represent for slightly less than half of the total number of photons detected. The radiation of hadrons and their interactions also make a significant contribution, especially at low transverse momentum. Meson decays and meson-meson bremsstrahlung are the most common hadronic sources.

### 1.4.6 Dilepton production

Dilepton production is another electromagnetic probe. Dileptons ( $e^+e^-$ ,  $\mu^+\mu^-$  pairs or virtual photons  $\gamma^*$ ) can be produced from all stages of the heavy-ion reactions as well as real photons. The virtual photons do not transfer energy from one place to another, while real photons do [77]. One of the advantages of dileptons versus photons is that they have an extra "degree of freedom": the invariant mass which allows various sources to be identified. The dilepton is characterized by dilepton invariant mass squared  $M^2 = (p^+ + p^-)^2$ , where  $p^+$  and  $p^-$  are the four-momenta of the two leptons. Also, the dilepton transverse momentum is defined as  $p_t = (p_t^+ + p_t^-)$ , where  $p_t^+$  and  $p_t^-$  are the transverse momenta of the two leptons. In pp, pA, and AA collisions, the following production sources of dileptons occur [71].

**Hadronic sources:** It can happen for different ranges of hadrons invariant masses. Hadronic sources are: i) At low invariant masses ( $M < 1 \text{ GeV}/c^2$ ), the Dalitz decays of mesons and baryons ( $\pi^0, \eta, \Delta, \dots$ ) and the direct decay of vector mesons ( $\rho, \omega, \phi$ ) as well as the hadronic bremsstrahlung [78].

ii) At intermediate masses ( $1 \text{ GeV}/c^2 < M < 3 \text{ GeV}/c^2$ ), leptons from correlated  $D^+D^-$  pairs [79], and radiation from multi-meson reactions ( $\pi + \pi, \pi + \rho, \pi + \omega, \rho + \rho, \pi + a_1, \dots$ ) [80].

iii) At high invariant masses ( $M > 3 \text{ GeV}/c^2$ ), the direct decay of vector mesons ( $J/\psi, \psi'$ ) [81] and initial 'hard' Drell-Yan annihilation to dileptons ( $q + \bar{q} \rightarrow l^+l^-$ , where  $l = e, \eta$ ) [81].

**Partonic sources:** Partonic interactions in HICs produces thermal QGP dileptons, which provide the majority of the intermediate masses. Thermal  $q\bar{q}$  annihilation ( $q + \bar{q} \rightarrow l^+ + l^-, q + \bar{q} \rightarrow g + l^+ + l^-$ ) and Compton scattering ( $q(\bar{q}) + g \rightarrow q(\bar{q}) + l^+ + l^-$ ) are the most important mechanisms [82].

These dileptons must then pass through the collision region on their way to particle detectors. They have large mean free paths and interact electromagnetically. As a result, the produced lepton pairs do not collide with each other before reaching the detectors, keeping the information about the inside of the fireball.

Fig. 1.16 indicates the invariant mass spectrum of dielectrons in minimum bias Au+Au collisions at  $\sqrt{s_{NN}}=200 \text{ GeV}$  in PHSD compare to the STAR data. From this figure it can be figured out that dielectrons from hadronic channels such as  $\pi^0$  and  $\eta$ , dominate the low-mass range, whereas partonic interactions and heavy flavor decays dominate the intermediate-mass range as we have already explained in the previous paragraphs. PHSD results for the sum over all decay channels are quite close to the real data except for the invariant mass at 3 GeV which might be due to neglecting some decay channels like  $J/\psi$  and  $\psi'$ .

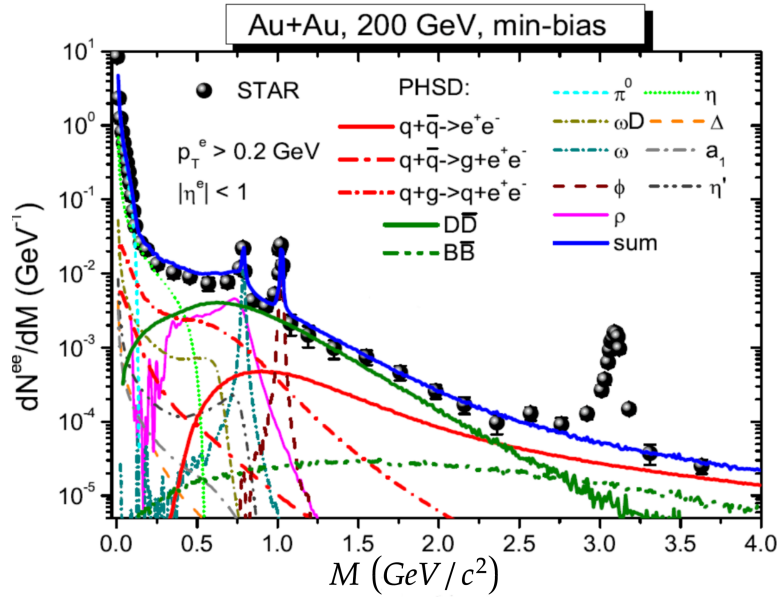


Figure 1.16: The invariant mass spectra of dielectrons from PHSD [83] in comparison to the STAR data in Au-Au collisions from  $\sqrt{s_{NN}} = 200$  GeV [84]. The total yield is displayed in terms of the blue lines while the different contributions are specified in the legends. Note that the contribution from  $J/\psi$  and  $\psi'$  decays are not included in the PHSD calculations.

## 1.5 Monte Carlo event generators

MC event generators are frequently used by experimentalists in analyses and many theorists in making predictions for collider experiments and developing ways to propose to the experiments [85]. MCs are critical tools in high-energy physics. They are also commonly employed as "black boxes" whose output is referred to as data. The most of recent Higgs discovery plots in CMS and ATLAS experiments, as an example of the importance of MC, depend essentially on MC predictions to set limits on Higgses in particular parameter space regions as well as to detect them [2, 86]. This should be enough to persuade us that event generators are needed for both discovery and precision physics.

One event in the event generator is identical to one pp or AA collision. The objective of a full event generator package is to reproduce the same amount of particles with the same characteristics as those created in an experiment. The structure of a pp collision formed by event generators at the LHC can be represented in a few key steps. As shown in Fig. 1.17 in most event generators, the color coding corresponds to the collision processes are separated into five stages for a pp as

- 1. Hard process:** this is performed by starting the simulation at the collision's center and estimating the probability distribution of a specific "hard scatter", which is the event's largest momentum transfer process, using perturbation theory. Simulating the hard process is simple because of the Parton Distribution Functions (PDFs), which describe how partons go into the process, and lowest order perturbation theory, which gives a probabilistic distribution of outgoing partons.

- 2. Parton shower:** what happens to the incoming and outgoing partons involved in the hard collision is a more interesting stage of event production. The parton shower phase of event generators explains this. Colored particles, quarks, and gluons are the

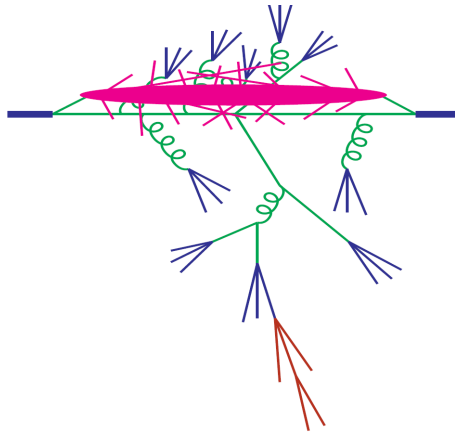


Figure 1.17: Diagram showing the structure of a proton-proton collision, where the different colours indicate the different stages involved in event generation [85]. Green, blue, deep pink and brown colors are related to parton shower, hadronization, underlying event, and particle decays, respectively.

partons engaged in the hard process. It is well known from QED that scattered electric charges emit photons, a phenomenon known as Bremsstrahlung. In the same way that scattered color charges emit gluons, partons emit gluons when they enter and leave a collision. The main difference from QED is that gluons are colored due to the non-Abelian structure of SU(3), and therefore an emitted gluon can affect additional radiation. The phase space starts up with soft gluons as a result of the extended shower. The parton shower may be described as a step-by-step process expressed in terms of momentum transfer scale evolution. The evolution of the parton shower begins with the hard process and continues down to lower and lower momentum scales till perturbation theory breaks.

**3. Hadronization:** everything we have learned so far has been predicated on pQCD, yet partons are not the final state particles that emerge after a collision since they cannot freely propagate. Hadrons are the physical final state particles, but we do not know how to compute them, therefore we need a model to describe how colored partons are confined into colorless hadrons, a process known as hadronization.

**4. Underlying event:** in the lab frame, a collision between two protons occurs when two pancakes (very fast protons) are totally overlapping one other in space time. The underlying event, which is made up of the production of the jet (hard partons) connected to its event, is produced as a result of this.

**5. Unstable particles decays:** The last element of event generation is that many of these hadrons have heavy resonances that decay after a short amount of time.

Pythia/Angantyr, Herwig, ISAJET, HIJING, AMPT, and EPOS are some of the famous hadronic event generators employed in current experiments, running from hard collisions to stable hadrons [87].

Pythia/Angantyr [88, 89] is a software for generating high-energy physics collision events, that is, collisions involving electrons, protons, photons, and heavy nuclei at high energies. It includes theory and models for hard and soft interactions, parton distributions, initial- and final-state parton showers, multiparton interactions, fragmentation, and decay, among many other physics topics. Inside Pythia, the Lund String Model is

utilized as an initial condition for PHSD [90]. In the third chapter, I will go through this approach in more detail.

Herwig [91] is a general-purpose event generator for simulating high-energy lepton-lepton, lepton-hadron, and hh collisions, with a focus on precise QCD radiative simulation.

ISAJET [92] is a MC simulation program for pp, p  $\bar{p}$ , and  $e^+e^-$  interactions at high energies. ISAJET is based on pQCD and parton and beam jet fragmentation phenomenological models.

HIJING [93] is a MC event generator for parton and particle production in high-energy hadronic and nuclear collisions. Based on QCD-inspired models for multiple jet production, it is designed in particular to study jet and mini-jet production and associated particle production in high energy pp, pA, and AA collisions. This model incorporates multiple mini-jet productions, soft excitation, nuclear shadowing of parton distribution functions, and jet interactions in the dense hadronic matter.

AMPT [94] is a MC transport model for HICs at relativistic energies. It provides a kinetic description of all stages of HICs. Additionally, it includes both types of interaction, i.e., partonic and hadronic levels, and the transition between two phases of matter.

Last but not least, there is also EPOS event generator [95]. This is one of the most effective event generators for many collision types, including lepton-lepton, lepton-proton, pp, pA, and AA collisions. It was written using the Parton-Based-Gribov-Regge Theory (PBGRT) as a basis. In the following chapter, I will explain everything about this event generator in more detail.

## 1.6 Summary and conclusion

In this chapter, I began writing some basic backgrounds that I would need to know in order to fulfill my Ph.D thesis.

The goal of this project is to integrate two advanced models, EPOS and PHSD, to investigate the QGP dynamics in heavy ion collisions. Despite the fact that these two models use distinct approaches to accomplish their goals, they both work on the same principles. The roles in the SM are followed by both of them. To do this, I opened this chapter by introducing fundamental particles such as quarks and leptons, and forces in the SM like strong, electromagnetic, and weak. Because all of spectra in this work are specified in natural units, I have presented them.

Then, in the second section, I talked about how the QGP is formed theoretically from QCD in the SM. The QGP can be produced in the lab by colliding heavy nuclei at ultra-relativistic energies, such as those performed at LHC and RHIC. After two heavy nuclei collided, there are several steps to consider, including pre-equilibrium, QGP, hadronization, and freeze-out. The Bjorken scenario was one of the first hydrodynamical models to take into account the stages discussed in the third section.

Following that, I went through some particular methods for studying the QGP characteristics including soft, hard, and electromagnetic probes. Since the QGP cannot be seen in real time, theoretical models must anticipate which characteristics of the inter-

actions' final state will be relevant in identifying QGP formation. Before being used as the QGP signatures, these properties must be proven.

I finished this chapter by summing up the MC event generators in hadron interactions. MC event generators are used by theorists and experiments to make predictions and plan for future experiments, and they are an essential part of nearly all experimental analyses. The hadronic event generators were discussed briefly.

In the following chapter, I will go through the philosophy behind EPOS event generator and how one event is generated within it.



**EPOS** stands for a particularly successful event generator to produce particles by simulating high energy collisions, based on the **MC** technique. It is a universal model for all varieties of collisions. First, I will go through the history of **EPOS** and explain the theory behind it, then I will go over the step-by-step procedure of how the particles are produced in this event generator.

## 2.1 A brief history of EPOS

The earliest predecessor of **EPOS** was **VENUS** [96] which stood as one of the primary event generators based on simple multiple interactions to represent the soft **pp** processes in 1990. **VENUS** also predicts more central baryons in **AA** collisions. It has been revealed throughout the time of **SPS** at **CERN** and **AGS** at **BNL**. In **VENUS** model not only color exchange between quarks is considered as basic reaction mechanism, but also color exchange between antiquarks. This model realizes a nuclear collision in three independent steps: i) From geometrical considerations, it is determined which nucleons from projectile and target nucleus collide with each other. ii) An individual collision leads to color exchange between quarks and also between antiquarks, these color rearrangements being the origin of color string formation. iii) After all strings have been formed due to color exchange, they are fragmented into observable hadrons by using an iterative fragmentation cascade. The fragmentation is assumed to be the same as in lepton scattering [97].

Klaus Werner, the inventor of **VENUS**, decided to develop **VENUS** into the "**NEXUS**" model in 2000 to have a comprehensive classification of both soft and hard processes of the hadronic collisions [98]. The new model provides more reliable extrapolation towards high energy since it has a more solid theoretical basis than it is used in **VENUS**. During these times, the **NEXUS** split into **QGSJET** [99] which has been successfully employed including triple pomeron contributions and more, to all orders in the field of high energy cosmic rays, and **EPOS** based on **PBGRT** [100]. It implies a consistent treatment of hard and soft processes, and allows the computation of both elastic and inelastic cross-sections, respecting energy sharing during the multiple pomeron exchanges. The main privilege of such a proposal is that **EPOS** can reliably simulate all types of hadronic collisions such as **pp**, **pA**, or even **AA**, and one can also model collective phenomena. Additionally, it can still treat the cosmic rays simulations by realizing fixed-target collisions.

In 2010, the event generator developed to **EPOS 2** [101, 102], including a perfect-fluid hydrodynamic evolution of matter, based on a core-corona separation procedure,

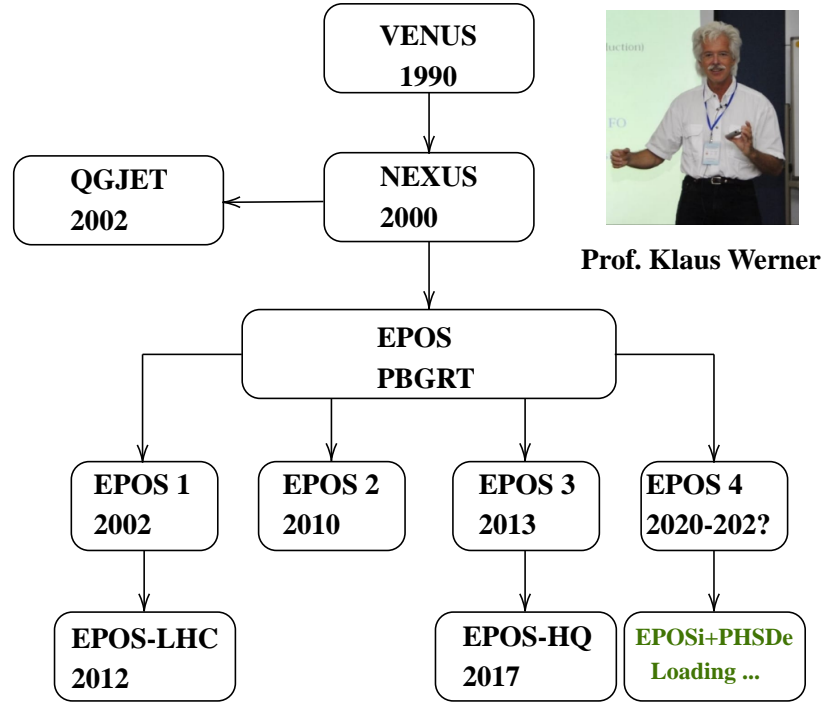


Figure 2.1: Pedigree of EPOS by year.

and finally using a hadronic cascade the [Ultrarelativistic Quantum Molecular Dynamics \(UrQMD\)](#) model [103].

[EPOS LHC](#) version [104] was written by tuning the model over minimum bias  $pp$ ,  $p$ -Pb, and Pb-Pb collisions provided by [LHC](#) experiments in 2012, at the end of the first RUN. [EPOS LHC](#) is based on [EPOS 1](#) (without hydrodynamic evolution). In particular, it discusses the effect of the collective hadronization in  $pp$  scattering.

The subsequent important upgrade, which led to [EPOS 3](#) [95], was the inclusion of heavy quarks [105], parton saturation, and viscous hydrodynamics [106]. [EPOS HQ](#) [107] has been developed in order to quantify the off-equilibrium dynamics of heavy flavor at lower transverse momentum  $p_T$  in 2017.

The newest version, [EPOS 4](#), implements a new saturation method, and will be published in the near future. In current investigation, [EPOSi+PHSDe](#), we endeavor to employ [EPOS 4](#) as an initial condition ([EPOSi](#)) to do the evolution of  $AA$  collision based on the [PHSD \(PHSDe\)](#) model. In Fig. 2.1, the pedigree of EPOS by year has been illustrated.

## 2.2 The theoretical foundation of EPOS

In this section, I want to represent the theories within EPOS that make up the main theory as [PBGRT](#). The [PBGRT](#) merges the [Parton Model \(PM\)](#) and the [Gribov-Regge Theory \(GRT\)](#), as its title implies. In the subsections that follow, we will take a short look at these two models. We will see why combining both of these approaches into a particular approach is necessary.

### 2.2.1 Parton Model

With the installation of the [Stanford Linear Accelerator Center \(SLAC\)](#) accelerator in 1962, the possibility of colliding two protons with a center of energy more than 10 GeV arose. These collisions tell that the proton is not an elementary particle. To explain the [pp](#) collisions, Feynman presented the [PM](#) in 1969 [108]. Feynman proposed that the proton was made up of point-like components called partons before quarks and gluons were widely recognized [109]. By using elementary parton interactions, Feynman decomposed the cross-section of a [pp](#) collision. At the same time, Bjorken derived the [PDFs](#) using the [PM](#) to describe [e<sup>-</sup>p](#) collisions. First, I will explain [e<sup>-</sup>p](#) collisions, and then I will go over [pp](#) collisions in the [PM](#).

#### Electron-proton collision

The main interaction in deep inelastic [e<sup>-</sup>p](#) scattering in the quark-parton model, as shown in [Fig. 2.2](#), is elastic scattering from a spin-half quark within the proton [1].

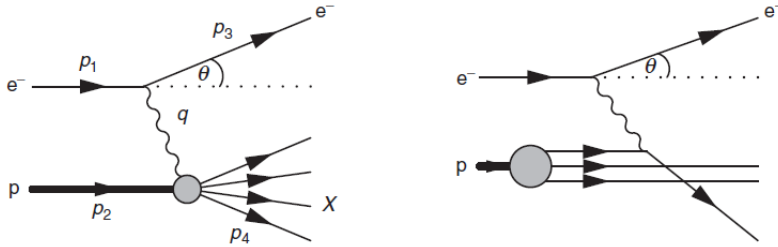


Figure 2.2: [e<sup>-</sup>p](#) scattering in the center-of-mass frame and the corresponding lowest-order Feynman diagram.

In the situation of  $E \gg m_p$ , when the proton has a very high energy, the quark-parton model for deep inelastic scattering is applicable. It uses the infinite momentum frame, which causes the proton's mass and any component of the struck quark's momentum that is transverse to the direction of the motion of the proton to be ignored. As a result, the struck quark's four-momentum may be written

$$p_q = \zeta p_2 = (\zeta E_2, 0, 0, \zeta E_2), \quad (2.2.1)$$

where  $\zeta$  is the proton's fractional momentum carried by the quark. After the interaction with the virtual photon, the quark's four-momentum is just  $\zeta p_2 + q$ . Because the final-state quark's four-momentum squared is equal to the square of its mass,

$$(\zeta p_2)^2 = \zeta^2 p_2^2 + 2\zeta p_2 \cdot q + q^2 = m_q^2. \quad (2.2.2)$$

Since  $\zeta p_2$  is the only four-momentum of the quark before the collision, therefore  $\zeta^2 p_2^2 = m_q^2$ . Thus, [Eq. 2.2.2](#) shows that  $q^2 + 2\zeta p_2 \cdot q = 0$  and the momentum fraction  $\zeta$  can be represented as

$$\zeta = \frac{-q^2}{2p_2 \cdot q} = \frac{Q^2}{2p_2 \cdot q} \equiv x. \quad (2.2.3)$$

The Bjorken variable is  $x$  in this context. The underlying electron-quark scattering system has kinematic parameters that are connected to the [e<sup>-</sup>p](#) collision such as  $x$ , [Eq. 2.2.3](#), and  $y$ , [Eq. 2.2.4](#), ignoring the electron and proton mass terms.

$$y = \frac{p_2 \cdot q}{p_2 \cdot p_1}. \quad (2.2.4)$$

The differential cross-section for  $e^-q \rightarrow e^-q$  can be written

$$\frac{d\sigma}{dQ^2} = \frac{4\pi\alpha^2 Q_q^2}{Q^4} \left[ (1-y) + \frac{y^2}{2} \right], \quad (2.2.5)$$

where  $y$  can be expressed as a function of  $x$

$$y = \frac{Q^2}{(s - m_p^2)x}. \quad (2.2.6)$$

Through the interchange of gluons, the quarks inside the proton will interact with one another. Within the proton, the dynamics of this interacting system will result in a distribution of quark momenta. PDFs are used to describe these distributions. For example, the up-quark PDFs for the proton  $u^p(x)$  is formulated by:

$$u^p(x)\delta x, \quad (2.2.7)$$

indicates the number of up-quarks inside the proton with momentum fraction between  $x$  and  $x + \delta x$ . The down-quarks are in a similar predicament. The PDFs are based on the proton's detailed dynamics, which they must get by experiment.

The  $e^-p$  deep inelastic scattering cross-section can be identified by the definition of the PDFs and the expression for the differential cross-section for underlying electron-quark elastic scattering process given in Eq. 2.2.5. The cross-section for elastic scattering from a particular flavour of quark  $i$  with charge  $Q_i$  and momentum fraction in the range  $x \rightarrow x + \delta x$ , is

$$\frac{d^2\sigma}{dQ^2} = \frac{4\pi\alpha^2}{Q^4} \left[ (1-y^2) + \frac{y^2}{2} \right] \times Q_i^2 q_i^p(x)\delta x, \quad (2.2.8)$$

where  $q_i^p(x)$  is the PDFs for that flavour of quark. Then the double-differential cross-section is obtained by dividing by  $\delta x$  and summing over all quark flavours

$$\frac{d^2\sigma^{ep}}{dx dQ^2} = \frac{4\pi\alpha^2}{Q^4} \left[ (1-y) + \frac{y^2}{2} \right] \sum_i Q_i^2 q_i^p(x). \quad (2.2.9)$$

This is the PM prediction for the  $e^-p$  deep inelastic scattering cross-section.

The general expression for the deep inelastic scattering cross-section in terms of structure function  $F(x, Q^2)$  can be determined by

$$\frac{d^2\sigma}{dx dQ^2} \approx \frac{4\pi\alpha^2}{Q^4} \left[ (1-y) \frac{F_2(x, Q^2)}{x} + y^2 F_1(x, Q^2) \right]. \quad (2.2.10)$$

Comparing Eqs. 2.2.9 and 2.2.10, one can write the relation between structure functions as:

$$F_2^{ep}(x, Q^2) = 2xF_1^{ep}(x, Q^2) = x\sum_i Q_i^2 q_i^p(x). \quad (2.2.11)$$

The PM predicts the Callan–Gross relation,  $F_2(x) = 2xF_1(x)$ . This is due to the underlying process being elastic scattering from spin-half Dirac particles; the quark magnetic moment is directly related to its charge and therefore the contributions from the electromagnetic ( $F_2$ ) and the pure magnetic ( $F_1$ ) structure functions are fixed with respect to one another.

For  $e^-p$  deep inelastic scattering, the structure function  $F_2^{ep}(x)$  for light quarks is related to the PDFs by

$$F_2^{ep}(x) = x\sum_i Q_i^2 q_i^p(x) \approx x \left( \frac{4}{9}u^p(x) + \frac{1}{9}d^p(x) + \frac{4}{9}\bar{u}^p(x) + \frac{1}{9}\bar{d}^p(x) \right), \quad (2.2.12)$$

where  $u^p(x)$ ,  $d^p(x)$ ,  $\bar{u}^p(x)$  and  $\bar{d}^p(x)$  are the up-, down-, anti-up and anti-down parton distribution functions for the proton, respectively. A similar expression can be written down for the structure functions for  $e^-n$  scattering. Integrating these expressions for the structure functions over the entire  $x$  range gives

$$\int_0^1 F_2^{ep}(x)dx = \frac{4}{9}f_u + \frac{1}{9}f_d, \quad (2.2.13)$$

where  $f_u$  and  $f_d$  are given by

$$f_u = \int_0^1 [xu^p(x) + x\bar{u}^p(x)]dx, \quad f_d = \int_0^1 [xd^p(x) + x\bar{d}^p(x)]dx. \quad (2.2.14)$$

The quantity  $f_u$  is the fraction of the momentum of the proton carried by the up- and anti-up quarks. Similarly  $f_d$  is the fraction carried by the down- and anti-down quarks. The momentum fractions  $f_u$  and  $f_d$  can be obtained directly from the experimental measurements of the proton and neutron structure functions. For instance, the experimental measurement of  $F_2^{ep}(x, Q^2)$  as a function of  $x$  for deep inelastic scattering events with  $2 \text{ (GeV}^2/c^2) < Q^2 < 30 \text{ (GeV}^2/c^2)$  as observed at SLAC gives [110]

$$\int F_2^{ep}(x)dx \approx 0.18. \quad (2.2.15)$$

Using the quark-parton model predictions of Eq. 2.2.14, these experimental results can be interpreted as measurements of the fractions of the proton momentum carried by the up- and anti-up- and down- and anti-down-quarks such as:

$$f_u \approx 0.36, \quad f_d \approx 0.18. \quad (2.2.16)$$

Given that the proton consists of two up-quarks and one down-quark. However, the total fraction of the momentum of the proton carried by quarks and antiquarks is just over 50 percent; the remainder is carried by the gluons that are the force carrying particles of the strong interaction. Because the gluons are electrically neutral, they do not contribute to the QED process of  $e^-p$  deep inelastic scattering.

### Proton-proton collision

The generalization of the  $e^-p$  collisions by a pure hadronic collision (here  $pp$ ) is used to describe all non-elementary interaction. This generalization describes all non-elementary interactions into elementary interactions between partons. We saw in the previous part that the measurements of the structure functions enable us to determine the PDFs, which are essential for the calculation of cross-sections at the  $pp$  colliders. Therefore, one can compute the cross-section of the  $pp$  collision based on the PM as:

$$\sigma(pp \rightarrow q_3q_4) \approx \int_0^1 \int_0^1 F_1(x_1, Q^2)F_2(x_2, Q^2)\sigma(q_1q_2 \rightarrow q_3q_4)dx_1dx_2. \quad (2.2.17)$$

The cross-section  $\sigma(q_1q_2 \rightarrow q_3q_4)$  can be calculated by the rules of QFT and Feynman diagram. The PM is only relevant to hard processes; we also want to have a model that applies to soft processes. To do so, the GRT is introduced in the next subsection.

### 2.2.2 Gribov-Regge Theory

In the [GRT](#), one can read the [Regge Theory \(RT\)](#). Regge theory is involved with non-relativistic potential scattering and its association in a significant theory such as [QCD](#) would consequently be an important action towards a comprehensive understanding of strong interaction. This theory investigates the scattering matrix properties by Regge in 1959 [96, 111]. Before entering into the technical part of [RT](#) it is worth describing the S-matrix and its attributes.

In quantum theory the S-matrix represents a transition between two states,  $|f\rangle$  and  $|k\rangle$ .  $|k\rangle$  is the initial state of free particles at  $t \rightarrow -\infty$  and  $|f\rangle$  is the final state of free particles at  $t \rightarrow +\infty$ . The matrix elements of the S-matrix is given by

$$S_{fk} = \langle f | S | k \rangle. \quad (2.2.18)$$

One can illustrate the S-matrix as an interaction formalism

$$S_{fk} = \delta_{fk} + i(2\pi)^4 \delta^4(P_i - P_k) T_{fk}. \quad (2.2.19)$$

If the state does not change  $|k\rangle = |f\rangle$ , it signifies there is no interaction, then we have  $\delta_{fk} = 1$ . The imaginary part of Eq. 2.2.19 denotes the interaction of two different states corresponding to T-matrix with scattering amplitude  $T_{fk}$  where the Dirac function exposes the conservation of energy and momentum. The S-matrix has some accurate features such as:

1. Lorentz-invariant
2. Unitary
3. Analytic in momentum variables.

The properties of the S-matrix is studied by the [RT](#). This theory is actually non-perturbative and investigates the amplitude's behavior of elastic collisions. The partial-wave amplitude T for the elastic collision  $a + b \rightarrow c + d$  using the Mandelstam's variables, s and t, can be written,

$$T(t, s) = \sum_{j=0}^{\infty} (2j+1) T(j, s) P_j(z). \quad (2.2.20)$$

In Eq. 2.2.20,  $P_j(z)$  is the j-th Legendre Polynomial with  $z = \cos\theta$  where  $\theta$  is the scattering angle. Applying the infinite energy ( $s \rightarrow \infty$ ), one can rewrite the amplitude as  $T(s, t) \approx s^{\alpha(t)}$  with regge poles  $\alpha$ . Therefore, the elastic cross-section with this amplitude is given

$$\frac{d\sigma}{dt} = \frac{1}{s^2} |T(s, t)|^2 \approx s^{2\alpha(t)-2}. \quad (2.2.21)$$

The linear trajectories observes a remarkable agreement with the data as

$$\alpha(t) = \alpha(0) + \alpha' t. \quad (2.2.22)$$

This is in complete agreement with the fact that if one plots the spin  $\alpha$  of resonances versus their mass squared s, one can obtain group of particles on linear Regge trajectories,

$$\alpha(s) = \alpha(0) + \alpha' s, \quad (2.2.23)$$

with  $\alpha(0) \leq 0.5$ . The Regge pole amplitude is represented by a Reggeon exchange between two hadrons. The Reggeon is a hypothetical particle which nature still has to be explained in the context of field theory. As a result of the optical theorem, the total cross-section is defined as

$$\sigma_{tot} \approx \frac{1}{s} \text{Im} T(s, 0), \quad (2.2.24)$$

which leads to

$$\sigma_{tot} \approx s^{\alpha(0)-1}. \quad (2.2.25)$$

The slow growing of  $\sigma_{tot}$  with  $s$  necessitates a prominent role of a special Reggeon with  $\alpha(0) = 1$ . We use the normal Reggeon just for  $\alpha(0) < 1$  and we call a Reggeon with  $\alpha(0) \geq 1$  as "pomeron". The Reggeons have the quantum numbers of the hadrons whereas at high energies the exchange of quantum numbers has to vanish, so the pomerons have the quantum numbers of the vacuum. A pomeron is an elementary interaction between two hadrons or two partons. Vladimir Gribov introduced it in the 1960s [112, 113] as a way to explain the slow growth of cross-sections in hadronic collisions at high energy.

We have already shown that RT is a great low-energy theory for studying the elastic scattering cross-sections. It is not valid at high energy, however, because the cross-sections increase dramatically and explode in case of just one pomeron exchange. We need to employ multiple pomeron exchanges to achieve reasonable cross-sections at a high energy scale, see Fig. 2.3. The GRT is presented using this idea. A significant criterion for developing a theory of multiple pomeron exchanges is to prevent violating unitarity. The elastic amplitude and inelastic processes are only accessible via unitarity. As a first application of the GRT, we consider the elastic scattering starting with its

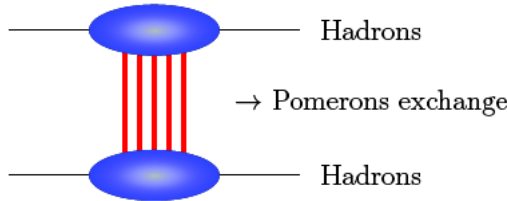


Figure 2.3: Multiple pomeron exchange representation in the GRT.

amplitude in Eq. 2.2.20. Therefore, one can rewrite the amplitude as [96]

$$T(s, t) = 2is \int d^2b \exp(i\vec{k}\vec{b})\gamma(s, b), \quad (2.2.26)$$

with

$$\gamma(s, b) := -iT(s, b)/8\pi, \quad (2.2.27)$$

introducing the impact parameter  $b$  and  $\vec{k} = \vec{p}_\perp$ . We employ Eq. 2.2.26 to compute the cross-sections. The total cross-section is calculated by  $\sigma_{tot} = \text{Im } T(s, 0)/s$ ,

$$\sigma_{tot} = 2 \int d^2b \text{Re}(\gamma(s, b)). \quad (2.2.28)$$

The elastic cross-section denotes

$$\frac{d\sigma_{el}}{dt} = \frac{1}{16\pi s^2} |T(s, t)|^2, \quad (2.2.29)$$

then

$$\sigma_{el} = \int d^2b |\gamma(s, b)|^2. \quad (2.2.30)$$

If we define an eikonal  $w(s, b)$ , and assume real  $w$ ,

$$\gamma(s, b) = 1 - \exp[-w(s, b)], \quad (2.2.31)$$

we obtain

$$\sigma_{tot} = \int d^2b 2\{1 - \exp[-w(s, b)]\}, \quad (2.2.32)$$

$$\sigma_{el} = \int d^2b \{1 - \exp[-w(s, b)]\}^2, \quad (2.2.33)$$

$$\sigma_{in} = \int d^2b \{1 - \exp[-2w(s, b)]\}. \quad (2.2.34)$$

The production of particle comes from the inelastic collision with cross-section in Eq. 2.2.34.

Multiple pomeron exchange cures unitarity, which would be broken for single pomeron exchange, as has been shown by comparing  $w(s, b)$  and  $\gamma(s, b) = 1 - \exp[-w(s, b)]$  as a function of impact parameter in the eikonal approximation.

To compute cross-sections for a single pomeron exchange,  $\gamma$  must be replaced by  $w$  in the calculations. When  $b$  is decreased, the  $w(s, b)$  function grows much beyond 1 at high energies. This function rises linearly with  $s$  for maximal overlapping at  $b = 0$ , resulting in an increase in total cross-section. This is a violation of the Froissart bound, and therefore unitarity. However, in the case of multiple pomeron exchange, we should take into account the  $\gamma = 1 - e^{-w}$  rather than  $w$ . For low overlapping, large  $b$ , the  $w$  function is small and we have the same situation for  $\gamma$ . In case of more central collision, small  $b$ , however, the  $w$  function grows beyond 1 and  $\gamma$  is always smaller than 1 and the cross-sections do not increase linearly with  $s$ . Therefore, the behavior of  $\gamma$  is good, and its dependence on  $b$  is comparable to a Fermi function. As including, everything is how it should be and in the scenario of multiple pomeron exchanges, we have unitarity [96].

Despite the fact that GRT preserves unitarity at high energies, the approach has two drawbacks. The first one is energy conservation. During the particle production treatment, the initial energy must be shared among the multiple pomerons, but during the cross-section computation, each pomeron takes the whole initial energy. The second flaw is that the initial pomeron is treated differently in the particle production process than other pomerons for no obvious reason.

We need to integrate these two models, the PM and GRT, to have a complete definition of both hard and soft processes and address the energy sharing dilemma. This is called the PBGRT. I will briefly describe this approach in the following subsection.

### 2.2.3 Parton Based Gribov Regge Theory

As I have already explained, the PBGRT contains the merging of two separate approaches, PM and GRT. The aim of this model is to cover both soft and hard processes properly. The main concept to form this theory is to do a realistic treatment of all processes during a collision using the multiple scattering. One has to explicitly care about the fact that the total energy should be distributed among the individual elementary interactions. All kinds of collisions are allowed, as pp, pA, or AA. This approach constitutes a strategy to determine the cross-sections and the particle production taking accurately care of the energy conservation. The PBGRT has been developed by Klaus Werner and his colleagues in 2000 with the main reference [100].

This theory has changed our vision regarding the schematic representation of the pp scattering as compare to the GRT. The pomeron or parton ladder was defined as elementary interaction between hadrons in GRT, black lines in Fig. 2.3, while it is defined as elementary interaction between partons using the PM in PBGRT, green lines in Fig. 2.4. As can be seen in Fig. 2.5, each parton ladder is considered to be a sum of a soft, a semi-hard and a hard contributions, being based on RT and pQCD (including Dokshitzer

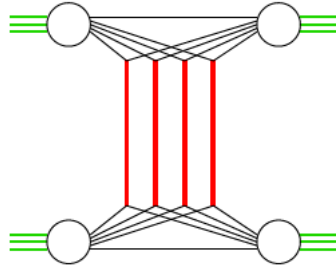


Figure 2.4: Schematic representation of the proton-proton scattering with multiple pomeron exchange (red lines) between partons (green lines) in the PBGR model.

Gribov Lipatov Altarelli Parisi (DGLAP) equations).

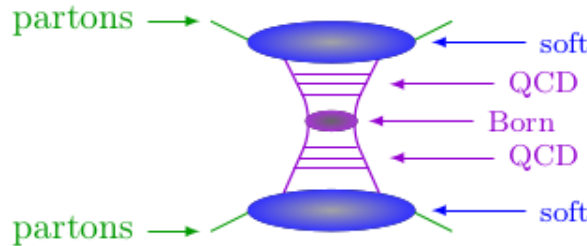


Figure 2.5: Representation of the elastic parton ladder

The semi-hard pomeron includes sea-sea, sea-valence, valence-sea and valence-valence contributions in order to have a complete description of the interaction between projectile and target. In the hard contribution, for the "Born" process, one can use the space-like and time-like cascade according to DGLAP equations to complete the color flow diagrams and produce the correct string segments. The pomerons are broken by quark-antiquark or quark-antiquarks or antiquark-diquark that lead to hadron formation.

We have two kinds of parton ladders, cut and uncut. A consistent quantum mechanical formulation of the multiple scattering requires not only the consideration of the cut parton ladders to produce particles but also the uncut ladders, expressing elastic scattering. The uncut ladders do not subscribe to particle production, but they are crucial since they affect extensively the calculations of partial cross-sections. The calculation of cross-sections are explained with more details in these references, [100] and [114].

In this model, the energy is conserved in particle production and computing cross-sections. Eventually, we should deal with the complex proposal of how these partons will be transformed into observable hadrons. Based on the idea that the parton ladders amount to essentially longitudinal color fields, which may be represented by strings, we employ the relativistic string model. Technically, the method consists of two steps: given the partons, strings are formed then these strings "fragment" into hadrons.

In the following the particle production with the cut ladder in a nucleus-nucleus collision is considered. One assumes that projectile parton always interacts with exactly one parton on the other side (target), elastically or inelastically which realized via uncut or cut ladders. They create the ladders as shown in Fig. 2.6.

We expect that we have "normal" hadronization in the case of a cut ladder, however,

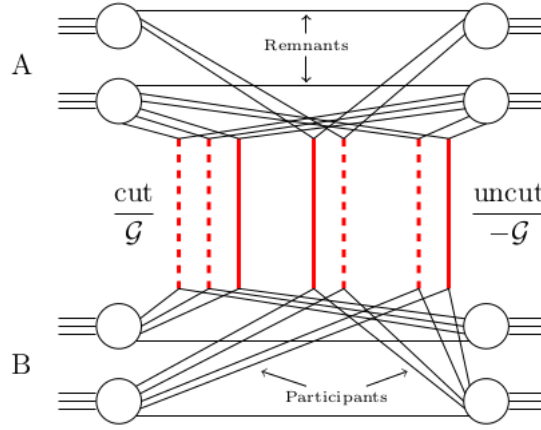


Figure 2.6: The two elements of the multiple scattering theory: cut ladders (dashed red lines), represent the inelastic interactions, and uncut ladders (red lines) show the elastic interactions in nucleus-nucleus collision.

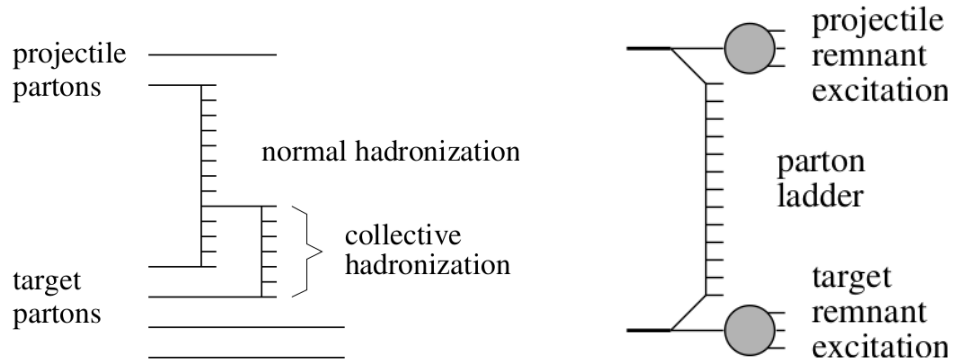


Figure 2.7: Left: hadron production from a cut ladder (normal hadronization) and two cut ladders interaction (collective hadronization). Right: the complete picture, including remnants. The remnants are an important source of particle production at RHIC energies. [115].

one can have interaction between partons from separate cut ladders. Therefore, the hadronization of the two ladders is certainly not independent and we expect that we have some kind of "collective" hadronization of two interacting ladders as can be seen on the l.h.s of Fig. 2.7.

As illustrated in the right hand side of Fig. 2.7 and Fig. 2.6, the complete representation of elementary interaction between partons contains three objects: two off-shell remnants (outer contributions) and the parton ladder between two active partons (inner contributions) on both sides, projectile and target. The remnants produce particles at large rapidities and the parton ladders produce particles at central rapidities.

In summary, we discussed how the [PBGRT](#) was created to tackle the issue of energy conservation. It is also used to provide a comprehensive definition of both soft and hard processes. As an event generator, one should understand how an event is generated in [EPOS](#). I will go through everything inside this event generator in the next section, although not in much detail.

## 2.3 How does the EPOS event generator work?

In this section, I will describe an event generated in EPOS for  $pp$ ,  $pA$  and  $AA$  collisions. Initial conditions, core-corona separation, viscous hydrodynamic expansion, statistical hadronization, and final state hadronic cascade are the five steps for generating each event.

### 2.3.1 Initial conditions (EPOS<sub>i</sub>)

The **PBGR**T, which is the theoretical basis of **EPOS**, is used to describe the initial conditions. As we have already explained in subsection 2.2.3, the number of pomerons per possible nucleon-nucleon pair is used to define the multiple scattering configuration. A sequence of partons are associated with each cut pomeron in a given configuration. The chain of partons corresponding to a given pomeron is referred to as parton ladder. These ladders are identified with flux tubes. Actually, the initial conditions are based on the flux tubes not partons [116].

For each cut pomeron and based on the semi-hard and hard contributions, one can construct the color flow diagram. We have four arrangements for these contributions that each of them has several possibilities to make a color connection between partons from projectile and target sides, as illustrated in Fig. 2.8. When the initial partons on both sides are valence quarks, we have a hard contribution, and when at least one side has a sea quark, we have a semi-hard contribution (being emitted from a soft pomeron). For example, if one or two of the initial pomerons ends are sea quark, we may determine whether the first emitted parton is a gluon or a quark to define the interaction from the projectile or target side, as shown in Fig. 2.8. We have various types of interactions between partons from both sides, as shown in table 2.1.

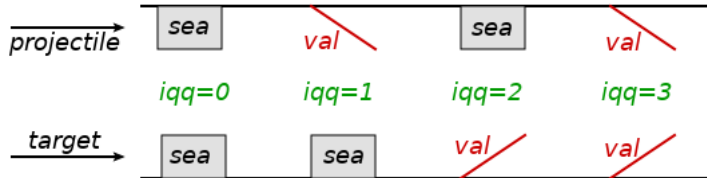


Figure 2.8: Different possibilities to build the color connection diagram via the semi-hard and hard contribution.

Table 2.1: Different possibilities for parton interaction in a pomeron.

Contribution types	Interaction between partons after soft emission
iqq=0 (sea-sea)	jqq=0, gluon-gluon jqq=1, quark-gluon jqq=2, gluon-quark jqq=3, quark-quark
iqq=1 (val-sea)	jqq=0, quark-gluon jqq=1, quark-quark
iqq=2 (sea-val)	jqq=0, gluon-quark jqq=1, quark-quark
iqq=3 (val-val)	jqq=0, quark-quark no gluon involved

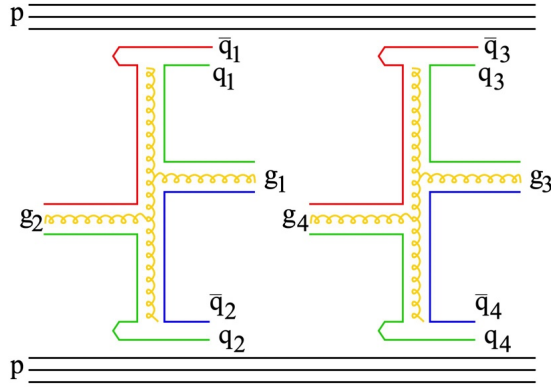


Figure 2.9: Color flow diagram for two pomerons exchange without initial- and final-state cascade and gluon-gluon scattering.

If the first parton is a quark, the flavor must be specified, while the anti-flavor is kept as a string end. As we see in Fig. 2.9, we have an example of two cut pomerons with the sea-sea parton contribution without initial- and final-state cascade. We have two elementary interactions of the type  $gg \rightarrow gg$ . The projectile and target remnants stay always color neutral. The color flow is considered by red, green and blue lines between partons. The color flow initiates from a quark with intermediate gluon (or gluons) until an antiquark is found. Therefore, in the example, we have  $q_1 - g_1 - \bar{q}_2$  and  $q_2 - g_2 - \bar{q}_1$  for the first pomeron and  $q_3 - g_3 - \bar{q}_4$  and  $q_4 - g_4 - \bar{q}_3$  for the second one. These four sequences of partons are called as kinky strings. The kinky string's physical representation is basically a one-dimensional "color flux tube" in longitudinal direction with a very small transverse dimension. I have included an example of how the color connection works to produce the kinky strings in EPOS code in Appendix B.3.

The relativistic string dynamics is derived from general principles as covariance and gauge invariance [117, 118]. The high energy scatterings provide the hard processes and high transverse momentum partons (jets), but these processes are rare and important tools. However, even when having high transverse momentum partons, the transverse momentum is much smaller than the longitudinal momenta. The strings will break by generating quark-antiquark pairs to produce string segments. The final hadrons are used as the initial state for the evolution of matter in EPOS framework (EPOS<sub>e</sub>) according to the following steps: the core-corona separation, hydrodynamic expansion, statistical hadronization, and final state rescattering.

### 2.3.2 Core-Corona separation (EPOS<sub>e</sub>)

As we have already seen in subsection 2.3.1, the string segments are produced via the initial conditions. In conventional EPOS, the density of these produced segments was considered. The density of the string segments in pp and pA collisions and in the high multiplicity events is so high that the string segments cannot decay separately [119]. The area where the density of the string segments is more than the critical density  $\rho_0$  ( $\rho_0$  segments per unit area in given transverse slices) is called "core", which forms the plasma. On the other hand, when the string density is lower than the critical density  $\rho_0$ , the area is named "corona". It is an old method of separating core and corona parts in EPOS.

The new method in EPOS to separate core and corona parts is defined based on the energy loss of string segments on the hyperbola. So as to know which kind of string

segments escape from the dense area, one can compute the energy loss for each one at a given time  $\tau$ ,

$$\Delta E = E_{segment} - E_{loss}. \quad (2.3.1)$$

One can rewrite Eq. 2.3.1 based on the string's transverse momentum and local string density  $\rho$  as,

$$P_t^{new} = P_t - f_{Eloss} \int_{\gamma} \rho dL, \quad (2.3.2)$$

where  $\gamma$  is a trajectory of the segment and  $f_{Eloss}$  is a nonzero constant [116]. If the  $P_t^{new}$  is positive, the string segment can escape from the core part, and it is categorized as a corona particle. If the  $P_t^{new}$  is negative, however, the string segment loses all its energy and is unable to leave, thus it will remain in the core part.

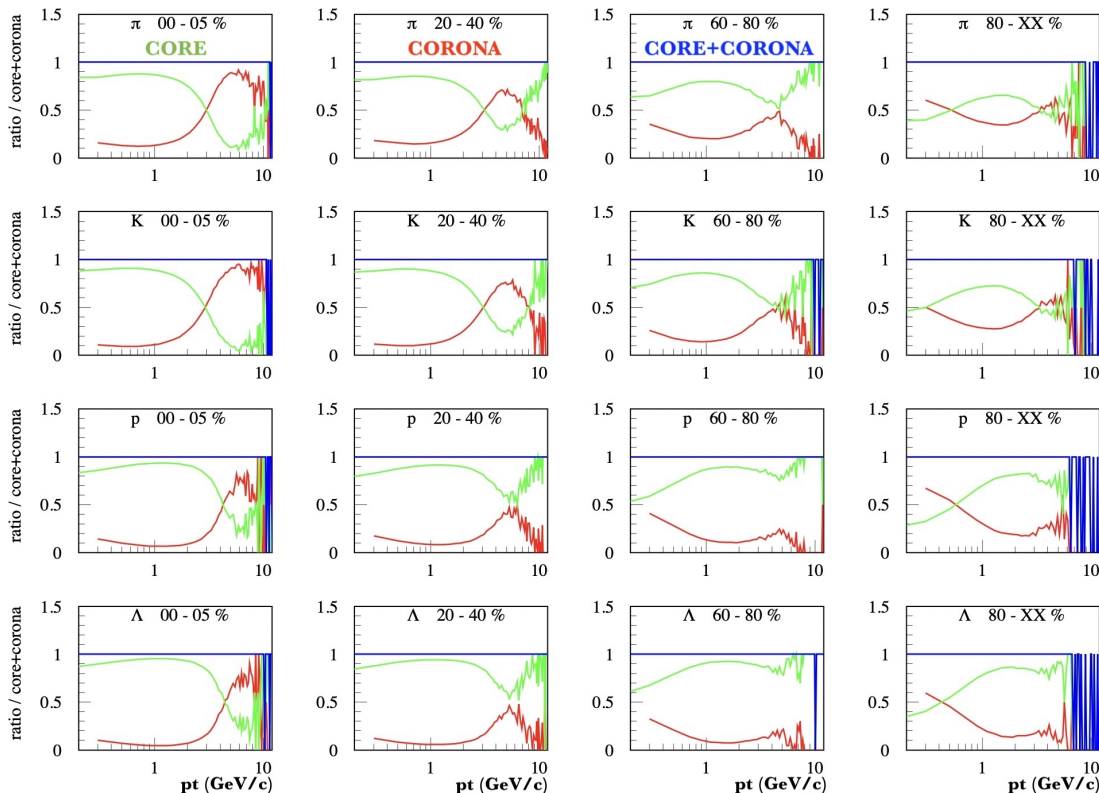


Figure 2.10: The ratios of core, corona, and core+corona to core+corona as a function of transverse momentum spectra for identified particles in Au-Au collisions at  $\sqrt{s_{NN}} = 200$  GeV in mid-rapidity region  $|\eta| < 1$ . For each particle, the transverse momentum spectra for most central (0-5%), mid-central (20-40%), mid-peripheral (60-80%), and most peripheral ( $> 80\%$ ) collisions are plotted. The green, red, and blue curves represent the core, corona, and core+corona productions, respectively.

The ratios of core, and corona parts to the core+corona as a function of transverse momentum spectra for different types of hadrons such as pion  $\pi$ , kaon  $K$ , proton  $p$ , and Lambda  $\Lambda$  have been shown in Fig. 2.10 for Au-Au collisions at  $\sqrt{s_{NN}} = 200$  GeV in mid-rapidity area. The core contribution dominates for central collisions. We see that the core part contributes stronger than corona part for different types of particles in the first column. As seen in the figures concerning the most central collisions, the corona part is not negligible. In more peripheral collisions, on the other hand, the low density contribution is significant and dominates. Additionally, core-corona model is able to

describe rapidity densities of charged hadrons in many types of collisions.

In **EPOS**, the energy density and the flow velocity components of the string segments in the core part are computed in the comoving frame [102]. To do so, we compute the energy momentum tensor and the flavor flow vector at some position  $x$  at  $\tau = \tau_0$  as [120]

$$T^{\mu\nu}(x) = \Sigma_i \frac{\delta p_i^\mu \delta p_i^\nu}{\delta p_i^0} g(x - x_i), \quad (2.3.3)$$

$$N_q^\mu(x) = \Sigma_i \frac{\delta p_i^\mu}{\delta p_i^0} q_i g(x - x_i). \quad (2.3.4)$$

The net flavor content and the four momenta of the string segments are represented by  $q \in u, d, s$ , and  $\delta p$ , respectively. The function  $g$  is a Gaussian smoothing kernel. The Lorentz transformation into the comoving frame of Eq. 2.3.3 with the first column can provide an equation for energy density  $\varepsilon$  and the flow velocity components  $v_i$

$$\varepsilon = T^{00} - \Sigma_{k=1}^3 T^{0k} v^k, \quad (2.3.5)$$

$$v^i = \frac{1}{\varepsilon} (T^{i0} - T^{ik} v^k). \quad (2.3.6)$$

The flavor density is then computed as

$$f_q = N_q u, \quad (2.3.7)$$

where  $u$  is the flow four-velocity. This procedure is carried out at the proper time  $\tau_0$ , which will be used as the starting time for the following stage, the hydrodynamic expansion. We assume that thermalization happens very quickly between some  $\tau_{flux}$ , where the system is described by flux tubes, and  $\tau_0$ . We suppose there is no transverse expansion between  $\tau_{flux}$  and  $\tau_0$  that the energy per unit of space-time rapidity does not change. We expect that at least the variables  $T^{00}$  and  $T^{0i}$  to remain close to the flux tube values, thus the energy density at starting time  $\tau_0$  will be computed using the flux tube findings.

Knowing  $\varepsilon$  and  $v^k$  at  $\tau_0$ , the core will then evolve according to hydrodynamics, whereas the corona segments are identified as hadrons. I will discuss this briefly in the following.

### 2.3.3 Hydrodynamic expansion (**EPOSe**)

Only the core part is concerned in this stage. The system expands hydrodynamically starting from  $\tau_0$ , using relativistic viscous hydrodynamic equations with  $\eta/s = 0.08$  [101,102,116]. Solving the equations provides the evolution of the space-time dependence of the macroscopic quantities energy density  $\varepsilon(x)$ , collective flow velocity  $\bar{v}(x)$ , and the net flavor densities  $n_k(x)$ .

### 2.3.4 Statistical hadronization (**EPOSe**)

The system will expand with time, leading to a reduction in temperature and energy density. The matter hadronizes into hadrons whenever the system's energy density drops below  $0.57 \text{ GeV}/\text{fm}^3$ . At this moment, the hydrodynamical evolution will cease, and we will use statistical hadronization, which should be understood as the early hadronization of the quark-gluon plasma state into a hadronic system, rather than the decay of an equilibrium resonance gas. The microcanonical method describes the hadronization of matter from the core part [121]. The corona particles have hadronized before these steps, using the string phenomenological model described in [122].

### 2.3.5 Final state rescattering (EPOSe)

After hadronization, the system continues to interact via hadronic scatterings, forming flow, but considerably less than an ideal thermal resonance gas evolution, which does not occur in reality. The particles at their hadronization positions are supplied into the UrQMD hadronic cascade model [123, 124], which performs hadronic interactions until the system's energy is low enough that no further interactions occur. If no hadronic interactions occur, the particles' final freeze-out position will be the last interaction point in the cascade process.

## 2.4 Summary and conclusion

I started this chapter with a description of the concepts that constituted the EPOS event generator: what are the elements that make up this method? What precisely is it? Who were its ancestors?

Klaus Werner developed EPOS in 2002 to describe all types of collisions using the PBGRT. Following that, it was further developed for various purposes. Thus, different versions of EPOS were born, such as EPOS 2, EPOS LHC, EPOS 3, and EPOS HQ. The EPOS group is still working to improve the model. EPOSi+PHSDe and EPOS 4 are two new EPOS versions that will be released in the near future.

Then, I explained the PM and GRT, although not in much detail. They make up the PBGRT. The PM was created by Feynman to replace protons with partons as elementary particles. One can determine the cross-sections for hard processes by integrating QFT and the PDFs in the PM. We use the GRT to calculate the cross-sections of soft processes. It is an effective field theory that describes hadronic interaction using many pomeron exchanges at the same time. The GRT cures the unitarity problem in the high energy region of the RT. For particle production, the energy exchanged between pomerons in the case of multiple scattering seems to be well preserved. The energy conservation, however, is not taken into account for the cross-section calculations. Consequently, the PBGRT was created to conserve energy in both particle production and cross-section computation.

Finally, I finished this chapter with an explanation of how to use EPOS event generator to create an event. This event generator has five steps for generating an event:

- i) Initial conditions (EPOSi): producing strings using the PBGRT based on elementary interactions between partons via parton ladders with saturation scale.
- ii) Core-corona strategy (EPOSe): the dense region of the strings is considered the core, while the low density part is termed the corona.
- iii) Hydrodynamic expansion (EPOSe): employing the equation of relativistic viscous hydrodynamics, consider and evolve just the core part.
- iv) Statistical hadronization (EPOSe): applying the Cooper-Frye procedure to investigate the core and corona hadronizations.
- v) Final state hadronic cascade (EPOSe): investigation of hadron-hadron scattering at high enough hadron density using the UrQMD model.

PHSD model, which I employed in the second part of my doctoral thesis, will be addressed in the following chapter.



# CHAPTER 3

## PARTON-HADRON-STRING DYNAMICS TRANSPORT APPROACH

In this chapter, I will discuss [PHSD](#), a different approach for studying relativistic [HICs](#). From the [SPS](#) to [RHIC](#) energies, it is used to investigate [AA](#), [pA](#), and  [\$\pi A\$](#)  reactions.

The [PHSD](#) is a microscopic covariant dynamical approach that relies on the Kadanoff-Baym equations that are used to assess strongly interacting systems out-of equilibrium. This approach properly describes the whole evolution of relativistic [HICs](#). First of all, the primary hard scatterings using [Pythia](#), as well as the string configuration based on the Lund-String model, are taken into account in [PHSD](#). The transition from the dynamical confinement phase to the quark-gluon plasma, hadronization, and interactions in the expanding hadronic phase are incorporated.

In the first section, I briefly review non-equilibrium [QFT](#) principles that are used in this model. Then I will present how we use them in [PHSD](#) to study [HICs](#) in the following section.

### 3.1 Non-equilibrium QFT

[QFT](#) is a theoretical framework in particle physics that combines classical field theory, special relativity, and quantum mechanics [125]. [QFT](#) is a crucial tool for describing quantum mechanics since it allows for transitions between states with different particle compositions. It describes an arbitrary number of particles in quantum mechanics. As a result, it has to be used in relativistic quantum theory since relativistic kinematics allows for particle formation and annihilation while preserving energy and mass conservation. The many-body systems are the foundation of the relativistic quantum theory. The non-equilibrium field theory technique can be used in practical approaches of the field theory, such as the renormalization group, to study the non-equilibrium states and transport phenomena [126]. The initial equilibrated state with some time-dependent external perturbation is generally referred to as non-equilibrium dynamics.

I will describe several remarkable tools for studying the quantum fields in non-equilibrium in the following subsections. I start by defining the Dyson series and the Keldysh formalism in order to obtain the Kadanoff-Baym equations.

### 3.1.1 Dyson series on the Keldysh contour

In this subsection, I will explain the time-evolution operators in two alternative representations, Schrödinger and Heisenberg. The time dependence of the system is defined by the quantum state in the Schrödinger representation, but the space-time dependence is carried by field operators in the Heisenberg representation. The interaction picture is an intermediate representation between the two latter pictures that we employ in the Dyson series. The time-evolution of the many-body wave function can be described using the Schrödinger equation [127]  $|\Psi(t)\rangle$  ( $|\Psi(t)\rangle$  is defined as the probability amplitude whose absolute square gives the probability that the particle is located at the given position):

$$i\partial_t|\Psi(t)\rangle = \hat{H}(t)|\Psi(t)\rangle. \quad (3.1.1)$$

The time evolution operator is responsible for the evolution of a closed quantum system. One unitary time evolution operator  $S$  [128] can solve Eq. 3.1.1. The wave function can be defined as  $|\Psi(t)\rangle = \hat{S}(t, t_0)|\Psi(t_0)\rangle$ . By replacing the new wave function into equation 3.1.1 we have:

$$i\partial_t\hat{S}(t, t_0) = \hat{H}(t)\hat{S}(t, t_0), \quad (3.1.2)$$

and the S-matrix evolution is

$$\hat{S}(t, t_0) = T \left[ \exp\left(-i \int_{t_0}^t dt' \hat{H}(t')\right) \right] = \sum_{n=0}^{\infty} \frac{T[-i \int_{t_0}^t dt' \hat{H}(t')]^n}{n!}, \quad (3.1.3)$$

where  $T$  is the causal time-ordering operator. The expectation value of a Hermitian operator  $\hat{O}(t)$  can be computed using the properties of the S-matrix and Eq. 3.1.1 as follows:

$$\langle \Psi(t) | \hat{O} | \Psi(t) \rangle = \langle \Psi(t_0) | \hat{O}_H(t) | \Psi(t_0) \rangle, \quad (3.1.4)$$

which relates the Schrödinger (left-hand side) and Heisenberg (right-hand side) representations. As a result, the latter one's defines:

$$\hat{O}_H(t) = \hat{S}^\dagger(t, t_0) \hat{O} \hat{S}(t, t_0), \quad (3.1.5)$$

that obeys the Heisenberg equation of motion,

$$i\partial_t \hat{O}_H(t) = [\hat{O}_H(t), \hat{H}(t)]. \quad (3.1.6)$$

The Hamiltonian in Eq. 3.1.6 is defined as  $\hat{H}(t) = \hat{H}_0(t) + \hat{V}(t)$ , which includes a noninteracting  $\hat{H}_0(t)$  and interaction  $\hat{V}(t)$  parts. The associated Hermitian operator  $\hat{O}$  to the noninteracting Hamiltonian  $\hat{H}_0(t)$  is given by:

$$\hat{O}_I(t) = \hat{S}_0^\dagger(t, t_0) \hat{O} \hat{S}_0(t, t_0), \quad (3.1.7)$$

where  $\hat{S}_0(t, t_0)$  is also defined the same as Eq. 3.1.3 but only contains the noninteracting part of the Hamiltonian  $\hat{H}_0(t)$ , and  $\hat{S}_0^\dagger(t, t_0)$  expresses as the conjugate transpose of  $\hat{S}$  as:

$$\hat{S}_0^\dagger(t, t_0) = T^a \left[ \exp\left(-i \int_t^{t_0} dt' \hat{H}(t')\right) \right]. \quad (3.1.8)$$

The anticausal time-ordering operator is denoted by  $T^a$ . In the interaction picture, for the Hermitian operator  $\hat{O}$ , Eq. 3.1.5 can be rewritten as:

$$\hat{O}_H(t) = \hat{U}^\dagger(t, t_0) \hat{O}_I(t) \hat{U}(t, t_0), \quad (3.1.9)$$

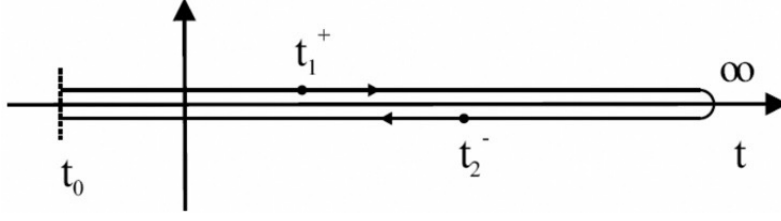


Figure 3.1: The closed time contour in the Keldysh formalism [130]. The time  $t_1$  lies on the chronological (+) branch and the time  $t_2$  lies on the antichronological (-) branch.

with the full Heisenberg picture operator  $\hat{U}(t, t_0)$  which obeys the evolution equation:

$$i\partial_t \hat{U}(t, t_0) = \hat{V}_I(t) \hat{U}(t, t_0). \quad (3.1.10)$$

Eq. 3.1.10 is identical to Eq. 3.1.2, which may be solved using the same method as in Eq. 3.1.3,

$$\hat{U}(t, t_0) = T \left[ \exp(-i \int_{t_0}^t dt' \hat{V}_I(t')) \right] = \sum_{n=0}^{\infty} \frac{T[-i \int_{t_0}^t dt' \hat{V}_I(t')]^n}{n!}. \quad (3.1.11)$$

Eqs. 3.1.3 and 3.1.11 are denoted as Dyson series [129]. The time-ordering operator  $T_C$  can be defined based on the Keldysh contour, see Fig 3.1, and where  $\hat{S}_C$  and  $\hat{U}_C$  are the time-evolution operators defined on the contour as:

$$\hat{S}_C = T_C \left[ \exp(-i \int_C dt' \hat{H}(t')) \right], \quad (3.1.12)$$

and

$$\hat{U}_C = T_C \left[ \exp(-i \int_C dt' \hat{V}(t')) \right]. \quad (3.1.13)$$

### 3.1.2 Green's functions

The quantum dynamics is described in terms of correlation functions or Green's functions of the quantum fields which is commonly determined as the vacuum expectation value of the time-ordered product [131]. The two points Green's function on the Keldysh contour in scalar field theory with scalar field operator  $\hat{\phi}_I$  in the Heisenberg picture is provided by:

$$iG(x, y) = \langle \hat{U}_C(\hat{\phi}_I(x) \hat{\phi}_I^\dagger(y)) \rangle, \quad (3.1.14)$$

where  $x$  and  $y$  are the space-time coordinates. By decomposing the Keldysh contour, one can define four different Green's functions,  $G^>$ ,  $G^<$ ,  $G^a$  and  $G^c$  as follows [132, 133]:

$$iG^c = iG^{++}(x, y) = \langle \hat{T}^c(\hat{\phi}_I(x) \hat{\phi}_I^\dagger(y)) \rangle, \quad (3.1.15)$$

$$iG^a = iG^{--}(x, y) = \langle \hat{T}^a(\hat{\phi}_I(x) \hat{\phi}_I^\dagger(y)) \rangle, \quad (3.1.16)$$

$$iG^< = iG^{+-}(x, y) = \langle (\hat{\phi}_I^\dagger(y) \hat{\phi}_I(x)) \rangle, \quad (3.1.17)$$

$$iG^> = iG^{-+}(x, y) = \langle (\hat{\phi}_I(x) \hat{\phi}_I^\dagger(y)) \rangle, \quad (3.1.18)$$

where  $T^c$  and  $T^a$  symbolize the causal and anticausal time-ordering operators, respectively.  $\pm$  indicate the time argument of  $x$  and  $y$  in the upper (chronologic) or lower (antichronologic) branch of the Keldysh contour, respectively, based on the [Closed Time Path \(CTP\)](#) in Fig. 3.1. The lesser and greater Green's functions,  $G^<$  and  $G^>$ , are

referred to the Wightman functions, and they include kinetic aspects of the many-body system such as particle density. The  $2 \times 2$  matrix can also be used to write Eqs. 3.1.15-3.1.18 as:

$$G(x, y) = \begin{pmatrix} G^c(x, y) & G^<(x, y) \\ G^>(x, y) & G^a(x, y) \end{pmatrix}. \quad (3.1.19)$$

We may also define the two other representations of the Green's functions, the retarded ( $G^R$ ) and advanced ( $G^A$ ), which are also formulated as a functions of Eq.3.1.15-3.1.18:

$$G^R(x, y) = \theta(x^0 - y^0)(G^>(x, y) - G^<(x, y)) = \theta(x^0 - y^0)A(x, y), \quad (3.1.20)$$

$$G^A(x, y) = -\theta(y^0 - x^0)(G^>(x, y) - G^<(x, y)) = -\theta(x^0 - y^0)A(x, y), \quad (3.1.21)$$

where the time coordinates are represented by  $x^0$  and  $y^0$ . The spectral function, which is used in momentum space to determine some spectral features of states, is denoted by  $A(x, y)$ .

### 3.1.3 Kadanoff-Baym equations

The quantum kinetics can be studied using the Kadanoff-Baym equations as a foundation. The Kadanoff-Baym equations are derived by starting with the Dyson Schwinger equation [132]. This is a thorough definition of the Green function  $G$ , which is related to the fully interacting system and the free Green function  $G_0$  with the proper self-energy  $\Sigma$ :

$$G(x, y) = G_0(x, y) + G_0(x, x') \odot \Sigma(x', y') \odot G(y', y). \quad (3.1.22)$$

Here  $\odot$  denotes an intermediate integration over the space-time on the CTP contour in Eq. 3.1.22. Eq. 3.1.22 can be written in matrix notation [71] in the form

$$\begin{aligned} \begin{pmatrix} G^c(x, y) & G^<(x, y) \\ G^>(x, y) & G^a(x, y) \end{pmatrix} &= \begin{pmatrix} G_0^c(x, y) & G_0^<(x, y) \\ G_0^>(x, y) & G_0^a(x, y) \end{pmatrix} + \begin{pmatrix} G_0^c(x, x') & G_0^<(x, x') \\ G_0^>(x, x') & G_0^a(x, x') \end{pmatrix} \\ &\odot \begin{pmatrix} \Sigma^c(x', y') & -\Sigma^<(x', y') \\ -\Sigma^>(x', y') & \Sigma^a(x', y') \end{pmatrix} \odot \begin{pmatrix} G^c(y', y) & G^<(y', y) \\ G^>(y', y) & G^a(y', y) \end{pmatrix}. \end{aligned} \quad (3.1.23)$$

We now use the free propagator of the Klein-Gordon equation  $G_{0x}^{-1} = -(\partial_\mu^x \partial_x^\mu + m^2)$  [134, 135] with the particle's bare mass  $m$ . To derive the Kadanoff-Baym equations, we multiply the Klein-Gordon equation to Eq. 3.1.23 from the left, which results in

$$-(\partial_\mu^x \partial_x^\mu + m^2)G^{\gtrless}(x, y) = \Sigma^R(x, x') \odot G^{\gtrless}(x', y) + \Sigma^{\gtrless}(x, x') \odot G^A(x', y). \quad (3.1.24)$$

The lesser  $\Sigma^<$ , greater  $\Sigma^>$ , causal  $\Sigma^c$ , and anticausal  $\Sigma^a$  self energies can be defined in the same way as the Green functions in Eqs. 3.1.15-3.1.18. The Kadanoff-Baym equations for the retarded and advanced green functions should also be derived as:

$$-(\partial_\mu^x \partial_x^\mu + m^2)G^{R/A}(x, y) = \delta(x - y) + \Sigma^{R/A}(x, x') \odot G^{R/A}(x', y), \quad (3.1.25)$$

where the delta function  $\delta(x - y)$  is derived from the Klein-Gordon equation applied to the free Green function  $G_0$ :

$$G_{0x}^{-1} \begin{pmatrix} G_0^c(x, y) & G_0^<(x, y) \\ G_0^>(x, y) & G_0^a(x, y) \end{pmatrix} = \delta(\mathbf{x} - \mathbf{y}) \begin{pmatrix} \delta(x_0 - y_0) & 0 \\ 0 & -\delta(x_0 - y_0) \end{pmatrix}, \quad (3.1.26)$$

$$G_{0x}^{-1}G_0^{R/A}(x, y) = \delta(x - y). \quad (3.1.27)$$

The key quantities such as energy, momentum, and causality are completely conserved by the self-energies. It is possible to obtain self-energy in a derivable approximation from [136] as:

$$\Sigma = 2i \frac{\partial \Phi}{\partial G}, \quad (3.1.28)$$

where  $\Phi$  is the sum of all closed two-particle irreducible (2PI) diagrams with full propagators  $G$ . The 2PI indicates that removing a propagator line will not result in two unconnected Feynman diagrams.

### 3.1.4 Spectral function and transport equation

We apply the Wigner-transformation [137] to obtain phase space variables and continue deriving the equations of motion of the Kadanoff-Baym equations. The Wigner-transformation for a function  $f(x, y)$  over the relative ( $r = x - y$ ) and central ( $R = (x + y)/2$ ) coordinates is simply a Fourier-transformation,

$$\bar{f}(R, p) = \int_{-\infty}^{+\infty} d^4 r f(R + r/2, R - r/2) e^{ip^\mu r_\mu}, \quad (3.1.29)$$

where  $p = (p^0, \mathbf{p})$  is the energy-momentum 4-vector. To apply the Wigner transform to the convolutions in Eq. 3.1.24 and 3.1.25 on the right hand side, the following integral can be used:

$$H(x, y) = F(x, y') \odot G(y', y), \quad (3.1.30)$$

and provides

$$\bar{H}(p, x) = e^{i/2(\partial_p^\mu \cdot \partial_{x'}^\mu - \partial_x^\mu \partial_{p'}^\mu)} [\bar{F}(p, x) \bar{G}(p', x')] |_{x'=x, p'=p}. \quad (3.1.31)$$

To deal with the exponential function, we restrict to the first order momentum and coordinate space derivatives is frequently used in transportation theory. This is also known as first-order gradient expansion:

$$\bar{H}(p, x) = \bar{F}(p, x) \bar{G}(p, x) + \frac{i}{2} \{ \bar{F}(p, x), \bar{G}(p, x) \}, \quad (3.1.32)$$

using the Poisson bracket's relativistic generalization:

$$\{ \bar{F}(p, x), \bar{G}(p, x) \} = \partial_\mu^p \bar{F}(p, x) \cdot \partial_x^\mu \bar{G}(p, x) - \partial_x^\mu \bar{F}(p, x) \cdot \partial_\mu^p \bar{G}(p, x). \quad (3.1.33)$$

The use of a gradient expansion is justified if the considered medium experiences only slowly-varying perturbations in space and time. To obtain the spectral function, we must first express Eq. 3.1.25 in terms of the relative and central coordinates, and then apply the Wigner transform to Eq. 3.1.25 for the retarded and advanced Green functions. The retarded and advanced Green functions, as well as the self-energies, can be decomposed as follows:

$$\bar{G}^{R/A} = Re \bar{G}^R \pm i Im \bar{G}^R, \quad (3.1.34)$$

$$\bar{\Sigma}^{R/A} = Re \bar{\Sigma}^R \pm i Im \bar{\Sigma}^R, \quad (3.1.35)$$

where the real components of the retarded and advanced Green's functions and self energies are the same in Wigner space. The imaginary parts give the spectral function  $\bar{A}$  and width  $\bar{\Gamma}$ ,

$$\bar{A} = \mp 2Im \bar{G}^{R/A}, \quad \bar{\Gamma} = \mp 2Im \bar{\Sigma}^{R/A} \quad (3.1.36)$$

They can also be represented in terms of the lesser and greater Green functions as follows:

$$\bar{A} = i\bar{G}^> - i\bar{G}^<, \quad \bar{\Gamma} = i\bar{\Sigma}^> - i\bar{\Sigma}^<. \quad (3.1.37)$$

The spectral function has a Breit-Wigner shape with the self-energy dependence that can be calculated in first-order gradient expansion as:

$$\bar{A} = \frac{\bar{\Gamma}}{[p_0^2 - \mathbf{p}^2 - m^2 - Re\bar{\Sigma}^R]^2 + \bar{\Gamma}^2/4} = \frac{\bar{\Gamma}}{\bar{M}^2 + \bar{\Gamma}^2/4}, \quad (3.1.38)$$

where the mass-function  $\bar{M}$  in the Wigner-space has been introduced. The transport equations are derived in the same way as the spectral function. To do so, we apply the Wigner transform on the Wightman Green functions in the Kadanoff-Baym equation (Eq. 3.1.24). As well as this, one introduces the out-of-equilibrium distribution functions for the Green functions and self-energies as follows:

$$i\bar{G}^<(p, x) = \bar{N}(p, x)\bar{A}(p, x), \quad i\bar{G}^>(p, x) = [1 + \bar{N}(p, x)]\bar{A}(p, x), \quad (3.1.39)$$

$$i\bar{\Sigma}^<(p, x) = \bar{N}^\Sigma(p, x)\bar{\Sigma}(p, x), \quad i\bar{\Sigma}^>(p, x) = [1 + \bar{N}^\Sigma(p, x)]\bar{\Gamma}(p, x). \quad (3.1.40)$$

We finally obtain the generalized transport equation within the Botermans-Malfliet [133, 138, 139] form

$$\frac{1}{2}\bar{A}\bar{\Gamma}\left[\{\bar{M}, i\bar{G}^<\} - \frac{1}{\bar{\Gamma}}\{\bar{\Gamma}, \bar{M}.i\bar{G}^<\}\right] = i\bar{\Sigma}^<i\bar{G}^> - i\bar{\Sigma}^>i\bar{G}^<. \quad (3.1.41)$$

For the quantum equilibration process, Eq. 3.1.41 retains the properties of the full Kadanoff-Baym equations and permits for a transport theoretical treatment. As a result, it is employed in the PHSD equations of motion.

We use the test-particle ansatz to approximate the Green function  $iG^<$  as a sum of point-like particles in order to solve the generalized transport equation Eq. 3.1.41 in first-order gradient expansion

$$i\bar{G}^<(x, p) \sim \sum_{i=1}^N \delta^{(3)}(\mathbf{x} - \mathbf{x}_i(t))\delta^{(3)}(\mathbf{p} - \mathbf{p}_i(t))\delta(p_0 - \epsilon_i(t)), \quad (3.1.42)$$

where  $\mathbf{x}_i(t)$  represents the position of the test particle  $i$  at time  $t$  and  $(\epsilon_i(t), \mathbf{p}_i(t))$  represents its 4-momentum for the off-mass-shell particles. By inserting Eq. 3.1.42 in Eq. 3.1.41 in the limit of  $N \rightarrow \infty$ , one obtains the equations of motion for the test-particles in the PHSD transport approach, which describe the dynamics of the system [130, 133, 140]:

$$\frac{d\mathbf{x}_i}{dt} = \frac{1}{1 - C_{(i)}} \frac{1}{2\epsilon_i} \left[ 2\mathbf{p}_i + \nabla_{p_i} Re\bar{\Sigma}_{(i)}^R + \frac{\epsilon_i^2 - \mathbf{p}_i^2 - M_0^2 - Re\bar{\Sigma}_{(i)}^R}{\bar{\Gamma}_{(i)}} \nabla_{p_i} \bar{\Gamma}_{(i)} \right], \quad (3.1.43)$$

$$\frac{d\mathbf{p}_i}{dt} = \frac{1}{1 - C_{(i)}} \frac{1}{2\epsilon_i} \left[ \nabla_{x_i} Re\bar{\Sigma}_{(i)}^R + \frac{\epsilon_i^2 - \mathbf{p}_i^2 - M_0^2 - Re\bar{\Sigma}_{(i)}^R}{\bar{\Gamma}_{(i)}} \nabla_{x_i} \bar{\Gamma}_{(i)} \right], \quad (3.1.44)$$

$$\frac{d\epsilon_i}{dt} = \frac{1}{1 - C_{(i)}} \frac{1}{2\epsilon_i} \left[ \frac{\partial Re\bar{\Sigma}_{(i)}^R}{\partial t} + \frac{\epsilon_i^2 - \mathbf{p}_i^2 - M_0^2 - Re\bar{\Sigma}_{(i)}^R}{\bar{\Gamma}_{(i)}} \frac{\partial \bar{\Gamma}_{(i)}}{\partial t} \right], \quad (3.1.45)$$

with

$$C_{(i)} = \frac{1}{2\epsilon_i} \left[ \frac{\partial Re\bar{\Sigma}_{(i)}^R}{\partial \epsilon_i} + \frac{\epsilon_i^2 - \mathbf{p}_i^2 - M_0^2 - Re\bar{\Sigma}_{(i)}^R}{\bar{\Gamma}_{(i)}} \frac{\partial \bar{\Gamma}_{(i)}}{\partial \epsilon_i} \right]. \quad (3.1.46)$$

This factor converts the system time  $t$  to the particle's eigentime  $i$ ,  $\tilde{t}_i = t/(1 - C_{(i)})$ . As a result, PHSD is used to model HICs with strongly interacting degrees of freedom, with finite-width dynamical spectral functions. It can describe the equilibration of systems far out-of-equilibrium because it is based on the Kadanoff-Baym equations.

## 3.2 Heavy-ion collisions in PHSD

The goal of this section is to show how the PHSD approach is used to investigate various stages of HICs. First of all, it employs the initial hard scatterings and the string formation based on the LUND string model. The second stage is related to the dynamical deconfinement phase transition to the strongly-interacting QGP. The theoretical transport description of quarks and gluons is based on the Dynamical Quasiparticle Model (DQPM) for partons, which is built to reproduce IQCD for QGP thermodynamics. The spectral function has a Breit Wigner shape with the self-energy dependence. The hadronization and subsequent interactions in the expanding hadronic phase are then studied.

The test-particle ansatz (specified in Eq. 3.1.42) is used in PHSD to characterize the dynamics of the system at a given time. Physical observations such as the particle density is estimated by treating  $N$  ensembles in parallel, each with an equal number of test-particles. We only have test-particle collisions inside the same ensemble. The evolution of the QGP phase, hadronization, and hadronic interaction will all be done in the space-time grid in PHSD. A collection of cells of volume  $V_{cell} = \Delta x \Delta y \Delta z$  makes up the grid.  $\Delta x = \Delta y = 1 fm$ , which is equal to the hadron size, and  $\Delta z = 1/\gamma_{cm} [fm]$ .  $\gamma_{cm}$  is the Lorentz gamma factor for the transformation into the center-of-mass of the colliding nuclei. The magnitude of the Lorentz factor  $\gamma$  is determined as  $1/\sqrt{1 - \beta^2}$  where  $\beta$  is the velocity of the given cell. The  $\gamma_{cm}$  for the Au-Au collision at  $200A \approx GeV$  is 106.61. Hence, the volume of each cell is  $V_{cell} = 9.38 \times 10^{-3} fm^3$ . Furthermore, the  $dt$  timestep is directly linked to  $\gamma_{cm}$ , which is defined as  $dt \approx 0.5/\gamma_{cm} [fm/c]$ . This is initially quite tiny, but when the system expands, the gamma factor reduces, leading the space-time grid to start increasing.

The list of mesons and baryons employed in PHSD have been presented in [125]. Every particle is considered as if it were off-shell, using Lorentzian spectral functions of certain widths and pole masses. The energies of the testparticles are determined based on the particle species' spectral function. We may convert the energy  $p_0$  and momentum  $\mathbf{p}$  of test particle  $i$  to a on-mass-shell using  $m_i^2 = p_{i0}^2 - \mathbf{p}_i^2$ . In order to have the accurate spectral functions a large number of ensembles  $N$  is needed.

### 3.2.1 Initialization (PHSDi)

In HICs, two cluster of nucleons fly towards each other with a certain energy and impact parameter. The coordinate and momentum distributions of nuclei in various approaches - such as PHSD - can be initialized by Wood-Saxon distribution [141] and the semiclassical Thomas-Fermi model [142], respectively. The initial nucleon distribution in coordinate and momentum space is relevant for the description of the heavy-ion measurements since it influences all following dynamics. The nuclear density profile  $\rho(r)$  is defined by the Wood-Saxon distribution as a function of the nucleus radius  $r$ . I will explain it in more detail in the next chapter.

The nuclei in PHSD are assumed to be in the semiclassical groundstate. The nucleons are given a momentum of  $0 < |\mathbf{p}| < p_F$  in the Tomas-Fermi approximation, with  $p_F$  denoting the Fermi momentum based on the nucleus' local density:

$$p_F(r) = \sqrt[3]{\frac{3}{2}\pi^2\rho(r)}. \quad (3.2.1)$$

Subsequently, the nuclei are boosted in  $z$ -direction towards each other depending on the

energy of interest.

### 3.2.2 String production in primary scatterings (PHSDi)

*Pythia* [143] is used by PHSD to perform primary hard scattering between nucleons. The Lund string model [122] is the principal fragmentation option in *Pythia*, and is a phenomenological hadronization model. One of the essential characteristics of QCD is confinement. It is considered to be the result of an approximately linear term in the QCD potential that the Lund string model is motivated by this term, which is given by:

$$V_{QCD}(r) \approx -\frac{4}{3} \frac{\alpha_s}{r} + \kappa r, \quad (3.2.2)$$

between a quark and an antiquark in an overall colour singlet state. This approach consists of building a string between two partons, similar to a color field. In Eq. 3.2.2,  $r$  signifies the distance between quark and an antiquark,  $\alpha_s$  is the strong coupling constant, and  $\kappa$  denotes the string tension ( $\approx 1$  GeV/fm) or energy per distance. At long distances, the linear component dominates, and only this term is utilized in the Lund string model to represent the breakup of the  $q\bar{q}$  string system into several string segments. The string is colorless and does not have any mass. To preserve flavor conservation, various color singlets are produced, such as  $q_a\bar{q}_b$  and  $q_b\bar{q}_a$ , with  $a$  and  $b$  being the quark flavors. The general representation of the String Model fragmentation is shown in Fig. 3.2, where the string ( $q\bar{q}$ ) can split into several (three, four, etc.) string segments.

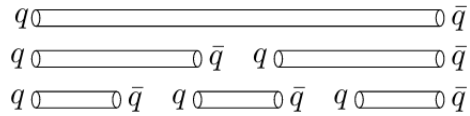


Figure 3.2: Illustration of fragmentations in the String Model.

The secondary strings formed in the Lund model are called the pre-hadrons in PHSD. The fragmentation function defines the probability of producing pre-hadrons with a transverse mass  $m_t$  and an energy fraction  $x$  in the Lund string model as follows:

$$f(x, m_t) \approx \frac{1}{x} (1-x)^a \exp\left(\frac{-bm_t^2}{x}\right), \quad (3.2.3)$$

with the  $a = 0.23$  and  $b = 0.34$  GeV<sup>-2</sup> parameters from the HSD [144]. According to this formula, the light particles with a low transverse mass are dominantly produced more for low energy fraction  $x$ . Massive particles, on the other hand, are more likely to be generated with a larger energy fraction  $x$ , as indicated on the left hand side of Fig. 3.3.

The pre-hadrons are produced with the string tension  $\kappa$ , and the massless quark and antiquark with the transverse momentum  $q_0$  and  $\bar{q}_0$ , respectively, as shown on the right hand side of Fig. 3.3. Let's assume that the  $q\bar{q}$  pair collides at  $t = 0$  with no distance  $r = 0$ . Generally, by separating the  $q\bar{q}$  by a distance  $r$ , the string potential is raised by a factor of  $2\kappa r$ . The enclosed sector is proportional to the pre-hadrons' transverse energy/mass, given as  $m_i^2/\kappa^2$ , where  $m_i$  is the mass of the pre-hadron  $i$ . The probability in Eq. 3.2.3 is relevant for each breakup point of the string on the right hand side of Fig. 3.3. The Schwinger formula, based on the tunneling amplitude [145], determines the possibility of massive quark formation:

$$J = \exp\left(-\frac{\pi m_t^2}{2\kappa}\right). \quad (3.2.4)$$

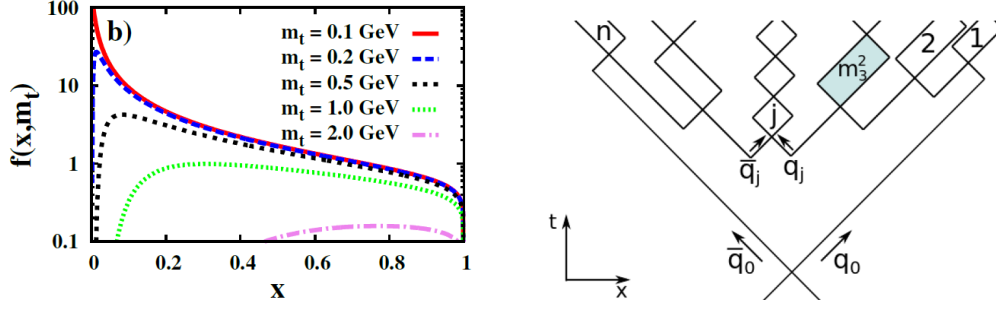


Figure 3.3: (Left) The Lund fragmentation function has been plotted as a function of the energy fraction  $x$  for various amounts of transverse masses  $0.1\text{GeV}/c^2 \leq m_t \leq 2\text{GeV}/c^2$ . (Right) Space-time evolution of pre-hadron production in the Lund string model.

Only the respective probability of generating an  $uu$ ,  $dd$ ,  $ss$  or any of the various diquark-antidiquark pairs are necessary for the string decay. Excluding Chiral Symmetry Restoration, the relative factors employed in PHSD are as follows [144]:

$$u : d : s : diquark = \begin{cases} 1 : 1 : 0.3 : 0.07 & \text{at SPS energies} \\ 1 : 1 : 0.4 : 0.07 & \text{at AGS energies} \end{cases} \quad (3.2.5)$$

The production probability of a  $s\bar{s}$  pair compared to a light quark pair can be calculated using Eq. 3.2.4:

$$\frac{P(s\bar{s})}{P(u\bar{u})} = \frac{P(s\bar{s})}{P(d\bar{d})} = \gamma_s = \exp\left(-\pi \frac{m_s^2 - m_{u,d}^2}{2\kappa}\right), \quad (3.2.6)$$

where the light quark masses  $m_u$  and  $m_d$  are equivalent. The leading and secondary pre-hadrons are the two types of pre-hadrons that exist in PHSD. The highest momenta in the center-of-mass of the strings define the leading mesons and baryons. They may interact instantly with other particles with reduced cross-sections. The reduced cross-sections are used to describe the interactions of the leading quarks/antiquarks in line with the constituent quark model as:

$$\sigma(q - B) = 1/3\sigma(B - B), \quad (3.2.7)$$

$$\sigma(qq - B) = 2/3\sigma(B - B), \quad (3.2.8)$$

$$\sigma(qq - q) = 2/9\sigma(B - B), \quad (3.2.9)$$

where  $\sigma(B - B)$  is the baryon-baryon cross-section at given  $\sqrt{s}$ . The leading particles are the same as the high  $p_t$  particles in the EPOS that can be created at the beginning of a collision. After the initial collision, the secondary pre-hadrons appear after  $\tau_f = 0.5 - 0.8$  fm/c formation time on a hyperbola, as seen in Fig 3.4. In order to distribute the energy to the secondary pre-hadrons, one employs the Lund fragmentation function, Eq. 3.2.3.

### 3.2.3 Quark-gluon plasma (PHSDe)

In the PHSD framework, the DQPM is employed to specify the properties of the quarks  $q$ , antiquarks  $\bar{q}$  and gluons  $g$  in the QGP phase [90, 146, 147] following the ideas of Peshier's

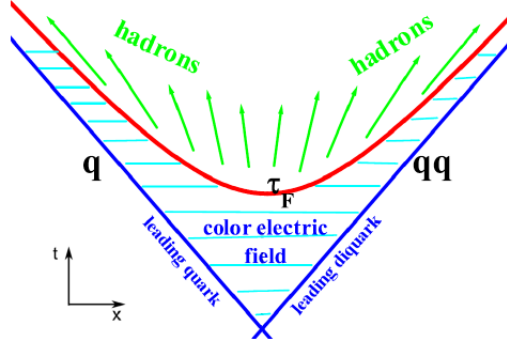


Figure 3.4: Schematic representation of the string formation and decay from the initial baryon. The string, which contains quarks and diquarks, is linked to the color electric field, which produces hadrons after the formation time  $\tau_f$ .

work [148, 149]. It starts with the entropy density in the quasiparticle limit,

$$\begin{aligned}
 s^{dqp} = & -d_g \int \frac{d^4p}{(2\pi)^4} \frac{\partial n_B(p_0/T)}{\partial T} (Im \ln(-\Delta^{-1}) + Im \Pi Re \Delta) \\
 & -d_q \int \frac{d^4p}{(2\pi)^4} \frac{\partial n_F((p_0 - \mu_q)/T)}{\partial T} (Im \ln(-S_q^{-1}) + Im \Sigma_q Re S_q) \\
 & -d_{\bar{q}} \int \frac{d^4p}{(2\pi)^4} \frac{\partial n_F((p_0 + \mu_q)/T)}{\partial T} (Im \ln(-S_{\bar{q}}^{-1}) + Im \Sigma_{\bar{q}} Re S_{\bar{q}}),
 \end{aligned} \tag{3.2.10}$$

where the degeneracy factor for quarks  $q$  and antiquarks  $\bar{q}$  (for three flavors  $N_f$  and three colors  $N_c$ ) is  $d_q = d_{\bar{q}} = 2N_c N_f = 18$ , whereas the gluon degeneracy factor is  $d_g = 2(N_c^2 - 1) = 16$ . In Eq. 3.2.10, the Bose and Fermi distribution functions, respectively, are

$$n_B(p_0/T) = \frac{1}{e^{p_0/T} - 1}, \tag{3.2.11}$$

$$n_F((p_0 - \mu_q)/T) = \frac{1}{e^{(p_0 - \mu_q)/T} + 1}. \tag{3.2.12}$$

The quasiparticle propagators of gluons, quarks and antiquarks are taken as

$$\Delta^{-1} = p^\mu p_\mu - \Pi, \quad S_q^{-1} = p^\mu p_\mu - \Sigma_q, \quad S_{\bar{q}} = p^\mu p_\mu - \Sigma_{\bar{q}}, \tag{3.2.13}$$

where the quasiparticle self-energies  $\Pi$  and  $\Sigma$  from the ansatz are given by

$$\Pi = M_g^2 - 2i\gamma_g p_0, \quad \Sigma_q = M_q^2 - 2i\gamma_q p_0. \tag{3.2.14}$$

In Eq. 3.2.14, the masses,  $M_{g/q}$ , and the spectral widths,  $\gamma_{g/q}$ , of gluons and quarks can be obtained from the Lorentzian spectral functions  $A$ :

$$A(p) = \frac{2\gamma p_0}{(p^\mu p_\mu - M^2)^2 + 4\gamma^2 p_0^2}. \tag{3.2.15}$$

Comparing Eq. 3.2.15 with Eq. 3.1.38, we identify:

$$\bar{\Gamma} = 2\gamma p_0, \quad M^2 = m^2 + Re \bar{\Sigma}^R. \tag{3.2.16}$$

The quasiparticle squared masses depend on the temperature  $T$  and quark chemical potential  $\mu_q$ , while the spectral widths are assumed to depend only on the temperature

$T$ . They can be estimated using the hard thermal loop calculations in the asymptotic high-momentum regime as [71]:

$$M_g^2(T, \mu_B) = \frac{g^2(T, \mu_B)}{6} \left( (N_c + \frac{1}{2}N_f)T^2 + \frac{N_c}{2}\Sigma_g \frac{\mu_q^2}{\pi^2} \right), \quad (3.2.17)$$

$$M_{q/\bar{q}}^2(T, \mu_B) = \frac{N_c^2 - 1}{8N_c} g^2(T, \mu_B) \left( T^2 + \frac{\mu_{q/\bar{q}}^2}{\pi^2} \right), \quad (3.2.18)$$

$$\gamma_g(T, \mu_B) = \frac{1}{3} N_c \frac{g^2(T, \mu_B) T}{8\pi} \ln\left(\frac{2c}{g^2(T, \mu_B)} + 1\right), \quad (3.2.19)$$

$$\gamma_{q/\bar{q}}(T, \mu_B) = \frac{1}{3} \frac{N_c^2 - 1}{2N_c} \frac{g^2(T, \mu_B) T}{8\pi} \ln\left(\frac{2c}{g^2(T, \mu_B)} + 1\right), \quad (3.2.20)$$

with the magnetic cut-off factor  $c = 14.4$ . The QGP's dynamical masses (Eq. 3.2.18) are large in comparison to the bare masses of light ( $u, d$ ) quarks. The strange quark has a larger bare mass, which modifies the dynamical mass  $M_s(T)$  to some extent. This clearly suppresses the channel  $g \rightarrow s + \bar{s}$  compared to the channels  $g \rightarrow u + \bar{u}$  or  $d + \bar{d}$  in the QGP and influences the strangeness ratio. The width of the strange quark is assumed to be the same as for the light ( $u, d$ ) quarks in the DQPM [150].

The dynamical masses ( $M_{(q/\bar{q})}, M_g$ ) and widths ( $\gamma_{q/\bar{q}}, \gamma_g$ ) in DQPM as a function of temperature  $T$  and quark chemical potential  $\mu_B$  have been displayed in the l.h.s of Fig 3.5. For  $\mu_q = 0$  the ratio  $\gamma_q/\gamma_g = 4/9$  is the same for the ratio of squared masses  $M_q^2/M_g^2 = 4/9$ . As a result, across the whole temperature range, the ratio of the width to the pole mass for quarks (antiquarks) is less than for gluons. The hard two-body scattering processes produce the spectral widths, such as:  $gg \leftrightarrow gg$ ,  $gg \leftrightarrow g$ ,  $g \leftrightarrow q\bar{q}$ ,  $gp \leftrightarrow gp$ ,  $gg \leftrightarrow ggg$ ,  $ggg \leftrightarrow gggg$ , and  $pp \leftrightarrow pp$  where  $p$  is an abbreviation for quarks  $q$  and antiquarks  $\bar{q}$ . In the last two equations, the running coupling squared has the form:

$$g^2(T/T_c, \mu_B) = g^2\left(\frac{T^*}{T_c(\mu_B)}, \mu_B = 0\right), \quad (3.2.21)$$

where  $T^* = \sqrt{T^2 + \mu_q^2/\pi^2}$  is the effective temperature,  $T_c(\mu_B)$  stands for the  $\mu_B$ -dependent critical temperature with  $\mu_B = 3\mu_q$ , and  $T_c(\mu_B) = T_c \sqrt{1 - \alpha\mu_B^2}$ .  $T_c$  is the critical temperature at vanishing chemical potential ( $\approx 158$  MeV) and  $\alpha = 0.974$  GeV<sup>-2</sup>. We use Eq. 3.2.21 to obtain the coupling constant at finite baryon chemical potential  $\mu_B$ ,  $\alpha_s = g^2(T, \mu_B)/(4\pi)$ , which is comparable with IQCD results [151].

Following thermodynamics we can use the following formula to compute various thermodynamical quantities. As we deal with a grand-canonical ensemble, the Maxwell relations provide

$$s = \frac{\partial P}{\partial T}, \quad n_B = \frac{\partial P}{\partial \mu_B}, \quad (3.2.22)$$

such that an integration of the entropy density  $s$  over  $T$  and the baryon density  $n_B$  over  $\mu_B$  give the pressure. Additionally, one can define the energy density  $\varepsilon$

$$\varepsilon = Ts(T, \mu_B) - P(T, \mu_B) + \mu_B n_B(T, \mu_B) \quad (3.2.23)$$

and interaction measure  $I$

$$I(T, \mu_B) := \varepsilon(T, \mu_B) - 3P(T, \mu_B) = Ts(T, \mu_B) - 4P(T, \mu_B) + \mu_B n_B(T, \mu_B). \quad (3.2.24)$$

The interaction measure vanishes for massless and noninteracting degrees of freedom at  $\mu_B=0$ . One can compare the thermodynamical properties of the **DQPM** to the **lQCD** results from the BMW group [152] at  $\mu_B=0$  (a) and  $\mu_B=400$  MeV (b) in the r.h.s of Fig. 3.5. For the dimensionless entropy density, energy density, pressure, and interaction measure, there is a good agreement between the **DQPM** and the **lQCD** calculations.

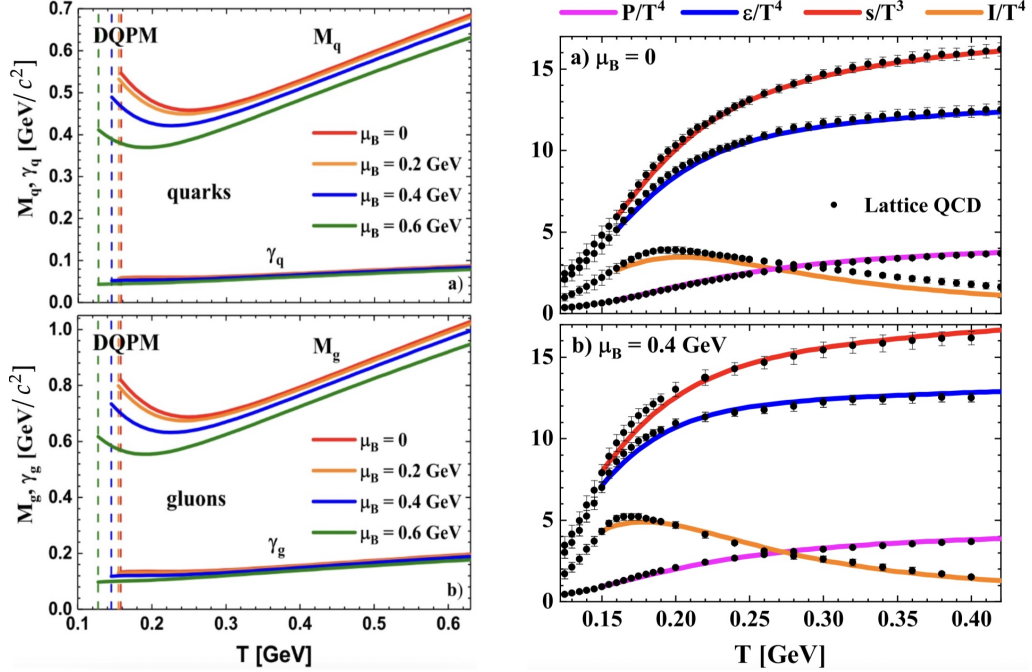


Figure 3.5: Left: (color lines) the effective quark (a) and gluon (b) masses  $M$  and widths  $\gamma$  as a function of the temperature  $T$  for different  $\mu_B$ . The vertical dashed lines correspond to the **DQPM**  $\mu_B$ -dependent critical temperature  $T_c(\mu_B)$  [150]. Right: (color lines) the scaled pressure  $P(T)/T^4$  (pink line), entropy density  $s(T)/T^3$  (red line), scaled energy density  $\varepsilon(T)/T^4$  (blue line), and interaction measure  $I(T)/T^4$  (orange line), from the **DQPM** [150] in comparison to the **lQCD** results from Ref. [152] (full dots) for  $\mu_B=0$  (a) and  $\mu_B=400$  MeV (b).

Due to the large quasiparticle masses and the disappearance of the width  $\gamma$  for  $T < T_c$  (see also l.h.s of Fig. 3.5), the **DQPM** entropy density reduces to zero, resulting in a vanishing parton density. As a result, the **DQPM** specifies the quasiparticle properties only above  $T_c$ .

Additionally, the **DQPM** allows to define a selfconsistent scalar mean-field  $U_s(x)$ , whose gradient generates a scalar force on quarks and antiquarks. The derivative below is used to calculate the scalar mean-field  $U_s(x)$  that acts on quarks and antiquarks,

$$U_s(\rho_s) = \frac{dV_p(\rho_s)}{d\rho_s}, \quad (3.2.25)$$

with the potential energy density  $V_p$  defined by

$$V_p(T, \mu_q) = T_g^{00}(T, \mu_q) + T_q^{00}(T, \mu_q) + T_{\bar{q}}^{00}(T, \mu_q), \quad (3.2.26)$$

and

$$T_i^{00}(T) = d_i \int \frac{d^4p}{(2\pi)^4} 2p_0^2 A_i(p_0) \theta(p_0) n_i(p_0, T) \theta(-P^2), \quad (3.2.27)$$

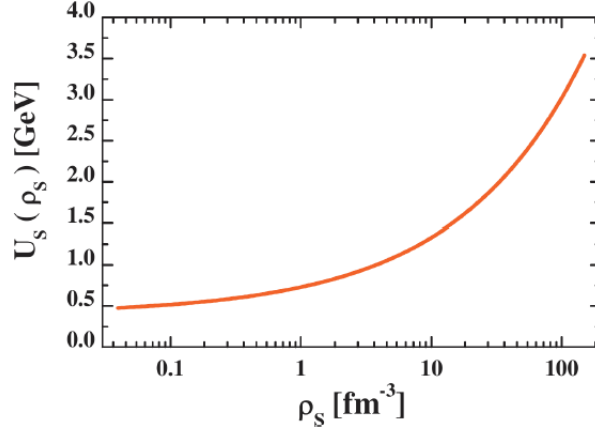


Figure 3.6: The DQPM scalar mean field  $U_s$  for quarks and antiquarks as a function of the scalar density  $\rho_s$ . The figure is taken from Ref. [147]

which is the space-like part of the energy-momentum tensor for parton  $i$ . In Eq. 3.2.27,  $A_i$ ,  $d_i$  and  $n_i$  denote the spectral function, degeneracy and respective occupation distribution, respectively. The scalar mean field  $U_s$  as a function of the scalar density  $\rho_s$  is demonstrated in Fig. 3.6. One can see that  $U_s$  does not change considerably for scalar density less than  $10 \text{fm}^{-3}$ , however, it does grow for  $\rho_s > 10 \text{fm}^{-3}$ . In the PHSD transport approach, the scalar mean field is used to calculate the force on a quasiparticle  $j$ , which is proportional to  $M_j/E_j dU_s/d\rho_s \nabla \rho_s(x)$ , where the scalar density  $\rho_s$  is calculated numerically on a space-time grid.

The partons interact with each other inside the QGP via cross-sections computed in the DQPM. In PHSD, the following elastic interactions,

$$q + q \rightarrow q + q, \quad q + \bar{q} \rightarrow q + \bar{q}, \quad \bar{q} + \bar{q} \rightarrow \bar{q} + \bar{q}, \quad (3.2.28)$$

$$g + g \rightarrow g + g, \quad g + q \rightarrow g + q, \quad g + \bar{q} \rightarrow g + \bar{q}, \quad (3.2.29)$$

and inelastic interaction,

$$q + \bar{q} \leftrightarrow g, \quad (3.2.30)$$

are studied. Since  $u$  and  $d$  have lighter masses than  $s$ , the decay of gluons into  $q\bar{q}$ , where  $q$  is  $u$  or  $d$ , is more probable than  $s\bar{s}$ .

The QGP phase in PHSD appears very quickly after the first collisions at high energy, although this appearance is softer at lower energies due to the nuclei's longer passing time. Furthermore, the QGP energy density and space-time volume are higher for high-energy collisions than for lower-energy collisions [125].

### 3.2.4 Hadronization and hadronic scattering (PHSDe)

As the system expands and cools, the energy density and temperature of the system decrease, and the system transforms from partonic to hadronic degrees of freedom, a process known as hadronization. In this process the colored off-shell partons fuse into color neutral off-shell hadrons. This transition is described by local covariant transition rates [153]; for instance for two off-shell quarks  $q + \bar{q}$  fusion to a meson  $m$  or fusion of three off-shell quarks ( $q_1 + q_2 + q_3 \leftrightarrow B$ ) to color neutral baryonic ( $B$  or  $\bar{B}$ ) resonances. The produced hadrons with higher masses ( $> 1.5 \text{ GeV}/c^2$  for baryons and  $> 1.3 \text{ GeV}/c^2$

for mesons) are treated as "strings" that decay to the known (low mass) hadrons according to the JETSET algorithm [154].

Hadrons interact with each other elastically or inelastically after hadronization in the final stage of the collision. The interaction happens when the impact parameter of the collision between two hadrons is less than the maximum impact parameter which is defined by the geometrical cross-section as,

$$b \leq b_{max} = \sqrt{\frac{\sigma}{\pi}}. \quad (3.2.31)$$

The cross-sections  $\sigma$  are measured either by experiment or calculated in effective theories when experimental data are not available. In PHSD, the interactions of two particles ( $2 \leftrightarrow 2$ ), formation of resonances and their decay ( $1 \leftrightarrow 2$ ), and the annihilation of baryon and antibaryon into three mesons ( $B\bar{B} \leftrightarrow 3m$ ) have been included [155].

### 3.3 Summary and conclusion

In this chapter, we briefly described the PHSD model and how it applies to HICs.

We started by discussing some key concepts of non-equilibrium quantum field theory. The expectation value of any time-dependent operator may be determined using the evolution operators specified on the Keldysh contour in this theory. We can compute the expectation value of 2-point Green's functions on the Keldysh contour, which can be decomposed into four separate Green's functions ( $G^>, G^<, G^a, G^c$ ), as well as retarded and advanced propagators  $G^R$  and  $G^A$ .

In scalar field theory ( $\hat{\phi} = \hat{\phi}^\dagger$ ), we have investigated the evolution equations for various Green's functions, known as Kadanoff-Baym equations. To investigate the properties of the medium, a Wigner transform is applied to the retarded and advanced Green's functions, providing spectral functions. The DQPM employs the spectral function to account for properties such as mass and spectral width of the particles in the medium.

We used the Wigner transform of the Wightman Green's functions in the Kadanoff-Baym equation to derive the dynamics of the medium, i.e., off-shell transport equations. To solve these equations in consistent first-order gradient expansion, we used the extended test-particle Ansatz, which leads to the equation of motions for test-particles. In each timestep, the derived equations of motions determines the particles' dynamics in the medium, including coordinates, momentum, and energy.

The application of PHSD to HICs was discussed in the second section. For the initial collisions of PHSD (PHSDi), the Pythia and the Lund string models are used. The created hadrons are then inserted into the QGP when fulfilling an energy density condition (starting the PHSDe). The DQPM and the equation of motions are used to study the QGP. The temperature and energy density of the system are reduced after expansion, and the shift from the partonic to the hadronic phase is performed via covariant transition rates. Then we have hadron-hadron interactions in the final hadronic state until freeze-out.

The study objective, as noted previously, is to merge EPOSi and PHSDe. These two models are discussed in this and the preceding chapters. We will describe how to merge these two models in the next chapter.

This chapter aims to figure out how the early stages of heavy-ion scattering influence its evolution. We develop a new method called **EPOSi+PHSDe**, in which the standard **EPOS 4** initial conditions (**EPOSi**) are employed as the starting point for **PHSD**-based parton and hadron evolution (**PHSDe**). In the first section, I will discuss how **EPOS 4** handles the initial conditions to produce particles and how they are inserted into **PHSD** as input in the second section. The space-time evolution of particles in the **EPOSi+PHSDe** is then studied using the **PHSD** theory at the end of this chapter.

## 4.1 Initial condition in EPOSi+PHSDe

A fully quantitative description of the experimental data requires, among other ingredients, realistic initial conditions. These initial conditions currently remain a significant source of uncertainty in predicting final state observables. I will discuss in detail how it is handled in **EPOS**.

### 4.1.1 Wood-Saxon distribution

In relativistic nucleus-nucleus collisions, the geometry of the initial overlap region affects the final momentum space distributions of produced particles [156]. A crucial part of specifying the initial conditions is accurately modeling the incoming nuclei's geometry. For many years in simulations for **HICs**, nuclei were approximated as smooth density distributions. The only anisotropies considered in the initial state were the intrinsic almond shape caused by the overlap of two spherical nuclei. As the accumulation of **RHIC** data gradually demonstrated that final state anisotropies were sensitive to the initial geometry and its fluctuations, it became necessary to take into account the lumpiness of the colliding nuclei. This requires an event-by-event treatment via **MC**, where nucleons are distributed in nuclei according to Wood-Saxon distribution [157] which is a collective model of nuclear density as a function of radius. It is also known as the Fermi-shape:

$$\rho(r) = \frac{\rho_0}{1 + \exp \frac{r-R}{a}}, \quad (4.1.1)$$

where  $r$  is the distance of a nucleon from the center of nuclei, for gold (copper) nuclei,  $R = 6.38$  (4.20641) fm and  $a = 0.535$  (0.5977) fm are the radius and diffuseness (surface thickness) of nuclei, respectively.  $\rho_0$  is the density at the center of the nucleus where  $\rho_{0(Au)}=0.1695 \text{ fm}^{-3}$ , and  $\rho_{0(Cu)}=0.1686 \text{ fm}^{-3}$ . The diagrams of the probability densities of the gold (Au) and copper (Cu) nuclei have been illustrated in Fig. 4.1:

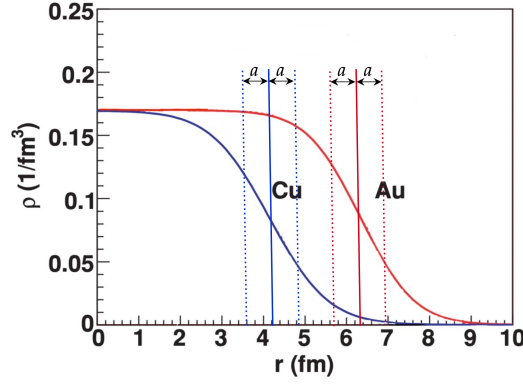


Figure 4.1: Nuclear density as a function of nuclear radius. Solid curves show nuclear density distribution for gold (Au) and copper (Cu) nuclei. The positions of nucleons are sampled according to the Woods-Saxon distribution with default parameter sets. The diffusenesses ( $a$ ) are shown, delimited by vertical dotted lines [157].

The probability of nucleons' existence decreases as one moves away from the center of nuclei, and it is very small on the surface of nuclei, as shown in Fig. 4.1 for both Au and Cu nuclei. We use the Wood-Saxon distribution to generate nucleon positions for both projectile and target in EPOS 4. In EPOS 4, one also has the possibility (for test purposes) to use hard spheres without diffuseness. In this method, it is impossible to have a nucleon outside the surface. We can recognize the difference between both of these definitions in Fig. 4.2 for semi-peripheral collisions of Au-Au at 200 GeV. In our simulations for both EPOS 4 and EPOSi+PHSDe, we employ the Wood-Saxon distribution.

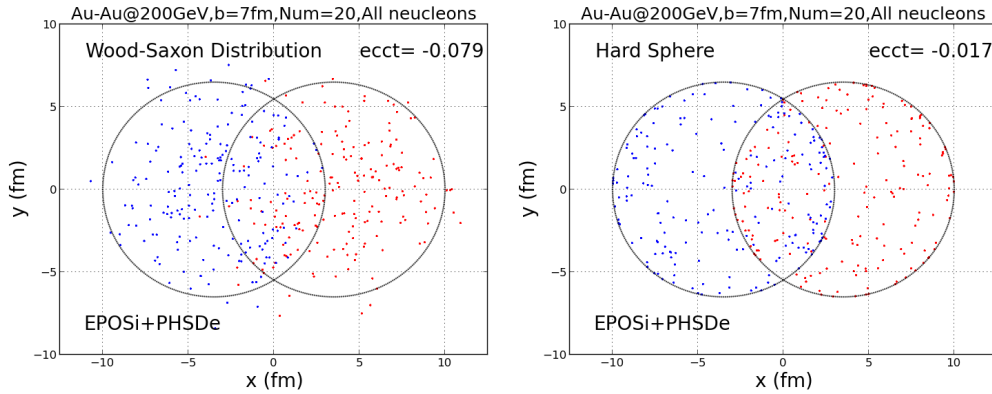


Figure 4.2: Coordinate determination of projectile and target nucleons by Wood-Saxon distribution (l.h.s), and hard sphere without surface thickness (r.h.s) for semi-peripheral Au-Au collisions at 200 GeV.

#### 4.1.2 How are particles identified in EPOS?

In EPOS, PBGRT allows determining pairs of interaction nucleons and the corresponding pomerons, the latter ones being identified by parton ladders and eventually kinky strings. The coordinates of string origins (pomerons) in the overlapping region are then determined by taking an average of the coordinates of shifted participants by impact parameter:

$$x_{(string\ origin)} = \frac{x_{proj} + \frac{b_x}{2} + x_{targ} - \frac{b_x}{2}}{2} = \frac{x_{proj} + x_{targ}}{2}, \quad (4.1.2)$$

$$y_{(\text{string origin})} = \frac{y_{\text{proj}} + \frac{b_y}{2} + y_{\text{targ}} - \frac{b_y}{2}}{2} = \frac{y_{\text{proj}} + y_{\text{targ}}}{2}. \quad (4.1.3)$$

As demonstrated in Fig. 4.3, one has string origins both inside and outside the overlapping zone (almond shape). In EPOS 4, we generate the nucleons for each subevent randomly; nevertheless, one should produce the initial subevent in EPOSi+PHSDe and then keep the nucleons' coordinates for other subevents in each run. It leads to a reduction in the fluctuations caused by particles outside the overlapping area. For example, we need to employ 20 parallel subevents; for the first subevent, Num=1, we generate random nucleon coordinates, which we subsequently use for the others Num=2,...,20.

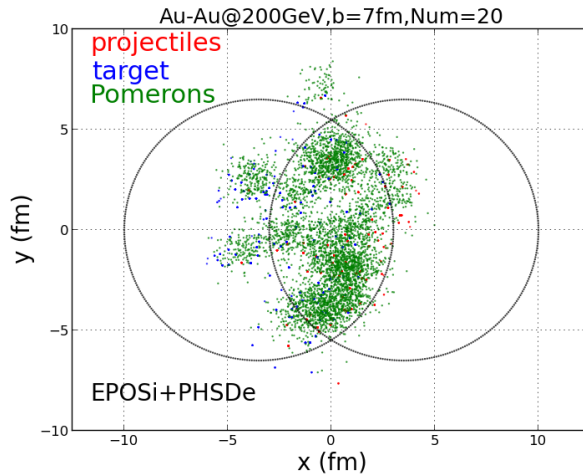


Figure 4.3: The projectile and target participants and their corresponding string origins (pomeron).

The elementary interaction between participants from the projectile and target sides results in several pomerons in the overlapping area, as seen in Fig. 4.4. Each pomeron is composed of several chains of partons (COP). These chains of partons are mapped to relativistic kinky strings, based on the idea that the pomerons amount to essentially longitudinal color fields. These strings are finally "decayed" into string segments.

Technically, the method consists of three steps: first, the pomerons produce several chains of partons (COP), then they are converted to strings (S) based on the color flow diagram (CFD), and finally, the strings are split into several string segments, as discussed in subsection 2.3.1 of chapter 2. In Fig. 4.5, we show the corresponding space-time picture of string segments production (with the blue and red points on the hyperbola) from string origins based on the color flow diagram (CFD). At the same time, we have remnants that are split into several string segments and come directly from the projectile or target. I have just shown the projectile remnants in Fig. 4.4; however, we should have the target remnants as well. The string segments may be very close to each other, this is why in EPOS a core-corona procedure is employed.

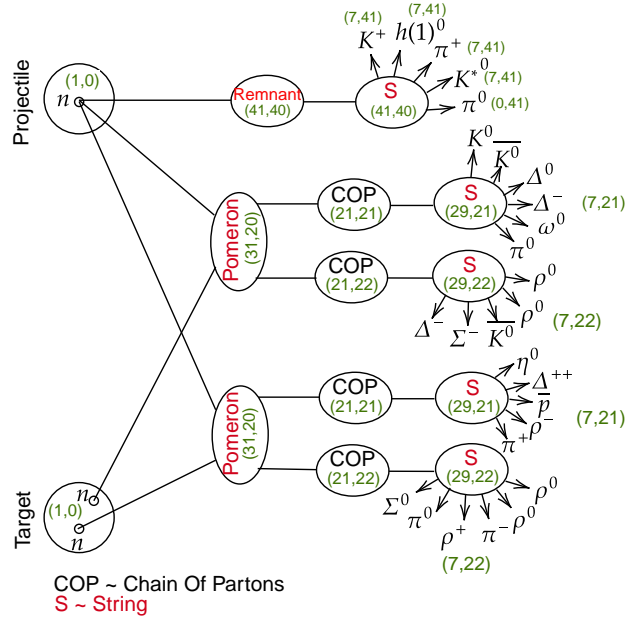


Figure 4.4: The sketch of initialization in EPOS based on the multiple pomerons exchange. Pomerons are formed from the interaction of neutrons ( $n$ ) from projectile and target sides. The pomerons convert into several chains of partons (COP), and then the COP is split into string segments based on the color flow diagram. The first and second numbers in parentheses represent the particle's status (istptl) and type (ityptl) (I will discuss these variables later).

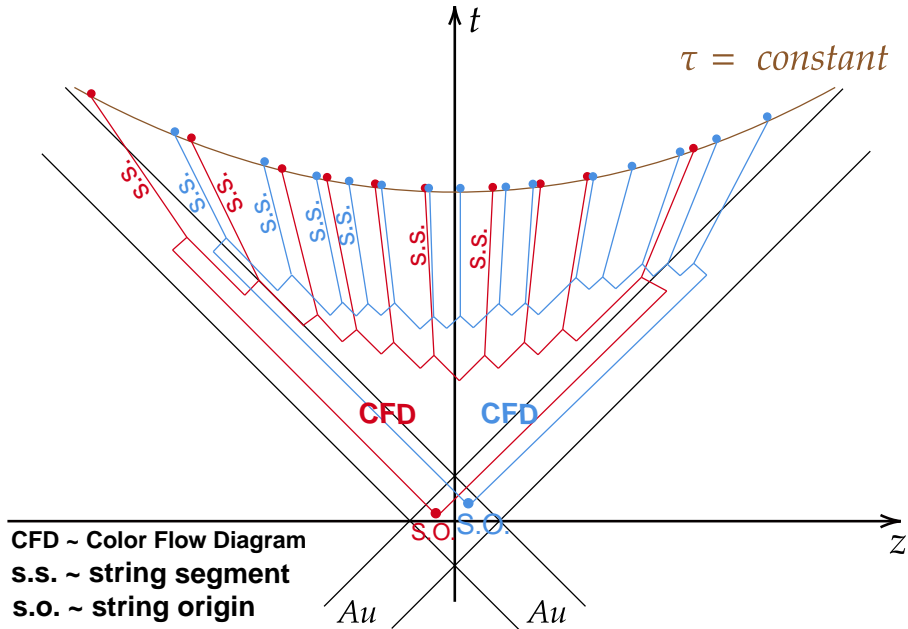


Figure 4.5: The production of string segments at given  $\tau$  on the hyperbola from the string origins (pomerons) in the overlapping area based on the color flow diagram (CFD).

To recall the properties of core particles, one can come back to subsection 2.3.2 of chapter 2. These string segments are those who lost all their energy and could not escape the dense area, so they stay in the dense area and form the core component. On the other hand, the corona part is made up of string segments which escaped the dense

region. They might originate from pomerons or remnants, like the core particles.

Fig. 4.6 shows an example of the different types of particles in a semi-peripheral Au-Au collision at 200 GeV. We show the projectile and target participants (l.h.s) and the core particles (r.h.s). We see a strong correlation between the participant positions and the core areas (the participant positions correspond to the pomeron positions, and the corresponding string segments will be close to their "parent" pomerons).

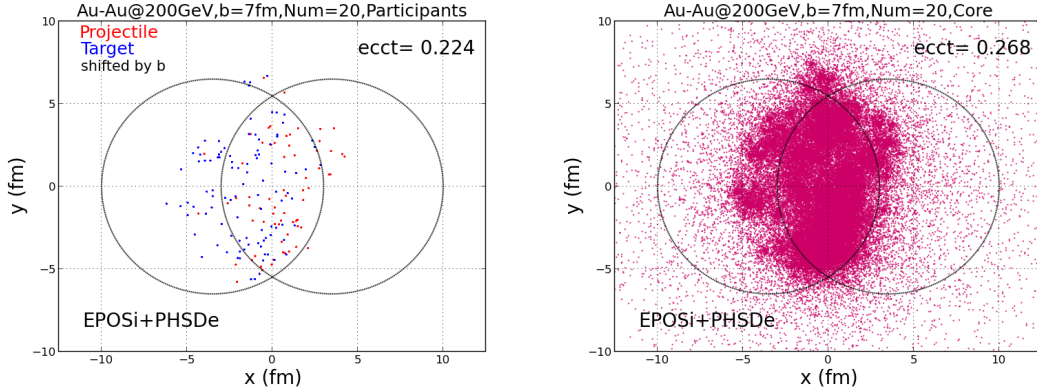


Figure 4.6: Production of particles on the hyperbola in EPOS. Participants from projectile and target sides (l.h.s). Core (dense region) and corona particles (r.h.s).

In EPOS, the core segments define the initial condition for a hydrodynamical evolution. Also, in our case (EPOSi+PHSDe), we use this core-corona picture, as discussed in more detail later.

In the EPOS code, one uses a "particle list" which contains the complete history of the particle production in an event. We use the notation "particle" in a general sense for all kinds of "objects" like pomerons, partons, string segments etc. Various variables are used to characterize the particles, as shown in table 4.1. Important for our discussion is in particular the "status" (istptl): string segments belong to the core ("core particles") get istptl=7, those contributing to the corona ("corona particles") get istptl=0. The variable "ityptl" is defined where the string segments (core and corona) are coming from (pomerons or remnants). Each particle's parent is defined by "ior" and "jor".

Table 4.1: Classify various types of particles in EPOS

type of particles	istptl	ityptl	ior	jor
participants	1	0	-1	0
spectators	0	0	0	0
soft pomerons	20-29	20-39	father	mother
hard pomerons	30-39	20-39	father	mother
partons in pomerons	21	20-39	father	0
remnants	40-59	40-59	father	0
core particles	7	20-39, 40-59	father	0
particles after Hydro	–	60	father	0
corona particles	0	20-39, 40-59	father	0

In Fig. 4.4, the first and second digits in parentheses denote the particle's status (istptl) and type (ityptl). The status of string segments in this figure might be either

7 (core) or 0 (corona). They may come from the soft/hard pomerons or the remnants. Pomerons having lower (higher) energy are known as soft (hard) pomerons.

### 4.1.3 From core-corona separation to pre-hadrons

As we have already discussed, [EPOS](#) employs a core-corona separation procedure, based on the energy loss of string segments. The string segments are shown in three dimensions (transverse plane vs. space-time rapidity  $\eta_s$ ) in [Fig. 4.7](#), employing  $\eta_s$  instead of  $z$  axis. The upper panel depicts the string segments at a given  $\tau$ ; technically, the dense region is referred to as the core part, while the scattered string segments area is referred to as the corona part.

In [EPOS<sub>i</sub>+PHSD<sub>e</sub>](#), we use as well this core-corona picture. Having identified the core, we have to transform it into an initial condition of [PHSD](#), which requires "pre-hadrons". Naively one may directly use all the string segments as pre-hadrons. But this turned out not to work at all. So we decided to consider connected areas of the core as a kind of "rope", which generally defines objects obtained from fusing strings. It is essentially what we do with the core construction. All the other string segments (those not contributing to the ropes) are referred to as corona particles. We sketch the "rope production" in the middle panel of [Fig. 4.7](#). Ropes are still considered longitudinal color fields similar to ordinary strings but with larger string tension, resulting in higher transverse momenta of its decay products.

We then break the rope segments into several pieces, called "clusters", for technical reasons. Technically, we employ a cluster algorithm, based on a cell-centered grid in three dimensions, which enables us to define slices in the longitudinal variable, and identify connected transverse areas and the corresponding transverse density distribution. These connected sections in transverse space amount to rope slices, as illustrated in the lower panel of [Fig. 4.7](#).

So as to prepare the evolution for [PHSD](#), we require to decay clusters into quasiparticles in their center of mass. In [EPOS<sub>i</sub>+PHSD<sub>e</sub>](#) language, we call these quasiparticles "**core pre-hadrons**". We use the term "pre-hadrons" because we want to distinguish between hadrons from hadronization before and after the plasma at the end of evolution. The pre-hadronization procedure happens quickly after the nuclei pass through each other at some early initial time.

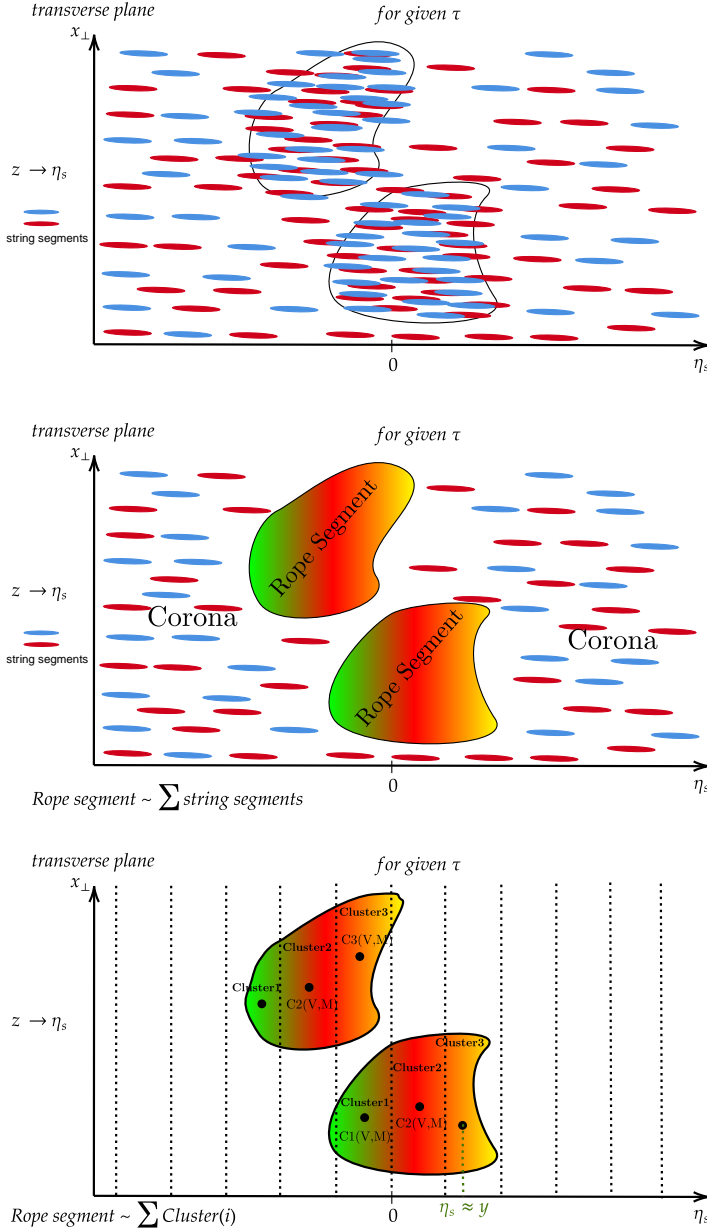


Figure 4.7: From string segments to cluster formation on the hyperbola at given  $\tau$  in EPOSi+PHSDe. String segments on the hyperbola with identifying the overlapping string segments region (upper panel), separating rope segments and corona parts (middle panel), and cutting rope segments into several clusters (lower panel).

The pre-hadronization will be realized slice by slice. Different slices correspond to different locations ( $z$ ) in space which we replaced by  $\eta_s$  being defined as

$$\eta_s = \frac{1}{2} \log\left(\frac{t+z}{t-z}\right), \quad (4.1.4)$$

and there is a strong correlation between  $\eta$  and rapidity  $y$  of the rope segment,

$$y = \frac{1}{2} \log\left(\frac{E+p_z}{E-p_z}\right). \quad (4.1.5)$$

Therefore, the core pre-hadrons are produced from the decay of a rope slice at given  $\eta$ , which shows up at  $y$  close to  $\eta$ . In addition to these "core pre-hadrons", we have

the corona particles, referred to as "**corona pre-hadrons**". I will explain more about corona pre-hadrons in the following.

All clusters are sitting in different places of rapidity, as seen in Fig. 4.8. In EPOS, the statistical method to decay of cluster or an effective object with mass  $M$  at rest is used by microcanonical decay [158] where mass  $M$  is the total available cluster's energy  $E$ . Let  $\{h_1, \dots, h_n\}$  be an ensemble of  $n$  hadrons  $h_i$  with four-momenta  $p_i$ . The probability distribution for the corresponding n-body decay is given by

$$dP = C_{vol} C_{deg} C_{ident} C_{flav} d\Phi_{NRPS}, \quad (4.1.6)$$

where

$$C_{vol} = \frac{V^n}{(2\pi\hbar)^{3n}}, \quad C_{deg} = \prod_{i=1}^n g_{k(i)}, \quad (4.1.7)$$

and

$$C_{ident} = \prod_{k \in S} \frac{1}{n_\alpha!}, \quad C_{flav} = \prod_A \delta_{Q_A, \Sigma q_{A_i}}, \quad (4.1.8)$$

and the non-relativistic phase space (NRPS) element,

$$d\Phi_{NRPS} = \delta(M - \Sigma E_i) \delta(\Sigma \vec{p}_i) \prod_{i=1}^n d^3 p_i, \quad (4.1.9)$$

where  $E_i = \sqrt{m_i^2 + p_i^2}$  and  $\vec{p}_i$  are the energy and 3-momentum of particle  $i$ . In Eqs. 4.1.7, and 4.1.8,  $C_{deg}$  stands degeneracies of particle  $i$ ,  $C_{ident}$  being the occurrence of identical particles in  $K$  with the number of particles in species  $\alpha$ ,  $n_\alpha$ , and the term  $\delta_{Q_A, \Sigma q_{A_i}}$  remains conservation laws (baryons  $A=B$ , electric charge  $A=C$  and strangeness  $A=S$ ). The core pre-hadrons are randomly produced from clusters based on the Markov chains method using MC approaches according to the microcanonical probability distribution in Eq. 4.1.6 in the rest frame.

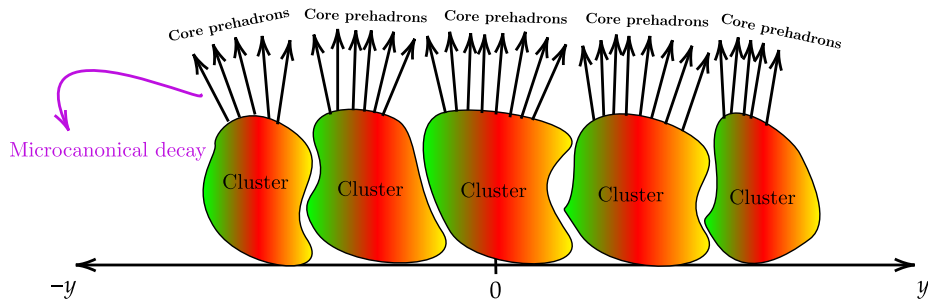


Figure 4.8: Distribution of clusters in the rapidity space. The clusters decay into core pre-hadrons based on the microcanonical decay.

After decaying the clusters, most of the core pre-hadrons are produced in the low momentum range,  $p < 2$  GeV/c, as seen on the l.h.s of Fig. 4.9. Additionally, one can see they are more produced in the mid-rapidity region.

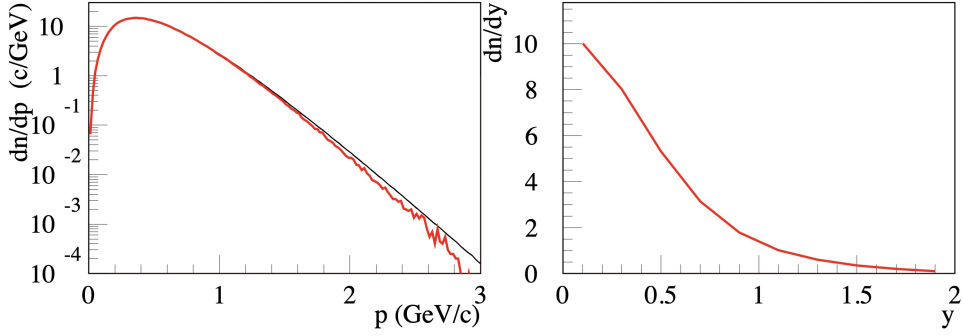


Figure 4.9: Momentum (l.h.s) and rapidity (r.h.s) distributions of core pre-hadrons from the microcanonical decay of clusters.

Since the microcanonical decays are done in the center of mass of each cluster, one finally needs to perform a Lorentz boost with the corresponding cluster rapidities. As a result, the rapidity distribution of our core pre-hadrons will be a sum of "bell-shaped" curves, see Fig. 4.10, which amounts to a relatively flat distribution.

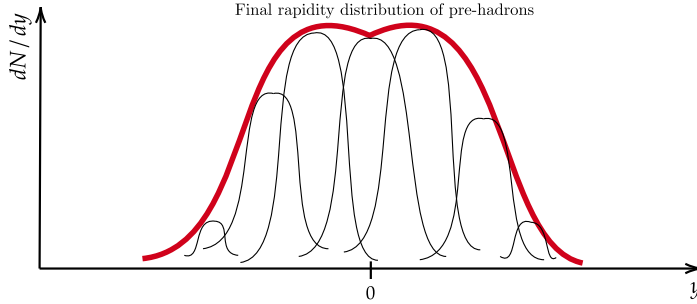


Figure 4.10: Schematic representation of final rapidity distribution of pre-hadrons.

## 4.2 Inserting pre-hadrons from EPOS to PHSD

The pre-hadrons as discussed in the previous section, are produced on a hyperbola in space-time. For technical reasons, one needs pre-hadrons at a given time, since the PHSD code used the cartesian coordinates  $(x,y,z,t)$  and not Milne coordinates as EPOS (see Appendix A.2), see Figs. 4.11 and 4.12.

In principle, we "just" need to extrapolate the pre-hadrons from the hyperbola back to the constant timeline, see Fig. 4.11. Since the positions and momenta are known, we know the trajectories,  $\vec{R}(t) = \vec{R}(0) + \vec{V} \times (t - t_0)$ , and we compute the position at the initial time in PHSD ( $t = t_{ini_{PHSD}}$ ). This is actually what is done for "corona pre-hadrons". We call this procedure "normal extrapolation", which can be seen by red and blue arrows in Fig. 4.13. As shown in table 4.2, spectators, high  $p_T$ , and particles formed before the start time of PHSD are all identified as the corona pre-hadrons. The spectators' corona pre-hadrons are mainly formed in most forward and backward rapidities. The rest of the corona pre-hadrons are produced in both mid-rapidity and forward and backward rapidities. Both models contain the same corona pre-hadrons.

Concerning the "core pre-hadrons", the situation is more complicated, since the "pre-hadrons" did not exist prior to the hyperbola line, but what does exist are their "parents". Therefore, we need to do the "technical extrapolation" involves the insertion of "core

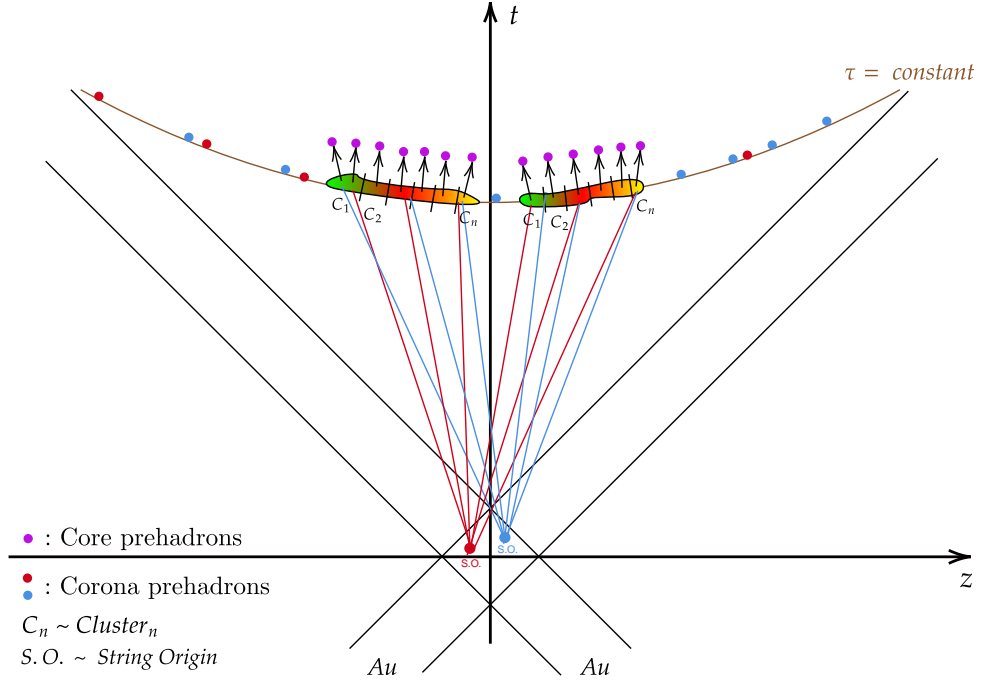
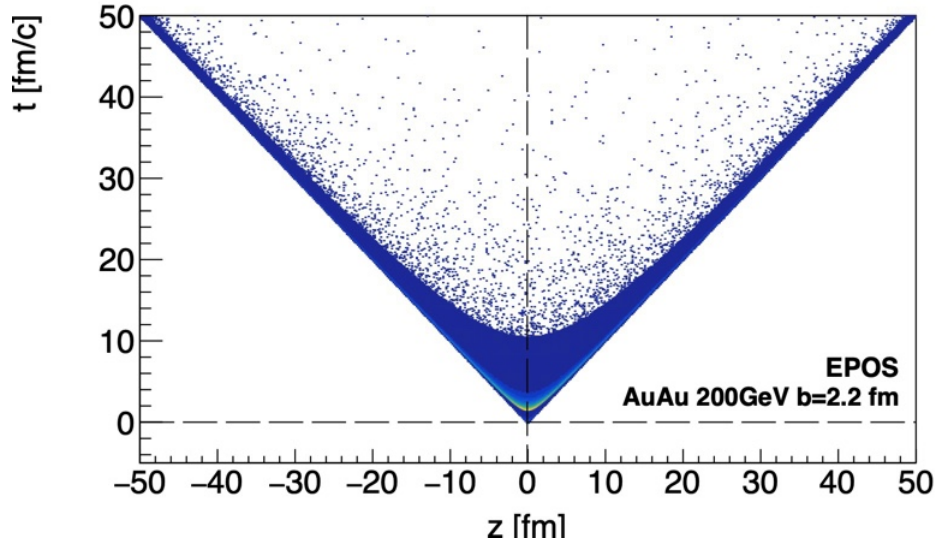

 Figure 4.11: Formation of the pre-hadrons on the hyperbola in EPOS at given  $\tau$ .


Figure 4.12: The same as Fig. 4.11 for the central Au-Au collision at 200 GeV.

pre-hadrons" into the PHSD start time. The cluster decay particles (core pre-hadrons) should be placed at the positions of string segments having produced the clusters. These segments are referred to as "parents" with respect to the clusters, whereas the decay products (core pre-hadrons) are referred to as "children".

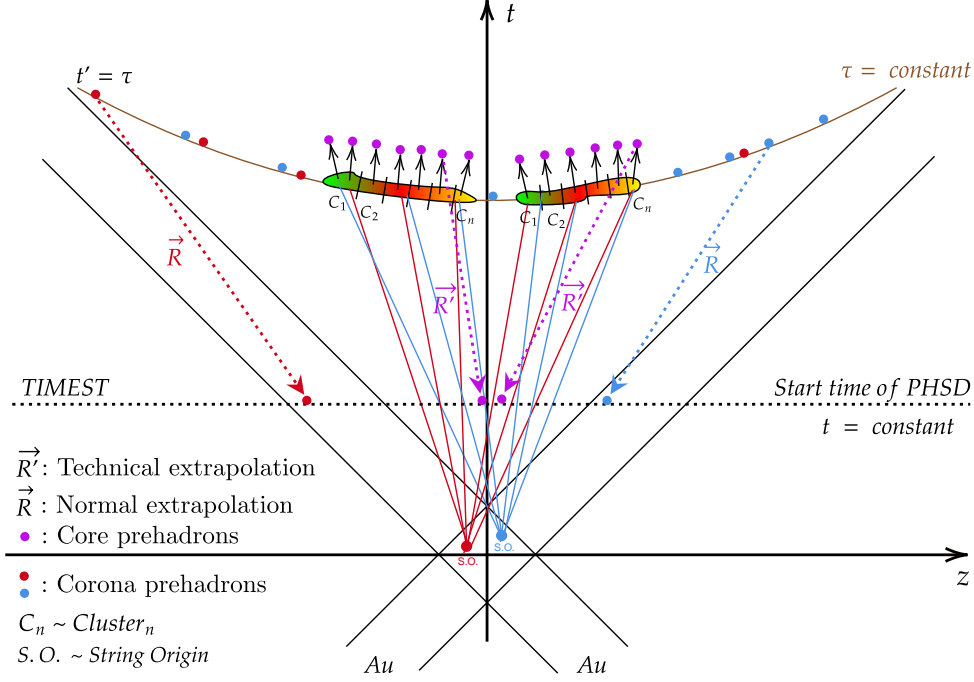


Figure 4.13: Extrapolation back in time procedure of core and corona pre-hadrons to the start time of PHSD.

Table 4.2: All types of pre-hadrons with their characteristics in EPOS and PHSD.

Au-Au@200GeV						
EPOS core pre-hadrons						
type	istptl	ityptl	ic	imelt	rapidity	status
strings	7	20<ity<39	1	1	-5<y<5	formed
remnants	29	40<ity<59	1	1	-5<y<5	formed
EPOS/PHSD corona pre-hadrons						
type	istptl	ityptl	ic	imelt	rapidity	status
strings/ remnants	41	40<ity<59	0	0	-5<y<5	formed
spectators	0	0	0	0	-5.4<y<- 5 or 5<y<5.4	leading/ formed

We have actually two kinds of "core pre-hadrons": All the string segments contributing to cluster formation are "EPOS core pre-hadrons", see table 4.2 (this table is purely technical in coding, with "ityptl" standing for the particle type, "istptl" for the particle status, "ic" for core (=1) or corona (=0) particles, "imelt" denoting whether (=1) or not (=0) the particle melted into a QGP, and "leading" for particles that collide with other particles with the lowest cross-section). The "EPOS core pre-hadrons" are mainly produced in mid-rapidity. However, what we use as the initial condition for PHSD are

the "children" from a cluster decay, extrapolated back to the positions of these string segments. They are referred to as "PHSD core pre-hadrons".

Some more details about the technical extrapolation: For a given cluster, we sum over all parents (string segments) and compute for each one the intersection of its trajectory with the constant time  $t = t_0$  (PHSD start time), see the violet arrows in Fig 4.13, as

$$\vec{R}'(t_0) = \vec{R}'(t_p) + \vec{V}_p \times (t_0 - t_p), \quad (4.2.1)$$

where  $\vec{R}'(t_p)$  is the known position of the parent at some time  $t_p$ . Here,  $\vec{V}_p$  is the parent's velocity. Then we define these positions to be the positions (at  $t = t_0$ ) of the children (the PHSD core pre-hadrons). However, this leads to a large violation of "Bjorken scaling", i.e., the expected approximate identity  $y = \eta_s$ . Therefore, we use the above formula only for the transverse components, and for the longitudinal component  $z$ , we compute the position as  $z(t_0) = V \times t_0$ , with  $V = \tanh(Y_c)$ , and  $Y_c$  being the cluster rapidity. In this way, we recover  $y \approx y_s$ . But this is not a very important point; using this prescription or using the above formula for all three components does not change much.

Fig. 4.14 shows a schematic picture of the final positions of core and corona pre-hadrons following extrapolation processes to the PHSD start time.

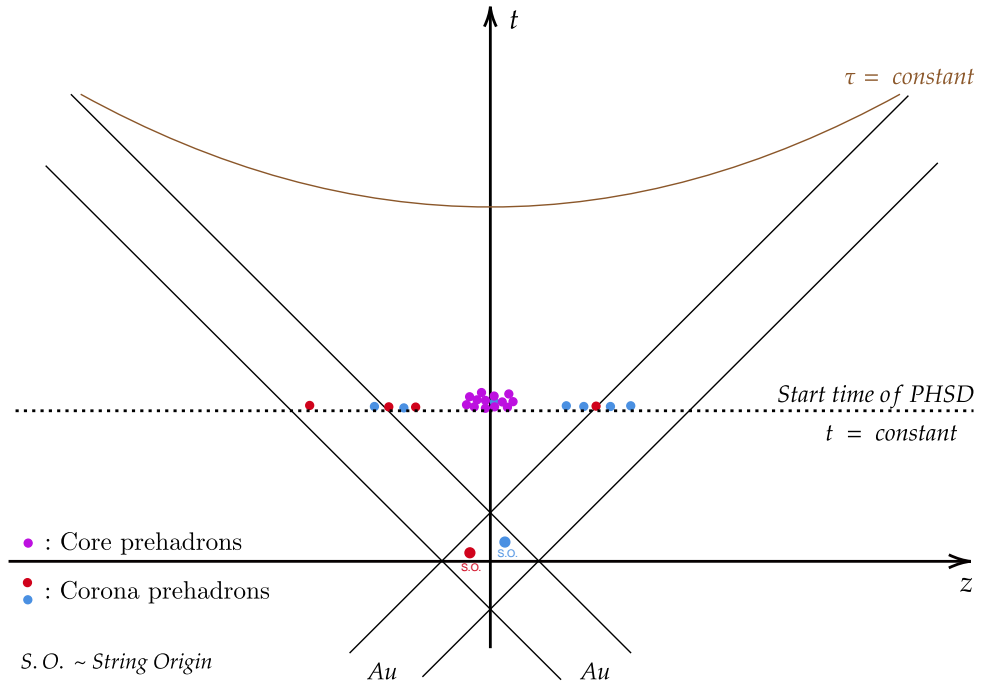


Figure 4.14: The schematic depiction of the final places of core and corona pre-hadrons after extrapolation at the start time of the PHSD evolution.

In Fig. 4.15, we plot the coordinates of core and corona pre-hadrons (EPOS and PHSD pre-hadrons) in the transverse plane. In addition to core and corona, we also distinguish particles coming from projectile and target remnants or strings (referring to "normal" strings from pomerons; there are also strings from remnant excitations). We also (for completeness) show spectator nucleon positions.

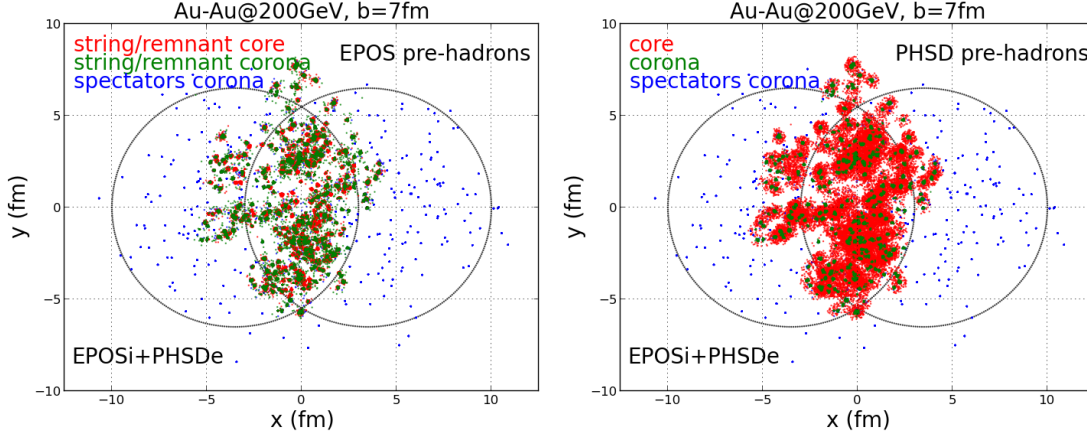


Figure 4.15: Schematic representation of pre-hadrons in transverse plane in [EPOS](#) (l.h.s) and [PHSD](#) (r.h.s). The simulation was done for semi-peripheral [Au-Au](#) collision at 200 GeV.

As I previously mentioned and seen in Fig. 4.15, the corona pre-hadrons in both models are precisely equivalent. Still, the core pre-hadrons in both models are different. The children do not perfectly map to the parent positions; rather, they are in general more frequent than the available parent positions, and therefore slightly spread in the transverse direction to avoid several particles at the same position. Nevertheless, we observe the same bumpy structure in both cases.

After inserting the pre-hadrons into the [PHSD](#) arrays, we must address the melting of the pre-hadrons into the partonic phase. The evolution of partonic and hadronic phases in [PHSD](#) is studied using a space-time grid, where a collection of cells make up the grid at each time step, as discussed in section 3.2 of chapter 3. We estimate the mean energy density of particles per cell based on "parents" and "corona pre-hadrons". If the mean energy density exceeds the critical energy density ( $0.5 \text{ GeV}/\text{fm}^3$ ), the corresponding core pre-hadrons are melted into the partonic phase (pre-hadrons with  $\text{imelt}=1$  and  $\text{ic}=1$  in table 4.2). Technically, this is called the "melting procedure". The corona pre-hadrons do not melt into the partonic phase, but they contribute to determining the energy density.

One can check the representation of pre-hadrons in the transverse plane with the melting condition. In general, using melting condition, we have approximately the same number of core pre-hadrons in [EPOS 4](#) and [PHSD](#). The corona pre-hadrons are exactly the same in both models, as shown in Fig. 4.16 since the melting condition does not affect these particles. However, as shown in Fig. 4.15, the number of core pre-hadrons in [PHSD](#) is more when the melting condition is absent than when it is present.

The rest of the evolution of matter is carried out using [PHSD](#) non-equilibrium dynamics once all pre-hadrons have been inserted into [PHSD](#) arrays.

I will compare the energy density evolution of matter in three different simulations, [EPOS 4](#), [EPOSi+PHSDe](#), and [PHSD](#), at the beginning of the next chapter. In the following section, I will explain the space-time evolution of particles in [EPOSi+PHSDe](#) from when we insert pre-hadrons from [EPOS 4](#) to the start time of [PHSD](#).

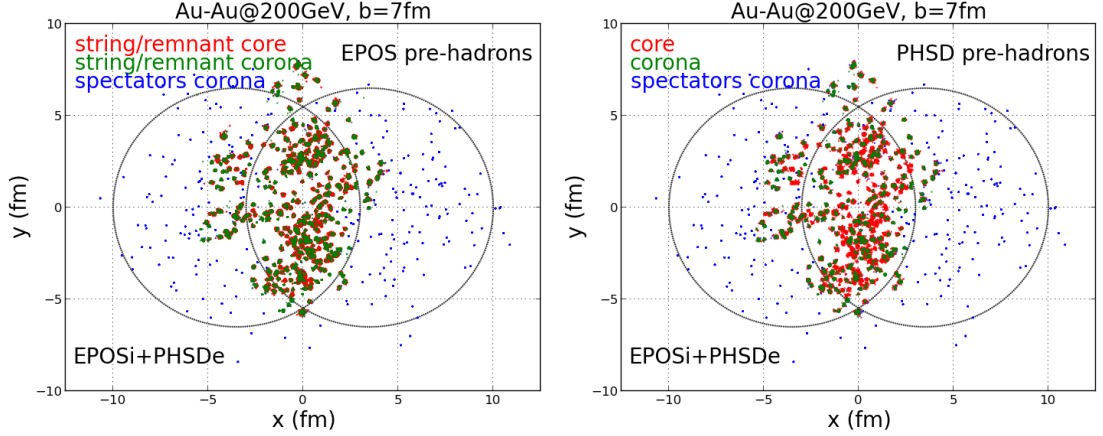


Figure 4.16: Schematic representation of pre-hadrons in transverse plane in **EPOS** (l.h.s) and **PHSD** (r.h.s). The simulation was done for semi-peripheral **Au-Au** collision at 200 GeV with melting condition.

### 4.3 Space-time evolution of particles in **EPOSi+PHSDe**

The equations of motion for the test-particles, Eqs. 3.1.43-3.1.45 in chapter 3, are used to study the evolution of particles in the space-time grid of **PHSD**. We used the parallel events in each run since the parallel ensemble approach is employed in **PHSD** to ensure that there are enough particles per cell. Collisions can only occur inside the same ensemble; however, macroscopic properties such as energy density and cross-section are averaged throughout the parallel ensemble. To melt particles in the **QGP** phase, we must supply the melting condition, which necessitates having enough particles per cell.

**PHSD** employs a space-time grid that expands over time to describe **HICs**. Since the particle densities during the start of the **PHSD** evolution are high, a considerable number of interactions are predicted. Therefore, the time-step must be short enough to consider their interactions reasonably. The system expands later, and the size of the cells steadily rises due to the Lorentz gamma factor. In the axis parallel to the beam direction, the **PHSD** grids are expanded (generally referred to as z-axis) over time.

Fig. 4.17 reveals the space-time evolution of particles in **EPOSi+PHSDe** for the **Au-Au** collision at 200 GeV with impact parameter of 7 fm. The time-step in which all the pre-hadrons were injected into the **PHSD** array is shown on the upper left of Fig. 4.17, and we compute the energy density per cell in this time step. Following the melting condition, the core-prehadrons deconfined into partons at time 0.064 fm/c. The partonic phase begins at this time, and we have a lot of partons in the overlapping region, as indicated by the red points. From the beginning to the end, the partonic phase evolves slowly and begins to hadronize (based on the hadronization process described in section 3.2.4 of chapter 3). They are more likely to be fused into mesons than baryons because mesons are cheaper to produce. In parallel, the number of mesons (baryons) rises with time due to hadronization, and they spread till the end, resulting in blue (green) points.

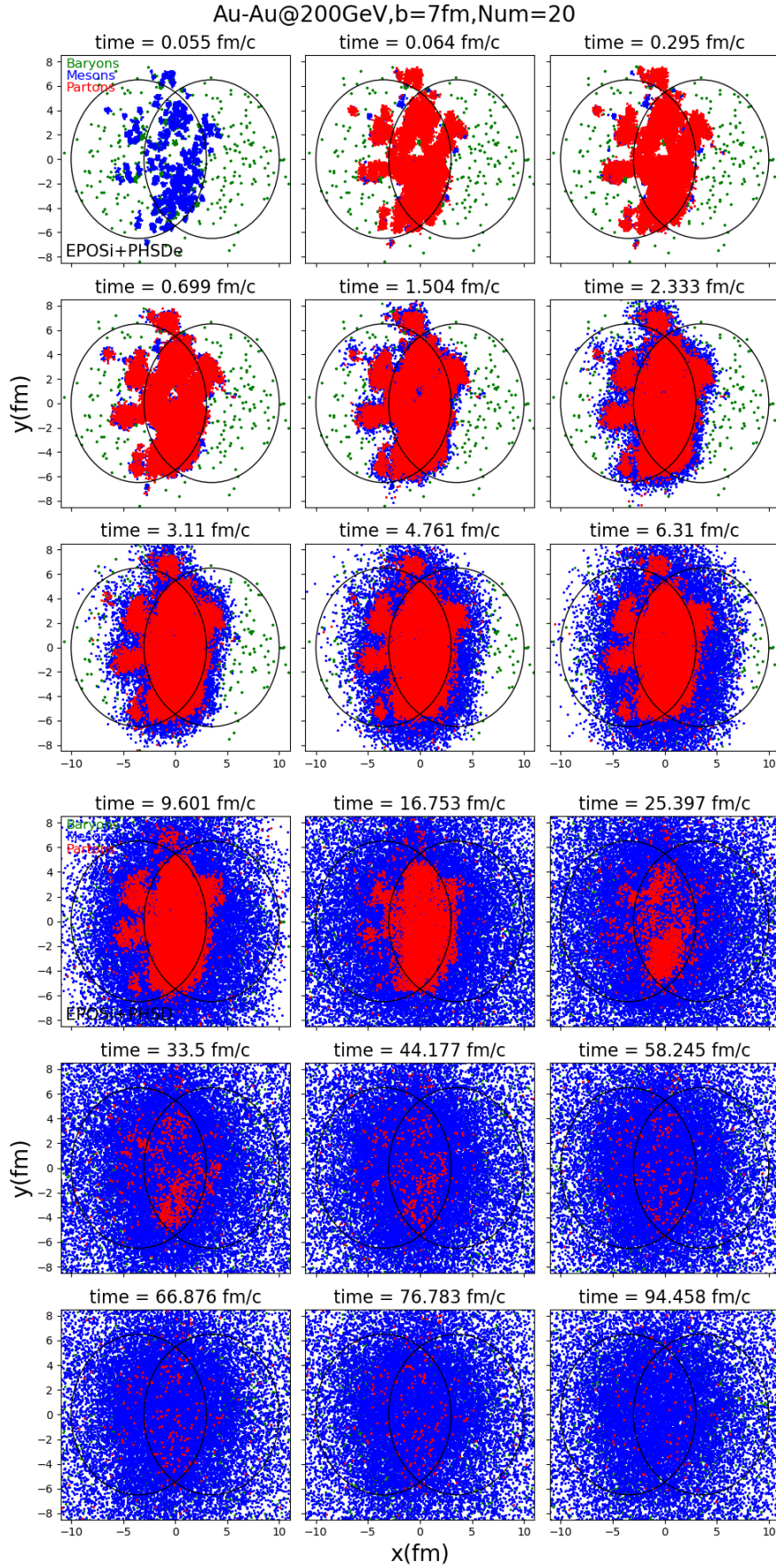


Figure 4.17: The space-time evolution of baryons, mesons, and partons in EPOSi+PHSDe for semi-peripheral Au-Au collision at 200 GeV.

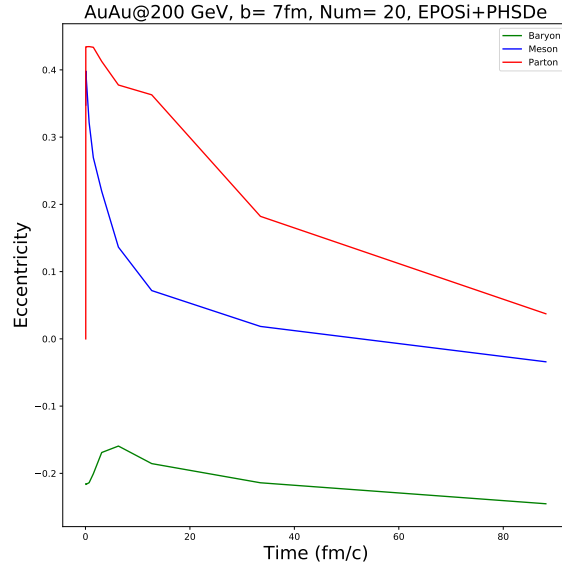


Figure 4.18: Eccentricity as a function of time for baryons (green curve), mesons (blue curve), and partons (red curve) with the same collision as Fig. 4.17.

It is also important to note that the corona pre-hadrons outside or inside the overlapping area do not move more in the transverse plane during the evolution and do not melt into the partonic phase. The majority of corona pre-hadrons are spectators. The "bulk" or "fireball" produced in HICs includes particles composed of light quarks with a small transverse momentum. High momentum particles are rare and mainly arise in the pre-equilibrium stage immediately after a collision. These particles can pass through the fireball due to their high momentum.

The eccentricity as a function of time corresponding to Fig. 4.17 can be seen in Fig. 4.18. The eccentricity  $\epsilon$  for each kind of particle (meson, baryon, and parton) at each time step is defined as

$$\epsilon = \frac{\langle y^2 - x^2 \rangle}{\langle y^2 + x^2 \rangle}, \quad (4.3.1)$$

where  $x$  and  $y$  are the transverse coordinates. Mesons are predominantly produced along the  $y$  axis at the beginning, time=0.055 fm/c, and have the most considerable eccentricity. Afterward, they scatter along the  $x$  and  $y$  axes, and the eccentricities decline. However, baryons are mainly produced along the  $x$ -axis and outside the overlapping zone; they have negative eccentricity at first. Last but not least, partons can be seen, which are produced in time = 0.064 fm/c under melting conditions. Partons, like mesons, are mostly produced in the overlapping region since we only melt the core pre-hadrons from participants, which most of the core pre-hadrons are mesons. According to the hadronization process in PHSD, they will disappear over time, and their eccentricity will decrease.

We use the EPOS analysis tools to analyze the final particles after the PHSD evolution. For both EPOSi+PHSDe and pure PHSD simulations, we do this work. The results of three different simulations, EPOS 4, EPOSi+PHSDe, and pure PHSD, will be compared in the next chapter.

## 4.4 Summary and conclusion

In this chapter, I presented the main topic of my Ph.D. thesis in theory, which involved merging two separate approaches, [EPOS<sub>i</sub>](#) and [PHSD<sub>e</sub>](#), to study the dynamical description of [HICs](#) and [QGP](#).

To do this, we used primary scattering based on the basic theory, [PBGRT](#), within [EPOS<sub>i</sub>](#) to generate particles as input for [PHSD<sub>e</sub>](#) space-time evolution in the first section. We employed the wood-Saxon distribution to determine the coordinates of nucleons in the projectile and target. Pomerons were created from the elementary interaction between participants on both sides. Pomerons eventually "split" into different types of string segments. Connected regions of high densities of string segments defined ropes. In a cell-centered grid, each rope segment was separated into several slices, which they called clusters. To prepare the evolution in [PHSD<sub>e</sub>](#), we decayed the clusters into core pre-hadrons. Microcanonical decay was employed as a statistical approach for decaying these clusters in [EPOS](#).

In the second section, the extrapolation procedures for inserting [EPOS](#) pre-hadrons into [PHSD](#) arrays were introduced. The main issue in our project is the fact that [EPOS](#) uses light-cone dynamics in Milne coordinates, whereas [PHSD](#) employs real-time dynamics in Minkovski space-time. These procedures allow us to map pre-hadrons on the hyperbola in space-time back to their origin segments, which formed before starting the [PHSD](#) evolution. The [EPOS2PHSD](#) interface was used to transition between two sophisticated codes. After the injection of pre-hadrons, the space-time evolution of matter began in the non-equilibrium [PHSD](#) framework.

In the third section, the space-time evolution of particles in [EPOS<sub>i</sub>+PHSD<sub>e</sub>](#) collisions at 200 GeV was studied for semi-peripheral [Au-Au](#) collisions. We inserted all of the [EPOS](#) pre-hadrons into [PHSD](#) at the beginning. For the [PHSD](#) evolution, the pre-hadrons (mesons and baryons) are the starting point. With respect to the melting condition, those pre-hadrons with a high enough energy density immediately transformed into partons, and the number of partons increased significantly. The partonic phase evolves slowly over time, but there is increased production of hadrons initially at the borders and then over all partons, particularly mesons (based on the hadronization in [PHSD](#)). All of the final particles in [EPOS<sub>i</sub>+PHSD<sub>e</sub>/PHSD](#) are stored in one table with their properties at the end of the evolution, and then they are sent to [EPOS](#) for analysis.

The results of three different simulations, [EPOS 4](#), [EPOS<sub>i</sub>+PHSD<sub>e</sub>](#), and pure [PHSD](#), will be presented and compared in the next chapter.



## CHAPTER 5

### COMPARING RESULTS IN THREE DIFFERENT APPROACHES

In the previous chapter, I introduced [EPOSi+PHSD<sub>e</sub>](#), a new model that combines the initial conditions from [EPOS 4 \(EPOSi\)](#) with the space-time evolution of partonic and hadronic phases in [PHSD \(PHSD<sub>e</sub>\)](#). In this chapter, I will present results compared to experimental data and also to simulations using [EPOS 4](#) and [PHSD](#).

The new approach's results try to understand the role of initial condition and the role of the space-time evolution in [HICs](#). [EPOS 4](#) and [PHSD](#) models have fundamentally different initial conditions and matter evolutions, but we can see similar results in some observables at the end. Therefore, it is useful to employ [EPOSi+PHSD<sub>e</sub>](#), in which the differences could be related to the initial conditions or evolutions. Comparing [EPOSi+PHSD<sub>e</sub>](#) and [EPOS 4 \(PHSD\)](#), we will see the differences between these two models with the same "initial conditions" ("evolutions") but different "evolutions" ("initial conditions").

Before showing the results, it would be helpful to clarify how we estimate the centrality bins in our analysis to compare the results to the experimental data. We performed all the analyses in the three models based on the analysis in [EPOS 4](#). In experiments, the centrality bins are measured using the multiplicity distributions, as explained in the first chapter; however, in [EPOS 4](#), the impact parameter distribution is employed. We show the distribution of events as a function of the impact parameter to identify the centrality bins in [Fig. 5.1](#) from most central (0-5%) to most peripheral (80-X %) from [EPOS 4](#) point of view.

We cannot compare our multiplicity distributions to those of the experimentalists since their distributions are usually presented as "raw data," without the necessary modifications (mainly efficiency issues). Therefore, unlike in our simulation, it does not correspond to the "true" multiplicity distributions. The centrality definition is stable for the same system with different energies when the impact parameter is used. The relationships between centrality classes and impact parameters for [Au-Au](#) collision have been defined in [Appendix B.2](#) in [EPOS](#) framework.

The results cover "bulk matter observables" such as transverse mass/transverse momentum spectra, rapidity/pseudorapidity densities, and anisotropic flow in these three simulations. The number of events used to plot particle yields is around four million in each simulation. To start, we will compare the evolution of matter in the three models in the following section.

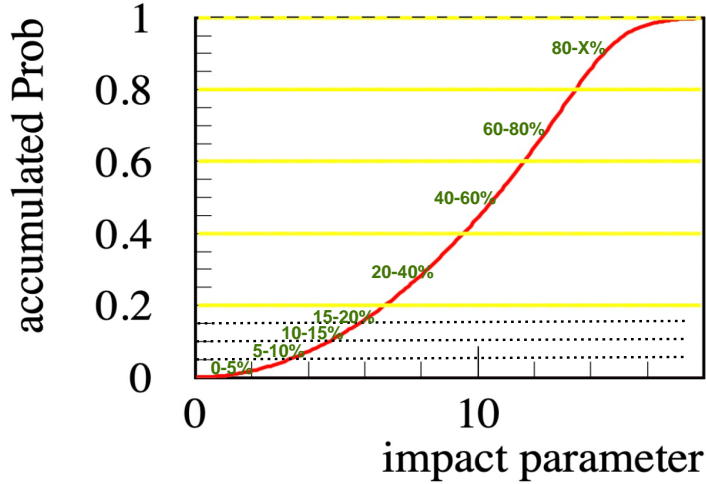


Figure 5.1: Distribution of events as a function of impact parameter to determine the centrality bins from most central (0-5%) to most peripheral (80-X%) [Au-Au](#) collisions in [EPOS 4](#) analysis.

## 5.1 Energy density evolutions

At the end of the first stage, once the two nuclei have penetrated each other, we can compute macroscopic parameters like energy density to describe how matter evolves. In this section, we compare the energy density evolutions in various simulations, including [EPOS 4](#), [EPOSi+PHSDe](#), and pure [PHSD](#).

To compute the energy density, we use the energy-momentum tensor  $T^{\mu\nu}$  from kinetic theory, which is given by [120]:

$$T^{\mu\nu}(\vec{q}) = \int \frac{d^3p}{E} p^\mu p^\nu f(\vec{q}, \vec{p}), \quad (5.1.1)$$

where  $\vec{q}$  is a position vector,  $\vec{p}$  indicates a momentum vector, and  $f$  denotes the phase space density for a given time. The energy density is given as  $T^{00}$  in the comoving frame.

In both [EPOSi+PHSDe](#) and [PHSD](#), we use the conventional approximation way to compute the energy density in the comoving frame as [159]:

$$\varepsilon = \frac{\sum_i E_i}{V_{cell}}, \quad (5.1.2)$$

where the sum of all particles in each cell is provided by  $\sum_i$ , and the volume of the cell is defined by  $V_{cell} = \Delta x \Delta y \Delta z$ .  $\Delta x = \Delta y = 1$  fm which is equal to the hadron size and  $\Delta z = 1/\gamma_{com}$  fm.  $\gamma_{com}$  is the Lorentz gamma factor for the transformation into the center-of-mass of the colliding nuclei. Therefore, the energy density of the cells is determined by

$$\varepsilon' = \frac{E'}{V'} = \frac{E/\gamma}{V \times \gamma} = \frac{\varepsilon}{\gamma^2}. \quad (5.1.3)$$

The energy density evolutions for semi-peripheral [Au-Au](#) collisions at 200 GeV in three models have been presented in Figs. 5.2 and 5.3. The left, middle, and right panels are related to the [EPOS 4](#), [EPOSi+PHSDe](#), and pure [PHSD](#) energy density profiles. One can see that the evolutions behave in fundamentally different ways, [EPOS 4](#) on one side and both [EPOSi+PHSDe](#) and pure [PHSD](#) on the other side.

Initially (time  $< 3$  fm/c), the energy density distributions in both [EPOS 4](#) and [EPOSi+PHSDe](#) are more or less the same in both shapes and magnitudes. This is due to the fact that both of these simulations have employed identical initial conditions. The evolution of energy density in pure [PHSD](#) begins later on (at time=1.518 fm/c). At the beginning of pure [PHSD](#) evolution, we have more energy density than two other simulations with different shapes.

Later on (time  $> 3$  fm/c), however, [EPOS 4](#) has a strong transverse expansion and evolves in an asymmetric fashion, which leads to having more transverse flows. This scenario presents the substantial asymmetric transverse expansion towards the direction perpendicular to the initial distribution's primary axis. On the other hand, both [EPOSi+PHSDe](#) and pure [PHSD](#) show substantially different behavior in both shape and magnitude compared to [EPOS 4](#). For times more than five fm/c, the energy density magnitudes in pure [PHSD](#) are approximately two times greater than [EPOSi+PHSDe](#).

Both [EPOSi+PHSDe](#) and pure [PHSD](#) show hardly any expansion, particularly in the transverse plane, indicating the systems do not grow near the transverse flow in [EPOS 4](#), which will have a drastic effect on observables like transverse momentum and elliptic flow. In the following, we will see the differences between these observables in different models.

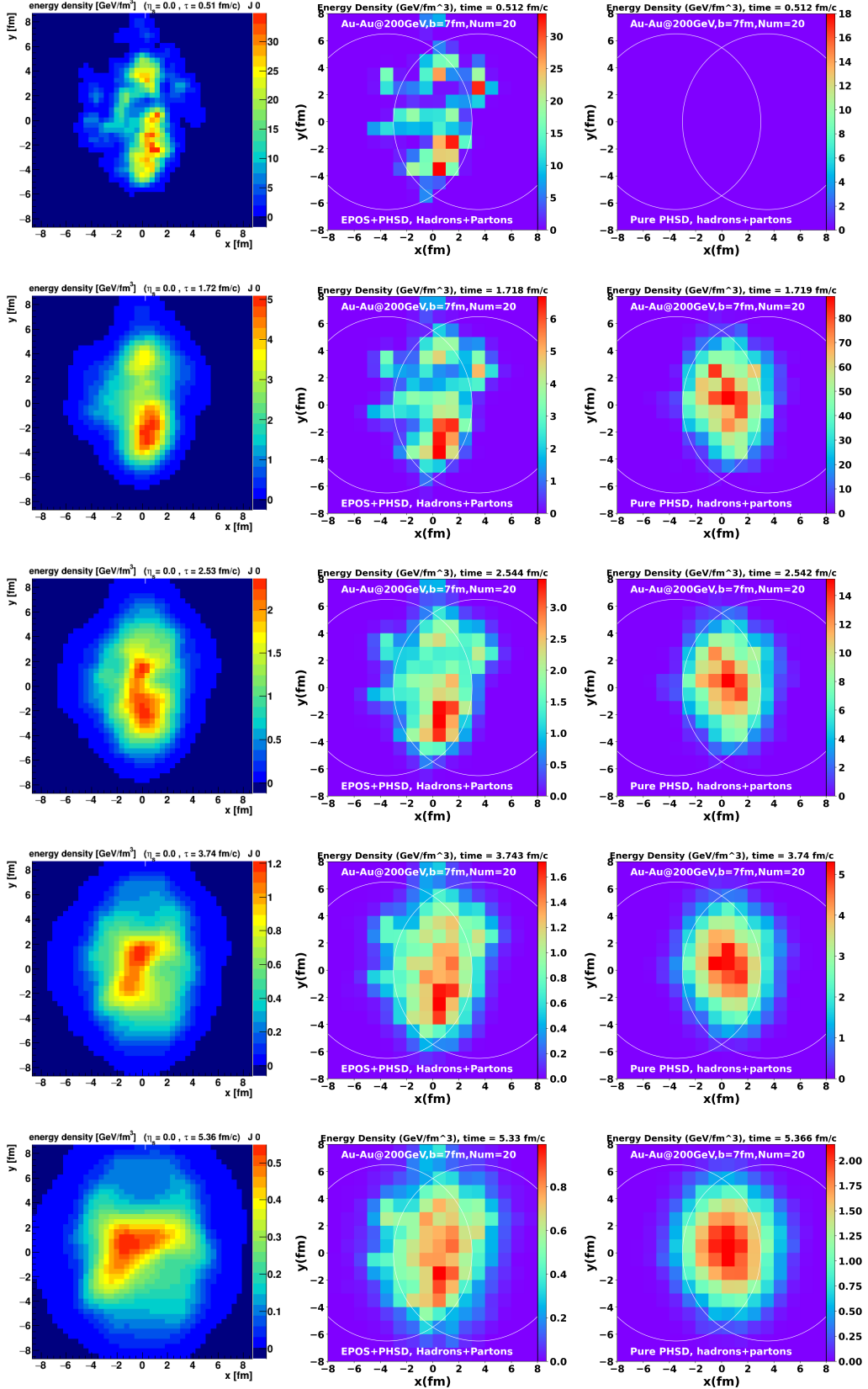


Figure 5.2: Time evolution of the energy density in the transverse plane (at  $z=0$ ) for Au-Au collisions at 200 GeV with an impact parameter of 7 fm, for three models, considering events with the same initial matter distribution (at 1.7fm/c). We show from left to right EPOS 4, EPOS+PHSD, and pure PHSD models, and from top to bottom the times (in fm/c) 0.5, 1.7, 2.5, 3.7, 5.3.

## 5.1. ENERGY DENSITY EVOLUTIONS

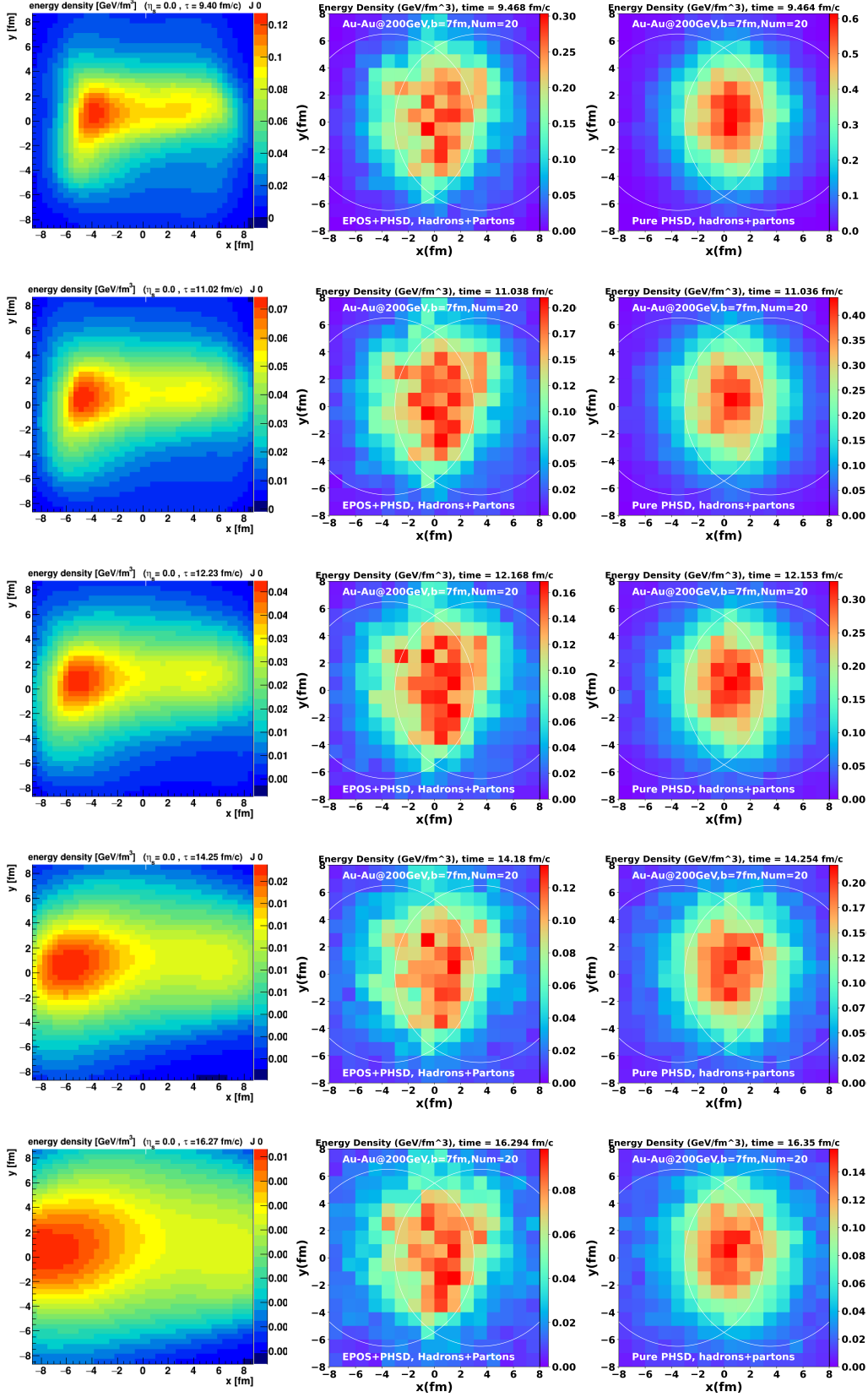


Figure 5.3: Same as Fig. 5.2, continuing the time evolution of the energy density for (from top to bottom, in fm/c) 9.4, 11.0, 12.2, 14.2, 16.3.

## 5.2 Bulk matter observables

**QCD** predicts the creation of a new type of matter, **QGP**, under extreme conditions, i.e., high energy density, which might be produced in relativistic **HICs**, as I discussed in the first chapter. Certain bulk properties may indicate **QGP** production. Strangeness and baryon production rates, and collective transverse radial flow are among such bulk properties. Particle spectra can be used to investigate these phenomena. The following subsections will present the transverse mass spectra, rapidity and pseudorapidity densities, transverse momentum spectra, and anisotropic flow results in the three models.

### 5.2.1 Transverse mass spectra

In this part, we present the transverse mass ( $m_T = \sqrt{p_T^2 + m^2}$ ) spectra for charged pion ( $\pi^\pm$ ), charged kaon ( $K^\pm$ ), proton ( $p$ ), and antiproton ( $\bar{p}$ ) in **Au-Au** collision at  $\sqrt{s_{NN}} = 200$  GeV for different simulations. The **Au-Au** events are divided into 9 centrality classes based on measured charged particle multiplicity within pseudorapidity  $|\eta| < 0.5$ . The geometrical cross-section is divided into these classes, ranging from central to peripheral collisions (0-80%), as seen in Figs. 5.4, 5.5, and 5.6.

The experimental data shown here were taken from the **STAR** experiment [160] using the same triggers as our simulations. The **STAR** time projection chamber (TPC) [161] detects charged particles. For **Au-Au** collisions, Zero degree calorimeters provide a minimum bias trigger.

Now, as shown in Figs. 5.4, 5.5, and 5.6, I try to compare particle yields from the different models to the experimental data. **EPOS 4** (left panel) can reproduce well the experimental results for all centrality classes in the case of the pions ( $\pi^\pm$ ). **EPOSi+PHSDe** (middle panel) is quite similar compared to **EPOS 4**. However, in pure **PHSD** (right panel), pion yields are lower compared to **EPOSi+PHSDe** and compared to the data.

As seen in Fig. 5.5, **EPOS 4** can quite well reproduce kaons ( $K^\pm$ ) in all centrality classes compared to the experimental data. For transverse mass lower than  $0.4 \text{ GeV}/c^2$ , the invariant yields of  $K^\pm$  in **EPOSi+PHSDe** are higher than **EPOS 4**, pure **PHSD**, and experimental data in all centrality classes. In pure **PHSD**, we have different behavior: in central collisions (0-20%), we have more  $K^+$  production; in mid-central/semi-peripheral collisions (20-50%), we have almost the same  $K^+$  production, but in most peripheral collisions ( $> 50\%$ ), we have fewer  $K^+$  compare to the real data and **EPOS 4** results. In all centrality bins,  $K^-$  is less produced in pure **PHSD** than in **EPOS 4**.

As shown in Fig. 5.6, **EPOS 4** can reproduce  $p$  and  $\bar{p}$  comparable to the data for all centrality classes. **EPOSi+PHSDe** and **PHSD**, on the other hand, produce  $p$ , and  $\bar{p}$  at a larger rate as compared to **EPOS 4** and the data for central and mid-central collisions. However, they produce much less  $p$  and  $\bar{p}$  than **EPOS 4** and the data for peripheral collisions. One can see that **EPOSi+PHSDe** improved the results compared to pure **PHSD** for peripheral collisions.

We checked the low transverse mass (or low transverse momentum) here. Concerning the comparison between the models, we observed some differences for  $\pi^\pm$  and  $K^\pm$ , but nothing fundamental; however, there are significant differences between **EPOS 4** and the two other models for  $p$  and  $\bar{p}$ , which we will discuss later in more detail.

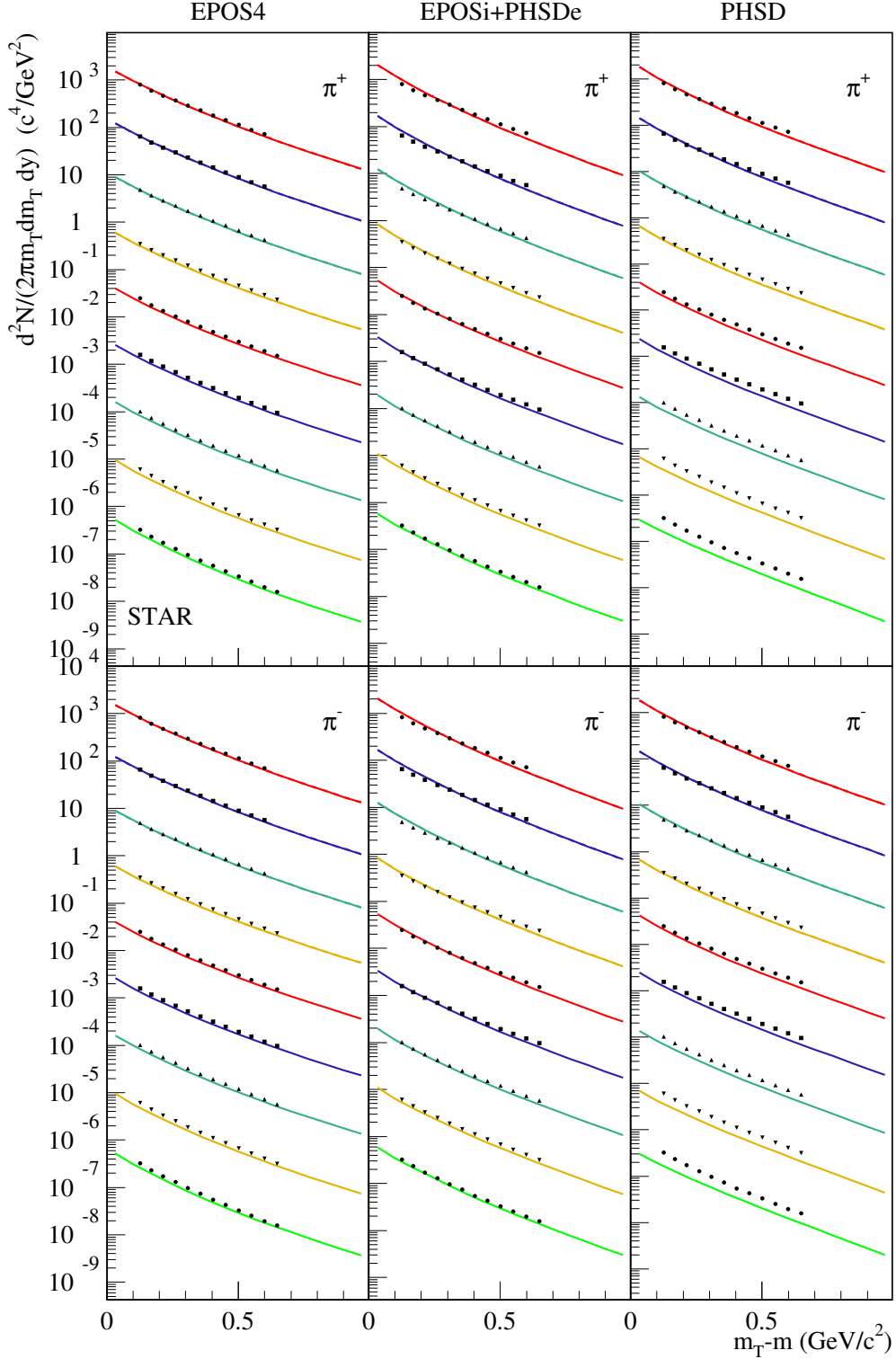


Figure 5.4: Invariant yield as a function of transverse mass for  $\pi^\pm$  for Au-Au collision at  $\sqrt{s_{NN}}=200$  GeV at mid-rapidity ( $|y| < 0.5$ ) in three different simulations: EPOS 4 (left panel), EPOSi+PHSDe (middle panel), and pure PHSD (right panel). The different transverse mass spectra are plotted with different centrality ranges 0-5%, 5-10%, 10-20%, 20-30%, 30-40%, 40-50%, 50-60%, 60-70%, 70-80% from top to bottom in each plot. All the results compared to the STAR experimental data [160] with the black points. All curves and experimental data are scaled by  $2 * 10^{-n}$  starting from the top most curve with  $2 * 10^0$ .

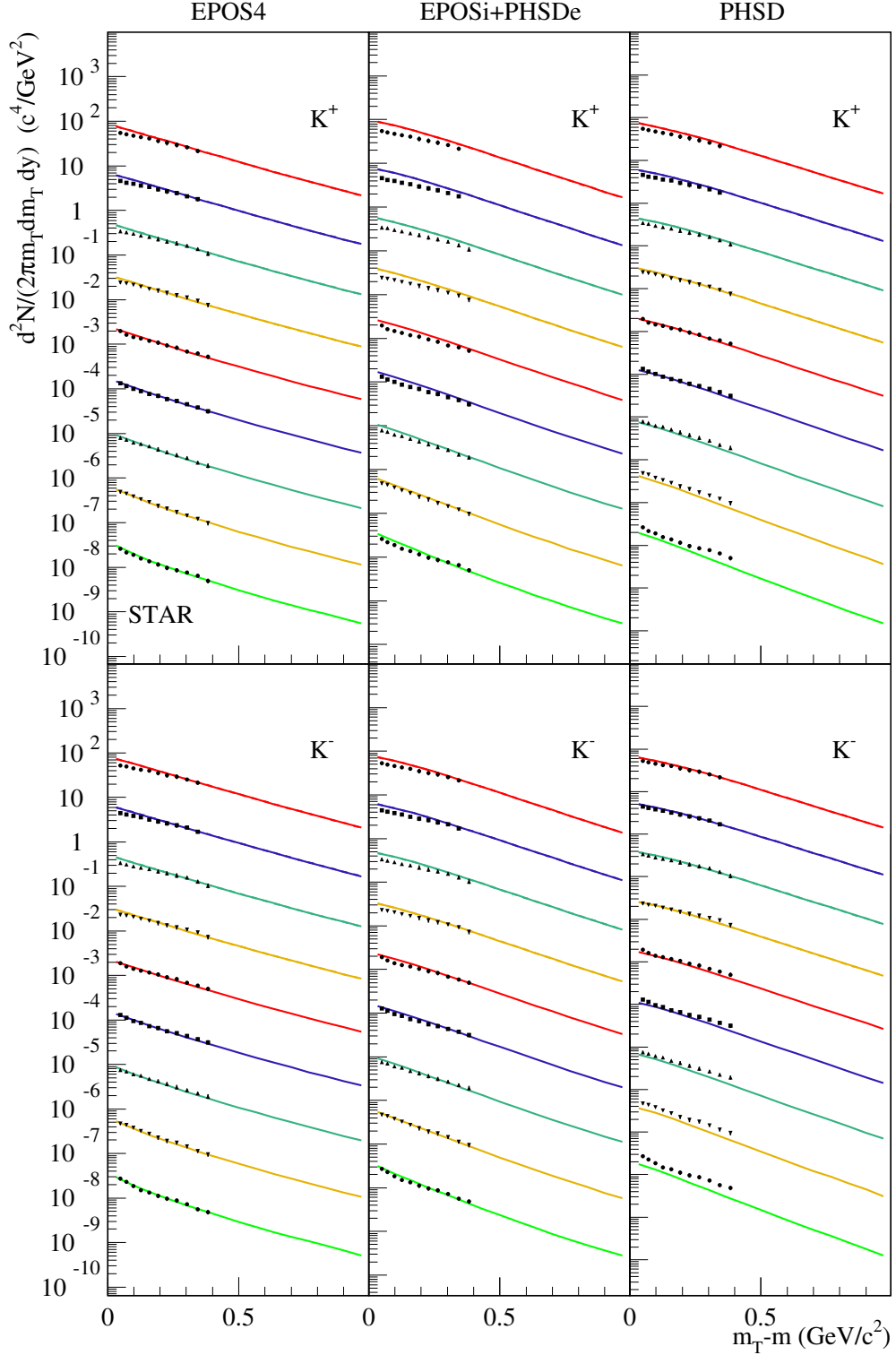


Figure 5.5: Invariant yield as a function of transverse mass for  $K^\pm$  for Au-Au collision at  $\sqrt{s_{NN}} = 200$  GeV at mid-rapidity ( $|y| < 0.5$ ) in three different simulations: EPOS 4 (left panel), EPOSi+PHSDe (middle panel), and pure PHSD (right panel). The different transverse mass spectra are plotted with different centrality ranges 0-5%, 5-10%, 10-20%, 20-30%, 30-40%, 40-50%, 50-60%, 60-70%, 70-80% from top to bottom in each plot. All the results compared to the STAR experimental data [160] with the black points. All curves and experimental data are scaled by  $2 * 10^{-n}$  starting from the top most curve with  $2 * 10^0$ .

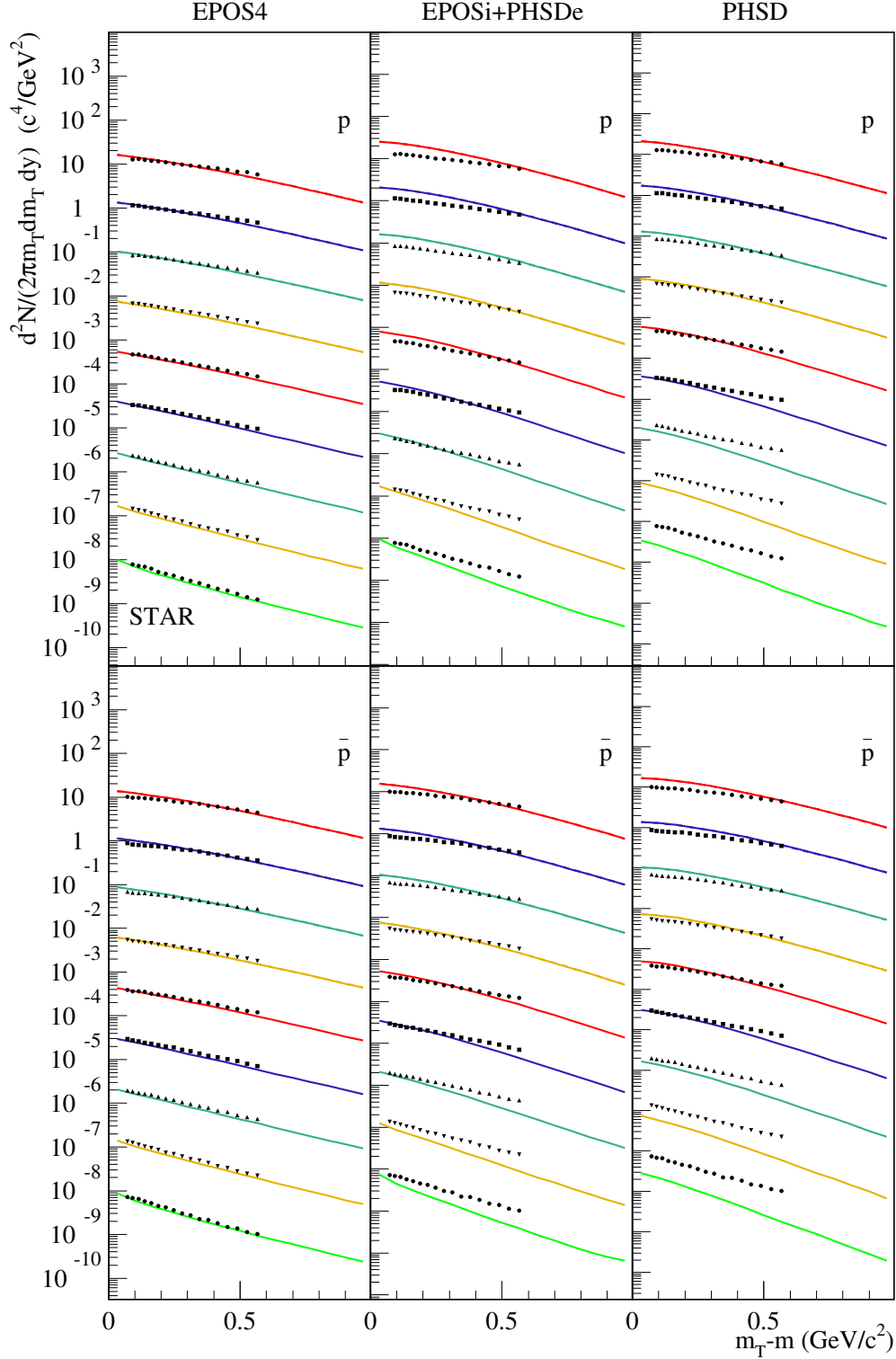


Figure 5.6: Invariant yield as a function of transverse mass for proton ( $p$ ), and antiproton ( $\bar{p}$ ) for  $\text{Au-Au}$  collision at  $\sqrt{s_{NN}} = 200$  GeV at mid-rapidity ( $|y| < 0.5$ ) in three different simulations: **EPOS 4** (left panel), **EPOSi+PHSDe** (middle panel), and pure **PHSD** (right panel). The different transverse mass spectra are plotted with different centrality ranges 0-5%, 5-10%, 10-20%, 20-30%, 30-40%, 40-50%, 50-60%, 60-70%, 70-80% from top to bottom in each plot. All the results compared to the **STAR** experimental data [160] with the black points. All curves and experimental data are scaled by  $2 * 10^{-n}$  starting from the top most curve with  $2 * 10^0$ .

### 5.2.2 Rapidity and pseudorapidity spectra

In the first part of this subsection, I will present results of the rapidity densities,  $dN/dy$ , of  $\pi^\pm$ ,  $K^\pm$ , proton  $p$ , antiproton  $\bar{p}$ , and net-protons ( $p - \bar{p}$ ) from central (0-5%) Au-Au collisions at  $\sqrt{s_{NN}} = 200$  GeV in various simulations. Then I will compare them to the experimental data and among each other. These results have important impacts on the dense system's dynamics that evolve following collisions. The rapidity distributions provide a sensitive test of theories that describe the reaction's space-time evolution.

We compare our rapidity density results with the [Broad RAnge Hadron Magnetic Spectrometers \(BRAHMS\)](#) [162,163] experiment. BRAHMS consists of two hadron spectrometers, a mid-rapidity arm (MRS) and a forward rapidity arm (FS), as well as a set of detectors for global event characterization. Particle identification (PID) for momenta below 2 GeV/c is performed via time-of-flight (TOF) in the MRS. In the FS, TOF capabilities allow  $\pi - K$  separation up to  $p = 4.5$  GeV/c, and is further extended up to 20 GeV/c using a ring imaging Cerenkov detector. The MRS can be rotated  $30^\circ < \theta < 95^\circ$  and the FS  $2.3^\circ < \theta < 30^\circ$ , where  $\theta$  is the polar angle with respect to the beam axis. By combining different setting of angle and magnetic fields, (anti)proton transverse momentum spectra at different rapidities ( $0 \leq y \leq 3$ ) were obtained. Proton and antiproton are identified using TOF, and FS [164].

The rapidity densities for identified charged particles in different simulations, [EPOS 4](#) (left column), [EPOSi+PHSDe](#) (middle column), and pure [PHSD](#) (right column), have been presented in Fig. 5.7. The rapidity densities of charged hadrons were computed over the entire  $p_T$  range. We show two types of curves: those where weak decays are considered (dashed) or not (full). This concerns pions, where weak decays of  $K$ s play an important role, and protons, where Lambda decays are significant.

The first two rows of Fig. 5.7 represent the  $\pi^\pm$  (red curves) and  $K^\pm$  (blue curves) rapidity densities. In all simulations, pions and kaons are somewhat above the experimental data. Except for  $K^-$ , [EPOSi+PHSDe](#) has higher production of both pions and kaons at mid-rapidity than two other simulations. We have more light mesons productions in pure [PHSD](#) than [EPOSi+PHSDe](#) and [EPOS 4](#) by increasing rapidity.

The rapidity densities of the proton (red curves), antiproton (blue curves), and net-proton are shown in the third and fourth rows of Fig. 5.7. The most striking feature of the experimental data is that, while proton and antiproton rapidity densities reduce at rapidities away from mid-rapidity, the net-proton density grows from zero to  $y = 3$ . Our results show a similar trend, although, in forward rapidity ( $3 < y < 4$ ), [EPOSi+PHSDe](#) has fewer proton and antiproton density than others. Protons (antiproton) with and without weak decays contribute more (less) in [EPOSi+PHSDe](#) than [EPOS 4](#) and pure [PHSD](#) at mid-rapidity.

Baryon stopping is one of the expressions used to describe the final hadrons. The stopping of the initial protons and antiprotons can be studied using the net-proton density. It determines how much the collision reduces the amount of the initial nuclei (from participants). Whereas the baryon number is conserved, the net-baryon number remains constant during the whole evolution of the collision. The spread of the net-baryon number along the longitudinal direction can tell us about the stopping of the initial baryons.

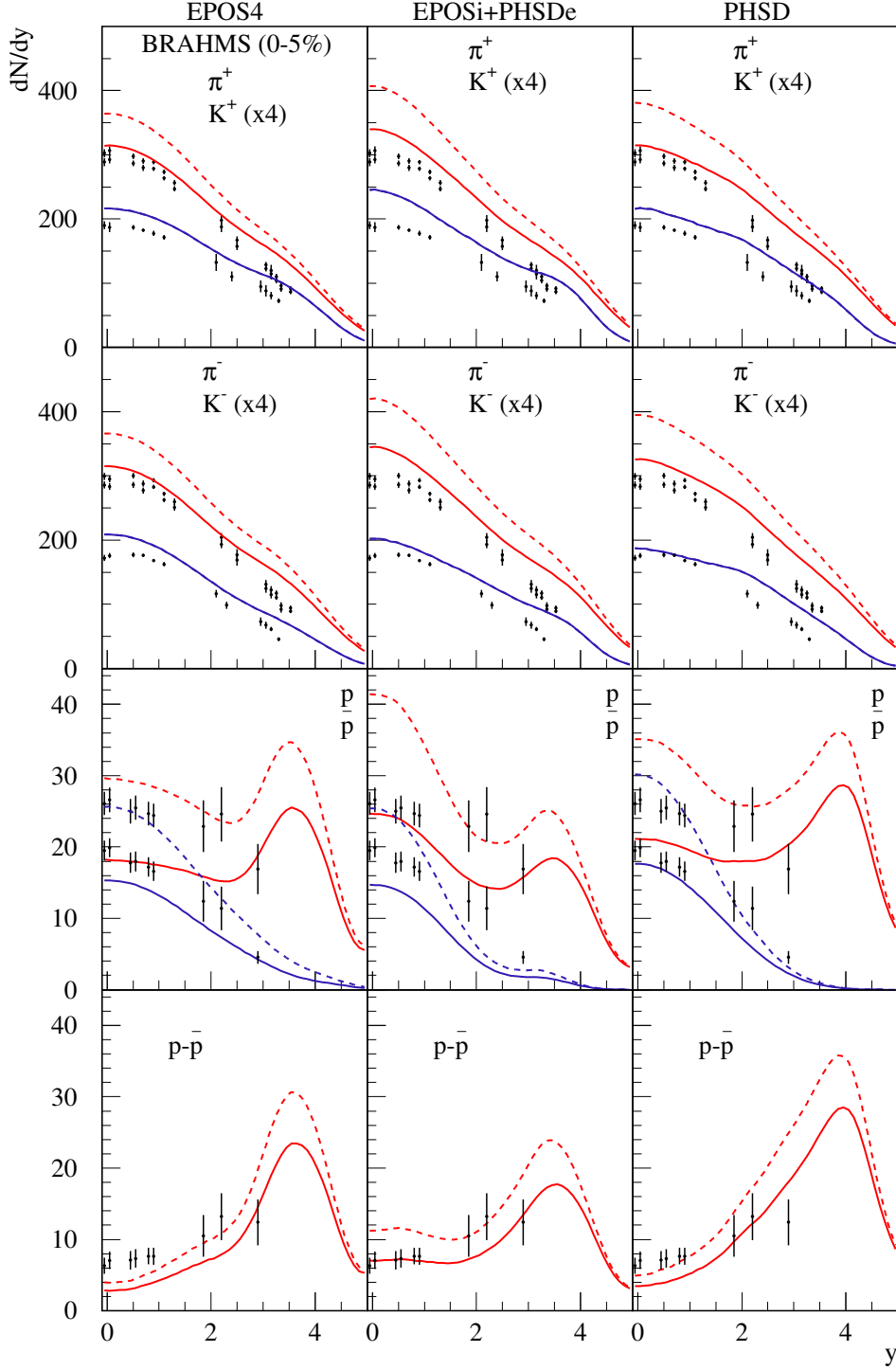


Figure 5.7: Pion  $\pi^\pm$ , kaon  $K^\pm$ , proton  $p$ , antiproton  $\bar{p}$ , and net proton  $p - \bar{p}$  rapidity densities (from top to bottom) for the 5% most central Au-Au collisions at  $\sqrt{s_{NN}} = 200$  GeV in three different simulations: EPOS 4 (left panel), EPOSi+PHSDe (middle panel), and pure PHSD (right panel). The kaon yields were multiplied by 4 for clarity. All the results compared to the BRAHMS experimental data [162, 163] with the black points.

Concerning weak decays, the situation is not clear from the experimental side. The data are not feed-down corrected, but from the detector design, we do not expect the weak decay products to contribute considerably. So we represent something between "feed-down corrected" and "all feed-down included". If we consider the average of the net-proton curves with and without the contribution of weak decays, we can find that

**EPOSi+PHSDe** produces results that are closer to the real data than **EPOS 4** and pure **PHSD**. In pure **PHSD**, the production of proton, antiproton, and net-proton density with or without weak decays contribution is higher than **EPOS 4** than **EPOSi+PHSDe** in forward rapidity ( $3 < y < 5$ ). Consequently, **EPOSi+PHSDe** has the biggest stopping even in forward rapidity, whereas pure **PHSD** has the least.

In the second part of this subsection, I present the charged particle multiplicities as a function of pseudorapidity for the same collision as rapidity densities. Fig. 5.8 shows the distributions of  $dN_{ch}/d\eta$  for different simulations, **EPOS 4**, **EPOSi+PHSDe**, and pure **PHSD**, from top to bottom.

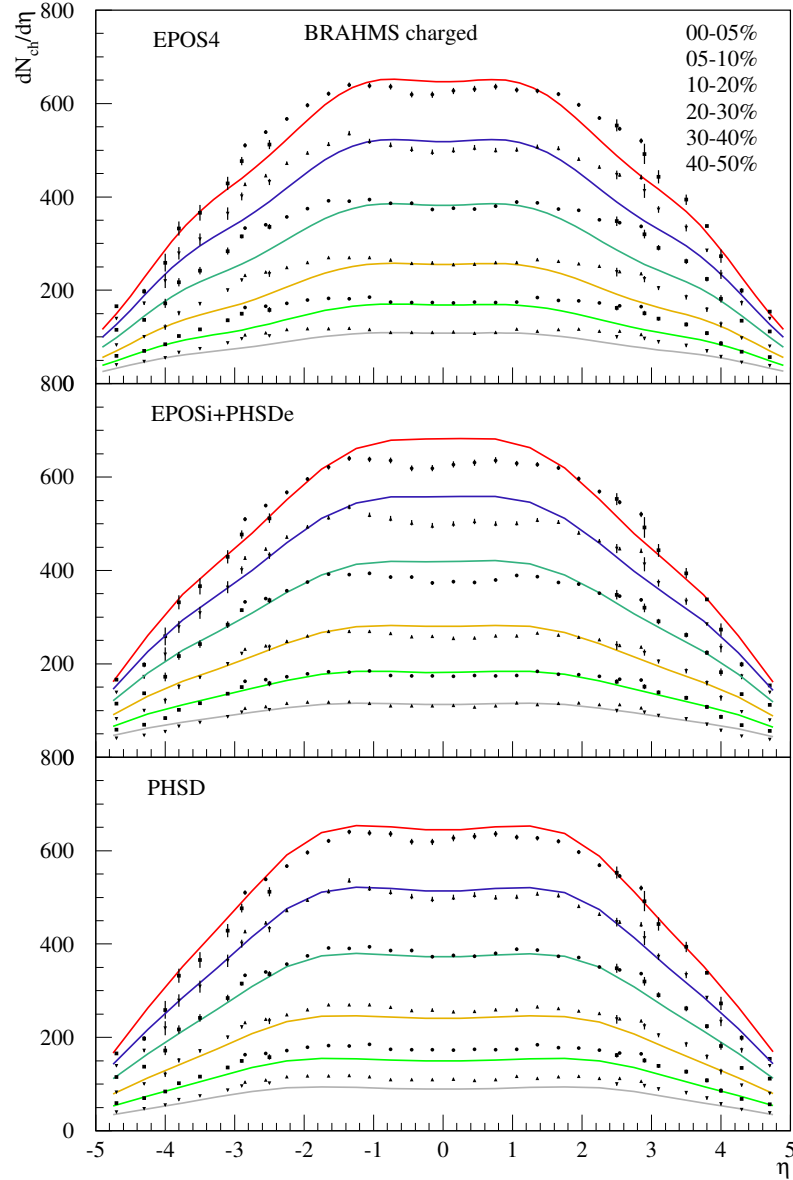


Figure 5.8: Charged particle multiplicities ( $dN_{ch}/d\eta$ ) as a function of pseudorapidity ( $\eta$ ) in **Au-Au** collisions at  $\sqrt{s_{NN}} = 200$  GeV for different simulations, **EPOS 4** (top panel), **EPOSi+PHSDe** (middle panel), and pure **PHSD** (lower panel) from central to semi-peripheral collisions in each plot from top to bottom, 0-5%, 5-10%, 10-20%, 20-30%, 30-40%, and 40-50%. The experimental data are taken from **BRAHMS** [165] with black points.

The experimental data were obtained using several subsystems of the BRAHMS [165] experiment: the Multiplicity Array (MA), the Beam-Beam Counter (BBC) arrays, and the Zero-Degree Calorimeters (ZDCs). The pseudorapidity variable  $\eta$  is related to the particle emission angle  $\theta$  with  $\eta = -\ln[\tan(\theta/2)]$ .

As shown in Fig. 5.8, going from most central (0-5%) to semi-peripheral (40-50%) collisions reduces the production of charged particles. EPOS 4 can reproduce reasonably charged particles when compared to the experimental data for all mentioned centrality bins. In central and mid-central collisions (0-30%), EPOSi+PHSDe reproduces more charged particles in the mid-pseudorapidity range. However, it can reproduce the same charged particles as experimental data for semi-peripheral collisions. EPOSi+PHSDe improves the charged particle productions in semi-peripheral (20-50%) collisions compare to pure PHSD.

Pure PHSD can successfully reproduce experimental data from most central to mid-central (0-20%) collisions with the same shape as the experiment. However, in this model, the charged particle productions are lower than the data for larger centralities (20-50%). It should be noted that pure PHSD, compared to the other two models, reproduces the shape of the pseudorapidity distributions remarkably well.

### 5.2.3 Transverse momentum spectra

In this subsection, I will show the invariant yields of identified hadrons as a function of transverse momentum  $p_T$  and centrality classes for the three simulations and compare them to each other and the experimental data. Transverse momentum spectra do not provide additional information compared to the  $m_T$  spectra discussed earlier, but the  $p_T$  spectra discussed here extend to much higher values. We do these studies in Au-Au collisions at the top RHIC energy because they allow us to investigate particle production mechanisms in a hot, dense nuclear medium, also probing the properties of the QGP [166].

The  $p_T$  spectra for identified charged hadrons are compared to the PHENIX measurement [166] in Fig. 5.9. The PHENIX experiment is a large, general-purpose detector with a wide variety of detector subsystems ideally suited to the study of nuclear matter in conditions of extreme temperature and density. PHENIX is composed of global event property detectors, forward and backward rapidity arms (North and South) dedicated to muon measurements, and two central arm spectrometers (East and West) at mid-rapidity covering the pseudorapidity region of  $|\eta| < 0.35$  for measurements of photons, electrons, and charged hadrons [167]. Centrality selection is performed with the BBCs using the Glauber Monte Carlo procedure [168], in which the charge in each BBC detector is assumed to be proportional to the number of participating nucleons traveling towards it.

The invariant yields of  $\pi^\pm$ ,  $K^\pm$ ,  $p$ , and  $\bar{p}$  as a function of transverse momentum  $p_T$  at mid-rapidity in Au-Au collisions at  $\sqrt{s_{NN}}=200$  GeV are shown in Fig. 5.9. Weak decays contribute to producing  $\pi^\pm$  and  $K^\pm$  but not for  $p$  and  $\bar{p}$ , both in the simulations and data. One can see that EPOS 4 can reproduce well the experimental data for all types of particles in all centrality bins in low ( $p_T < 2$  GeV/c), intermediate ( $2$  GeV/c  $< p_T < 5$  GeV/c), and high ( $p_T > 5$  GeV/c) transverse momentum. We can also notice that just for the most peripheral collisions, the simulations exceed the data somewhat.

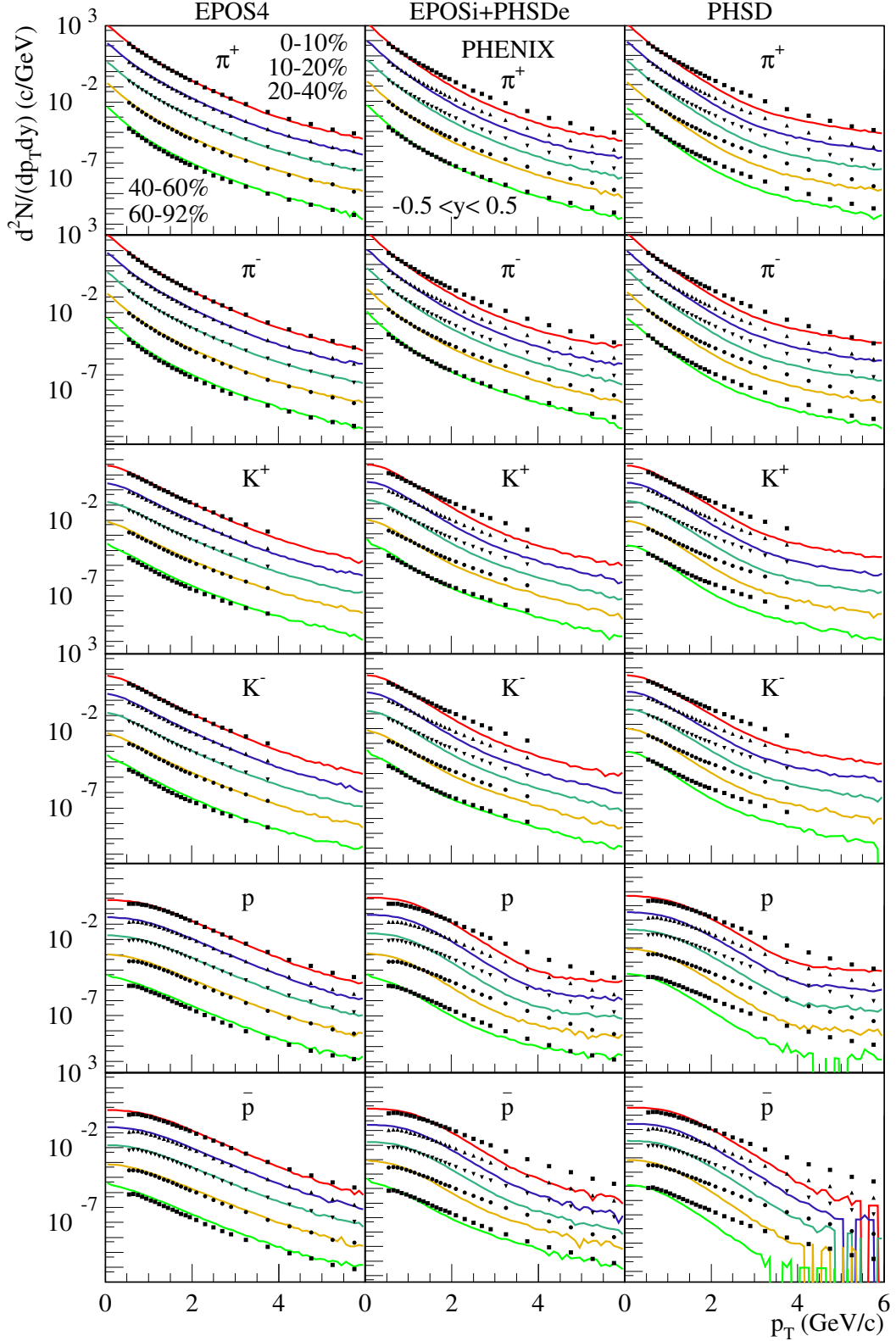


Figure 5.9: Invariant yield of  $\pi^\pm$ ,  $K^\pm$ , proton  $p$ , and antiproton  $\bar{p}$  as a function of transverse momentum  $p_T$  at mid-rapidity ( $|y| < 0.5$ ) in Au-Au collisions at  $\sqrt{s_{NN}}=200$  GeV from most central (0-10%) to most peripheral (60-92%) collisions, from top to bottom in each plot, in different simulations, EPOS 4 (left panel), EPOSi+PHSDe (middle panel), and pure PHSD (right panel). The experimental data are taken from PHENIX with black symbols [166]. All curves and experimental data are scaled by  $10^{-n}$  starting from the top most curve with  $10^0$ .

Both [EPOSi+PHSDe](#) and pure [PHSD](#) reproduce data reasonably well at small  $p_T$ , in all cases, but they very much underestimate the data at intermediate and large values of  $p_T$ . Just for peripheral events, [EPOSi+PHSDe](#) performs a bit better than pure [PHSD](#), which is due to the fact that in [EPOSi+PHSDe](#) there is some "initial flow" from the decay of the clusters, before implementing particles to [PHSD](#).

As we have already discussed in Figs. [5.2](#) and [5.3](#), the expansion in [EPOS 4](#) on one side and [EPOSi+PHSDe](#) and pure [PHSD](#) on the other side, is very different. Starting from an elongated initial shape, there is a strong transverse expansion in the case of [EPOS 4](#), and strong transverse flow is created. Then this transverse flow translates into more particle productions at intermediate  $p_T$ . This flow effect becomes even bigger when considering heavy particles (like protons, compared to pions).

In the two other models, [EPOSi+PHSDe](#) and pure [PHSD](#), this transverse flow is missing, and therefore the simulations dramatically underestimate the data for  $p_T$  larger than 1 GeV/c. These are significant observations. It means in these two models; the partons do not interact strongly enough to produce something equivalent to "strong pressure gradients," which are reasonable to the transverse flow in [EPOS 4](#).

When comparing the system expansion in [EPOSi+PHSDe](#) and pure [PHSD](#) simulations (see Figs. [5.2](#) and [5.3](#)), it can notice that the system expands a bit more in the transverse plane in [EPOSi+PHSDe](#), which results in improved particle production in intermediate  $p_T$  as compared to pure [PHSD](#). This effect is more visible for peripheral collisions, as indicated in Fig. [5.9](#).

In the following, we investigate the rapidity dependence of  $p_T$  spectra. We show invariant yields of identified hadrons as a function of  $p_T$  in different rapidity ranges for central (0-5%) [Au-Au](#) collisions at  $\sqrt{s_{NN}}=200$  GeV, see Figs. [5.10](#), [5.11](#), and [5.12](#). Solid lines refer to simulations not considering weak decays, and the dashed lines are those including weak decays. We show both in the case of protons (since the experimental procedures consider weak decay products 'partly'). The left, middle, and right panels are related to [EPOS 4](#), [EPOSi+PHSDe](#), and pure [PHSD](#) simulations. The results compared to the [BRAHMS](#) experiment [[162](#)] with black points.

Concerning pions and kaons production, the rapidity dependence of the  $p_T$  spectra is in all cases similar to the data. However, we see also here in the case of [EPOSi+PHSDe](#) and pure [PHSD](#) deviations for  $p_T > 1$  GeV/c: simulations results are below the data, and the effect is bigger for kaons compared to pions. This is consistent with what we observed already: too little transverse flow is produced. Looking at the proton results, this effect is even more clearly visible. [EPOS 4](#) is essentially acceptable, whereas the two other models heavily underestimate proton production at intermediate values of  $p_T$ .

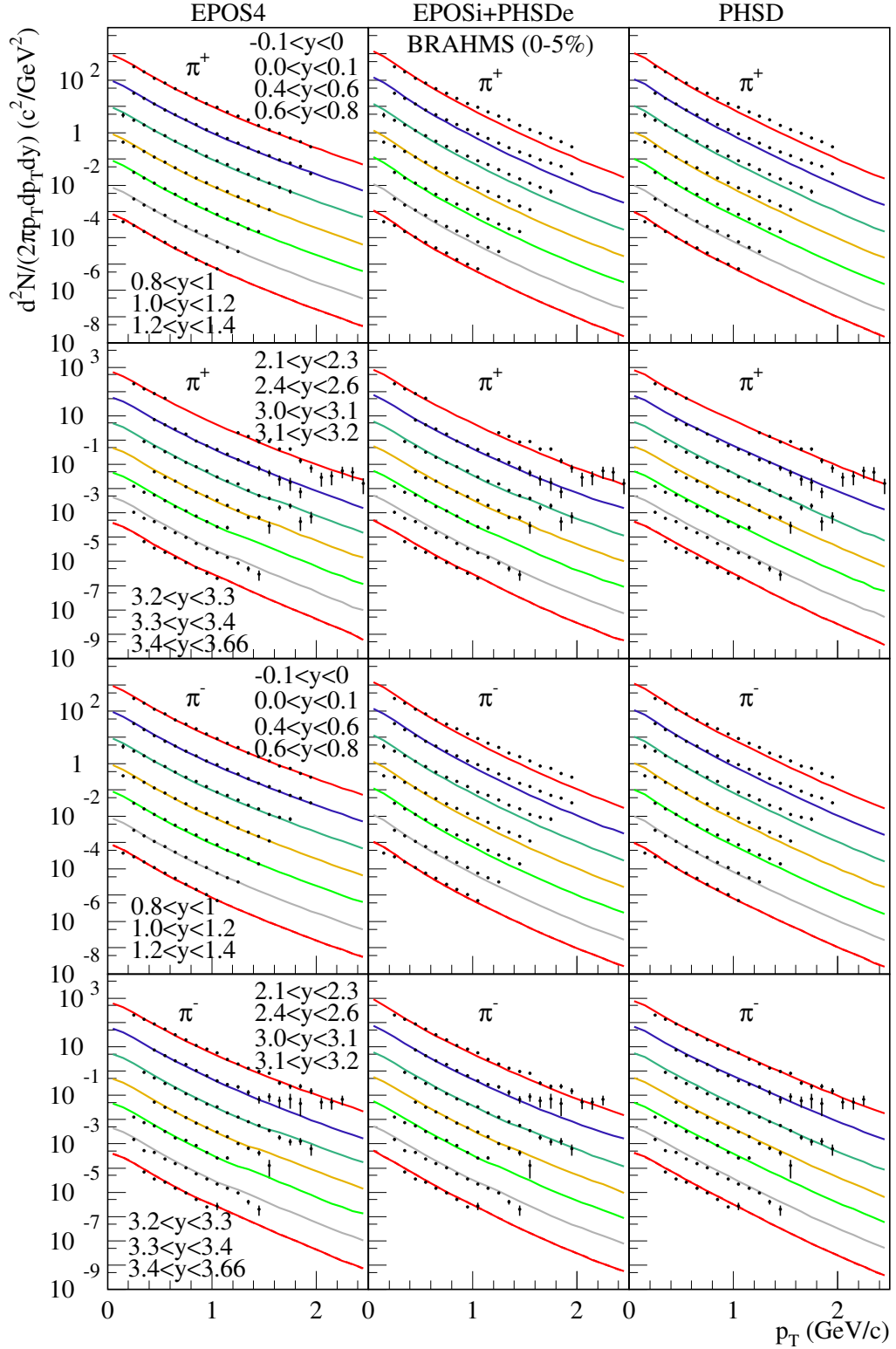


Figure 5.10: Pions  $\pi^\pm$  transverse momentum spectra at selected rapidities (in each plot from top to bottom, from  $-0.1 < y < 0$  to  $3.4 < y < 3.66$ ) from central (0-5%) Au-Au collisions at  $\sqrt{s_{NN}} = 200$  GeV in different simulations, EPOS 4 (left panel), EPOSi+PHSDe (middle panel), and pure PHSD (right panel). There is no weak decays contribution in these measurements. The results compared to the BRAHMS experiment [162] with black points. The experimental data and simulation's results are scaled by  $10^{-n}$  and  $(1/dy) * 10^{-n}$ , respectively, starting from the top most curve with  $10^0$ .

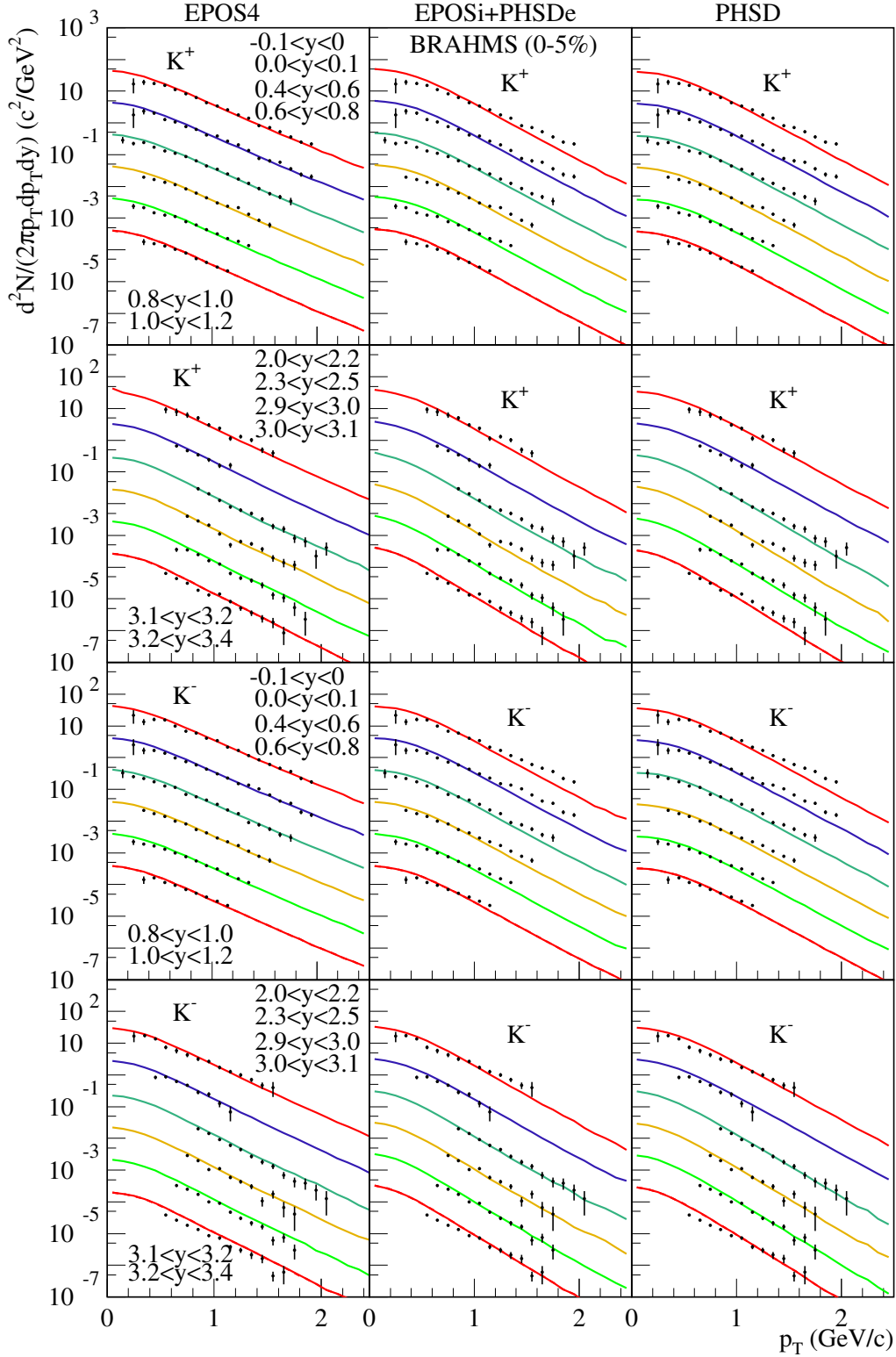


Figure 5.11: Kaons  $K^\pm$  transverse momentum spectra at selected rapidities (in each plot from top to bottom, from  $-0.1 < y < 0$  to  $3.2 < y < 3.4$ ) from central (0-5%) Au-Au collisions at  $\sqrt{s_{NN}} = 200$  GeV in different simulations, EPOS 4 (left panel), EPOSi+PHSDe (middle panel), and pure PHSD (right panel). There is no weak decays contribution in these measurements. The results compared to the BRAHMS experiment [162] with black points. The experimental data and simulation's results are scaled by  $10^{-n}$  and  $(1/dy) * 10^{-n}$ , respectively, starting from the top most curve with  $10^0$ .

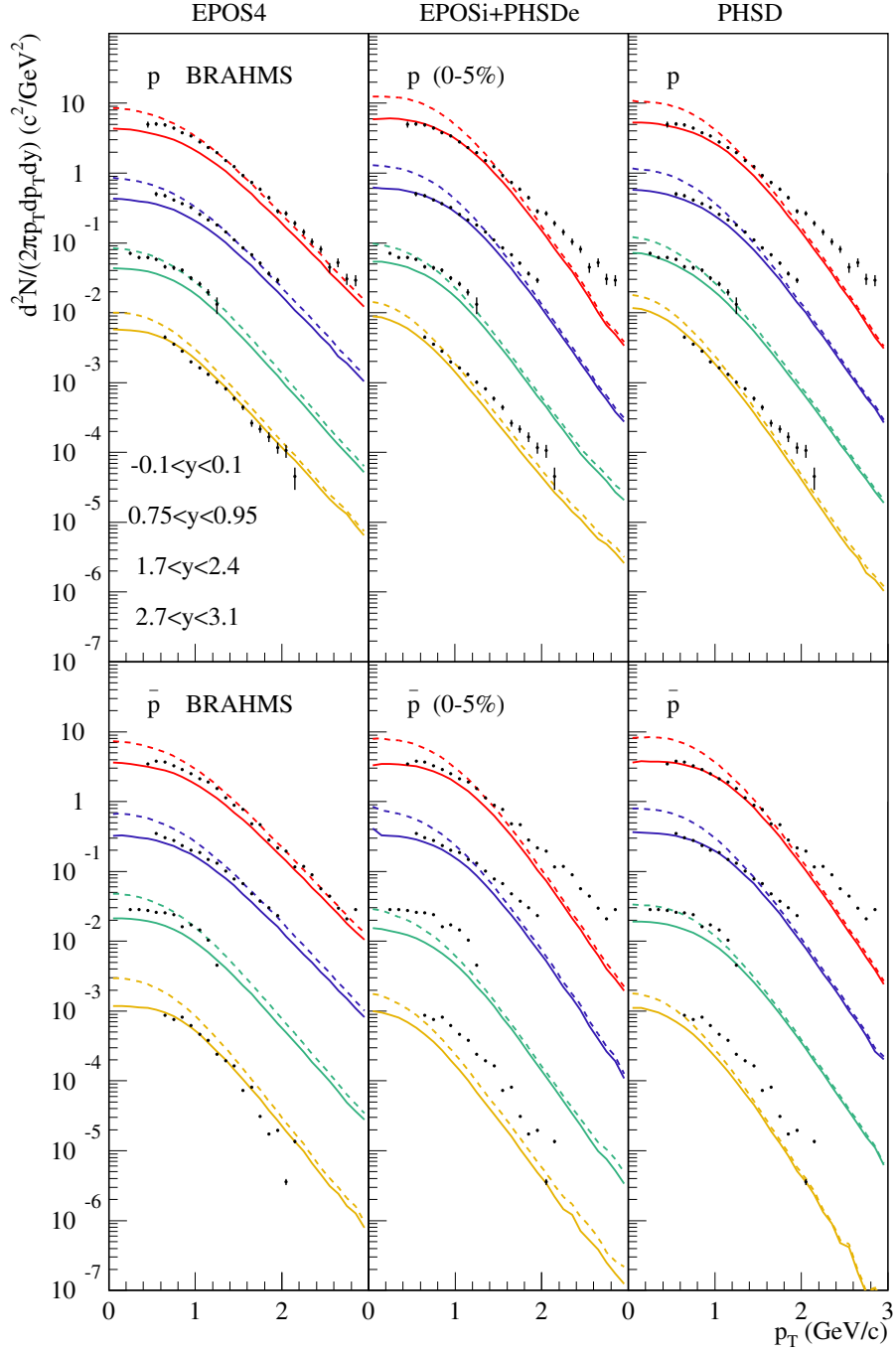


Figure 5.12: Proton ( $p$ ), anti-proton ( $\bar{p}$ ) transverse momentum spectra at selected rapidities (in each plot from top to bottom, from  $-0.1 < y < 0.1$  to  $2.7 < y < 3.1$ ) from central (0-5%) Au-Au collisions at  $\sqrt{s_{NN}} = 200$  GeV in different simulations, EPOS 4 (left panel), EPOSi+PHSDe (middle panel), and pure PHSD (right panel). The results compared to the BRAHMS experiment [163] with black points. The experimental data and simulation's results are scaled by  $10^{-n}$  and  $(1/dy) * 10^{-n}$ , respectively, starting from the top most curve with  $10^0$ .

Strange particle measurements, such as charged kaons and hyperons, have also been an important research topic in HICs. A baryon with one or more strange quarks is known as a hyperon. Strangeness enhancement, as I explained in subsection 1.4.4 of Chapter 1, is a probable signature of deconfinement and thermalization. The measurement of charged kaons and hyperons across a wide  $p_T$  range and different centrality classes is

crucial for better understanding the system's thermalization and strangeness production mechanism.

In the high-temperature QGP phase, strange quarks with masses similar to the critical temperature are expected to be abundantly produced through thermal parton interactions. Hyperon production is predicted in high-energy nuclear collisions due to the corresponding increase in strange quark density. The number of strange valence quarks in the hyperon enhances hyperon production [169].

We investigated the hyperon production, including  $\Lambda(uds)$ ,  $\bar{\Lambda}(\bar{u}\bar{d}\bar{s})$ ,  $\Xi^-(dss)$ ,  $\Xi^+(\bar{d}\bar{s}\bar{s})$ ,  $K_s^0((K^+ + K^-)/2)$ , and  $\Omega^-(sss) + \Omega^+(\bar{s}\bar{s}\bar{s})$  at mid-rapidity in Au-Au collisions at  $\sqrt{s_{NN}} = 200$  GeV for various simulations from most central (0-5%) to peripheral (60-80%) collisions, as seen in Fig. 5.13. We compare our results with the STAR experiment [170]. The STAR TPC measures the trajectories and momenta of charged particles produced in each collision in the pseudorapidity range  $|\eta| < 1.8$  [171].

As shown in Fig. 5.13, EPOS 4 can accurately reproduce hyperons at low, intermediate, and high  $p_T$  for all centrality bins, except for most central collisions, but they are reasonable.

In Fig. 5.13, both EPOSi+PHSDe and pure PHSD have the same trend for hyperon productions as charged particles in Fig. 5.9; we have more hyperon productions at low  $p_T$  compared to EPOS 4 and experimental data, but they cannot reproduce well hyperons at intermediate  $p_T$ : they are substantially below the data. EPOSi+PHSDe does a little bit better than pure PHSD.

In the following, I will compare the  $p_T$  spectra of all charged hadrons in these three simulations, which is essentially a sum of the identified particle spectra discussed earlier, to the experimental data for Au-Au collisions at  $\sqrt{s_{NN}}=200$  GeV. The results are shown in Fig. 5.14. EPOS 4 can accurately reproduce all charged particles in all ranges of  $p_T$ , from the most central (0-6%) to peripheral (45-50%) collisions in a rapidity range of  $0.2 < y < 1.4$ .

We see that both EPOSi+PHSDe and pure PHSD cannot reproduce sufficiently particles at intermediate and high  $p_T$  compared to the experimental data and EPOS 4. So from identified particle spectra, as well as charged particle spectra, we observe that EPOS 4 reproduces the data correctly in particular at intermediate values of  $p_T$ , whereas EPOSi+PHSDe and pure PHSD underestimate particle production by a large amount. This is compatible with the fact, seen in Figs. 5.2 and 5.3, that the system expands strongly in the transverse plane, producing large transverse flow, which then automatically translates into an increased particle production at higher  $p_T$ . All this is based on the fundamental assumption that the system thermalized quickly, and hydrodynamics can be used for the following evolution.

And most importantly, in the case of a hydrodynamically expanding expansion, large gradients (in energy density) at early times translate into the big transverse flow. In EPOSi+PHSDe and pure PHSD, there is no assumption of equilibration, so it is needed to develop via parton-parton scatterings. But seemingly, this does not happen, there is no transverse expansion happening, and as a consequence, the shift of particles towards intermediate  $p_T$  values is missing. This gives a coherent picture: in both EPOSi+PHSDe and pure PHSD, the strong gradients (which are also present) do not translate into the

transverse flow, which means the system does not reach equilibrium at an early stage. This is the main message of this thesis work. To confirm it, we will study flow anisotropies in the following.

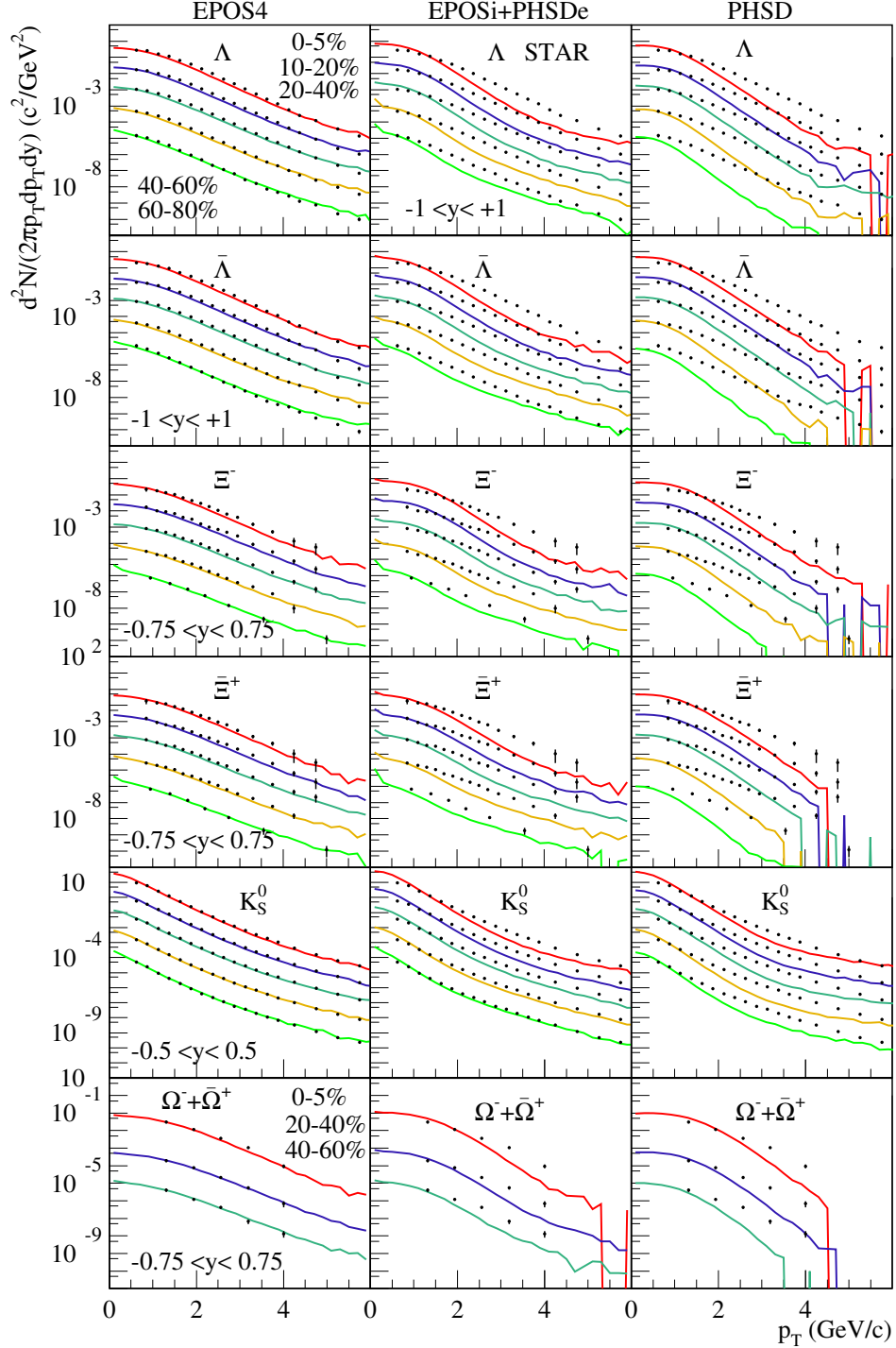


Figure 5.13: Invariant yield of  $\Lambda$ ,  $\bar{\Lambda}$ ,  $\Xi^-$ ,  $\bar{\Xi}^+$ ,  $K_S^0$ , and  $\Omega^- + \bar{\Omega}^+$  as a function of transverse momentum  $p_T$  at mid-rapidity in Au-Au collisions at  $\sqrt{s_{NN}}=200$  GeV from most central (0-5%) to peripheral collisions (60-80%), from top to bottom in each plot, in different simulations, **EPOS 4** (left panel), **EPOSi+PHSD** (middle panel), and pure **PHSD** (right panel). The experimental data are taken from **STAR** with black points [170]. The experimental data and simulation's results are scaled by  $10^{-n}$  and  $(1/dy) * 10^{-n}$ , respectively, starting from the top most curve with  $10^0$ .

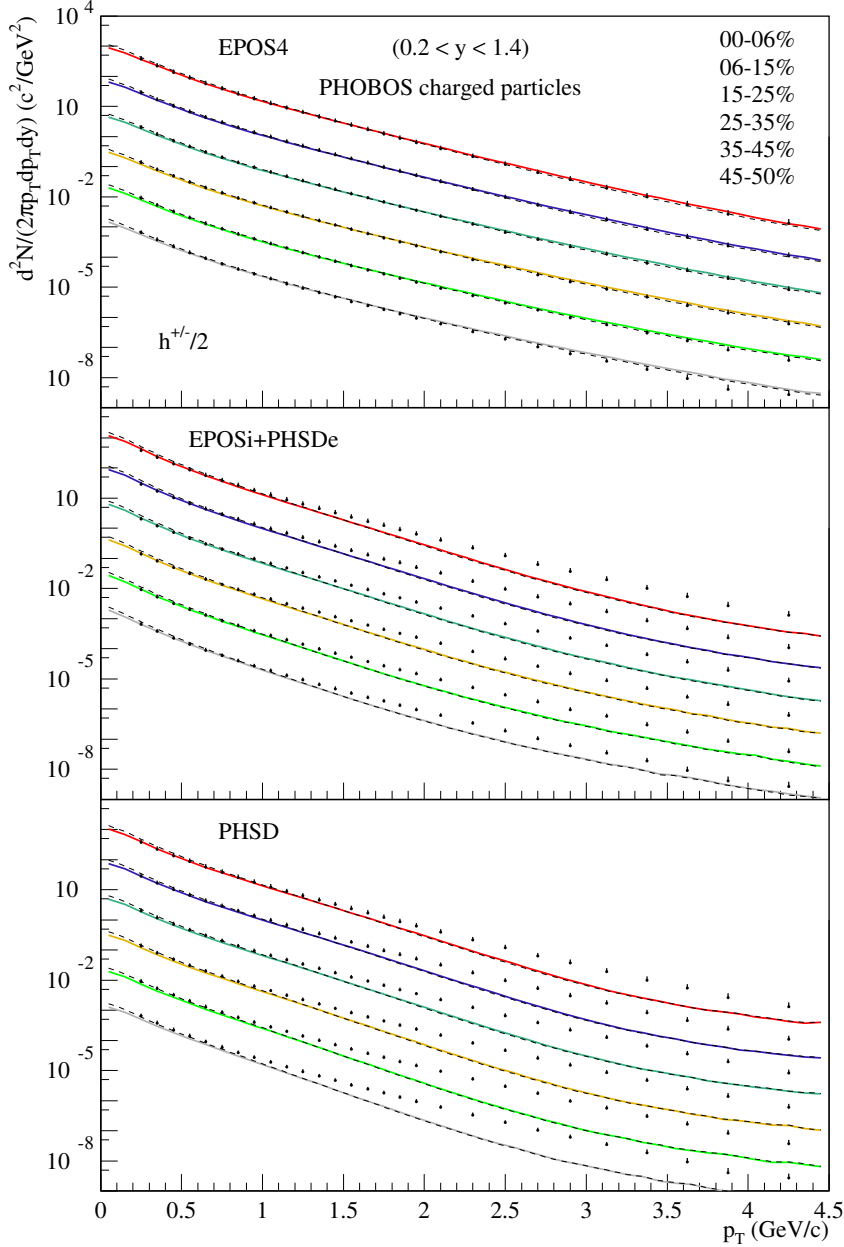


Figure 5.14: Invariant yields for charged hadrons as a function of  $p_T$  for 6 centrality bins (0-6%, 6-15%, 15-25%, 25-35%, 35-45%, and 45-50%) in a rapidity range of  $0.2 < y < 1.4$  in Au-Au collisions at  $\sqrt{s_{NN}}=200$  GeV in different simulations, **EPOS 4** (upper panel), **EPOSi+PHSDe** (middle panel), and pure **PHSD** (lower panel). The experimental data are taken from **PHOBOS** with black points [172]. The experimental data and simulation's results are scaled by  $10^{-n}$  and  $(1/dy) * 10^{-n}$ , respectively, starting from the top most curve with  $10^0$ .

#### 5.2.4 Anisotropic flow

The study of the azimuthal distribution of particle production provides important information about the system's space-time evolution [102]. The discovery of a large azimuthal anisotropic flow of hadrons at RHIC [173] provides strong evidence for dense partonic matter formation in ultra-relativistic nucleus-nucleus collisions. The collision zone's strongly interacting medium is predicted to reach a local equilibrium and show an approximately hydrodynamic flow [174].

In subsection 1.4.3 of chapter 1, the general definition of anisotropic flow was discussed. To summarize this section, anisotropic flow describes the fact that produced particle azimuthal distributions are not uniform. In non-central collisions, pressure gradients generate momentum anisotropy in a collective expansion of an initial geometry of an "almond-shaped" collision zone [175]. The pressure gradients convert early-stage asymmetry in coordinate space to anisotropy in momentum space in the final state.

Various experimental groups have worked out many anisotropic flow measurements during the last 30 years. As initially observed at the AGS [176], anisotropic transverse flow is sensitive to the early stages of a collision. Following that, a much stronger flow was measured at the SPS [177], RHIC [173, 178, 179], and, most recently, the LHC [180, 181]. Hydrodynamic model calculations produce elliptic flow at RHIC and the LHC with a small value of the ratio of shear viscosity to entropy density  $\eta/s$  [182]. The shear viscosity of a fluid describes its ability to flow freely. The medium created in ultra-relativistic collisions for a few fm/c. It has collective properties comparable to those of a liquid with a very low shear viscosity to entropy density ratio, which is close to a nearly perfect fluid [183]. When we use EPOS 4, the shear viscosity is set at  $\eta/s=0.08$  [101]. Therefore, we anticipate having a good fluid and flow.

In this section, I want to compare the different order anisotropy harmonics in three simulations: EPOS 4, EPOSi+PHSDe, and pure PHSD. As I have already mentioned, all of the analyses in these three simulations are done based on EPOS 4 analysis. First, I will explain the flow analysis theory, then compare the results of the three simulations to each other and to the experimental data. Event Plane (EP) method is employed in our flow analysis. As a basic definition of anisotropic transverse flow, we refer to subsection 1.4.3 of chapter 1. Then I will explain the EP method.

### Basic definitions for anisotropic flow

We use the Fourier series to describe the different patterns of anisotropic flow, from the momentum distribution of final-state particles [54],

$$E \frac{d^3N}{d^3\mathbf{p}} = \frac{1}{2\pi} \frac{d^2N}{p_T dp_T dy} \left[ 1 + 2 \sum_{n=1}^{\infty} v_n \cos [n(\phi - \Psi_{RP})] \right], \quad (5.2.1)$$

where  $E$  is the energy of the particle,  $\mathbf{p}$  the momentum,  $p_T$  the transverse momentum,  $\phi$  the azimuthal angle,  $y$  the rapidity,  $\psi_{RP}$  the reaction plane angle, see Fig. 5.15.  $v_n$  is a set of anisotropic flow observables defined by

$$v_n(p_t, y) = \langle \cos [n(\phi - \psi_{RP})] \rangle, \quad (5.2.2)$$

where the angular brackets denote an average over the particles, sum over all events. As stated previously, directed, elliptic, triangular, and quadrangular flows are represented by  $v_1$ ,  $v_2$ ,  $v_3$ , and  $v_4$ , respectively. The integrated and differential flow are two different types of anisotropic flow. The integrated flow is included when the  $v_n$  coefficients are averaged over transverse momentum and rapidity. The differential flow is used when the  $v_n$  coefficients are considered as a function of pseudorapidity and transverse momentum.

### Event plane method

The EP approach [185, 186] is an old method used to compute anisotropic flow. In the following, I will explain how we modify the Fourier coefficient, Eq. 5.2.2, corresponding

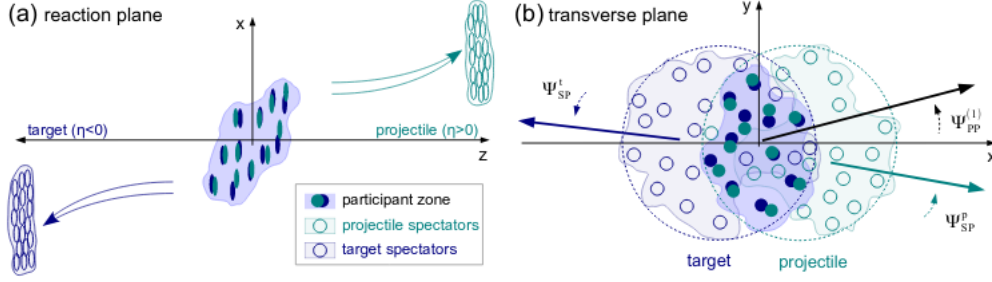


Figure 5.15: Sketch of a non-central HICs in reaction and transverse planes [184].

to the EP method. To derive the Fourier expansion, we start with the general definition of triple differential distribution as Eq. 5.2.1 for event plane method:

$$E \frac{d^3 N}{dp^3} = \frac{d^3 N}{p_t dp_t dy d\phi} = \frac{d^2 N}{p_T dp_T dy} \times R(p_T, y, \phi). \quad (5.2.3)$$

In the experiment, the rapidity ( $y$ ) is replaced by pseudorapidity ( $\eta$ ) since  $\eta$  is simpler to measure. Therefore, we replace  $R(p_T, y, \phi)$  by  $R(p_T, \eta, \phi)$ . We assume that the function of  $R(p_T, \eta, \phi)$  satisfies the normalization condition  $\int_0^{2\pi} d\phi R(p_T, \eta, \phi) = 1$ . We expand the Fourier series of this function:

$$R(p_T, \eta, \phi) = \frac{1}{2\pi} \left[ 1 + 2 \times \sum_{n=1}^{\infty} Q_x(p_T, \eta, n) \cos(n\phi) + \sum_{n=1}^{\infty} Q_y(p_T, \eta, n) \sin(n\phi) \right], \quad (5.2.4)$$

where:

$$Q_x(p_T, \eta, n) = \int_0^{2\pi} d\phi \times R(p_T, \eta, \phi) \cos(n\phi), \quad Q_y(p_T, \eta, n) = \int_0^{2\pi} d\phi \times R(p_T, \eta, \phi) \sin(n\phi). \quad (5.2.5)$$

$Q_x$  and  $Q_y$  are the components of Q-vector or "flow vector" or "event flow vector". The Q-vector can be defined as a function of  $p_T$  and  $\eta$  as follows:

$$\vec{Q}(p_T, \eta, n) = \{Q_x(p_T, \eta, n), Q_y(p_T, \eta, n)\}. \quad (5.2.6)$$

$Q_{\{x,y\}}$  can be rewritten as a function of  $\{V_n(p_T, \eta), n\Psi_{EP}\}$ , where EP stands for Event Plane, as follows:

$$Q_x(p_T, \eta, n) = V_n(p_T, \eta) \cos(n\Psi_{EP}), \quad (5.2.7)$$

$$Q_y(p_T, \eta, n) = V_n(p_T, \eta) \sin(n\Psi_{EP}). \quad (5.2.8)$$

Now we replace Eqs. 5.2.7, and 5.2.8 into Eq. 5.2.4:

$$R(p_T, \eta, \phi) = \frac{1}{2\pi} \left\{ 1 + 2 \times \sum_{n=1}^{\infty} V_n(p_T, \eta) \cos[n(\phi - \Psi_{EP})] \right\}. \quad (5.2.9)$$

Therefore, the particle invariant spectrum, Eq. 5.2.3, can be written based on the new  $R(p_T, \eta, \phi)$  definition in Eq. 5.2.9:

$$E \frac{d^3 N}{dp^3} = \frac{d^2 N}{2\pi p_T dp_T dy} \times \left\{ 1 + 2 \times \sum_{n=1}^{\infty} V_n(p_T, \eta) \cos[n(\phi - \Psi_{EP})] \right\}, \quad (5.2.10)$$

where  $V_n$  defines a complete set of anisotropic flow in the EP. Therefore, one can determine the equation of anisotropic flow in the EP method with respect to the final particles in a similar way as Eq. 5.2.2 as:

$$v_n = \langle \cos [n(\phi - \Psi_{EP})] \rangle. \quad (5.2.11)$$

In an ideal world, the anisotropic flow is considered relative to the reaction plane; however, the  $\Psi_{RP}$  cannot be determined in the experiment, and anyhow, due to fluctuations, the RP is not the correct reference. Thus we develop the EP method defined by the final particles, which allows measuring its angle,  $\Psi_{EP}$ . We compute the anisotropic flow using EP method in EPOS analysis as experimentalists do. It also means that each harmonic of the anisotropic flow's EP can be computed independently. The event flow vector  $Q_n$  and the EP angle  $\Psi_n$  from the  $n$ th harmonic of the distribution are defined by the equations [186]

$$Q_n \cos(n\Psi_n) = X_n = \sum_i w_i \cos(n\phi_i), \quad (5.2.12)$$

$$Q_n \sin(n\Psi_n) = Y_n = \sum_i w_i \sin(n\phi_i), \quad (5.2.13)$$

or

$$\Psi_n = \frac{1}{n} \tan^{-1} \left( \frac{\sum_i w_i \sin(n\phi_i)}{\sum_i w_i \cos(n\phi_i)} \right). \quad (5.2.14)$$

The sum go over the  $i$  particles used in the EP determination and  $w_i$  are weights, and  $\phi_i$  is the azimuthal angle of the particles. The weights are also optimized in general to reach the EP resolution. It can be done by choosing particles of a certain type, or by weighting particles based on their transverse momentum. Weights for odd and even harmonic planes are different. Using Eq. 5.2.14, one can rewrite the anisotropic flow in EP, Eq. 5.2.11, as

$$v_n^{obs}(p_T, y) = \langle \cos[n(\phi - \Psi_n)] \rangle, \quad (5.2.15)$$

where the average of all particles in all events is denoted by brackets. Since we developed the EP approach based on the reaction plane, many fluctuations can happen, which leads to reducing the anisotropic flow. We need to perform some corrections to our computations to reduce the event-by-event fluctuations in the EP approach. These corrections are referred to as "resolution" for each harmonic of the event plane, which is given by

$$R_n = \langle \cos[n(\Psi_n - \Psi_{RP})] \rangle. \quad (5.2.16)$$

The resolution of the event plane is influenced by correlations that do not directly connect all particles to the reaction plane. This type of factor creates a bias in anisotropic flow  $v_n$  measurement. We use the "gap" approach to remove biases such as this. Additionally, the multi-particle correlations or "cumulants" method [187], which is not employed in the current analysis, can be used to eliminate these biases.

### Add rapidity gap

In the EP approach, this is a way to reduce the non-flow effect on anisotropic flow. We need to define a method for reducing the resolution. To do so, we use one (or more) separate sub-events of the same multiplicity. The sub-events can be created in one of two ways: i) generate two  $\eta$  symmetrical ranges,  $[\eta_{min}; \eta_{max}]$  and  $[-\eta_{max}; -\eta_{min}]$ , and add a  $\eta$  gap between them, ii) randomly divide the total particles into two sub-events, each with the same multiplicity. We termed these events "random sub-events."

For example, at STAR [188], they employ two sub-events in two pseudorapidity ranges: one with negative pseudorapidity (A) and the other with positive pseudorapidity (B) to have almost the same multiplicity. Between A and B, they create a small gap (0.1). Therefore, the auto-correlation efficiency is reduced. The resolution of EP is modified by:

$$R_{n,sub} = \sqrt{\langle \cos[n(\Psi_n^A - \Psi_n^B)] \rangle}. \quad (5.2.17)$$

The modified anisotropic flow is calculated by using the following formula:

$$v_n = \frac{v_n^{obs}(p_T, y)}{R_{n,sub}} = \frac{\langle \cos[n(\phi_i - \Psi_n)] \rangle}{\sqrt{\langle \cos[n(\Psi_n^A - \Psi_n^B)] \rangle}} \quad (5.2.18)$$

In the following, I will show three harmonics of integrated and differential anisotropic flow results ( $v_2$ ,  $v_3$ , and  $v_4$ ) for **Au-Au** collisions in different simulations, **EPOS 4**, **EPOSi+PHSDe**, and **PHSD**.

### Transverse momentum dependence

In the same way, as in the previous section, I will present various flow harmonics results in different simulations. Then, I will compare them to the experimental data and among each other.

The experimental data presented here for  $v_2$ ,  $v_3$ , and  $v_4$  were taken from the **PHENIX** experiment [189] from an analysis of  $4.14 \times 10^9$  minimum-bias events obtained during the 2007 running period. Charged hadrons are reconstructed in a  $|\eta| < 0.35$  pseudorapidity range. The **EP** approach is used to provide measurements of flow coefficients as a function of centrality and  $p_T$  for  $\pi^\pm$ ,  $K^\pm$ ,  $p$ , and  $\bar{p}$ . Using the south and north reaction-plane detectors (RXN), the **EP** method determines a measured **EP** direction  $\Psi_m^{obs}$  for every event and for each order  $m$ , covering  $\Delta\phi = 2\pi$  and  $1 < |\eta| < 2.8$  [190].

Figs. 5.16, 5.17, and 5.18 show the differential flow ( $v_2, v_3, v_4$ ) of charged hadrons,  $\pi$ ,  $K$ , and  $p$  using the **EP** method for **Au-Au** at  $\sqrt{s_{NN}}=200$  GeV for different centralities in various simulations, **EPOS 4** (blue), **EPOSi+PHSDe** (red), and **PHSD** (green). In our analysis, we selected the  $|\eta| < 0.35$  as in the experiment.

As shown in Fig. 5.16, we have a good agreement of  $v_2$  results for  $\pi$ ,  $K$ , and  $p$  in the case of **EPOS 4** simulation compared to the real data at low (0-2 GeV/c) and intermediate (2-3 GeV/c)  $p_T$ , for the central collisions (0-10 %). By increasing the centrality in this simulation, the elliptic flow results are a little below the real data, although we have the same trends for all types of identified particles.

In **EPOSi+PHSDe** and pure **PHSD** simulations,  $\pi$  for  $p_T < 1$  GeV/c and kaon  $K$  for  $p_T < 1.5$  GeV/c successfully reproduce the elliptic flow but they fail for intermediate  $p_T$  for all ranges of centrality. In the case of the proton, the results of these two models are higher than **EPOS 4** and the experimental data for central collisions, however; the flow is decreased in **EPOSi+PHSDe** by increasing the centrality compared to other models and the real data. For all types of identified particles and non-central collisions, one can see that pure **PHSD** results are above the **EPOSi+PHSDe** results and it is more visible for heavier particles like protons.

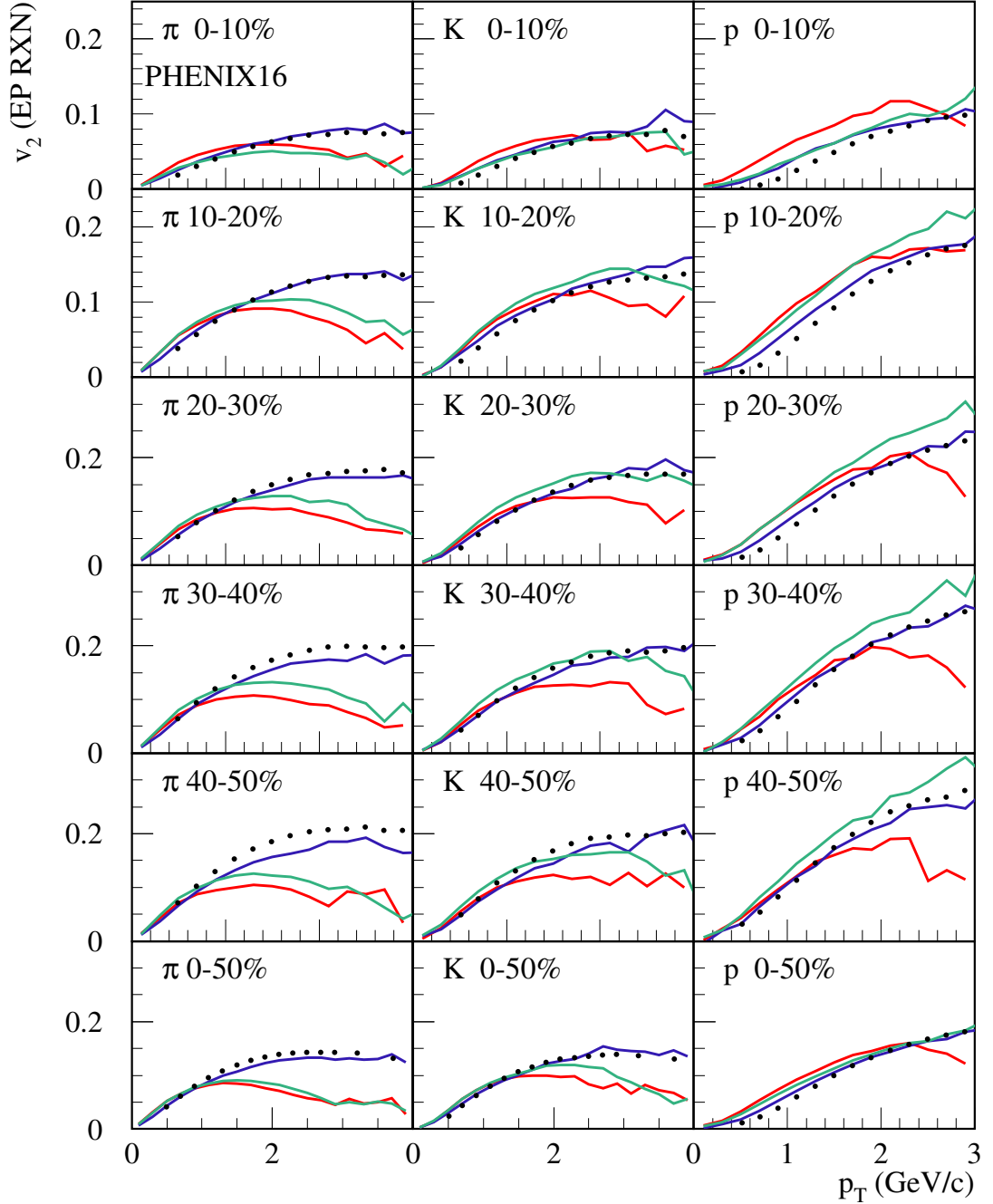


Figure 5.16: Differential elliptic flow ( $v_2$ ) of charged hadrons,  $\pi$ ,  $K$ , and  $p$ , at mid-rapidity for Au-Au collisions at  $\sqrt{s_{NN}}=200$  GeV for different centrality bins. Blue, red, green colors, and dots indicate EPOS 4, EPOSi+PHSDe, pure PHSD results, and PHENIX experimental data [189], respectively.

Let's look at the triangular flow  $v_3$  in these simulations and experiments. We have a very excellent agreement to the real data for differential triangular flow in EPOS 4 for pions, kaons, and protons in the most central and mid-central collisions, as shown in Fig. 5.17. However, for light particles such as  $\pi$  at intermediate  $p_T$  (2-3 GeV/c), it can create less  $v_3$  for semi-peripheral collisions (40-50%) compared to the data.

As seen in Fig. 5.17, EPOSi+PHSDe and pure PHSD work well for triangular flow, much like elliptic flow, at low  $p_T$ . At high  $p_T$  the situation somewhat complicated in the sense that  $v_3$  for pion results are much too low, whereas the triangular flow in particular

for protons look reasonable. When we compare the  $v_3$  results in these two models, one can see that **EPOSi+PHSDe** results are a bit above pure **PHSD** from central (0-10%) to semi-peripheral (40-50%) collisions. This could be related to the fact that we had a bit more  $p_T$  spectra in **EPOSi+PHSDe** than pure **PHSD** as seen in Fig 5.9.

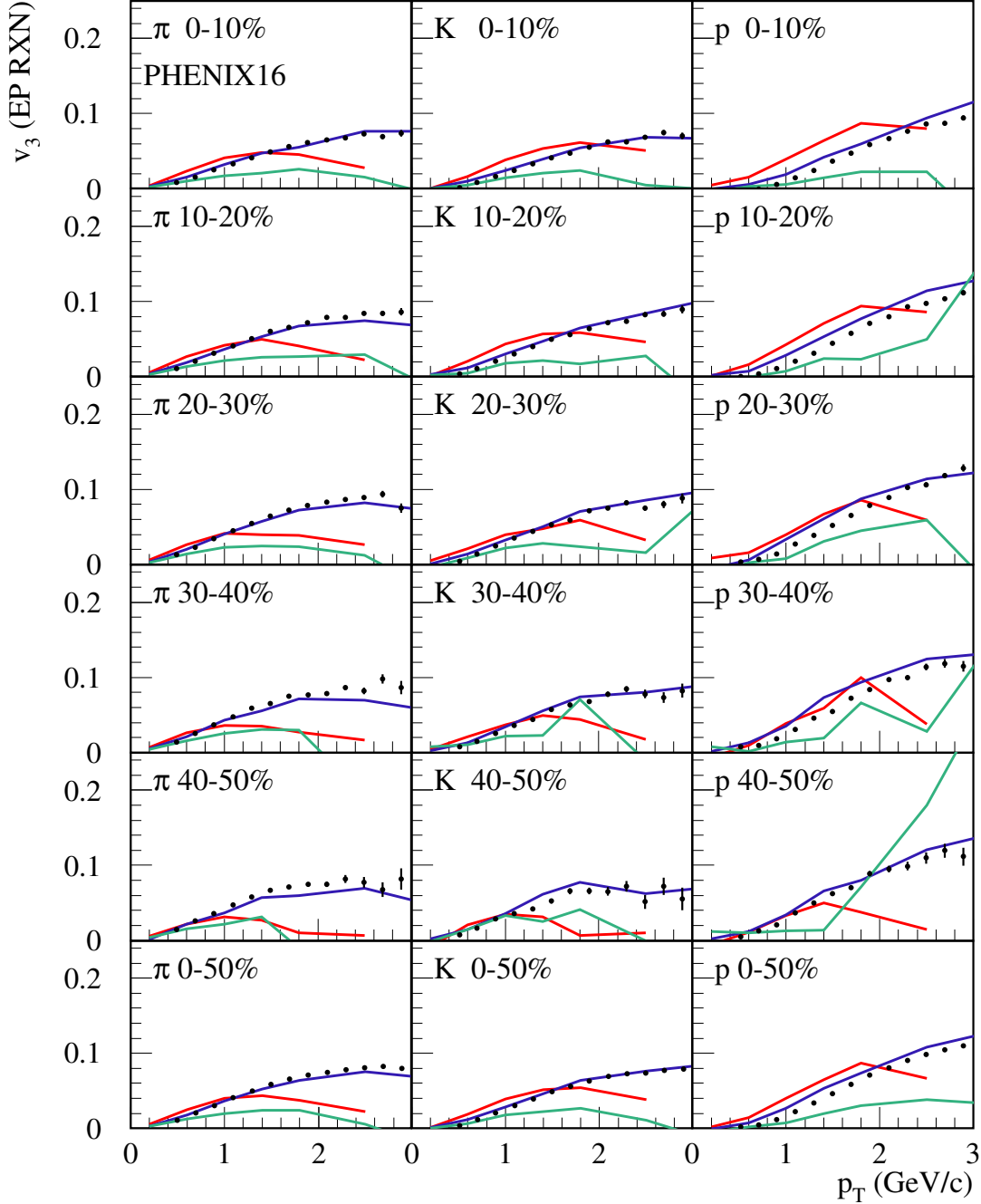


Figure 5.17: Differential triangular flow ( $v_3$ ) of charged hadrons,  $\pi$ ,  $K$ , and  $p$ , at mid-rapidity for **Au-Au** at  $\sqrt{s_{NN}}=200$  GeV for different centrality ranges. Blue, red, green colors, and dots indicate **EPOS 4**, **EPOSi+PHSDe**, pure **PHSD** results, and **PHENIX** experimental data [189], respectively.

Fig. 5.18 compares the differential quadrangular flow  $v_4$  in various simulations with experimental data from most central to semi-peripheral collisions. The magnitude of  $\eta/s$  and the freeze-out dynamics [191] are more sensitive to higher-order anisotropic harmonics, particularly  $v_4$ . This is why we are also studying  $v_4$ .

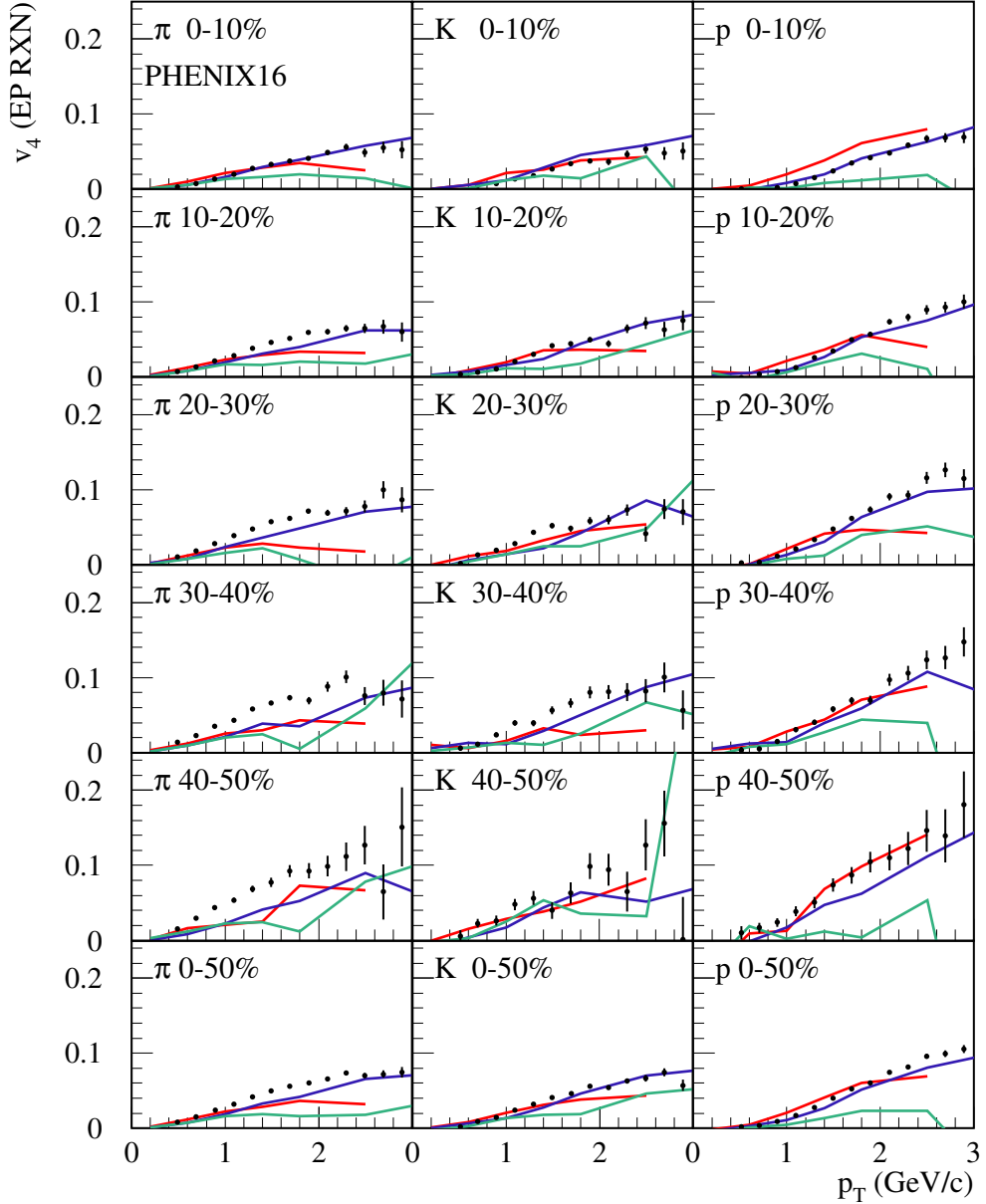


Figure 5.18: Differential quadrangular flow ( $v_2$ ) of charged hadrons,  $\pi$ ,  $K$ , and  $p$ , at mid-rapidity for Au-Au at  $\sqrt{s_{NN}}=200$  GeV for different centrality ranges. Blue, red, green colors, and dots indicate EPOS 4, EPOSi+PHSDe, pure PHSD results, and PHENIX experimental data [189], respectively.

In EPOS 4 (blue curves), both low and intermediate  $p_T$  have contributions to reproduce this order of flow as compared to the real data for most central collisions (0-10 %). EPOSi+PHSDe (red curves) can produce  $v_4$  reasonably compared to the experimental data and EPOS 4 at low  $p_T$ , and it has more quadrangular flow when compared to pure PHSD in this range of  $p_T$ .

In summary, one can say that EPOS 4 gives good results for central collisions, and it is too low for more peripheral ones. Pure PHSD again under-predicts data at high  $p_T$ , whereas EPOSi+PHSDe is somewhat better for kaons and protons, but not for pions.

In general (for  $v_2$ ,  $v_3$ , and  $v_4$ ) **EPOSi+PHSDe** does a little bit better than pure **PHSD**, although the radial flow (as seen from spectra) is equally bad in both models.

### Pseudorapidity dependence

In this section, I will present the elliptic flow of charged particles as a function of pseudorapidity for **Au-Au** collisions at  $\sqrt{s_{NN}}=200$  GeV in various simulations, including **EPOS 4**, **EPOSi+PHSDe**, and pure **PHSD**. In addition, I compare them among each other and the experimental data.

The experimental data presented here for  $v_2$  were obtained using the **PHOBOS** experiment, during the 2001 **Au-Au** run of **RHIC**, which used the track-based method [59]. As described in [192], the **PHOBOS** detector is composed of silicon pad detectors arranged in single and multiple-layer configurations around the interaction region. The octagonal multiplicity detector (OCT) with  $|\eta| < 3.2$  and six annular silicon ring multiplicity detectors (RINGS) with  $3.0 < |\eta| < 5.4$  make up the single layer configuration.

The elliptic flow as a function of pseudorapidity from central to semi-peripheral and minimum bias **Au-Au** collisions at  $\sqrt{s_{NN}} = 200$  GeV are displayed in Fig. 5.19. With raising  $|\eta|$ , the experimental results reveal a steady decrease in  $v_2$ . In addition, we see the same trend of results in our simulations in mid-, forward-, and backward-pseudorapidity regions. The flow signal is smallest at the most central collisions (3-15%). As stated previously, the flow is growing by raising the centrality classes from central to semi-peripheral collisions.

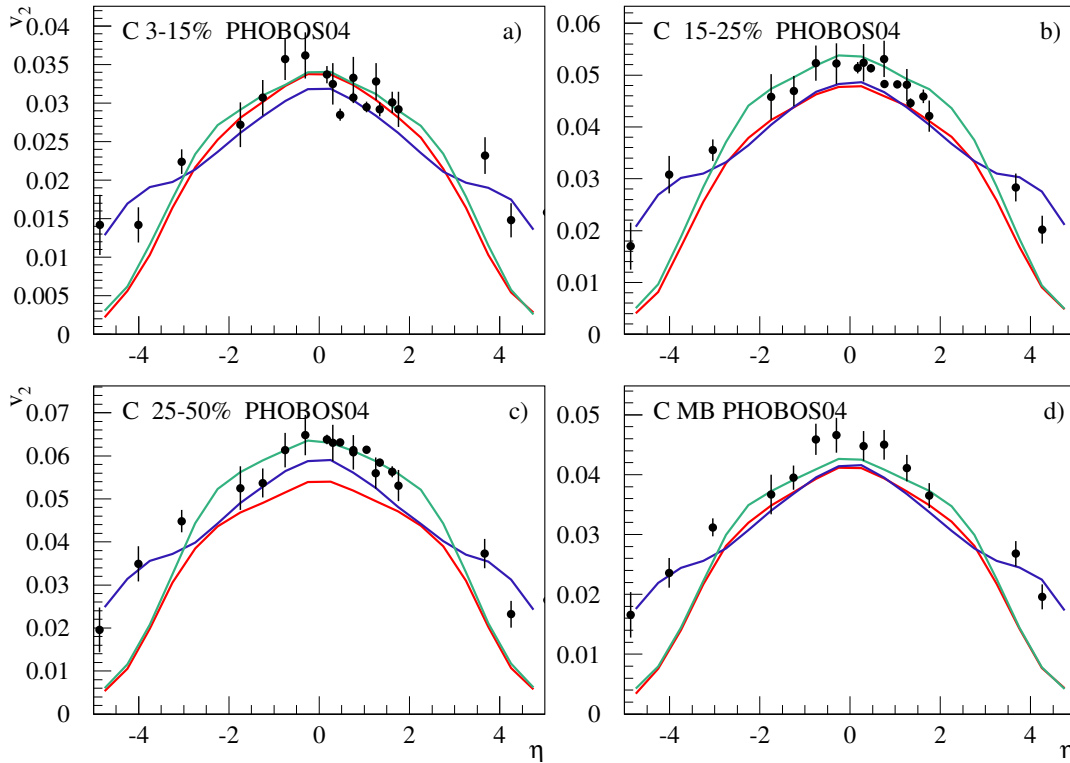


Figure 5.19: Elliptic flow as a function of pseudorapidity ( $v_2(\eta)$ ) for charged hadrons in **Au-Au** collisions at  $\sqrt{s_{NN}}=200$  GeV for different centrality classes, ranging from central to semi-peripheral and minimum bias collisions ( a): 3-15%, b): 15-25%, c): 25-50%, and d): minimum bias). Blue, red, green colors, and dots indicate **EPOS 4**, **EPOSi+PHSDe**, pure **PHSD** results, and **PHOBOS** experimental data [59], respectively.

The pseudorapidity densities ( $dn/d\eta$ ) essentially summarizes the low  $p_T$  results (see Fig. 5.8), where high  $p_T$  does not contribute since  $p_T$  spectra ( $dn/dp_T$ ) drops fast with  $p_T$ . The tails in Fig. 5.19 are interesting since **EPOS 4** has more  $v_2$ , but **EPOSi+PHSDe** and pure **PHSD** drop to zero, indicating that there is no flow created at large  $\eta$  in these two models.

Additionally, as shown in Fig. 5.20, the centrality dependence of  $v_2$  at mid-rapidity can be checked. This plot summarizes what we have already seen earlier:  $v_2$  increases when we go from central (large  $N_{part}$ ) to semi-peripheral collisions.

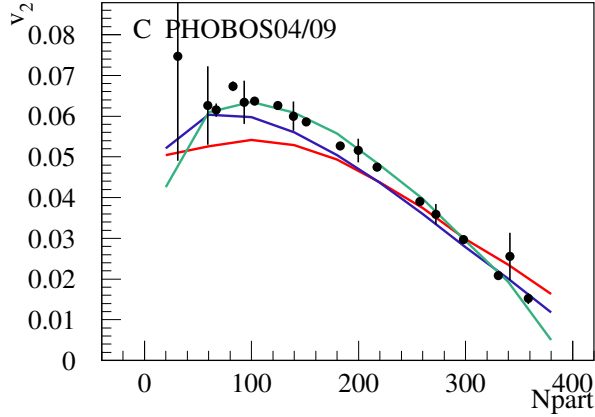


Figure 5.20: Elliptic flow ( $v_2(|\eta| < 1)$ ) as a function of the number of participants ( $N_{part}$ ) in three different simulations (**EPOS 4** (blue), **EPOSi+PHSDe** (red), pure **PHSD** (green)) and **PHOBOS** experimental data (dots) [59] for **Au-Au** collisions at  $\sqrt{s_{NN}} = 200$  GeV.

### 5.3 Summary and conclusion

The main results of my Ph.D. thesis have been presented in this chapter. As I explained in the previous one, we developed a new framework called **EPOSi+PHSDe**. We used a sophisticated **EPOS 4** approach to determine the initial distribution of matter (parton-s/hadrons), followed by a non-equilibrium **PHSD** transport approach.

Comparing two alternative dynamical descriptions with the same initial condition is what **EPOSi+PHSDe** is all about. It is useful to also consider **EPOSi+PHSDe**, because **EPOSi+PHSDe** and **EPOS** have different evolutions, but share the same initial condition. In this way one can disentangle "initial condition" and "evolution".

The results of **Au-Au** collisions at  $\sqrt{s_{NN}} = 200$  GeV were presented in this chapter, including bulk matter observables such as transverse mass/momentum spectra, and rapidity/pseudorapidity densities in the first section. In the following, the anisotropic flow was discussed.

In terms of particle  $p_T$  spectra, all three models provide comparable results at low  $p_T$  (essentially below 1GeV/c), but they differ significantly at higher  $p_T$ : although **EPOS 4** is close to the data, both **EPOSi+PHSDe** and pure **PHSD** drastically underestimate it. We are talking about a factor of ten for kaons and protons, and considerably more for hyperons. In both **EPOSi+PHSDe** and pure **PHSD**, this is a strong indicator that radial flow is absent. Despite the differences in initial conditions, both models are very similar, indicating that evolution has had a significant impact.

The fact that [EPOS 4](#) and [EPOSi+PHSDe](#) have the same initial condition but produce substantially different results in terms of flow variables supports this conclusion. All of this is in line with the previous study of the different radial expansions in the three models (Figs. [5.2](#) and [5.3](#)), which demonstrate that [EPOSi+PHSDe](#) and pure [PHSD](#) expand slowly compared to [EPOS 4](#), which expands strongly in the transverse plane. When we look at the details, we will notice significant discrepancies between [EPOSi+PHSDe](#) and pure [PHSD](#) in terms of protons that are not well understood.

Because there were considerable fluctuations, we "rebinned" the  $v_3$  and  $v_4$  results. We would require an unreasonable amount of computing resources to decrease the fluctuations, which takes time.

The electromagnetic probes in [EPOSi+PHSDe](#) and pure [PHSD](#) will be compared in the next chapter.



As I have already explained in section 1.4 of chapter 1, electromagnetic probes, like dileptons and photons, are practical tools to study the early hot and dense stage of **HICs** since they are unaffected by final-state interactions. They transfer information about the conditions and properties of the environment in which they are emitted to the detector via their invariant mass and momentum distributions. They provide a deep look into the bulk of the strongly interacting matter produced in these collisions.

Since dileptons are emitted throughout the **HICs**, from initial nucleon-nucleon collisions to the hot and dense phase and hadron decays after freeze-out, microscopic covariant transport models, such as **PHSD**, play an important role in identifying the various sources that contribute to the final dileptons spectra observed in experiments [79].

In this chapter, we focus on dileptons production in **EPOSi+PHSDe** and pure **PHSD**, which I will discuss briefly in the following.

## 6.1 Dileptons enhancement

The dileptons production can be investigated using the **PHSD** transport approach, in which quarks and gluons in the **QGP** are off-shell massive strongly interacting quasi-particles. The description of quarks and gluons in **PHSD** is based on a **DQPM** for partons matched to reproduce **lQCD** results [146] in thermodynamic equilibrium.

In **PHSD**, three types of production channels for dileptons are defined for **HICs**: i) hadronic production channels, ii) partonic production channels, and iii) semi-leptonic decay of the heavy-flavor pairs contribution [193, 194]. In the following paragraphs, I will simply discuss these channels.

**Hadronic production channels:** The hadronic sector of **PHSD** is equivalent to the **Hadron String Dynamics (HSD)** transport approach [195, 196]. **HSD** has been used to simulate **pA** and **AA** collisions from **An Accelerator Facility for Relativistic Heavy Ions (SIS)** to **SPS** energies, resulting in reliable reproduction of hadron abundances, rapidity distributions, transverse momentum spectra, and dilepton spectra. **HSD** incorporates off-shell dynamics for vector mesons [133] and a set of vector-meson spectral functions [197] covering various possibilities for in-medium modification, such as the collisional expansion of the vector resonances [194]. The following is a schematic representation of the dileptons

production by a resonance  $R$  decay:

$$BB \rightarrow RX, \quad (6.1.1)$$

$$mB \rightarrow RX, \quad (6.1.2)$$

$$R \rightarrow e^+e^-X, \quad (6.1.3)$$

$$R \rightarrow mX, \quad m \rightarrow e^+e^-X, \quad (6.1.4)$$

$$R \rightarrow R'X, \quad R' \rightarrow e^+e^-X, \quad (6.1.5)$$

where the resonance  $R$  could be produced in baryon-baryon ( $BB$ ) or meson-baryon ( $mB$ ) collisions in the first step. The resonance can then simply couple to dileptons (Eq. 6.1.3) (for example Dalitz decay of the  $\Delta$  resonance:  $\Delta \rightarrow e^+e^-N$ ) or decay to meson  $m$  (+ baryon) (Eq. 6.1.4) that produces dileptons via direct decays ( $\rho, \omega, \phi$ ) or Dalitz decays ( $\pi^0, \eta, \omega$ ). In Eq. 6.1.5, the resonance  $R$  may decay into a second resonance  $R'$ , which then yields dileptons by Dalitz decay. The final particles that couple to dileptons in the PHSD framework can potentially be produced by non-resonant mechanisms, such as "background" channels at low and intermediate energy or string decay at high energies.

**Partonic production channels:** The elementary interaction of the strongly interacting QGP can be addressed to study the electromagnetic radiation of the partonic phase. As seen in Fig. 6.1, the partonic production channels can be a) the basic Born  $q + \bar{q} \rightarrow \gamma^*$  annihilation mechanism, b) Gluon-Compton scattering (GCS) ( $q(\bar{q}) + g \rightarrow \gamma^* + q(\bar{q})$ ), c) vertex correction, and d) quark + anti-quark annihilation with gluon Bremsstrahlung (NLODY) in the final state ( $q + \bar{q} \rightarrow g + \gamma^*$ ), where  $\gamma^*$  stands for the  $e^+e^-$  or  $\mu^+\mu^-$  pair.

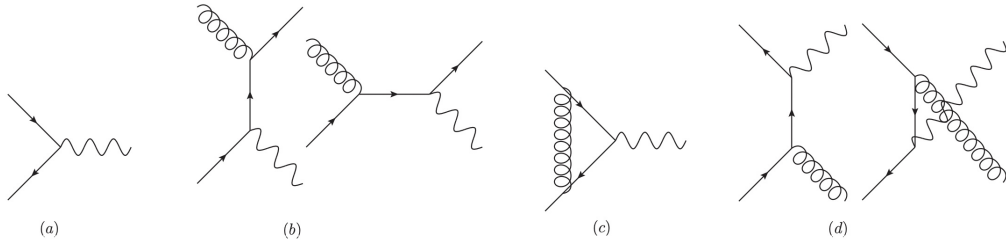


Figure 6.1: Diagrams contributing to the dileptons production from QGP: a) Drell-Yan mechanism, b) gluon-Compton scattering, c) vertex correction, d) gluon Bremsstrahlung, where virtual photons  $\gamma^*$ , gluons, and quarks are depicted by wavy lines, spiral lines, and arrows, respectively. In each diagram, the time runs from left to right [79].

A dilepton pair can be produced according to the off-shell cross-sections whenever quark-antiquark, quark-gluon, and antiquark-gluon collisions occur in the MC simulation of the partonic phase in PHSD. The cross-sections for parton collisions have been computed in line with the DQPM, taking into account the off-shell nature of the interacting partons [194].

**Heavy-flavor pairs:** Since the lepton and antilepton are produced in separate semi-leptonic decays, the production of dileptons from heavy-flavor pairs is different from the other channels. However, since the heavy flavor is always produced by pairs, one should consider the dilepton production with the probability that both heavy flavor and anti-heavy flavors decay into semi-leptons. Furthermore, the kinematics of the heavy-flavor pairs produced early in HICs are affected by strong interactions with the partonic or

hadronic medium, and their kinematics change over time.

I will show some hadronic production channels in Au-Au collisions at 200 GeV from the STAR experiment in the following. Then I will compare our simulations to these data.

### 6.1.1 Cocktail in Au-Au collisions

As stated recently, the dileptons are produced from hadronic and partonic sources. Using the HICs one can have the partonic sources in addition to hadronic sources to produce the dileptons. Theoretical calculations indicate that at top RHIC energy, QGP thermal dilepton production will become a dominant source in the intermediate-mass region ( $M_\phi < M_{e^+e^-} < M_{J/\psi}$ ). Virtual photons can be produced via initial hard scattering processes, which can then be converted into low ( $M_{e^+e^-} < M_\phi$ ) and high ( $M_{e^+e^-} > M_{J/\psi}$ ) invariant-mass dielectrons with high transverse momentum.

Long-lived hadrons (such as  $\pi^0$ ,  $\eta$ ,  $D\bar{D}$ , etc.) can decay into lepton pairs and be measured by the detector system at the end of the collisions when all particles decouple from the system. Their contributions can be computed and incorporated into the so-called "hadron cocktail" based on the predicted invariant yields of the respective parent particles.

Comparing the cocktail and data for Au-Au collisions in Fig. 6.2 (upper panel), one can see some deviations, and the data excess amounts to "the interesting physics" which we try to incorporate in our models.

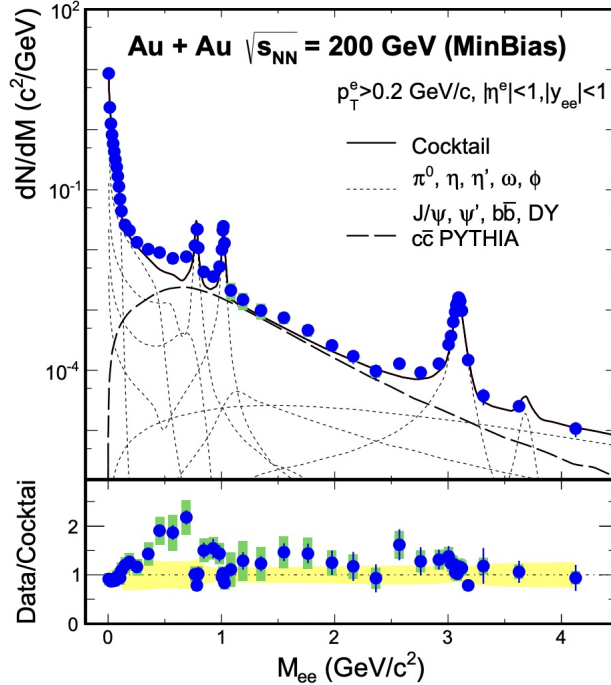


Figure 6.2: (Color online) Invariant mass spectrum in the STAR acceptance ( $p_T^e > 0.2$  GeV/c,  $|\eta^e| < 1$ , and  $|y_{ee}| < 1$ ) from  $\sqrt{s_{NN}} = 200$  GeV Au-Au minimum-bias collisions. The mass spectrum is compared to the hadronic cocktail simulations (upper panel) [84].

In the following, I will compare the invariant mass, transverse momentum, and rapidity spectra of dileptons (dielectrons and dimuons) production in pure PHSD and

EPOSi+PHSDe simulations.

### 6.1.2 Invariant mass spectrum

As previously noted, compared to photons in HICs, dileptons have the invariant mass as an additional degree of freedom, which might also provide more information on the matter produced in the collisions. In Fig. 6.3, the invariant mass spectrum of dielectrons in minimum-bias Au-Au collisions at 200 GeV is shown for pure PHSD and EPOSi+PHSDe in comparison to the STAR experimental data with specific cuts in transverse momentum ( $p_T > 0.2$  GeV/c) and rapidity/pseudorapidity ( $|y_e|, |\eta_e| < 1$ ).

As seen in Fig. 6.3, in both simulations, pure PHSD and EPOSi+PHSDe, various hadronic sources, such as  $\pi^0, \eta, \eta', \Delta, a_1, \omega$ , and vector mesons  $\omega, \rho, \phi$  contribute to the low-mass ( $M < 1.1$  GeV/c<sup>2</sup>) dileptons spectrum. When the sum of all channels in these two simulations are compared, it can be seen that the results in EPOSi+PHSDe (black line) are somewhat better than pure PHSD (black dotted line), especially in the 0.2 to 0.8 GeV/c<sup>2</sup> region. We are still looking for an answer to the question, "why does the vector meson  $\omega$  tend to produce more in the region of 0.5-0.7 GeV/c<sup>2</sup> in EPOSi+PHSDe compared to pure PHSD?" Furthermore, in pure PHSD, we have a bit more dilepton production from  $\Delta$  compared to EPOSi+PHSDe, for reasons that are unknown yet, and we will see this in the transverse momentum and rapidity spectra.

The partonic radiation, on the other hand, is visible in the mass range  $M = 1.1$ - $3$  GeV/c<sup>2</sup>, where dielectrons are produced by quark-antiquark annihilation in strongly QGP. When the sums of all channels in these two models are compared, it can be seen that partonic sources, specially GCS (with dashed and full red-orange curves), contribute more to the production of dielectrons in pure PHSD than in EPOSi+PHSDe in this mass area. It can also be seen in other spectra, and there is an issue not yet understood. It is worth noting that heavy-flavor contributions like  $D\bar{D}, B\bar{B}, J/\psi$ , and  $\psi'$  are not included in this analysis.

Fig. 6.4 is similar to Fig. 6.3, with the exception that in Fig. 6.4, pure PHSD includes the contributions of heavy-flavor pairs,  $D\bar{D}$  and  $B\bar{B}$ . The description of the inclusive dielectrons spectra is roughly perfect for lower invariant mass when looking at the sum of all channels in pure PHSD (black dotted line). In addition, the contribution from heavy-flavor pairs and partonic interaction dominates the intermediate mass range (between the masses of the  $\phi$  and 2.4 GeV/c<sup>2</sup>). EPOSi+PHSDe has not accounted for the heavy-flavor contributions, which is crucial (work in progress). We obtained a bit higher contributions from hadronic sources in EPOSi+PHSDe compared to pure PHSD, as seen in Fig. 6.3, and I guess after accounting for the heavy-flavors, we will also have more dielectrons production in EPOSi+PHSDe compared to pure PHSD.

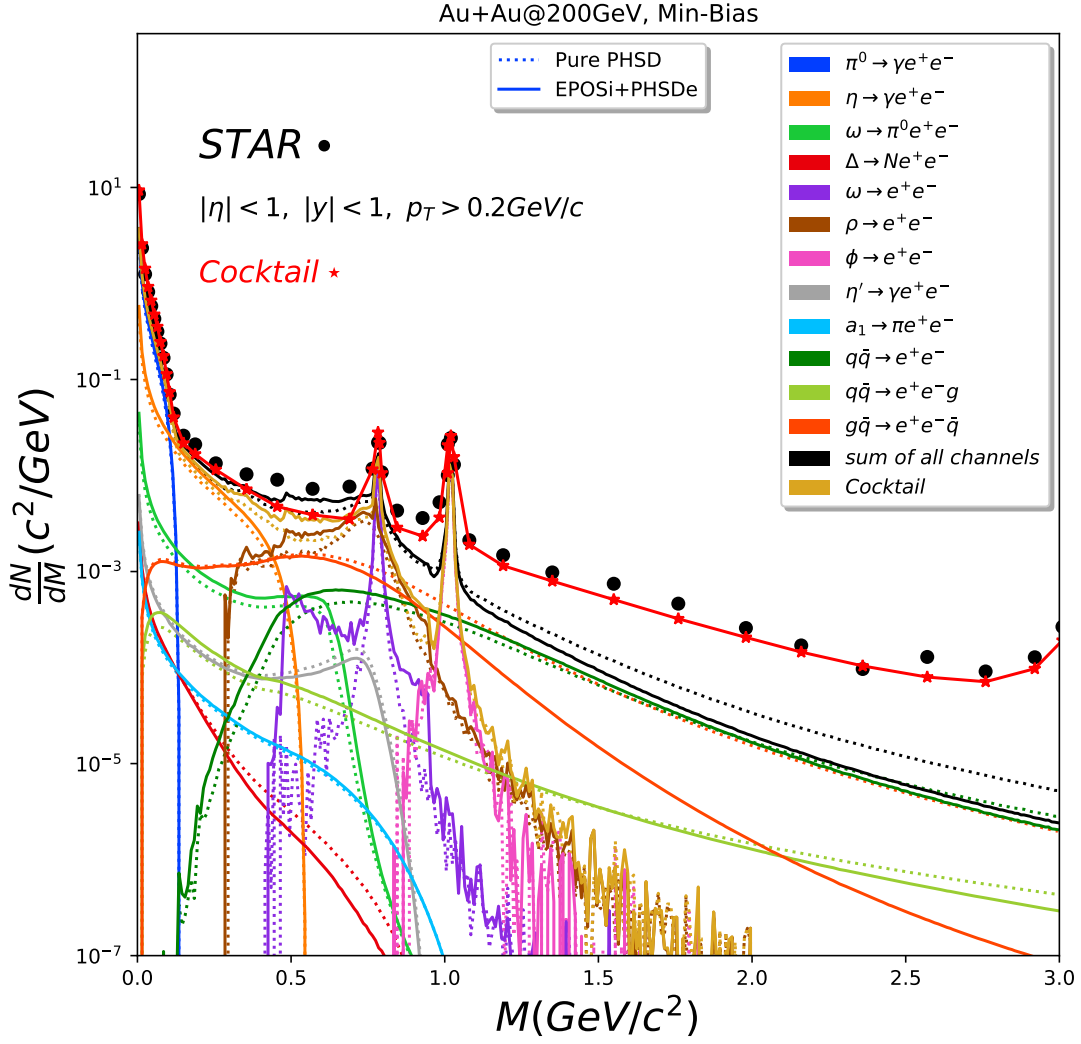


Figure 6.3: Invariant mass spectrum of dielectrons in minimum-bias Au-Au collisions at 200 GeV from pure PHSD (dotted lines) and EPOSi+PHSDe (solid lines) in comparison to the data from the STAR experiment [84]. The different channels are specified in the legend.

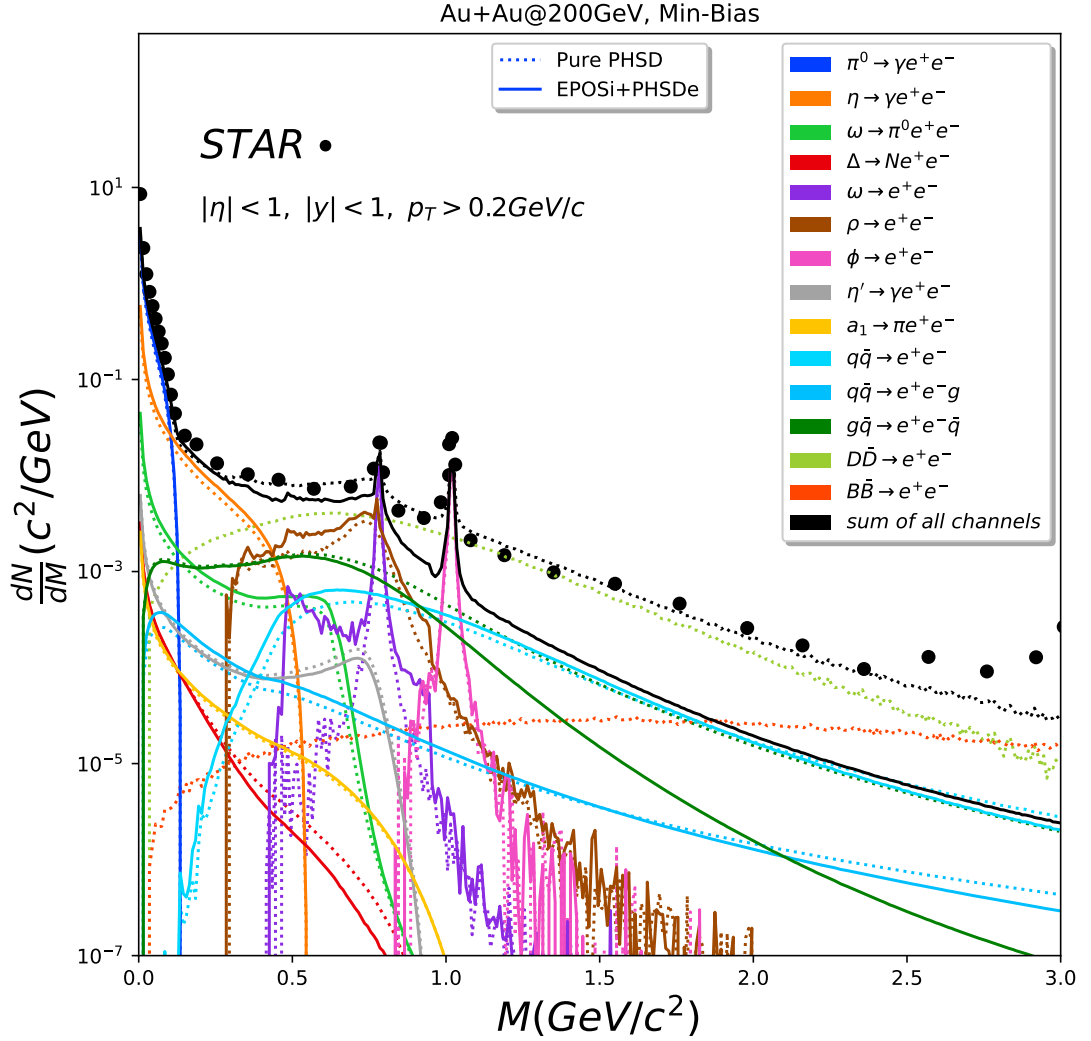


Figure 6.4: Same as Fig. 6.3, including the contributions from  $D\bar{D}$  and  $B\bar{B}$  decays in pure PHSD and without cocktail curves in both models.

If we look at our results in Fig. 6.3, the cocktail curves in both models are less than their total sum, also less than the cocktail curve from the experimental data. Ideally, one should have the same cocktail curves in our simulations as Fig. 6.2, taking into account those particle contributions that were missed in our simulations.

As shown in Figs. 6.5 and 6.6, the dileptons enhancements in these two models have been compared without any cuts in rapidity/pseudorapidity or transverse momentum. When we look at both dielectrons and dimuons, the summing of all channels shows that EPOSi+PHSDe is above pure PHSD in the low invariant mass range. This is mainly due to increased contributions of vector mesons  $\rho$  and  $\phi$  ( $\rho \rightarrow l^+ l^-$ ,  $\phi \rightarrow l^+ l^-$ ).

However, when we look at the sum of all channels in the intermediate invariant mass ( $M > 1.1 \text{ GeV}/\text{c}^2$ ), we notice that pure PHSD is above EPOSi+PHSDe, and it comes mostly from partonic radiation, Gluon-Compton scattering (GCS) ( $g\bar{q} \rightarrow l^+ l^- g$ ). Unfortunately, in the case of dimuons invariant mass spectrum, there is no experimental data with which we may compare our results.

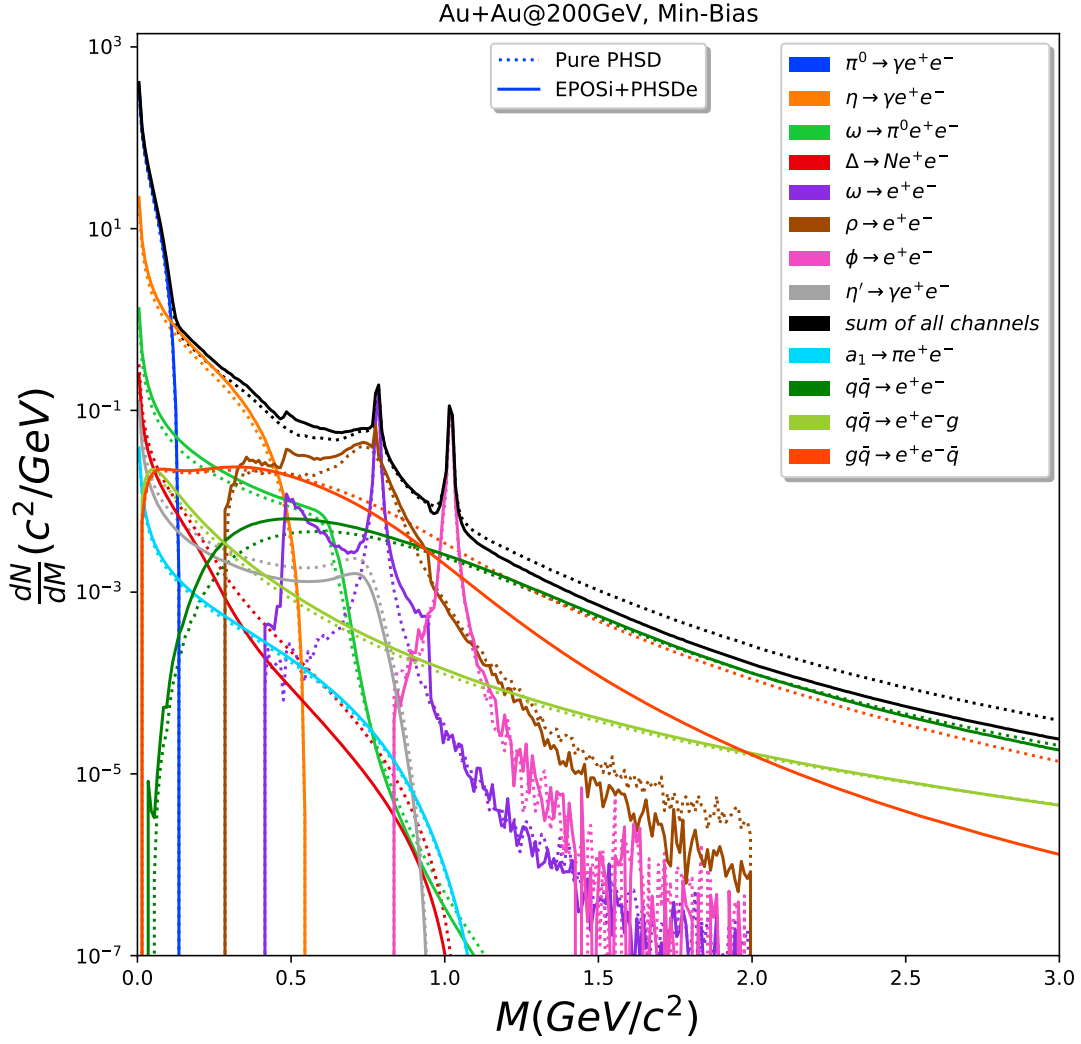


Figure 6.5: Invariant mass spectrum of dielectrons in minimum-bias Au-Au collisions at 200 GeV from pure PHSD (dotted lines) in comparison to EPOSi+PHSDe (solid lines). The different channels are specified in the legend. In this plot, the heavy-flavor contributions (such as  $D\bar{D}$ ,  $B\bar{B}$ ,  $J/\psi$ , and  $\psi'$ ) have been skipped.

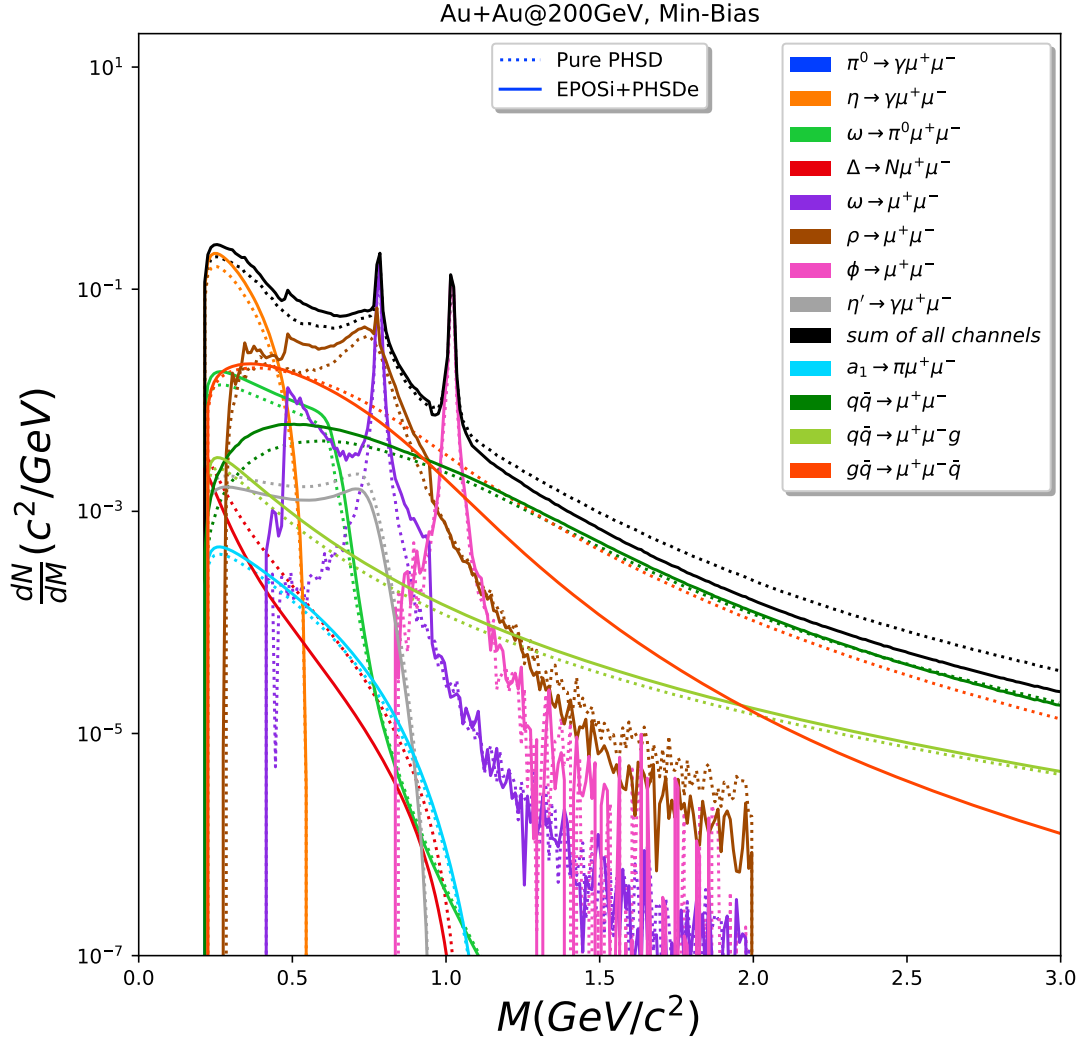


Figure 6.6: Same as Fig. 6.5 for dimuons.

### 6.1.3 Transverse momentum and rapidity spectra

The transverse momentum spectra of dileptons for minimum-bias Au-Au collisions at 200 GeV in EPOSi+PHSDe and pure PHSD are shown in Figs. 6.7 and 6.8. In this analysis, we sum over all masses. For both dielectrons and dimuons, the sums of all channels reveal that EPOSi+PHSDe (black solid line) is somewhat higher than pure PHSD (black dotted line) results. It might be because EPOSi+PHSDe employs the initial condition from EPOS 4, which causes the system to expand somewhat more in the transverse plane than pure PHSD, as we discussed in the previous chapter. Increased transverse flow results from this expansion, resulting in more particle production at higher  $p_T$ . We have almost the same dileptons production in both simulations in low  $p_T$ . However, EPOSi+PHSDe produces more dileptons in intermediate  $p_T$  for all channels except GCS and  $\Delta$  channels compared to pure PHSD.

In both models, since the  $dN/dM$  drops quickly (as seen in the previous section), we essentially see the low invariant mass  $M$  results. And, we see dominant contributions from some resonance decays for  $p_T$  spectra such as  $\pi^0$ ,  $\eta$ , and  $\omega$ .

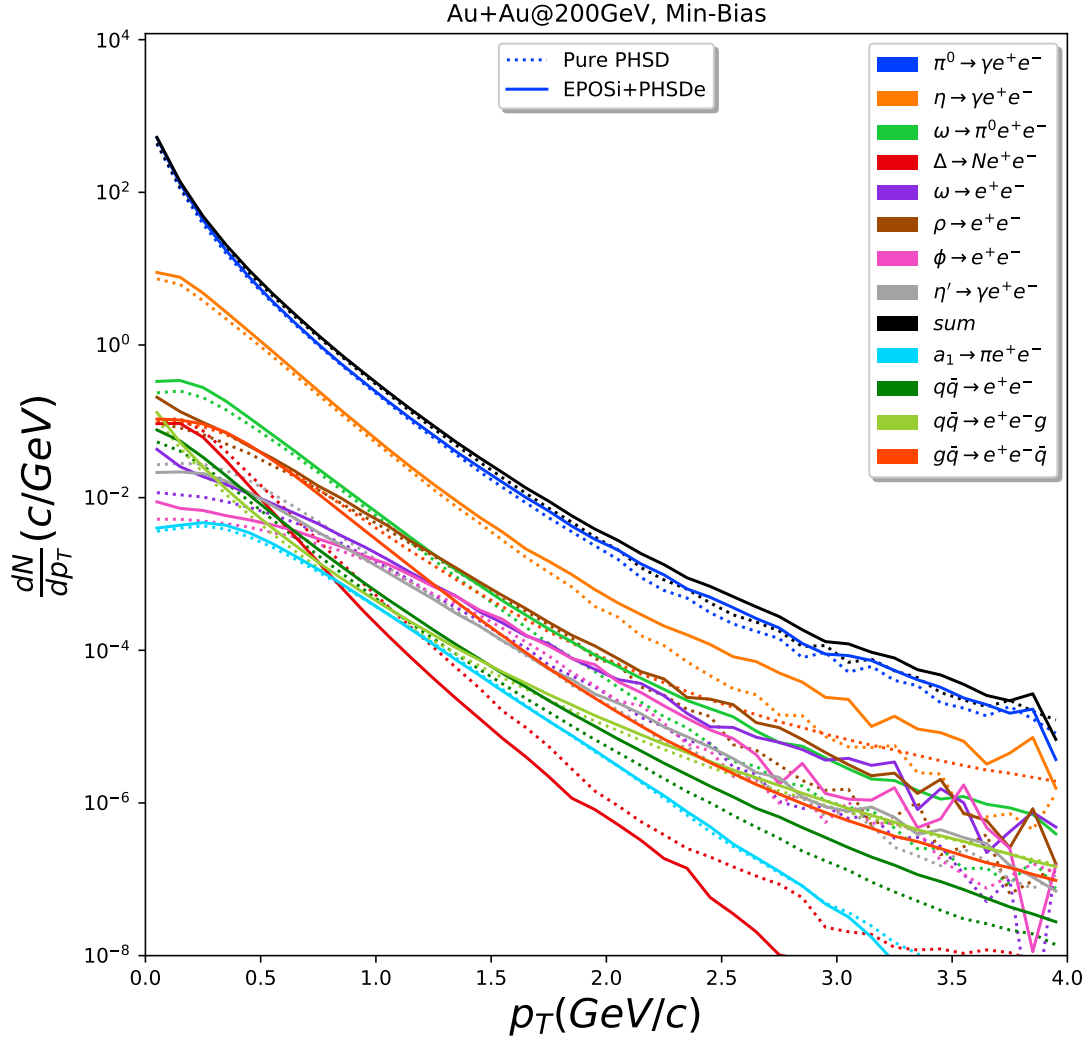


Figure 6.7: Transverse momentum spectra of dielectrons in minimum-bias Au-Au collisions at 200 GeV from pure PHSD (dotted lines) in comparison to EPOSi+PHSDe (solid lines). The different channels are specified in the legend. In this plot, the heavy-flavor contributions (such as  $D\bar{D}$ ,  $B\bar{B}$ ,  $J/\psi$ , and  $\psi'$ ) have been skipped.

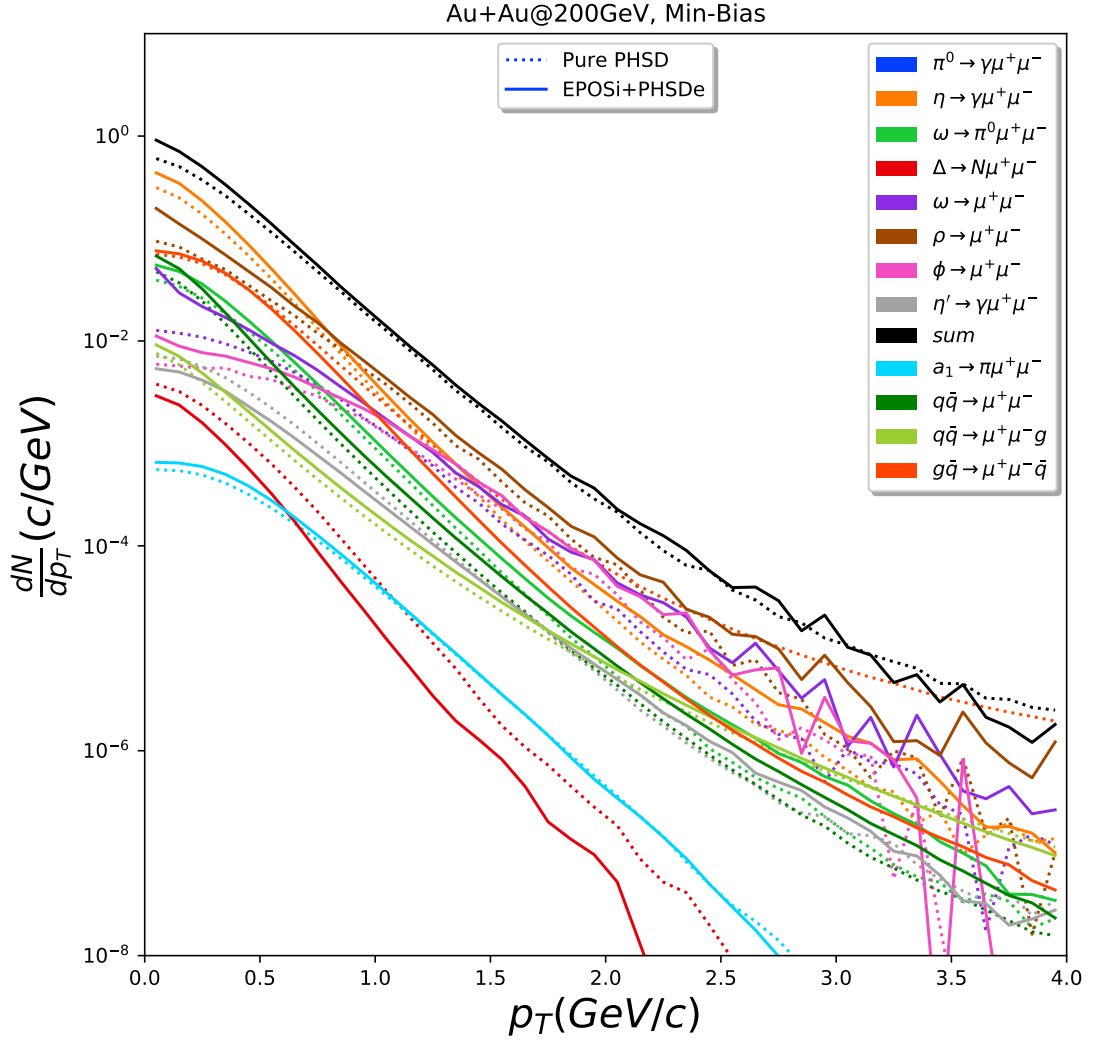


Figure 6.8: Same as Fig. 6.7 for dimuons.

The rapidity spectra of dileptons for minimum-bias Au-Au collisions at 200 GeV in EPOS+PHSDe and pure PHSD are shown in Figs. 6.9 and 6.10. The plots refer to the sum of all channels and the sum over all masses. As we have already seen in the transverse momentum spectra, dilepton production in EPOS+PHSDe is slightly higher compared to pure PHSD. If we look more carefully at the figures (Figs. 6.9 and 6.10), we can see that all channels' contributions in EPOS+PHSDe are above pure PHSD in mid and forward/backward rapidities except for GCS, and  $\Delta$ . The partonic channels have narrower  $dN/dy$  than hadronic channels, producing more dileptons in the mid-rapidity region.

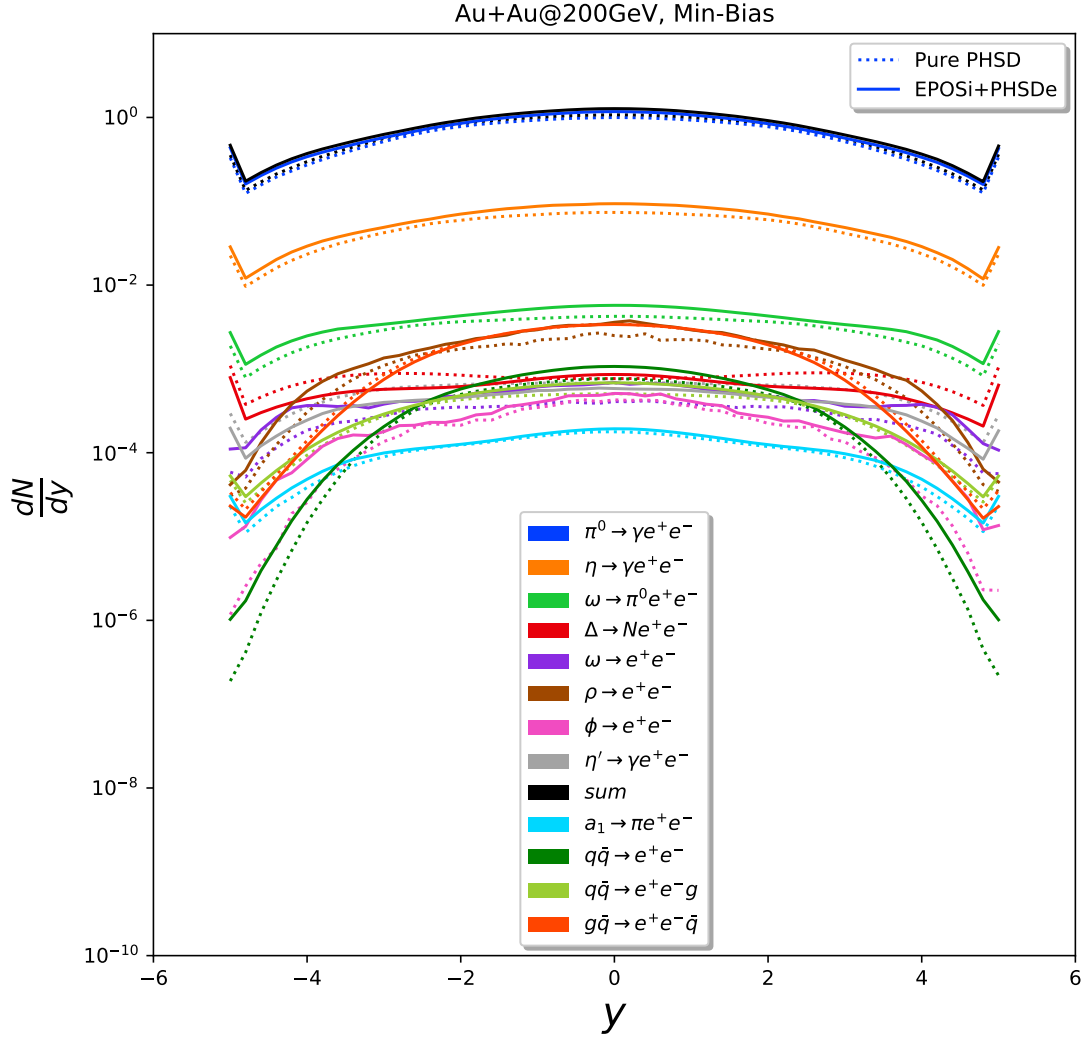


Figure 6.9: The rapidity spectra of dielectrons from pure PHSD in comparison to EPOSi+PHSDe in minimum-bias Au-Au collisions at 200 GeV. The different contributions are specified in the legend. In this plot, the heavy-flavor contributions (such as  $D\bar{D}$ ,  $B\bar{B}$ ,  $J/\psi$ , and  $\psi'$ ) have been skipped.

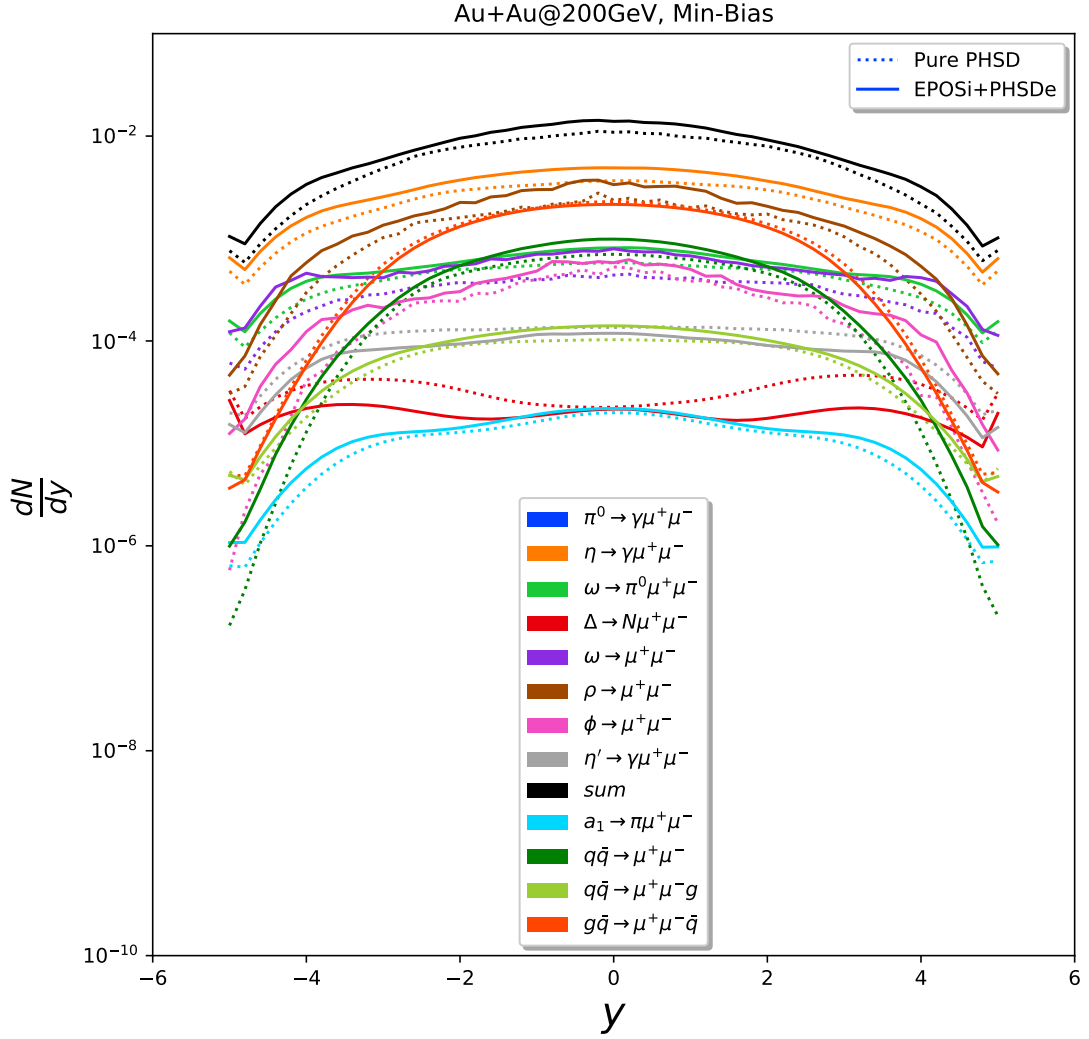


Figure 6.10: Same as Fig. 6.9 for dimuons.

## 6.2 Summary and conclusion

In this chapter, we investigated the dileptons enhancement, which is one of the electromagnetic probes to study QGP. We presented and compared the dileptons production results like invariant mass, transverse momentum, and rapidity distribution in EPOSi+PHSDe and pure PHSD.

We employed the non-equilibrium parton/hadron evolutions from PHSD in this study. PHSD incorporates the relevant off-shell dynamics of the vector mesons as well as the explicit partonic phase in the early hot and dense reaction region. In this model, the production channels for dileptons in HICs are separated into three different classes: i) hadronic production channels, ii) partonic production channels, and iii) the contribution from the semi-leptonic decay of heavy-flavor pairs. In EPOSi+PHSDe, the third class has not been yet taken into account.

From the invariant mass spectra, we saw that many hadronic sources contribute to

the low-mass dileptons spectrum, whereas the intermediate-mass range is dominated by the contribution from partonic interactions in both models. Comparing both models, one noticed that **EPOSi+PHSDe** has more contributions in the low-mass region while pure **PHSD** has more contributions in intermediate-mass. When we counted the heavy-flavor pairs channels like  $D\bar{D}$  and  $B\bar{B}$  in pure **PHSD**, we saw that the description of the total dileptons spectra is very good for invariant mass less than  $2.5 \text{ GeV}/c^2$  compared to the experimental data.

From transverse momentum and rapidity spectra plots, we saw that the total yield of dileptons production in **EPOSi+PHSDe** are above pure **PHSD**. This might be due to **EPOSi+PHSDe** having a bit more system expansion in the transverse plane than pure **PHSD**, resulting in a little bit more transverse flow, which then automatically translates into increased particle production, as we discussed in the previous chapter.

We had a deviation from the cocktail curves in our results compared to the experimental results. Ideally, our model would have the identical cocktail curves as an experiment, accounting for any particle contributions overlooked in our calculations. The electromagnetic probes in **EPOSi+PHSDe** are still being developed. We will look into other dileptons production channels, such as heavy-flavor pairs. The inclusive photon yield can also be studied in this model.



---

## CONCLUSION AND OUTLOOK

**QGP** is a hot and ultra-dense form of matter made of deconfined quarks and gluons produced by ultrarelativistic **HICs** at the **RHIC** and **LHC**. Different models, such as **EPOS** and **PHSD**, can be used to investigate the space-time evolution of such **HICs**. Their dynamics is complicated; thus, several stages should be addressed. The first is the primary scattering which defines to a large extent the matter distribution in the phase-space. The second stage concerns the evolution of the partonic system until the system is sufficiently dilute to hadronize. The **EPOSi+PHSDe** approach was introduced in this thesis, a new model that combines the initial conditions from **EPOS 4 (EPOSi)** with the space-time evolution of partonic and hadronic phases in **PHSD (PHSDe)**.

The results of the new approach tried to study the role of the initial condition and the role of space-time evolution in **HICs**. Although the initial conditions and matter evolutions in the **EPOS 4** and **PHSD** models are fundamentally different, we observed similarities in several observables at the end. So **EPOSi+PHSDe** is helpful, as the differences might be related to the initial conditions or evolutions. We saw the differences between **EPOSi+PHSDe** and **EPOS 4 (PHSD)** by comparing the two models with the same "initial conditions" ("evolutions") but different "evolutions" ("initial conditions").

Comparing the three models, **EPOS 4**, **EPOSi+PHSDe**, and pure **PHSD**, interesting results were found concerning their respective space-time evolutions and bulk matter observables for **Au-Au** collisions at 200 GeV/A. The results are the following:

To see the differences between these three models, we started by studying the radial expansions in the three models via energy density evolutions. From the energy density evolutions, we observed that the systems in **EPOSi+PHSDe** and pure **PHSD** expand slowly compared to **EPOS 4**, which expands strongly in the transverse plane. The system expansions drastically affect observables like transverse momentum ( $p_T$ ) and elliptic flow.

One of the key observables in our investigation is  $p_T$ . **EPOS 4** accurately reproduces data from charged particle spectra, particularly at intermediate  $p_T$  rates. This is because the system expands substantially in the transverse plane, resulting in a large transverse flow, which immediately translates to enhanced particle production at larger  $p_T$ . All of this is predicated on the assumption that the system thermalized quickly and that hydrodynamics can be used to simulate the following evolution. Most notably, large gradients (in energy density) at early periods translate into a large transverse flow in the case of a hydrodynamically expanding expansion.

In comparison to the experimental data and **EPOS 4**, **EPOSi+PHSDe** and pure **PHSD** are unable to reproduce sufficient particles at intermediate and high  $p_T$ . Because there is no assumption of equilibration in **EPOSi+PHSDe** and pure **PHSD**, it is necessary to evolve via parton-parton scatterings. However, obviously these interactions are not strong enough; there is no transverse expansion, and as a result, the shift of particles towards intermediate  $p_T$  values is missing. This provides a clear picture: the significant gradients in **EPOSi+PHSDe** and pure **PHSD** do not convert into the transverse flow, implying that the system does not reach equilibrium at an early stage.

We looked at flow anisotropies to confirm this. In **EPOS 4**, large asymmetries (via  $v_2$ ,  $v_3$ , and  $v_4$ ) are observed both at low and high  $p_T$ , very similar to the experimental data. However, in **EPOSi+PHSDe** and pure **PHSD**, only low  $p_T$  results agree with the data, whereas at high  $p_T$ , the values are far too low. This is somehow expected, since from  $p_T$  spectra we know already, that these two models show too little transverse flow, and transverse flow is a necessary condition to have asymmetric transverse flow. In general, **EPOSi+PHSDe** performs somewhat better than pure **PHSD** (for  $v_2$ ,  $v_3$ , and  $v_4$ ), while the radial flow is similarly bad in both models.

**With the current results, the first question of this thesis could be answered: "What is the difference between pure **EPOS** and pure **PHSD**?" The distinctions between these two models are related to their "evolutions", whereas differences in the initial conditions play a minor role. More precisely, the development of radial flow is fundamentally different, the partonic scatterings do not provide sufficient "thermalization".**

We compared also the dilepton enhancement results in **EPOSi+PHSDe** and pure **PHSD**. The results are the following:

Many hadronic sources from the invariant mass spectra contribute to the low-mass dileptons spectrum; in contrast, partonic interactions dominate the intermediate-mass range in [EPOSi+PHSDe](#) and pure [PHSD](#) models. Comparing the two models, we notice that [EPOSi+PHSDe](#) contributes more in the low-mass region, whereas pure [PHSD](#) contributes more in the intermediate-mass area. The total yield of dilepton productions in [EPOSi+PHSDe](#) is above pure [PHSD](#) in transverse momentum and rapidity spectra plots. It is because [EPOSi+PHSDe](#) has somewhat more system transverse expansion than pure [PHSD](#). The electromagnetic probes in [EPOSi+PHSDe](#) are still being developed.

**The perspectives of this work are already established:**

- Adding the heavy-flavor contributions such as  $D\bar{D}$ ,  $B\bar{B}$ ,  $J/\psi$ , and  $\psi'$  into [EPOSi+PHSDe](#) for studying the dilepton enhancement. Also, Studying the inclusive photon yield in the new approach.
- Employing the early hydrodynamical evolution from [EPOS](#) ([EPOSh](#)), then use the [PHSD](#) evolution ([PHSDe](#)) to study the production of particles in higher  $p_T$ .
- Checking the heavy-flavor particle behavior in [EPOSi+PHSDe](#) and comparing the results with two other models.
- Comparing [EPOSi+PHSDe](#) with different ranges energies from [RHIC](#) to [LHC](#) for various systems like [pp](#) and [Au-Au](#).



Le titre de cette thèse est "Dynamical Thermalization in Heavy Ion Collisions (HICs)", qui étudie le rôle de l'étape initiale concernant la dynamique des HICs en utilisant les modèles, EPOS et PHSD. Les HICs ultrarelativistes au RHIC et au LHC produisent une forme de matière chaude et ultra-dense composée de quarks et de gluons déconfinés, appelée QGP.

Différents modèles, comme EPOS et PHSD, peuvent être utilisés pour étudier l'évolution spatio-temporelle de ces HICs. Leur dynamique est compliquée; ainsi, plusieurs étapes doivent être abordées. La première est la diffusion primaire qui définit dans une large mesure la distribution de la matière dans l'espace des phases. La deuxième étape concerne l'évolution du système partonique jusqu'à ce que le système soit suffisamment dilué pour se hadroniser. L'approche EPOSi+PHSDe a été introduite dans cette thèse, un nouveau modèle qui combine les conditions initiales de EPOS 4 (EPOSi) avec l'évolution spatio-temporelle des phases partoniques et hadroniques dans PHSD (PHSDe).

Les résultats de cette nouvelle approche ont permis d'étudier le rôle de la condition initiale et le rôle de l'évolution spatio-temporelle dans le modèle HICs. Bien que les conditions initiales et les évolutions de la matière dans les modèles EPOS 4 et PHSD soient fondamentalement différentes, nous avons observé des similitudes dans plusieurs observables à la fin. Par conséquent, EPOSi+PHSDe est utile, car les différences pourraient être liées aux conditions initiales ou aux évolutions. Nous avons vu les différences entre EPOSi+PHSDe et EPOS 4 (PHSD) en comparant les deux modèles avec les mêmes "conditions initiales" ("évolutions") mais des "évolutions" différentes ("conditions initiales").

En comparant les trois modèles, EPOS 4, EPOSi+PHSDe et PHSD pur, des résultats intéressants ont été trouvés concernant leurs évolutions spatio-temporelles respectives et les observables de la matière en vrac pour les collisions Au-Au à 200 GeV/A. Les résultats sont les suivants:

Pour voir les différences entre ces trois modèles, nous avons commencé par étudier les expansions radiales dans les trois modèles via les évolutions de la densité d'énergie. À partir des évolutions de la densité d'énergie, nous avons observé que les systèmes de EPOSi+PHSDe et de PHSD pur se dilatent lentement par rapport à EPOS 4, qui se dilate fortement dans le plan transversal. Les expansions des systèmes affectent radicalement les observables comme le moment transversal ( $p_T$ ) et le flux elliptique.

L'une des observables clés de notre étude est  $p_T$ . EPOS 4 reproduit avec précision les

données des spectres de particules chargées, en particulier aux taux intermédiaires de  $p_T$ . Cela est dû au fait que le système se dilate considérablement dans le plan transversal, ce qui entraîne un flux transversal important, qui se traduit immédiatement par une production accrue de particules à des taux  $p_T$  plus élevés. Tout ceci repose sur l'hypothèse que le système s'est rapidement thermalisé et que l'hydrodynamique peut être utilisée pour simuler l'évolution suivante. Plus particulièrement, les grands gradients (en densité d'énergie) aux premières périodes se traduisent par un grand flux transversal dans le cas d'une expansion hydrodynamique.

Par rapport aux données expérimentales et à [EPOS 4](#), [EPOSi+PHSDe](#) et [PHSD](#) pur sont incapables de reproduire suffisamment de particules à des  $p_T$  intermédiaires et élevés. Parce qu'il n'y a pas d'hypothèse d'équilibrage dans [EPOSi+PHSDe](#) et [PHSD](#) pur, il est nécessaire d'évoluer via des diffusions parton-parton. Cependant, il est évident que ces interactions ne sont pas assez fortes ; il n'y a pas d'expansion transversale, et par conséquent, le déplacement des particules vers les valeurs intermédiaires de  $p_T$  est absent. Cela donne une image claire : les gradients significatifs de [EPOSi+PHSDe](#) et de [PHSD](#) pur ne se transforment pas en flux transversal, ce qui implique que le système n'atteint pas l'équilibre à un stade précoce.

Nous avons examiné les anisotropies d'écoulement pour le confirmer. Dans [EPOS 4](#), de grandes asymétries (via  $v_2$ ,  $v_3$ , et  $v_4$ ) sont observées à la fois à faible et à fort  $p_T$ , très similaires aux données expérimentales. Cependant, dans les [EPOSi+PHSDe](#) et les [PHSD](#) purs, seuls les résultats à faible  $p_T$  sont en accord avec les données, alors qu'à fort  $p_T$ , les valeurs sont beaucoup trop faibles. Ceci est en quelque sorte attendu, puisque d'après les spectres  $p_T$ , nous savons déjà que ces deux modèles présentent un flux transversal trop faible, et que le flux transversal est une condition nécessaire pour avoir un flux transversal asymétrique. En général, [EPOSi+PHSDe](#) est un peu plus performant que [PHSD](#) pur (pour  $v_2$ ,  $v_3$ , et  $v_4$ ), alors que le flux radial est aussi mauvais dans les deux modèles.

Avec les résultats actuels, il a été possible de répondre à la première question de cette thèse : "Quelle est la différence entre le [EPOS](#) pur et le [PHSD](#) pur?". Les distinctions entre ces deux modèles sont liées à leurs "évolutions", alors que les différences dans les conditions initiales jouent un rôle mineur. Plus précisément, le développement de l'écoulement radial est fondamentalement différent, les diffusions partoniques ne fournissent pas une "thermalisation" suffisante.

Nous avons également comparé les résultats du renforcement des dileptons dans le [EPOSi+PHSDe](#) et le [PHSD](#) pur. Les résultats sont les suivants:

De nombreuses sources hadroniques issues des spectres de masse invariante contribuent au spectre des dileptons de faible masse ; en revanche, les interactions partoniques dominent la gamme de masse intermédiaire dans les modèles [EPOSi+PHSDe](#) et [PHSD](#) pur. En comparant les deux modèles, nous remarquons que le modèle [EPOSi+PHSDe](#) contribue davantage dans la région de faible masse, alors que le modèle [PHSD](#) pur contribue davantage dans la région de masse intermédiaire. Le rendement total des productions de dileptons dans [EPOSi+PHSDe](#) est supérieur à celui de [PHSD](#) pur dans les tracés des spectres de moment transversal et de rapidité. C'est parce que [EPOSi+PHSDe](#) a une expansion transversale du système un peu plus importante que [PHSD](#) pur. Les sondes électromagnétiques de [EPOSi+PHSDe](#) sont encore en cours de développement.

Les perspectives de ce travail sont déjà établies:

- Ajout des contributions de saveur lourde telles que  $D\bar{D}$ ,  $B\bar{B}$ ,  $J/\psi$ , et  $\psi'$  dans [EPOSi+PHSDe](#) pour étudier le renforcement des dileptons. Etudier également le rendement inclusif en photons dans la nouvelle approche.
- En utilisant l'évolution hydrodynamique précoce de [EPOS](#) (EPOSh), puis en utilisant l'évolution de [PHSD](#) (PHSDe) pour étudier la production de particules dans des  $p_T$  plus élevés.
- Vérification du comportement des particules de saveur lourde dans le modèle [EPOSi+PHSDe](#) et comparaison des résultats avec deux autres modèles.
- Comparaison de [EPOSi+PHSDe](#) avec différentes gammes d'énergies de [RHIC](#) à [LHC](#) pour divers systèmes comme [pp](#) et [Au-Au](#).



# Appendices



## A.1 Kinematics in accelerators

We need to know about some kinematics variables such as light cone dynamics, hyperbola definition, transverse momentum, transverse mass, rapidity, pseudo-rapidity, and so on to compare our results from different simulations to the experimental data. I will go over a few variables I employed in my thesis.

### A.1.1 Light Cone dynamics

In a space-time diagram, the rule is that time is directed upwards while one or two spatial axes are located in the horizontal plane. Several fruitful concepts can be visualized in space-time diagrams, such as events, worldline, light cone, timelike and spacelike, see Fig. [A.1](#).

The points in the space-time diagram are known as events. A worldline is defined as a line that shows the position of a point-like material thing as a function of time. The tangent of the worldline at an event determines the four-velocity of the particle at this event. The light cone is known as plotting events related via null intervals in two spaces, and one-time dimension results in a light cone with two components, one future and one past of the event. An object can never be observed to move faster than light speed and outside the light cone.

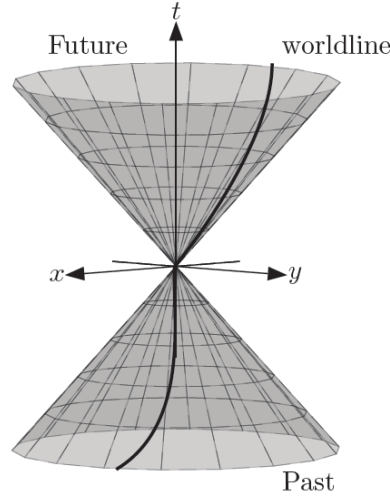


Figure A.1: Schematic representation of the light cone in the Minkowski space-time.

In Cartesian coordinates, one can describe Euclidean geometry with the line element  $ds^2 = dx^2 + dy^2 + dz^2$ , representing the extremely small distance between two nearby points. In the case of Minkowski space-time, one instead has four coordinates

$$(t, x, y, z) = (x^0, x^1, x^2, x^3) \quad (\text{A.1.1})$$

and a line element that takes the form

$$ds^2 = -dt^2 + dx^2 + dy^2 + dz^2. \quad (\text{A.1.2})$$

Here, the only distinct form that is different from Euclidean geometry is the  $-dt^2$  term; however, this yields some new features. Presently,  $ds^2$  can still be positive or zero, although it is sometimes negative.

If  $ds^2 < 0$ , in this case, the space-time interval  $ds^2$  is assumed to be timelike. On the other hand, if it is positive, the space-time interval  $ds^2$  is called spacelike.  $ds^2 = 0$  corresponds to two various situations, one  $dx^\mu$ , one  $dt^2 = dx^2 + dy^2 + dz^2 \neq 0$  indicates the distance is the same in time as it is in space; however,  $ds^2$  is still zero and one declares that this represents a null interval.

One can employ the Minkowski's coordinates, Eq. A.1.1, to define the light cone time coordinates as,

$$x^+ = x^0 + x^3, \quad x^- = x^0 - x^3, \quad x_\perp = [x^1, x^2]. \quad (\text{A.1.3})$$

One of the most profitable parameters in relativity is rapidity which can be computed as the relativistic velocity of particles in light-cone coordinates within the Lorentz boost,

$$y = \tanh^{-1} v, \quad (\text{A.1.4})$$

the velocity can be established as a function of energy  $E$  and scalar momentum  $|p|$ ,

$$y = \tanh^{-1} \frac{|p|}{E} = \frac{1}{2} \ln \left( \frac{E + |p|}{E - |p|} \right) \approx \frac{1}{2} \ln \left( \frac{E + |p_z|}{E - |p_z|} \right), \quad (\text{A.1.5})$$

where  $|p_z|$  means the momentum component along the beam axis. Pseudorapidity plays an important role in experimental particle physicists. It is an ordinarily utilized spatial coordinate defining the angle of a particle relative to the beam axis, which defines:

$$\eta = -\ln\left(\tan \frac{\theta}{2}\right), \quad (\text{A.1.6})$$

where  $\theta$  is the angle between the particle three-momentum  $\mathbf{p}$  and the positive direction of the beam axis. Pseudorapidity only depends on the polar angle of the particle's trajectory and not on the energy of particles. Pseudorapidity also can be written as a function of momentum like:

$$\eta = \frac{1}{2} \ln\left(\frac{|\mathbf{p}| + p_z}{|\mathbf{p}| - p_z}\right). \quad (\text{A.1.7})$$

In the limit, where the particle is moving close to the speed of light, or approximately the mass of the particles signifies negligible, one can expect  $m \ll |\mathbf{p}| \rightarrow \mathbf{E} \approx |\mathbf{p}| \rightarrow \eta \approx \mathbf{y}$ . Midrapidity is determined where pseudorapidity is near zero.

### A.1.2 Hyperbola definition

We should look at cones to better understand the hyperbola. When you cut a cone into multiple portions, you may get various forms. When a plane touches the surface of a single or double cone, a conic section is formed. The section is determined by the angle of intersection between the plane and the cone. The conic sections are as follows: Circles, Ellipses, Parabola, and Hyperbola.

A hyperbola is formed when a plane slices through the edges of a right circular double cone at an angle greater than the slope of the cone. It has two symmetrical components which look like two opposing bow-shaped curves. A hyperbola can also be described as the set of all points  $(x, y)$  in a coordinate plane whereby the difference of the distances between the foci and  $(x, y)$  is a positive constant. The foci are the two fixed points located inside each curve of a hyperbola, see Fig. A.2.

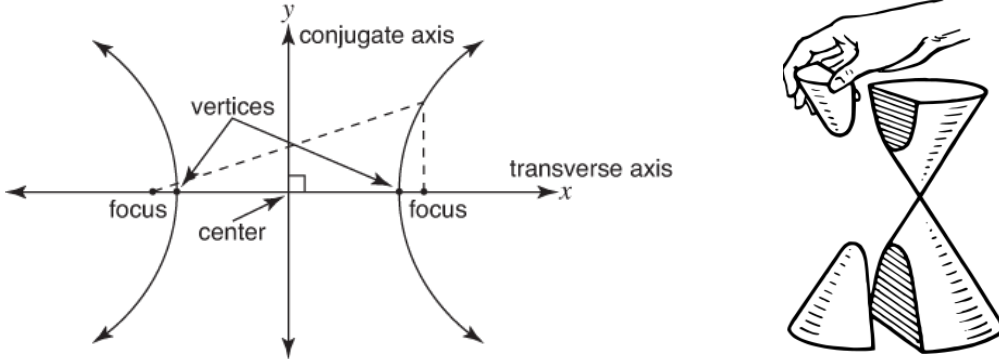


Figure A.2: Definition of hyperbola in cone.

### A.1.3 Transverse momentum and transverse mass

Transverse momentum  $p_T$  and transverse mass  $m_T$  are two essential variables that we consider. They determine in the transverse plane perpendicular to the beam line  $z$ . The transverse momentum can be calculated mathematically by

$$p_T = \sqrt{p_x^2 + p_y^2} = p \cos \theta. \quad (\text{A.1.8})$$

The momentum components in the transverse plane are  $p_x$  and  $p_y$ . In Eq. A.1.8,  $p$  denotes the particle's vector momentum, and  $\theta$  is the azimuthal scattering angle. The

variables  $p_T$  and  $m_T$  are interdependent. The relationship between momentum and energy can be written in natural units as

$$E^2 = m^2 + p^2, \quad (\text{A.1.9})$$

where  $p$  is the vector momentum. Therefore, the transverse mass can be defined as

$$m_T^2 = m^2 + p_x^2 + p_y^2 = E^2 - p_z^2, \quad (\text{A.1.10})$$

with invariant mass  $m$ . These variables are invariant in all frames when the Lorentz boost is performed in the  $z$ -direction.

In the following section, I will represent the transformation of momentum components and velocity between two various coordinates, Minkowski and Milne coordinates.

## A.2 Milne coordinates definition

Milne coordinates are determined and formulated as a function of the Minkowski real space-time coordinates to achieve hydrodynamic simulations in relativistic heavy-ion collisions as:

$$\text{Milne} : \begin{cases} \tau = \sqrt{t^2 - z^2} \\ x \\ y \\ \eta = \frac{1}{2} \ln\left(\frac{t+z}{t-z}\right), \end{cases} \quad \text{Minkowski} : \begin{cases} t = \tau \cosh \eta \\ x \\ y \\ z = \tau \sinh \eta. \end{cases} \quad (\text{A.2.1})$$

Additionally, the velocity vector in Milne coordinate is given by

$$u^\mu = \{u^\tau, u^x, u^y, u^\eta\} = \gamma\{1, \beta^x, \beta^y, \beta^\eta\}, \quad (\text{A.2.2})$$

where  $\gamma$ -factor is connected with the cell velocity, which measured as

$$\gamma = (1 - \beta_x^2 - \beta_y^2 - \tau^2 \beta_\eta^2)^{-\frac{1}{2}} = u^\tau. \quad (\text{A.2.3})$$

The transformation of three-dimensional velocity vector  $\beta$  between Milne and Cartesian coordinates determined by:

$$\text{Milne} : \begin{cases} \beta^x = \frac{v^x}{\cosh \eta - v^z \sinh \eta} \\ \beta^y = \frac{v^y}{\cosh \eta - v^z \sinh \eta} \\ \beta^\eta = \frac{1}{\tau} \frac{v^z \cosh \eta - \sinh \eta}{\cosh \eta - v^z \sinh \eta}, \end{cases} \quad (\text{A.2.4})$$

$$\text{Cartesian} : \begin{cases} v^x = \beta^x (\cosh \eta - v^z \sinh \eta) \\ v^y = \beta^y (\cosh \eta - v^z \sinh \eta) \\ v^z = \frac{\tau \beta^\eta \cosh \eta + \sinh \eta}{\tau \beta^\eta \sinh \eta + \cosh \eta}. \end{cases} \quad (\text{A.2.5})$$

With respect to the Jacobian matrix, one can compute the coordinate transformation of the four-velocity  $u^\mu$  between Milne coordinates and Cartesian coordinates as:

$$\text{Milne} : \begin{cases} u^\tau = \frac{\partial \tau}{\partial t} u^t + \frac{\partial \tau}{\partial z} u^z = \cosh \eta u^t - \sinh \eta u^z \\ u^x \\ u^y \\ u^\eta = \frac{\partial \eta}{\partial t} u^t + \frac{\partial \eta}{\partial z} u^z = \frac{-\sinh \eta}{\tau} u^t + \frac{\cosh \eta}{\tau} u^z, \end{cases} \quad (\text{A.2.6})$$

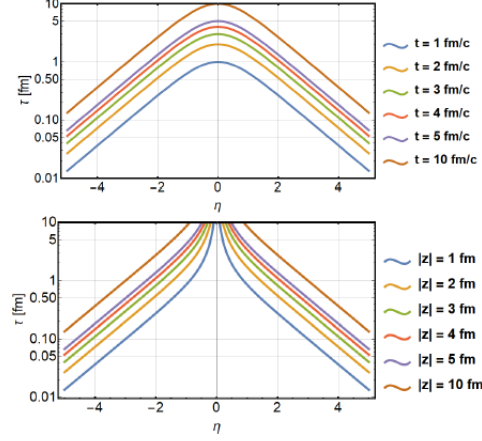


Figure A.4: Lines in the  $\tau - \eta$  plane for constant values of  $t$  and  $z$ .

$$\text{Cartesian : } \begin{cases} u^t = \frac{\partial t}{\partial \tau} u^\tau + \frac{\partial t}{\partial \eta} u^\eta = \cosh \eta u^\tau + \tau \sinh \eta u^\eta \\ u^x \\ u^y \\ u^z = \frac{\partial z}{\partial \tau} u^\tau + \frac{\partial z}{\partial \eta} u^\eta = \sinh \eta u^\tau + \tau \cosh \eta u^\eta, \end{cases} \quad (\text{A.2.7})$$

For a massive particle, the four-momentum is supplied by the particle's invariant mass  $m$  multiplied by the particle's four-velocity  $u^\mu$  in Milne coordinate,

$$p^\mu = m u^\mu = (p^\tau, p^x, p^y, p^\eta). \quad (\text{A.2.8})$$

Similar to Eq. A.2.6 and Eq. A.2.7, one can obtain four-momentum components,

$$\begin{cases} p^\tau = \cosh \eta p^t - \sinh \eta p^z \\ p^\eta = -\frac{\sinh \eta}{\tau} p^t + \frac{\cosh \eta}{\tau} p^z. \end{cases} \quad (\text{A.2.9})$$

As illustrated in Fig. A.3 and Fig. A.4, one can see the trajectories in the  $t - z$  plane for constant values of  $\eta$  and  $\tau$  and, trajectories in the  $\tau - \eta$  plane for constant values of  $t$  and  $z$  (these figures are taken from [125]).

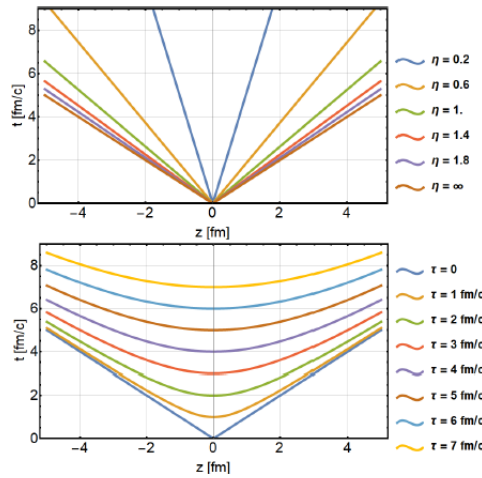


Figure A.3: Lines in the  $t - z$  plane for constant values of  $\tau$  and  $\eta$ .



## APPENDIX B

### REQUIRED CODE IN EPOSI+PHSDE APPROACH

#### B.1 Input file

Generally, in each classification, to have one complete collision simulation for the various systems, one requires the input file that recognizes the collision's specific characteristics. In the [EPOS](#) framework, we also have particular input file which runs the simulation by specific command as,

```
EPOS -eee A name - optnsfile 1 N
```

where A can be labeled as "rp" or "ro/rp", "rq", "my", "ma" for [EPOSi+PHSDe](#), pure [PHSD](#), [EPOS+hydro](#) (simulation with hydro evolution), and [EPOS-hydro](#) (simulation without hydro evolution) respectively. N denotes the number of jobs. The principal optns file employed in our work is the below optns file (named gg2.optns) which includes the below parameters for [Au-Au](#) collisions at 200 GeV.

```
----- gg2.optns -----  
- application hadron  
- set laproj 79 set maproj 197 set latarg 79 set matarg 197 set ecms 200  
- set istmax 50 set phimin 0 set phimax 0 set centrality 0  
- set ninicon 1 set iranphi 1 ftime on set taurem 0  
- xinput KWt/iclau.optns  
- nodecays 110 end  
- #if1 rp core rope set corcor(4) 0.50 set yrrope 0.9 set ylope 2.3 set iPHSD 2 set nfull  
1 set ninicon 1 set nfreeze 20 set modsho 1 set centrality -1 #fi  
- #if1 ro set corcor(4) 0.10 set ninicon -20 core rope set yrrope 0.0 set ylope 2.5 set  
iPHSD 1 set nfull 1 set nfreeze 1 set modsho 100 set centrality -1 #fi  
- #if1 rq core off set iPHSD 9 set nfull 1 set ninicon 20 set nfreeze 1 set modsho 1 set  
centrality -1 #fi  
- #if1 ma core off hydro x3ffoff hacas off set nfull 1 set nfreeze 1 set modsho 100 set  
centrality -1 #fi  
- #if1 my core full hydro x3ff hacas full set nfull 1 set nfreeze 5 set modsho 100 set  
centrality -1 set ijetfluid 1 #fi  
- echo off  
- fillTree(C1)  
- getTree(160,20000)  
- #if3 -  
- B5->defineBins%(0,5;5,10;10,20;30,40;50,60;70,80;80,90;90,100)  
ZM->defineCentrality(B5,C1)  
- xinput ../optns/iKWWhd/ihd.optns
```

```
- xinput ../optns/pp/irhic.optns
- xinput ../optns/pp/ietc.optns
- xinput ../optns/pp/igg2.optns
- xinput ../optns/gs/aaa.optns
- xinput ../optns/gs/igg200a.optns
- B2->defineBins(10,12;7,10) ZJ->defineRanges(B2)
- B3->defineBins- plot HydroEpsilon plot HydroFoEpsilon plot HydroFoRadius plot HydroFoRadVelocity
- #fi
- #if3 1
- xinput ../optns/pp/igg1.optns
- #fi
```

In this optns file, we have some lines which start with `#if` condition. In the following, the A (rp, rq, my, ma) argument is determined for various simulations. It will run with the options specified in this line.

The options are:

- laproj and maproj or latarg and matarg: atomic and mass numbers of projectile or target.
- ecms: center of mass energy.
- istmax: compose particles with istptl (status) up to 50 into root files.
- phimin and phimax: set the range of impact parameter angle.
- iranphi: make rotation of fluid in inicon, so that the axis is along y-axis
- ftime on: use formation time for string decay.
- taurem: formation time of particles in EPOS.
- bminim and bmaxim: minimum and maximum impact parameter.
- core rope: active rope segments from core part in EPOSi+PHSDe.
- core: active or not the core-corona procedure in pure EPOS and pure PHSD.
- hydro: active or not the hydro evolution for the core part in pure EPOS ('x3ff' when the core is 'on' and 'x3ffoff' when the core is 'off').
- corcor(4): sets the spatial distributions of partons applicable to the position of the nucleon. Large corcor(4) indicates more spread, more distance from the nucleon center.
- yrrope: radial boost of rope segments in EPOSi+PHSDe.
- ylrope: longitudinal boost of rope segments in EPOSi+PHSDe.
- iphsd: characteristic of simulations (1,...,8: EPOSi+PHSDe, 9: pure PHSD).
- nfull: number of initial evolutions in one simulation.
- nfreeze and ninicon: number of different final evolutions from the same initial evolution in pure EPOS and number of parallel events in EPOSi+PHSDe .
- modsho: establishes after how many events which event is currently simulated.
- centrality: represent the centrality range for various impact parameters in KWt/i-clau.optns (-1: generate the centrality randomly between 0 and 100).
- hacas: hadronic cascade after the core-corona procedure.
- ijetfluid: interaction of particles with the fluid formed in the core (0: no hydro, 1: hydro).
- nodecays: permits to block the certain resonances with particles' ID that defined in KWt/idt.dt.
- echo: print or not the entire steps of simulations on screen.
- print\*2: print all the particles with their parents and characteristics (like coordinates, momenta, status, type, etc) in different tables like before fragmentation, after fragmentation, and final decay in histo file.
- xinput: compare the new simulation with former ones (with their optns file) and real

data.

## B.2 Relationship between centrality classes and impact parameters

In [EPOS 4](#), the relation between centrality classes and impact parameters are defined based on table for [Au-Au](#) collisions at 200 GeV in `KWt/iclAuAu200.optns`.

Table B.1: The relationship between centrality classes (C) and impact parameters (b) for Au-Au collision at 200 GeV.

Centrality	b (fm)	Centrality	b (fm)	Centrality	b (fm)
0	minimum bias	7 (30-35%)	8.27-8.92	14 (65-70%)	12.16-12.62
1 (0-5%)	0-3.37	8 (35-40%)	8.92-9.54	15 (70-75%)	12.62-13.07
2 (5-10%)	3.37-4.78	9 (40-45%)	9.54-10.12	16 (75-80%)	13.07-13.51
3 (10-15%)	4.78-5.85	10 (45-50%)	10.12-10.67	17 (80-85%)	13.51-13.98
4 (15-20%)	5.85-6.75	11 (50-55%)	10.67-11.19	18 (85-90%)	13.98-14.50
5 (20-25%)	6.75-7.55	12 (55-60%)	11.19-11.69	19 (90-95%)	14.50-14.76
6 (25-30%)	7.55-8.27	13 (60-65%)	11.69-12.16	20 (95-100%)	14.76-15.23

## B.3 Construction of the color flow diagram in EPOS code

To generate string segments from a cut ladder in [EPOS](#), we employ subroutines `psreti`, `psjarr`, and `pshot` in `KW/rsh.f`. We may follow the technique to construct color flow diagrams by putting some print statements in different places in these subroutines. We have one contribution between projectile and target, as shown in [Fig. B.1](#), with  $iqq = 0$  (sea-sea) and  $jqj = 2$  (gluon-quark interaction after soft emission), see [table 2.1](#). It signifies that the gluon initiates the space-like cascade on the projectile side and the quark on the target side. The color orientation is always from anti-quark to quark.

It is necessary to use some variables to complete the color flow diagrams, such as `"jort"`, `"jj"`, `"ncr"`, `"nci"`, and `"ncj"` by following and printing the parameters inside the `"if(ish.ge.4)then"` condition in the `KW/rsh.f/psreti` subroutine. `jort` is the color orientation for gluons (if `jort=1`, evolution begins with anti-quarks, and if `jort=2`, evolution starts from quarks). Starting evolution is determined by `jj`; if `jj=1`, evolution begins on the projectile side, whereas if `jj=2`, evolution begins on the target side. The time-like cascade is created by `ncr` (which is the color connection of partons), while the color connection `nci` refers to a space-like cascade. I will explain the color connection of partons based on [Fig. B.1](#) for the sake of clarity.

We have two numbers for gluons in the case of `nci=[a b]` because gluons have connections on both sides, such as gluon number 13 (`nci=[15 8]`), but only one number for quarks or anti-quarks since they only have connections on one side, such as parton number 3 or 2 (`nci=[3 0]`). We also have two numbers in the case of `ncj=[a b]`, where `"a"` is an anti-quark connection, and `"b"` is a quark connection like parton number 6 (`ncj=7 2`), indicating that parton number 7 is gluon but comes from anti-quark.

The red line in the diagram is connected to the Born process and leads to the completion of the procedure and production of the appropriate string segments (or kinky

strings) such as  $D^+$ ,  $k^+$ ,  $\pi^-$  and  $\bar{D}^0$ .

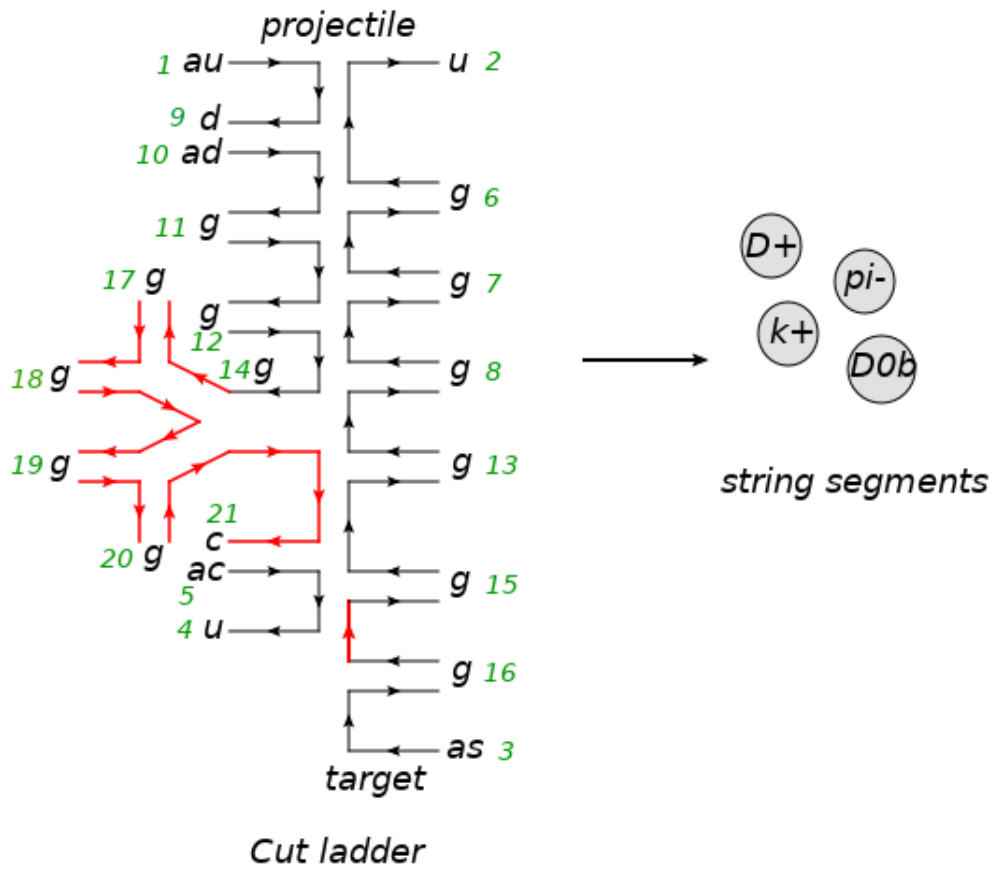


Figure B.1: String segments production from cut ladder.

1	The EPOS and PHSD stages to investigate the entire space-time evolution of matter in HICs. The new approach is called EPOSi+PHSDe since it integrates the initial conditions of EPOS (EPOSi) with the evolution of matter in a non-equilibrium transport approach (PHSDe). . . . .	4
1.1	Summary of measurements of $\alpha_s$ as a function of the momentum transfer $Q$ . The respective degree of QCD perturbation theory used in the extraction of $\alpha_s$ is indicated in brackets (NLO: next-to-leading order; NNLO: next-to-next-to leading order; res. NNLO: NNLO matched with resummed next-to-leading logs; N <sup>3</sup> LO: next-to-NNLO) [7]. . . . .	9
1.2	Phase diagram of nuclear matter. . . . .	11
1.3	Exposition of QGP space-time evolution. . . . .	12
1.4	Two heavy ions before the collision with impact parameter $b$ (l.h.s). The spectator nucleons remain unaffected while particle production takes place in the participants' zone (r.h.s) [37]. . . . .	14
1.5	The measured charged-particle multiplicity distribution in the STAR experiment in $ \eta  < 0.5$ for Au-Au collisions at 62.4 GeV and 200 GeV [38]. The shaded regions indicate the centrality bins used in the analysis. The 200 GeV data are scaled by a factor 5 for clarity. . . . .	15
1.6	Nuclear modification factor of several mesons in the central (0–20%) Au-Au collisions [43] in the PHENIX experiment. . . . .	17
1.7	A comparison of the nuclear modification factors for central (0 – 5%) Pb-Pb and p-Pb collisions measured by ALICE and CMS [44]. . . . .	17
1.8	$R_{AA}$ of prompt $D_s^+$ and non-strange $D$ mesons (average of $D^0$ , $D^+$ and $D^{*+}$ ) in the 0-10% centrality class, compared to TAMU model predictions [47]. . . . .	18
1.9	Nuclear modification factor $R_{AA}$ of $J/\psi$ as a function of the number of participant nucleons $N_{part}$ in the central (0–10%) Au-Au collisions at $\sqrt{s_{NN}} = 200$ GeV [49]. . . . .	19
1.10	Almond shaped interaction volume after a non-central collision of two nuclei. The spatial anisotropy with respect to the x-z plane (reaction plane) translates into a momentum anisotropy of the produced particles [54].	19
1.11	Measured directed flow as a function of space-time rapidity $\eta$ of Au-Au collisions at $\sqrt{s_{NN}} = 19.6, 62.4, 130,$ and $200$ GeV averaged over centrality (0 – 40%) from the PHOBOS experiment [56]. . . . .	20

1.12	Elliptic flow as a function of pseudorapidity $\eta$ for charged hadrons in minimum-bias Au-Au collisions at $\sqrt{s_{NN}}=130$ GeV (open triangles) and 200 GeV (closed triangles). One sigma statistical errors are shown as the error bars. Systematic errors (90% C.L.) are shown as gray boxes only for the 200 GeV data [59]. . . . .	21
1.13	(Color online) The final-flow coefficients $v_n$ as a function of impact parameter $b$ [60] in Au-Au collisions at 200 GeV. . . . .	21
1.14	(Color online) Strange particles (Kaon $K$ (l.h.s), and Omega $\Omega$ (r.h.s)) yields to pion ratio versus multiplicity $\langle dn/d\eta(0) \rangle$ , for different contributions from the EPOS 3 simulations [62], and different systems (pp, p-Pb, and Pb-Pb). The green dashed-dotted, blue dotted, yellow dashed, red full, and blue triangles are related to particles from the core only (core), particles from corona only (corona), particles from core and corona (co-co), all particles with hadronic cascade (full), and particles from pure string decay, respectively. The thin, intermediate, and thick lines refer to pp, p-Pb, and Pb-Pb collisions. The results compared to the ALICE data with open circles (pp), open squares (p-Pb), and open stars (Pb-Pb) from [63–68]. . . . .	23
1.15	Photon production as a function of transverse momentum $p_T$ spectrum from PHSD for minimal bias Au-Au collisions at $\sqrt{s_{NN}}= 200$ GeV at midrapidity $ y  < 0.35$ [74]. Left: (color online) the channel decomposition of the inclusive photon $p_T$ spectrum. Right: (color online) direct photons (sum of all photon production channels except the $\pi$ - and $\eta$ -mesons decays) from PHSD approach (red solid line) in comparison to the PHENIX experiments [76]. The channel description is given in the legend. . . . .	24
1.16	The invariant mass spectra of dielectrons from PHSD [83] in comparison to the STAR data in Au-Au collisions from $\sqrt{s_{NN}} = 200$ GeV [84]. The total yield is displayed in terms of the blue lines while the different contributions are specified in the legends. Note that the contribution from $J/\psi$ and $\psi'$ decays are not included in the PHSD calculations. . . . .	26
1.17	Diagram showing the structure of a proton-proton collision, where the different colours indicate the different stages involved in event generation [85]. Green, blue, deep pink and brown colors are related to parton shower, hadronization, underlying event, and particle decays, respectively. . . . .	27
2.1	Pedigree of EPOS by year. . . . .	32
2.2	$e^-p$ scattering in the center-of-mass frame and the corresponding lowest-order Feynman diagram. . . . .	33
2.3	Multiple pomeron exchange representation in the GRT. . . . .	37
2.4	Schematic representation of the proton-proton scattering with multiple pomeron exchange (red lines) between partons (green lines) in the PBGRT. . . . .	39
2.5	Representation of the elastic parton ladder . . . . .	39
2.6	The two elements of the multiple scattering theory: cut ladders (dashed red lines), represent the inelastic interactions, and uncut ladders (red lines) show the elastic interactions in nucleus-nucleus collision. . . . .	40
2.7	Left: hadron production from a cut ladder (normal hadronization) and two cut ladders interaction (collective hadronization). Right: the complete picture, including remnants. The remnants are an important source of particle production at RHIC energies. [115]. . . . .	40
2.8	Different possibilities to build the color connection diagram via the semi-hard and hard contribution. . . . .	41

2.9	Color flow diagram for two pomerons exchange without initial- and final-state cascade and gluon-gluon scattering. . . . .	42
2.10	The ratios of core, corona, and core+corona to core+corona as a function of transverse momentum spectra for identified particles in Au-Au collisions at $\sqrt{s_{NN}} = 200$ GeV in mid-rapidity region $ \eta  < 1$ . For each particle, the transverse momentum spectra for most central (0-5%), mid-central (20-40%), mid-peripheral (60-80%), and most peripheral ( $> 80\%$ ) collisions are plotted. The green, red, and blue curves represent the core, corona, and core+corona productions, respectively. . . . .	43
3.1	The closed time contour in the Keldysh formalism [130]. The time $t_1$ lies on the chronological (+) branch and the time $t_2$ lies on the antichronological (-) branch. . . . .	49
3.2	Illustration of fragmentations in the String Model. . . . .	54
3.3	(Left) The Lund fragmentation function has been plotted as a function of the energy fraction $x$ for various amounts of transverse masses $0.1\text{GeV}/c^2 \leq m_t \leq 2\text{GeV}/c^2$ . (Right) Space-time evolution of pre-hadron production in the Lund string model. . . . .	55
3.4	Schematic representation of the string formation and decay from the initial baryon. The string, which contains quarks and diquarks, is linked to the color electric field, which produces hadrons after the formation time $\tau_f$ . . . . .	56
3.5	Left: (color lines) the effective quark (a) and gluon (b) masses $M$ and widths $\gamma$ as a function of the temperature $T$ for different $\mu_B$ . The vertical dashed lines correspond to the DQPM $\mu_B$ -dependent critical temperature $T_c(\mu_B)$ [150]. Right: (color lines) the scaled pressure $P(T)/T^4$ (pink line), entropy density $s(T)/T^3$ (red line), scaled energy density $\varepsilon(T)/T^4$ (blue line), and interaction measure $I(T)/T^4$ (orange line), from the DQPM [150] in comparison to the IQCD results from Ref. [152] (full dots) for $\mu_B = 0$ (a) and $\mu_B = 400$ MeV (b). . . . .	58
3.6	The DQPM scalar mean field $U_s$ for quarks and antiquarks as a function of the scalar density $\rho_s$ . The figure is taken from Ref. [147] . . . . .	59
4.1	Nuclear density as a function of nuclear radius. Solid curves show nuclear density distribution for gold (Au) and copper (Cu) nuclei. The positions of nucleons are sampled according to the Woods-Saxon distribution with default parameter sets. The diffusenesses (a) are shown, delimited by vertical dotted lines [157]. . . . .	62
4.2	Coordinate determination of projectile and target nucleons by Wood-Saxon distribution (l.h.s), and hard sphere without surface thickness (r.h.s) for semi-peripheral Au-Au collisions at 200 GeV. . . . .	62
4.3	The projectile and target participants and their corresponding string origins (pomerons). . . . .	63
4.4	The sketch of initialization in EPOS based on the multiple pomerons exchange. Pomerons are formed from the interaction of neutrons (n) from projectile and target sides. The pomerons convert into several chains of partons (COP), and then the COP is split into string segments based on the color flow diagram. The first and second numbers in parentheses represent the particle's status (istptl) and type (ityptl) (I will discuss these variables later). . . . .	64
4.5	The production of string segments at given $\tau$ on the hyperbola from the string origins (pomerons) in the overlapping area based on the color flow diagram (CFD). . . . .	64

4.6	Production of particles on the hyperbola in EPOS. Participants from projectile and target sides (l.h.s). Core (dense region) and corona particles (r.h.s). . . . .	65
4.7	From string segments to cluster formation on the hyperbola at given $\tau$ in EPOSi+PHSDe. String segments on the hyperbola with identifying the overlapping string segments region (upper panel), separating rope segments and corona parts (middle panel), and cutting rope segments into several clusters (lower panel). . . . .	67
4.8	Distribution of clusters in the rapidity space. The clusters decay into core pre-hadrons based on the microcanonical decay. . . . .	68
4.9	Momentum (l.h.s) and rapidity (r.h.s) distributions of core pre-hadrons from the microcanonical decay of clusters. . . . .	69
4.10	Schematic representation of final rapidity distribution of pre-hadrons. . . . .	69
4.11	Formation of the pre-hadrons on the hyperbola in EPOS at given $\tau$ . . . . .	70
4.12	The same as Fig. 4.11 for the central Au-Au collision at 200 GeV. . . . .	70
4.13	Extrapolation back in time procedure of core and corona pre-hadrons to the start time of PHSD. . . . .	71
4.14	The schematic depiction of the final places of core and corona pre-hadrons after extrapolation at the start time of the PHSD evolution. . . . .	72
4.15	Schematic representation of pre-hadrons in transverse plane in EPOS (l.h.s) and PHSD (r.h.s). The simulation was done for semi-peripheral Au-Au collision at 200 GeV. . . . .	73
4.16	Schematic representation of pre-hadrons in transverse plane in EPOS (l.h.s) and PHSD (r.h.s). The simulation was done for semi-peripheral Au-Au collision at 200 GeV with melting condition. . . . .	74
4.17	The space-time evolution of baryons, mesons, and partons in EPOSi+PHSDe for semi-peripheral Au-Au collision at 200 GeV. . . . .	75
4.18	Eccentricity as a function of time for baryons (green curve), mesons (blue curve), and partons (red curve) with the same collision as Fig. 4.17. . . . .	76
5.1	Distribution of events as a function of impact parameter to determine the centrality bins from most central (0-5%) to most peripheral (80-X%) Au-Au collisions in EPOS 4 analysis. . . . .	80
5.2	Time evolution of the energy density in the transverse plane (at $z=0$ ) for Au-Au collisions at 200 GeV with an impact parameter of 7 fm, for three models, considering events with the same initial matter distribution (at 1.7fm/c). We show from left to right EPOS 4, EPOSi+PHSDe, and pure PHSD models, and from top to bottom the times (in fm/c) 0.5, 1.7, 2.5, 3.7, 5.3. . . . .	82
5.3	Same as Fig. 5.2, continuing the time evolution of the energy density for (from top to bottom, in fm/c) 9.4, 11.0, 12.2, 14.2, 16.3. . . . .	83
5.4	Invariant yield as a function of transverse mass for $\pi^\pm$ for Au-Au collision at $\sqrt{s_{NN}}=200$ GeV at mid-rapidity ( $ y  < 0.5$ ) in three different simulations: EPOS 4 (left panel), EPOSi+PHSDe (middle panel), and pure PHSD (right panel). The different transverse mass spectra are plotted with different centrality ranges 0-5%, 5-10%, 10-20%, 20-30%, 30-40%, 40-50%, 50-60%, 60-70%, 70-80% from top to bottom in each plot. All the results compared to the STAR experimental data [160] with the black points. All curves and experimental data are scaled by $2 * 10^{-n}$ starting from the top most curve with $2 * 10^0$ . . . . .	85

- 5.5 Invariant yield as a function of transverse mass for  $K^\pm$  for Au-Au collision at  $\sqrt{s_{NN}} = 200$  GeV at mid-rapidity ( $|y| < 0.5$ ) in three different simulations: EPOS 4 (left panel), EPOSi+PHSDe (middle panel), and pure PHSD (right panel). The different transverse mass spectra are plotted with different centrality ranges 0-5%, 5-10%, 10-20%, 20-30%, 30-40%, 40-50%, 50-60%, 60-70%, 70-80% from top to bottom in each plot. All the results compared to the STAR experimental data [160] with the black points. All curves and experimental data are scaled by  $2 * 10^{-n}$  starting from the top most curve with  $2 * 10^0$ . . . . . 86
- 5.6 Invariant yield as a function of transverse mass for proton ( $p$ ), and antiproton ( $\bar{p}$ ) for Au-Au collision at  $\sqrt{s_{NN}} = 200$  GeV at mid-rapidity ( $|y| < 0.5$ ) in three different simulations: EPOS 4 (left panel), EPOSi+PHSDe (middle panel), and pure PHSD (right panel). The different transverse mass spectra are plotted with different centrality ranges 0-5%, 5-10%, 10-20%, 20-30%, 30-40%, 40-50%, 50-60%, 60-70%, 70-80% from top to bottom in each plot. All the results compared to the STAR experimental data [160] with the black points. All curves and experimental data are scaled by  $2 * 10^{-n}$  starting from the top most curve with  $2 * 10^0$ . . . . . 87
- 5.7 Pion  $\pi^\pm$ , kaon  $K^\pm$ , proton  $p$ , antiproton  $\bar{p}$ , and net proton  $p - \bar{p}$  rapidity densities (from top to bottom) for the 5% most central Au-Au collisions at  $\sqrt{s_{NN}} = 200$  GeV in three different simulations: EPOS 4 (left panel), EPOSi+PHSDe (middle panel), and pure PHSD (right panel). The kaon yields were multiplied by 4 for clarity. All the results compared to the BRAHMS experimental data [162, 163] with the black points. . . . . 89
- 5.8 Charged particle multiplicities ( $dN_{ch}/d\eta$ ) as a function of pseudorapidity ( $\eta$ ) in Au-Au collisions at  $\sqrt{s_{NN}} = 200$  GeV for different simulations, EPOS 4 (top panel), EPOSi+PHSDe (middle panel), and pure PHSD (lower panel) from central to semi-peripheral collisions in each plot from top to bottom, 0-5%, 5-10%, 10-20%, 20-30%, 30-40%, and 40-50%. The experimental data are taken from BRAHMS [165] with black points. . . . . 90
- 5.9 Invariant yield of  $\pi^\pm$ ,  $K^\pm$ , proton  $p$ , and antiproton  $\bar{p}$  as a function of transverse momentum  $p_T$  at mid-rapidity ( $|y| < 0.5$ ) in Au-Au collisions at  $\sqrt{s_{NN}} = 200$  GeV from most central (0-10%) to most peripheral (60-92%) collisions, from top to bottom in each plot, in different simulations, EPOS 4 (left panel), EPOSi+PHSDe (middle panel), and pure PHSD (right panel). The experimental data are taken from PHENIX with black symbols [166]. All curves and experimental data are scaled by  $10^{-n}$  starting from the top most curve with  $10^0$ . . . . . 92
- 5.10 Pions  $\pi^\pm$  transverse momentum spectra at selected rapidities (in each plot from top to bottom, from  $-0.1 < y < 0$  to  $3.4 < y < 3.66$ ) from central (0-5%) Au-Au collisions at  $\sqrt{s_{NN}} = 200$  GeV in different simulations, EPOS 4 (left panel), EPOSi+PHSDe (middle panel), and pure PHSD (right panel). There is no weak decays contribution in these measurements. The results compared to the BRAHMS experiment [162] with black points. The experimental data and simulation's results are scaled by  $10^{-n}$  and  $(1/dy) * 10^{-n}$ , respectively, starting from the top most curve with  $10^0$ . . . . . 94

5.11	Kaons $K^\pm$ transverse momentum spectra at selected rapidities (in each plot from top to bottom, from $-0.1 < y < 0$ to $3.2 < y < 3.4$ ) from central (0-5%) Au-Au collisions at $\sqrt{s_{NN}} = 200$ GeV in different simulations, EPOS 4 (left panel), EPOSi+PHSDe (middle panel), and pure PHSD (right panel). There is no weak decays contribution in these measurements. The results compared to the BRAHMS experiment [162] with black points. The experimental data and simulation's results are scaled by $10^{-n}$ and $(1/dy) * 10^{-n}$ , respectively, starting from the top most curve with $10^0$ . . . . .	95
5.12	Proton ( $p$ ), anti-proton ( $\bar{p}$ ) transverse momentum spectra at selected rapidities (in each plot from top to bottom, from $-0.1 < y < 0.1$ to $2.7 < y < 3.1$ ) from central (0-5%) Au-Au collisions at $\sqrt{s_{NN}} = 200$ GeV in different simulations, EPOS 4 (left panel), EPOSi+PHSDe (middle panel), and pure PHSD (right panel). The results compared to the BRAHMS experiment [163] with black points. The experimental data and simulation's results are scaled by $10^{-n}$ and $(1/dy) * 10^{-n}$ , respectively, starting from the top most curve with $10^0$ . . . . .	96
5.13	Invariant yield of $\Lambda$ , $\bar{\Lambda}$ , $\Xi^-$ , $\bar{\Xi}^+$ , $K_S^0$ , and $\Omega^- + \bar{\Omega}^+$ as a function of transverse momentum $p_T$ at mid-rapidity in Au-Au collisions at $\sqrt{s_{NN}}=200$ GeV from most central (0-5%) to peripheral collisions (60-80%), from top to bottom in each plot, in different simulations, EPOS 4 (left panel), EPOSi+PHSDe (middle panel), and pure PHSD (right panel). The experimental data are taken from STAR with black points [170]. The experimental data and simulation's results are scaled by $10^{-n}$ and $(1/dy) * 10^{-n}$ , respectively, starting from the top most curve with $10^0$ . . . . .	98
5.14	Invariant yields for charged hadrons as a function of $p_T$ for 6 centrality bins (0-6%, 6-15%, 15-25%, 25-35%, 35-45%, and 45-50%) in a rapidity range of $0.2 < y < 1.4$ in Au-Au collisions at $\sqrt{s_{NN}}=200$ GeV in different simulations, EPOS 4 (upper panel), EPOSi+PHSDe (middle panel), and pure PHSD (lower panel). The experimental data are taken from PHOBOS with black points [172]. The experimental data and simulation's results are scaled by $10^{-n}$ and $(1/dy) * 10^{-n}$ , respectively, starting from the top most curve with $10^0$ . . . . .	99
5.15	Sketch of a non-central HICs in reaction and transverse planes [184]. . . . .	101
5.16	Differential elliptic flow ( $v_2$ ) of charged hadrons, $\pi$ , $K$ , and $p$ , at mid-rapidity for Au-Au collisions at $\sqrt{s_{NN}}=200$ GeV for different centrality bins. Blue, red, green colors, and dots indicate EPOS 4, EPOSi+PHSDe, pure PHSD results, and PHENIX experimental data [189], respectively. . . . .	104
5.17	Differential triangular flow ( $v_3$ ) of charged hadrons, $\pi$ , $K$ , and $p$ , at mid-rapidity for Au-Au at $\sqrt{s_{NN}}=200$ GeV for different centrality ranges. Blue, red, green colors, and dots indicate EPOS 4, EPOSi+PHSDe, pure PHSD results, and PHENIX experimental data [189], respectively. . . . .	105
5.18	Differential quadrangular flow ( $v_4$ ) of charged hadrons, $\pi$ , $K$ , and $p$ , at mid-rapidity for Au-Au at $\sqrt{s_{NN}}=200$ GeV for different centrality ranges. Blue, red, green colors, and dots indicate EPOS 4, EPOSi+PHSDe, pure PHSD results, and PHENIX experimental data [189], respectively. . . . .	106
5.19	Elliptic flow as a function of pseudorapidity ( $v_2(\eta)$ ) for charged hadrons in Au-Au collisions at $\sqrt{s_{NN}}=200$ GeV for different centrality classes, ranging from central to semi-peripheral and minimum bias collisions ( a): 3-15%, b): 15-25%, c): 25-50%, and d): minimum bias). Blue, red, green colors, and dots indicate EPOS 4, EPOSi+PHSDe, pure PHSD results, and PHOBOS experimental data [59], respectively. . . . .	107

5.20	Elliptic flow ( $v_2( \eta  < 1)$ ) as a function of the number of participants ( $N_{part}$ ) in three different simulations (EPOS 4 (blue), EPOSi+PHSDe (red), pure PHSD (green)) and PHOBOS experimental data (dots) [59] for Au-Au collisions at $\sqrt{s_{NN}} = 200$ GeV. . . . .	108
6.1	Diagrams contributing to the dileptons production from QGP: a) Drell-Yan mechanism, b) gluon-Compton scattering, c) vertex correction, d) gluon Bremsstrahlung, where virtual photons $\gamma^*$ , gluons, and quarks are depicted by wavy lines, spiral lines, and arrows, respectively. In each diagram, the time runs from left to right [79]. . . . .	112
6.2	(Color online) Invariant mass spectrum in the STAR acceptance ( $p_T^e > 0.2$ GeV/c, $ \eta^e  < 1$ , and $ y_{ee}  < 1$ ) from $\sqrt{s_{NN}} = 200$ GeV Au-Au minimum-bias collisions. The mass spectrum is compared to the hadronic cocktail simulations (upper panel) [84]. . . . .	113
6.3	Invariant mass spectrum of dielectrons in minimum-bias Au-Au collisions at 200 GeV from pure PHSD (dotted lines) and EPOSi+PHSDe (solid lines) in comparison to the data from the STAR experiment [84]. The different channels are specified in the legend. . . . .	115
6.4	Same as Fig. 6.3, including the contributions from $D\bar{D}$ and $B\bar{B}$ decays in pure PHSD and without cocktail curves in both models. . . . .	116
6.5	Invariant mass spectrum of dielectrons in minimum-bias Au-Au collisions at 200 GeV from pure PHSD (dotted lines) in comparison to EPOSi+PHSDe (solid lines). The different channels are specified in the legend. In this plot, the heavy-flavor contributions (such as $D\bar{D}$ , $B\bar{B}$ , $J/\psi$ , and $\psi'$ ) have been skipped. . . . .	117
6.6	Same as Fig. 6.5 for dimuons. . . . .	118
6.7	Transverse momentum spectra of dielectrons in minimum-bias Au-Au collisions at 200 GeV from pure PHSD (dotted lines) in comparison to EPOSi+PHSDe (solid lines). The different channels are specified in the legend. In this plot, the heavy-flavor contributions (such as $D\bar{D}$ , $B\bar{B}$ , $J/\psi$ , and $\psi'$ ) have been skipped. . . . .	119
6.8	Same as Fig. 6.7 for dimuons. . . . .	120
6.9	The rapidity spectra of dielectrons from pure PHSD in comparison to EPOSi+PHSDe in minimum-bias Au-Au collisions at 200 GeV. The different contributions are specified in the legend. In this plot, the heavy-flavor contributions (such as $D\bar{D}$ , $B\bar{B}$ , $J/\psi$ , and $\psi'$ ) have been skipped. . . . .	121
6.10	Same as Fig. 6.9 for dimuons. . . . .	122
A.1	Schematic representation of the light cone in the Minkowski space-time. . . . .	136
A.2	Definition of hyperbola in cone. . . . .	137
A.4	Lines in the $\tau - \eta$ plane for constant values of $t$ and $z$ . . . . .	139
A.3	Lines in the $t-z$ plane for constant values of $\tau$ and $\eta$ . . . . .	139
B.1	String segments production from cut ladder. . . . .	144



## LIST OF TABLES

1.1	List of leptons and quarks in Standard Model [1]. . . . .	6
1.2	The four known forces of nature [1]. . . . .	6
1.3	The forces experienced by leptons and quarks. . . . .	7
1.4	Relationship between S.I. and natural units. . . . .	9
2.1	Different possibilities for parton interaction in a pomeron. . . . .	41
4.1	Classify various types of particles in EPOS . . . . .	65
4.2	All types of pre-hadrons with their characteristics in EPOS and PHSD. . . . .	71
B.1	The relationship between centrality classes (C) and impact parameters (b) for Au-Au collision at 200 GeV. . . . .	143



- [1] Mark Thomson. *Modern particle physics*. Cambridge University Press, 2013. (Cited on pages [5](#), [6](#), [33](#), and [153](#).)
- [2] Atlas Collaboration et al. Observation of a new particle in the search for the Standard Model Higgs boson with the ATLAS detector at the LHC. *arXiv preprint arXiv:1207.7214*, 2012. (Cited on pages [5](#) and [26](#).)
- [3] Georges Aad et al. Observation of a new particle in the search for the Standard Model Higgs boson with the ATLAS detector at the LHC. *Phys. Lett. B*, 716:1–29, 2012. (Cited on page [7](#).)
- [4] Serguei Chatrchyan et al. Observation of a New Boson at a Mass of 125 GeV with the CMS Experiment at the LHC. *Phys. Lett. B*, 716:30–61, 2012. (Cited on page [7](#).)
- [5] Higgs mechanism. [https://www.quora.com/Is the Higgs field the only quantum field with a non-zero vacuum expectation value at every point in spacetime?](https://www.quora.com/Is-the-Higgs-field-the-only-quantum-field-with-a-non-zero-vacuum-expectation-value-at-every-point-in-spacetime?) (Cited on page [8](#).)
- [6] Jeremy Bernstein. Spontaneous symmetry breaking, gauge theories, the Higgs mechanism and all that. *Reviews of modern physics*, 46(1):7, 1974. (Cited on page [8](#).)
- [7] CPDG Patrignani, K Agashe, G Aielli, C AMSler, M Antonelli, DM Asner, H Baer, Sw Banerjee, RM Barnett, T Basaglia, et al. Review of particle physics. 2016. (Cited on pages [9](#) and [145](#).)
- [8] Vernon D Barger and Roger JN Phillips. *Collider physics*. CRC Press, 2018. (Cited on page [10](#).)
- [9] Jeff Greensite. *An introduction to the confinement problem*, volume 821. Springer, 2011. (Cited on page [10](#).)
- [10] Vladimir A Miransky. *Dynamical symmetry breaking in quantum field theories*. World Scientific, 1994. (Cited on page [10](#).)
- [11] Nobel prize 2008. <https://www.nobelprize.org/prizes/physics/2008/nambu/facts/>. (Cited on page [10](#).)
- [12] G Zweig. Cern preprint th-401 (1964); h. fritzsch and m. gell-mann, econf c720906v2 (1972) 135 [arxiv: hep-ph/0208010]; dj gross and f. wilczek. *Phys. Rev. Lett*, 30:1343, 1973. (Cited on page [10](#).)

- [13] Ao Zee. Electron-positron annihilation in stagnant field theories. *Physical Review D*, 8(11):4038, 1973. (Cited on page 10.)
- [14] Platinum-Antonio de Ulloa, Charles Wood, Leyden Jar-Ewald Georg von Kleist, and Pieter van Musschenbroek. List of multiple discoveries. (Cited on page 10.)
- [15] John C Collins and Malcolm J Perry. Superdense matter: neutrons or asymptotically free quarks? *Physical Review Letters*, 34(21):1353, 1975. (Cited on page 10.)
- [16] John W Harris and Berndt Müller. The search for the quark-gluon plasma. *Annual Review of Nuclear and Particle Science*, 46(1):71–107, 1996. (Cited on page 11.)
- [17] Helmut Satz. The transition from hadron matter to quark-gluon plasma. *Annual Review of Nuclear and Particle Science*, 35(1):245–270, 1985. (Cited on page 11.)
- [18] Edward Shuryak. What RHIC experiments and theory tell us about properties of quark-gluon plasma? *Nuclear Physics A*, 750(1):64–83, 2005. (Cited on page 11.)
- [19] TD Lee and GC Wick. Vacuum stability and vacuum excitation in a spin-0 field theory. *Physical Review D*, 9(8):2291, 1974. (Cited on page 11.)
- [20] T Ludlam and A Schwarzschild. Report Of Task Force For Relativistic Heavy Ion Physics. Technical report, Brookhaven National Lab.(BNL), Upton, NY (United States), 1983. (Cited on page 11.)
- [21] S Abatzis, F Antinori, RP Barnes, M Benayoun, W Beusch, IJ Bloodworth, A Bravar, JN Carney, D Di Bari, JP Dufey, et al. Production of multistrange baryons and antibaryons in sulphur-tungsten interactions at 200 GeV per nucleon. *Physics Letters B*, 259(4):508–510, 1991. (Cited on page 11.)
- [22] E Andersen, F Antinori, N Armenise, H Bakke, J Ban, D Barberis, H Beker, W Beusch, IJ Bloodworth, J Böhm, et al. Strangeness enhancement at mid-rapidity in Pb–Pb collisions at 158 A GeV/c. *Physics Letters B*, 449(3-4):401–406, 1999. (Cited on page 11.)
- [23] Federico Antinori et al. Transverse mass spectra of strange and multi-strange particles in Pb–Pb collisions at 158 A GeV/c. *The European Physical Journal C-Particles and Fields*, 14(4):633–641, 2000. (Cited on page 11.)
- [24] Mark G Alford, Andreas Schmitt, Krishna Rajagopal, and Thomas Schäfer. Color superconductivity in dense quark matter. *Reviews of Modern Physics*, 80(4):1455, 2008. (Cited on page 11.)
- [25] Jean-François Paquet. Probing the space-time evolution of heavy ion collisions with photons and dileptons. *Nuclear Physics A*, 967:184–191, 2017. (Cited on page 11.)
- [26] BK Patra, Jan-e Alam, Pradip Roy, Sourav Sarkar, and Bikash Sinha. Space-time evolution of ultra-relativistic heavy ion collisions and hadronic spectra. *Nuclear Physics A*, 709(1-4):440–450, 2002. (Cited on page 11.)
- [27] Peter Steinberg. Relativistic heavy ion physics: Results from AGS to RHIC. *arXiv preprint nucl-ex/0210009*, 2002. (Cited on page 12.)
- [28] Miklos Gyulassy and Larry McLerran. New forms of QCD matter discovered at RHIC. *Nuclear Physics A*, 750(1):30–63, 2005. (Cited on page 12.)

- 
- [29] Berndt Müller, Jürgen Schukraft, and Bolesław Wysłouch. First results from Pb+Pb collisions at the LHC. *Annual Review of Nuclear and Particle Science*, 62:361–386, 2012. (Cited on page 12.)
- [30] Jaroslav Adam, Dagmar Adamová, Madan M Aggarwal, G Aglieri Rinella, Maria Agnello, Nikita Agrawal, Zubayer Ahammed, S Ahmad, Sang Un Ahn, Salvatore Aiola, et al. Centrality Dependence of the Charged-Particle Multiplicity Density at Midrapidity in Pb-Pb Collisions at  $\sqrt{s_{NN}}=5.02$  TeV. *Physical review letters*, 116(22):222302, 2016. (Cited on page 12.)
- [31] Ulrich W Heinz. Concepts of heavy-ion physics. *arXiv preprint hep-ph/0407360*, 2004. (Cited on page 12.)
- [32] A Bazavov, H-T Ding, P Hegde, Olaf Kaczmarek, Frithjof Karsch, N Karthik, Edwin Laermann, Anirban Lahiri, R Larsen, S-T Li, et al. Chiral crossover in QCD at zero and non-zero chemical potentials. *Physics Letters B*, 795:15–21, 2019. (Cited on page 12.)
- [33] Frithjof Karsch and Edwin Laermann. Thermodynamics and in-medium hadron properties from lattice QCD. In *Quark–Gluon Plasma 3*, pages 1–59. World Scientific, 2004. (Cited on page 13.)
- [34] James D Bjorken. Highly relativistic nucleus-nucleus collisions: The central rapidity region. *Physical review D*, 27(1):140, 1983. (Cited on page 13.)
- [35] Iu Karpenko, Pasi Huovinen, and Marcus Bleicher. A 3+ 1 dimensional viscous hydrodynamic code for relativistic heavy ion collisions. *Computer Physics Communications*, 185(11):3016–3027, 2014. (Cited on page 13.)
- [36] Wojciech Broniowski and Wojciech Florkowski. Geometric relation between centrality and the impact parameter in relativistic heavy-ion collisions. *Physical Review C*, 65(2):024905, 2002. (Cited on page 13.)
- [37] Alberica Toia. Participants and spectators at the heavy-ion fireball. *CERN courier*, page 4, 2013. (Cited on pages 14 and 145.)
- [38] BI Abelev, MM Aggarwal, Z Ahammed, BD Anderson, D Arkhipkin, GS Averichev, Y Bai, J Balewski, O Barannikova, LS Barnby, et al. Systematic measurements of identified particle spectra in pp, d+Au, and Au+Au collisions at the STAR detector. *Physical Review C*, 79(3):034909, 2009. (Cited on pages 15 and 145.)
- [39] Yasuyuki Akiba. Quest for the quark–gluon plasma—hard and electromagnetic probes. *Progress of Theoretical and Experimental Physics*, 2015(3), 2015. (Cited on pages 15 and 16.)
- [40] Guang-You Qin and Xin-Nian Wang. Jet quenching in high-energy heavy-ion collisions. In *Quark–Gluon Plasma 5*, pages 309–372. World Scientific, 2016. (Cited on page 16.)
- [41] Benedikt Volkel. Extension of the mcplots project and rivet to cover specific needs arising from heavy-ion analyses. Technical report, 2016. (Cited on page 16.)
- [42] JW Cronin, Henry J Frisch, MJ Shochet, JP Boymond, PA Piroué, and RL Sumner. Production of hadrons at large transverse momentum at 200, 300, and 400 gev. *Physical Review D*, 11(11):3105, 1975. (Cited on page 16.)

- [43] Deepali Sharma, PHENIX Collaboration, et al. Measurement of light mesons by the PHENIX experiment at the RHIC. *Journal of Physics G: Nuclear and Particle Physics*, 38(12):124082, 2011. (Cited on pages 17 and 145.)
- [44] Shreyasi Acharya, D Adamová, J Adolfsson, MM Aggarwal, G Aglieri Rinella, M Agnello, N Agrawal, Z Ahammed, SU Ahn, S Aiola, et al. Transverse momentum spectra and nuclear modification factors of charged particles in pp, p-Pb and Pb-Pb collisions at the LHC. *Journal of high energy physics*, 2018(11):1–33, 2018. (Cited on pages 17 and 145.)
- [45] Fabio Catalano. Open heavy-flavour production from small to large collision systems with ALICE at the LHC. *arXiv preprint arXiv:2007.13419*, 2020. (Cited on page 17.)
- [46] CERN website.SPS. <https://home.cern/science/accelerators/super-proton-synchrotron>. (Cited on page 17.)
- [47] Elisa Meninno. Open-charm production measurements in pp, p-Pb and Pb-Pb collisions with ALICE at the LHC. In *EPJ Web of Conferences*, volume 137, page 06018. EDP Sciences, 2017. (Cited on pages 18 and 145.)
- [48] Tetsuo Matsui and Helmut Satz.  $J/\psi$  suppression by quark-gluon plasma formation. *Physics Letters B*, 178(4):416–422, 1986. (Cited on page 18.)
- [49] Andrew Adare, S Afanasiev, C Aidala, NN Ajitanand, Y Akiba, H Al-Bataineh, J Alexander, A Al-Jamel, K Aoki, Laurent Aphecetche, et al.  $J/\psi$  Production versus Centrality, Transverse Momentum, and Rapidity in Au+Au Collisions at  $\sqrt{s_{NN}}=200$  GeV. *Physical review letters*, 98(23):232301, 2007. (Cited on pages 19 and 145.)
- [50] Miklos Gyulassy, Dirk H Rischke, and Bin Zhang. Hot spots and turbulent initial conditions of quark-gluon plasmas in nuclear collisions. *Nuclear Physics A*, 613(4):397–434, 1997. (Cited on page 18.)
- [51] CE Aguiar, Yojiro Hama, T Kodama, and T Osada. Event-by-event fluctuations in hydrodynamical description of heavy-ion collisions. *arXiv preprint hep-ph/0106266*, 2001. (Cited on page 18.)
- [52] Wojciech Broniowski, Piotr Bożek, and Maciej Rybczyński. Fluctuating initial conditions in heavy ion collisions from the Glauber approach. *Physical Review C*, 76(5):054905, 2007. (Cited on page 18.)
- [53] RPG Andrade, F Grassi, Yojiro Hama, T Kodama, and WL Qian. Importance of granular structure in the initial conditions for the elliptic flow. *Physical review letters*, 101(11):112301, 2008. (Cited on page 18.)
- [54] Raimond Snellings. Elliptic flow: a brief review. *New Journal of Physics*, 13(5):055008, 2011. (Cited on pages 19, 100, and 145.)
- [55] SA Voloshin. Anisotropic flow. *arXiv preprint nucl-ex/0210014*, 2002. (Cited on page 20.)
- [56] BB Back, MD Baker, M Ballintijn, DS Barton, RR Betts, AA Bickley, R Bindel, A Budzanowski, W Busza, A Carroll, et al. Energy dependence of directed flow over a wide range of pseudorapidity in Au+Au collisions at the BNL relativistic heavy ion collider. *Physical review letters*, 97(1):012301, 2006. (Cited on pages 20 and 145.)

- [57] Heinz Sorge. Elliptical flow: A signature for early pressure in ultrarelativistic nucleus-nucleus collisions. *Physical Review Letters*, 78(12):2309, 1997. (Cited on pages 20 and 21.)
- [58] VN Russkikh and Yu B Ivanov. Collective flow in heavy-ion collisions for  $E_{\text{lab}}=1\text{--}160$  GeV/nucleon. *Physical Review C*, 74(3):034904, 2006. (Cited on page 20.)
- [59] BB Back, MD Baker, M Ballintijn, DS Barton, RR Betts, AA Bickley, R Bindel, A Budzanowski, W Busza, A Carroll, et al. Centrality and pseudorapidity dependence of elliptic flow for charged hadrons in Au+Au collisions at  $\sqrt{s_{NN}}=200$  GeV. *Physical Review C*, 72(5):051901, 2005. (Cited on pages 21, 107, 108, 146, 150, and 151.)
- [60] Guang-You Qin, Hannah Petersen, Steffen A Bass, and Berndt Müller. Translation of collision geometry fluctuations into momentum anisotropies in relativistic heavy-ion collisions. *Physical Review C*, 82(6):064903, 2010. (Cited on pages 21 and 146.)
- [61] Christoph Hartnack, Helmut Oeschler, Yvonne Leifels, Elena L Bratkovskaya, and Jörg Aichelin. Strangeness production close to the threshold in proton–nucleus and heavy-ion collisions. *Physics reports*, 510(4-5):119–200, 2012. (Cited on page 22.)
- [62] K Werner, AG Knospe, C Markert, B Guiot, Iu Karpenko, T Pierog, G Sophys, M Stefaniak, M Bleicher, and J Steinheimer. Resonance production in high energy collisions from small to big systems. In *EPJ Web of Conferences*, volume 171, page 09002. EDP Sciences, 2018. (Cited on pages 22, 23, and 146.)
- [63] ALICE Collaboration. Multi-strange baryon production in p–Pb collisions at. *arXiv preprint arXiv:1512.07227*, 2015. (Cited on pages 23 and 146.)
- [64] ALICE Collaboration. Multiplicity dependence of pion, kaon, proton and lambda production in p–Pb collisions. *Physics Letters B*, 728:25–38, 2014. (Cited on pages 23 and 146.)
- [65] ALICE Collaboration, O Busch, T Chujo, and Y Miake. Production of  $K(892)^0$  and  $(1020)$  in p–Pb collisions at  $\sqrt{s_{NN}}=5.02$  TeV. *Eur. Phys. J. C*, 76:245, 2016. (Cited on pages 23 and 146.)
- [66] B Abelev, J Adam, D Adamová, AM Adare, MM Aggarwal, G Aglieri Rinella, M Agnello, AG Agocs, A Agostinelli, Z Ahammed, et al. Multi-strange baryon production at mid-rapidity in Pb–Pb collisions at  $\sqrt{s_{NN}}=2.76$  TeV. *Physics Letters B*, 728:216–227, 2014. (Cited on pages 23 and 146.)
- [67] A Large Ion Collider Experiment Collaboration, BeomSu Chang, Dong Jo Kim, Jiri Kral, Astrid Morreale, Jan Rak, Sami Räsänen, Wladyslaw Trzaska, and Jussi Viinikainen. Multi-strange baryon production at mid-rapidity in Pb–Pb collisions at root  $\sqrt{s_{NN}}=2.76$  TeV. *Physics Letters B*, 728(January), 2014. (Cited on pages 22, 23, and 146.)
- [68] DSD Albuquerque, Alice Collaboration, et al. Hadronic resonances, strange and multi-strange particle production in Xe–Xe and Pb–Pb collisions with ALICE at the LHC. *Nuclear Physics A*, 982:823–826, 2019. (Cited on pages 23 and 146.)
- [69] Federico Antinori, H Bakke, W Beusch, IJ Bloodworth, R Caliendo, N Carrer, D Di Bari, S Di Liberto, D Elia, D Evans, et al. Production of strange and multistrange hadrons in nucleus–nucleus collisions at the SPS. *Nuclear Physics A*, 661(1-4):130–139, 1999. (Cited on page 22.)

- [70] G Agakishiev, MM Aggarwal, Z Ahammed, AV Alakhverdyants, I Alekseev, J Alford, BD Anderson, CD Anson, D Arkhipkin, GS Averichev, et al. Strangeness enhancement in Cu-Cu and Au-Au collisions at  $\sqrt{s_{NN}}=200$  GeV. *Physical review letters*, 108(7):072301, 2012. (Cited on page 22.)
- [71] O Linnyk, EL Bratkovskaya, and W Cassing. Effective QCD and transport description of dilepton and photon production in heavy-ion collisions and elementary processes. *Progress in Particle and Nuclear Physics*, 87:50–115, 2016. (Cited on pages 23, 25, 50, and 57.)
- [72] Juerg Beringer, JF Arguin, RM Barnett, K Copic, O Dahl, DE Groom, CJ Lin, J Lys, H Murayama, CG Wohl, et al. Review of particle physics. *Physical Review D-Particles, Fields, Gravitation and Cosmology*, 86(1):010001, 2012. (Cited on page 23.)
- [73] K Haglin, C Gale, and V Emel’yanov. Soft dilepton production in relativistic heavy-ion collisions. *Physical Review D*, 47(3):973, 1993. (Cited on page 24.)
- [74] O Linnyk, VP Konchakovski, W Cassing, and EL Bratkovskaya. Photon elliptic flow in relativistic heavy-ion collisions: hadronic versus partonic sources. *Physical Review C*, 88(3):034904, 2013. (Cited on pages 24 and 146.)
- [75] Nathan PM Holt, Paul M Hohler, and Ralf Rapp. Thermal photon emission from the  $\pi\rho$  system. *Nuclear Physics A*, 945:1–20, 2016. (Cited on page 24.)
- [76] Andrew Adare, S Afanasiev, C Aidala, NN Ajitanand, Y Akiba, H Al-Bataineh, J Alexander, A Al-Jamel, K Aoki, Laurent Aphecetche, et al. Enhanced production of direct photons in Au+Au collisions at  $\sqrt{s_{NN}}=200$  GeV and implications for the initial temperature. *Physical review letters*, 104(13):132301, 2010. (Cited on pages 24 and 146.)
- [77] Ruth E Kastner. On real and virtual photons in the davies theory of time-symmetric quantum electrodynamics. *arXiv preprint arXiv:1312.4007*, 2013. (Cited on page 25.)
- [78] EL Bratkovskaya, SM Kiselev, and GB Sharkov. Direct photon production from hadronic sources in high-energy heavy-ion collisions. *Physical Review C*, 78(3):034905, 2008. (Cited on page 25.)
- [79] Olena Linnyk, EL Bratkovskaya, V Ozvenchuk, W Cassing, and CM Ko. Dilepton production in nucleus-nucleus collisions at top SPS energy within the Parton-Hadron-String Dynamics (PHSD) transport approach. *arXiv preprint arXiv:1107.3402*, 2011. (Cited on pages 25, 111, 112, and 151.)
- [80] Chungsik Song, Che Ming Ko, and Charles Gale. Role of the  $a_1$  meson in dilepton production from hot hadronic matter. *Physical Review D*, 50(3):R1827, 1994. (Cited on page 25.)
- [81] Olena Linnyk, EL Bratkovskaya, and W Cassing. Dileptons from the strongly-interacting Quark-Gluon Plasma within the Parton-Hadron-String-Dynamics (PHSD) approach. *Nuclear Physics A*, 830(1-4):491c–494c, 2009. (Cited on page 25.)
- [82] Joseph Kapusta, Peter Lichard, and David Seibert. High-energy photons from quark-gluon plasma versus hot hadronic gas. *Physical Review D*, 44(9):2774, 1991. (Cited on page 25.)

- [83] T Song, EL Bratkovskaya, W Cassing, and P Moreau. Electromagnetic emissivity of hot and dense matter. In *Journal of Physics: Conference Series*, volume 1070, page 012006. IOP Publishing, 2018. (Cited on pages 26 and 146.)
- [84] L Adamczyk, JK Adkins, G Agakishiev, MM Aggarwal, Z Ahammed, I Alekseev, J Alford, A Aparin, D Arkhipkin, EC Aschenauer, et al. Measurements of dielectron production in Au+Au collisions at  $\sqrt{s_{NN}}=200$  GeV from the STAR experiment. *Physical Review C*, 92(2):024912, 2015. (Cited on pages 26, 113, 115, 146, and 151.)
- [85] Michael H Seymour and Marilyn Marx. Monte Carlo event generators. In *LHC Phenomenology*, pages 287–319. Springer, 2015. (Cited on pages 26, 27, and 146.)
- [86] Serguei Chatrchyan, Vardan Khachatryan, Albert M Sirunyan, Armen Tumasyan, Wolfgang Adam, Ernest Aguilo, Thomas Bergauer, M Dragicevic, J Erö, C Fabjan, et al. Observation of a new boson at a mass of 125 GeV with the CMS experiment at the LHC. *Physics Letters B*, 716(1):30–61, 2012. (Cited on page 26.)
- [87] JM Campbell, M Diefenthaler, TJ Hobbs, S Höche, J Isaacson, F Kling, S Mrenna, J Reuter, S Alioli, JR Andersen, et al. Event Generators for High-Energy Physics Experiments. *arXiv preprint arXiv:2203.11110*, 2022. (Cited on page 27.)
- [88] Pythia website. <https://pythia.org/>. (Cited on page 27.)
- [89] Christian Bierlich, Gösta Gustafson, Leif Lönnblad, and Harsh Shah. The Angantyr model for heavy-ion collisions in PYTHIA8. *Journal of High Energy Physics*, 2018(10):1–55, 2018. (Cited on page 27.)
- [90] W Cassing and EL Bratkovskaya. Parton–hadron–string dynamics: An off-shell transport approach for relativistic energies. *Nuclear Physics A*, 831(3-4):215–242, 2009. (Cited on pages 28 and 55.)
- [91] Herwing website. <https://www.hep.phy.cam.ac.uk/theory/webber/Herwig/herwig65.html>. (Cited on page 28.)
- [92] H Baer, FE Paige, SD Protopescu, and X Tata. ISAJET 7.69: A Monte Carlo Event Generator for pp, pp, and  $e^+e^-$  Reactions. *arXiv preprint hep-ph/0312045*, 2003. (Cited on page 28.)
- [93] Wei-Tian Deng, Xin-Nian Wang, and Rong Xu. Hadron production in p+p, p+Pb, and Pb+Pb collisions with the HIJING 2.0 model at energies available at the CERN Large Hadron Collider. *Physical Review C*, 83(1):014915, 2011. (Cited on page 28.)
- [94] Zi-Wei Lin, Che Ming Ko, Bao-An Li, Bin Zhang, and Subrata Pal. Multi-phase transport model for relativistic heavy ion collisions. *Physical Review C*, 72(6):064901, 2005. (Cited on page 28.)
- [95] Klaus Werner, B Guiot, Iu Karpenko, and T Pierog. Analyzing radial flow features in p-Pb and p-p collisions at several TeV by studying identified-particle production with the event generator EPOS3. *Physical Review C*, 89(6):064903, 2014. (Cited on pages 28 and 32.)
- [96] Klaus Werner. Strings, pomerons and the VENUS model of hadronic interactions at ultrarelativistic energies. *Physics Reports*, 232(2-5):87–299, 1993. (Cited on pages 31, 36, 37, and 38.)

- [97] Klaus Werner. A new string model (venus 2) for hadronic collisions based on color exchange between quarks and antiquarks. Technical report, Brookhaven National Lab., Upton, NY (USA), 1989. (Cited on page 31.)
- [98] G Bossard, HJ Drescher, NN Kalmykov, S Ostapchenko, AI Pavlov, T Pierog, EA Vishnevskaya, and K Werner. Cosmic ray air shower characteristics in the framework of the parton-based Gribov-Regge model NEXUS. *Physical Review D*, 63(5):054030, 2001. (Cited on page 31.)
- [99] S Ostapchenko. QGSJET-II: towards reliable description of very high energy hadronic interactions. *Nuclear Physics B-Proceedings Supplements*, 151(1):143–146, 2006. (Cited on page 31.)
- [100] Hans Joachim Drescher, M Hladik, S Ostapchenko, T Pierog, and Klaus Werner. Parton-based Gribov–Regge theory. *Physics Reports*, 350(2-4):93–289, 2001. (Cited on pages 31, 38, and 39.)
- [101] Iurii Karpenko. *Développement d’approches hydrodynamique et hydrocinétique aux collisions noyau-noyau ultra-relativistes*. PhD thesis, Bogolyubov Institute for Theoretical Physics, 2010. (Cited on pages 31, 44, and 100.)
- [102] Klaus Werner, Iu Karpenko, Tanguy Pierog, Marcus Bleicher, and K Mikhailov. Event-by-event simulation of the three-dimensional hydrodynamic evolution from flux tube initial conditions in ultrarelativistic heavy ion collisions. *Physical Review C*, 82(4):044904, 2010. (Cited on pages 31, 44, and 99.)
- [103] Marcus Bleicher, E Zabrodin, Christian Spieles, Steffen A Bass, Christoph Ernst, Sven Soff, L Bravina, Mohamed Belkacem, Henning Weber, Horst Stöcker, et al. Relativistic hadron-hadron collisions in the ultra-relativistic quantum molecular dynamics model. *Journal of Physics G: Nuclear and Particle Physics*, 25(9):1859, 1999. (Cited on page 32.)
- [104] T Pierog, Iu Karpenko, Judith Maria Katzy, E Yatsenko, and Klaus Werner. EPOS LHC: Test of collective hadronization with data measured at the CERN Large Hadron Collider. *Physical Review C*, 92(3):034906, 2015. (Cited on page 32.)
- [105] Benjamin Guiot. *Production de charmes et de photons prompts avec le générateur d’évènements EPOS*. PhD thesis, Ecole des Mines de Nantes, 2014. (Cited on page 32.)
- [106] Klaus Werner, B Guiot, Iu Karpenko, and T Pierog. Analyzing radial flow features in p-Pb and p-p collisions at several TeV by studying identified-particle production with the event generator EPOS3. *Physical Review C*, 89(6):064903, 2014. (Cited on page 32.)
- [107] Pol Bernard Gossiaux, Joerg Aichelin, Marlene Nahrgang, Vitalii Ozvenchuk, and Klaus Werner. Global view on coupled dynamics of heavy and light flavor observables from EPOSHQ. *Nuclear Physics A*, 967:672–675, 2017. (Cited on page 32.)
- [108] Richard P Feynman. Very high-energy collisions of hadrons. *Physical Review Letters*, 23(24):1415, 1969. (Cited on page 33.)
- [109] Richard P Feynman. The behavior of hadron collisions at extreme energies. In *Special Relativity and Quantum Theory*, pages 289–304. Springer, 1988. (Cited on page 33.)

- [110] LW Whitlow, EM Riordan, S Dasu, Stephen Rock, and A Bodek. Precise measurements of the proton and deuteron structure functions from a global analysis of the SLAC deep inelastic electron scattering cross sections. *Physics Letters B*, 282(3-4):475–482, 1992. (Cited on page 35.)
- [111] Grégory Soyez. *Deep Inelastic Scattering at small x*. PhD thesis, PhD thesis, Liege U., 2004.(Cited on page 54.), 2004. (Cited on page 36.)
- [112] VN Gribov. A reggeon diagram technique. *Sov. Phys. JETP*, 26(2):414–423, 1968. (Cited on page 37.)
- [113] VN Gribov and I Ya Pomeranchuk. Complex Angular Momenta and the Relation between the Cross Sections of Various Processes at High Energies. *Physical Review Letters*, 8(8):343, 1962. (Cited on page 37.)
- [114] Benjamin Guiot. *Production de charms et de photons prompts avec le générateur d'évènements EPOS*. PhD thesis, Ecole des Mines de Nantes, 2014. (Cited on page 39.)
- [115] Klaus Werner. The hadronic interaction model EPOS. *Nuclear Physics B-Proceedings Supplements*, 175:81–87, 2008. (Cited on pages 40 and 146.)
- [116] Klaus Werner, B Guiot, Iu Karpenko, and T Pierog. Analyzing radial flow features in p-Pb and p-p collisions at several TeV by studying identified-particle production with the event generator EPOS3. *Physical Review C*, 89(6):064903, 2014. (Cited on pages 41, 43, and 44.)
- [117] Joel Scherk. An introduction to the theory of dual models and strings. *Reviews of Modern Physics*, 47(1):123, 1975. (Cited on page 42.)
- [118] Claudio Rebbi. Dual models and relativistic quantum strings. *Physics Reports*, 12(1):1–73, 1974. (Cited on page 42.)
- [119] Klaus Werner. Core-corona separation in ultrarelativistic heavy ion collisions. *Physical review letters*, 98(15):152301, 2007. (Cited on page 42.)
- [120] HJ Drescher, FM Liu, S Ostapchenko, T Pierog, and Klaus Werner. Initial condition for quark-gluon plasma evolution. *Physical Review C*, 65(5):054902, 2002. (Cited on pages 44 and 80.)
- [121] Klaus Werner. Latest developments in EPOS. In *COST THOR Working Group I and II and GDRI Meeting*, 2018. (Cited on page 44.)
- [122] Bo Andersson, Gösta Gustafson, Gunnar Ingelman, and Torbjörn Sjöstrand. Parton fragmentation and string dynamics. *Physics Reports*, 97(2-3):31–145, 1983. (Cited on pages 44 and 54.)
- [123] Marcus Bleicher, E Zabrodin, Christian Spieles, Steffen A Bass, Christoph Ernst, Sven Soff, L Bravina, Mohamed Belkacem, Henning Weber, Horst Stöcker, et al. Relativistic hadron-hadron collisions in the ultra-relativistic quantum molecular dynamics model. *Journal of Physics G: Nuclear and Particle Physics*, 25(9):1859, 1999. (Cited on page 45.)
- [124] Hannah Petersen, Jan Steinheimer, Gerhard Burau, Marcus Bleicher, and Horst Stöcker. Fully integrated transport approach to heavy ion reactions with an intermediate hydrodynamic stage. *Physical Review C*, 78(4):044901, 2008. (Cited on page 45.)

- [125] Pierre Moreau. *Dynamical description of relativistic heavy-ion collisions out-of-equilibrium*. PhD thesis, Universitätsbibliothek Johann Christian Senckenberg, 2019. (Cited on pages [47](#), [53](#), [59](#), and [139](#).)
- [126] Jørgen Rammer. *Quantum field theory of non-equilibrium states*, volume 22. Cambridge University Press Cambridge, 2007. (Cited on page [47](#).)
- [127] Takafumi Kita. Introduction to nonequilibrium statistical mechanics with quantum field theory. *Progress of theoretical physics*, 123(4):581–658, 2010. (Cited on page [48](#).)
- [128] Matthew D Schwartz. *Quantum field theory and the standard model*. Cambridge University Press, 2014. (Cited on page [48](#).)
- [129] Freeman J Dyson. The S matrix in quantum electrodynamics. *Physical Review*, 75(11):1736, 1949. (Cited on page [49](#).)
- [130] Wolfgang Cassing. From Kadanoff-Baym dynamics to off-shell parton transport. *The European Physical Journal Special Topics*, 168(1):3–87, 2009. (Cited on pages [49](#), [52](#), and [147](#).)
- [131] Christian Brouder. The structure of green functions in quantum field theory with a general state. In *Quantum Field Theory*, pages 163–175. Springer, 2009. (Cited on page [49](#).)
- [132] Stanisław Mrówczyński and Paweł Danielewicz. Green function approach to transport theory of scalar fields. *Nuclear Physics B*, 342(2):345–380, 1990. (Cited on pages [49](#) and [50](#).)
- [133] W Cassing and S Juchem. Semiclassical transport of particles with dynamical spectral functions. *Nuclear Physics A*, 665(3-4):377–400, 2000. (Cited on pages [49](#), [52](#), and [111](#).)
- [134] Oskar Klein. Quantentheorie und fünfdimensionale Relativitätstheorie. *Zeitschrift für Physik*, 37(12):895–906, 1926. (Cited on page [50](#).)
- [135] Walter Gordon. Der comptoneffekt nach der schrödingerschen theorie. *Zeitschrift für Physik*, 40(1-2):117–133, 1926. (Cited on page [50](#).)
- [136] Gordon Baym. Self-consistent approximations in many-body systems. *Physical review*, 127(4):1391, 1962. (Cited on page [51](#).)
- [137] Eugene P Wigner. On the quantum correction for thermodynamic equilibrium. In *Part I: Physical Chemistry. Part II: Solid State Physics*, pages 110–120. Springer, 1997. (Cited on page [51](#).)
- [138] LP Kadanoff and G Baym. Quantum Statistical Mechanics Benjamin. *New York*, 1962. (Cited on page [52](#).)
- [139] Wim Botermans and Rudi Malfliet. Quantum transport theory of nuclear matter. *Physics Reports*, 198(3):115–194, 1990. (Cited on page [52](#).)
- [140] Sascha Juchem, W Cassing, and C Greiner. Nonequilibrium quantum-field dynamics and off-shell transport. In *Ph. D. thesis, JLU Giessen*. Citeseer, 2003. (Cited on page [52](#).)
- [141] Roger D Woods and David S Saxon. Diffuse surface optical model for nucleon-nuclei scattering. *Physical Review*, 95(2):577, 1954. (Cited on page [53](#).)

- 
- [142] Llewellyn H Thomas. The calculation of atomic fields. In *Mathematical proceedings of the Cambridge philosophical society*, volume 23, pages 542–548. Cambridge University Press, 1927. (Cited on page 53.)
- [143] Torbjörn Sjöstrand, Stephen Mrenna, and Peter Skands. PYTHIA 6.4 physics and manual. *Journal of High Energy Physics*, 2006(05):026, 2006. (Cited on page 54.)
- [144] J Geiss, W Cassing, and C Greiner. Strangeness production in the HSD transport approach from SIS to SPS energies. *Nuclear Physics A*, 644(1-2):107–138, 1998. (Cited on pages 54 and 55.)
- [145] Julian Schwinger. On gauge invariance and vacuum polarization. *Physical Review*, 82(5):664, 1951. (Cited on page 54.)
- [146] W Cassing. Dynamical quasiparticles properties and effective interactions in the sQGP. *Nuclear Physics A*, 795(1-4):70–97, 2007. (Cited on pages 55 and 111.)
- [147] EL Bratkovskaya, W Cassing, VP Konchakovski, and O Linnyk. Parton–Hadron–String Dynamics at relativistic collider energies. *Nuclear Physics A*, 856(1):162–182, 2011. (Cited on pages 55, 59, and 147.)
- [148] André Peshier. Hard gluon damping in hot QCD. *Physical Review D*, 70(3):034016, 2004. (Cited on page 56.)
- [149] André Peshier. Hard parton damping in hot QCD. *Journal of Physics G: Nuclear and Particle Physics*, 31(4):S371, 2005. (Cited on page 56.)
- [150] Pierre Moreau, Olga Soloveva, Lucia Oliva, Taesoo Song, Wolfgang Cassing, and Elena Bratkovskaya. Exploring the partonic phase at finite chemical potential within an extended off-shell transport approach. *Physical Review C*, 100(1):014911, 2019. (Cited on pages 57, 58, and 147.)
- [151] Olaf Kaczmarek, F Karsch, F Zantow, and P Petreczky. Static quark-antiquark free energy and the running coupling at finite temperature. *Physical Review D*, 70(7):074505, 2004. (Cited on page 57.)
- [152] Yasumichi Aoki, Szabolcs Borsanyi, Stephan Dürr, Zoltan Fodor, Sandor D Katz, Stefan Krieg, and Kalman Szabo. The QCD transition temperature: results with physical masses in the continuum limit II. *Journal of High Energy Physics*, 2009(06):088, 2009. (Cited on pages 58 and 147.)
- [153] W Cassing and EL Bratkovskaya. Parton transport and hadronization from the dynamical quasiparticle point of view. *Physical Review C*, 78(3):034919, 2008. (Cited on page 59.)
- [154] Torbjörn Sjöstrand and Mats Bengtsson. The lund monte carlo for jet fragmentation and  $e^-e^+$  physics-jetset version 6.3-an update. *Computer Physics Communications*, 43(3):367–379, 1987. (Cited on page 60.)
- [155] Eduard Seifert. Many-body channels in baryon-antibaryon annihilation in relativistic heavy-ion collisions. 2018. (Cited on page 60.)
- [156] Jean-Yves Ollitrault. Anisotropy as a signature of transverse collective flow. *Physical Review D*, 46(1):229, 1992. (Cited on page 61.)
- [157] Tetsufumi Hirano and Yasushi Nara. Eccentricity fluctuation effects on elliptic flow in relativistic heavy ion collisions. *Physical Review C*, 79(6):064904, 2009. (Cited on pages 61, 62, and 147.)

- [158] Klaus Werner and Jörg Aichelin. Microcanonical treatment of hadronizing the quark-gluon plasma. *Physical Review C*, 52(3):1584, 1995. (Cited on page 68.)
- [159] Rudy Marty, Elena Bratkovskaya, Wolfgang Cassing, and Joerg Aichelin. Observables in ultrarelativistic heavy-ion collisions from two different transport approaches for the same initial conditions. *Physical Review C*, 92(1):015201, 2015. (Cited on page 80.)
- [160] John Adams, C Adler, MM Aggarwal, Z Ahammed, J Amonett, BD Anderson, M Anderson, D Arkhipkin, GS Averichev, SK Badyal, et al. Identified particle distributions in p p and Au+Au collisions at  $\sqrt{s_{NN}}=200$  GeV. *Physical Review Letters*, 92(11):112301, 2004. (Cited on pages 84, 85, 86, 87, 148, and 149.)
- [161] K. H. Ackermann et al. STAR detector overview. *Nucl. Instrum. Meth. A*, 499:624–632, 2003. (Cited on page 84.)
- [162] IG Bearden, D Beavis, C Besliu, B Budick, H Bøggild, C Chasman, CH Christensen, P Christiansen, J Cibor, R Debye, et al. Charged meson rapidity distributions in central Au+Au collisions at  $\sqrt{s_{NN}}=200$  GeV. *Physical review letters*, 94(16):162301, 2005. (Cited on pages 88, 89, 93, 94, 95, 149, and 150.)
- [163] IG Bearden, D Beavis, C Besliu, B Budick, H Bøggild, C Chasman, CH Christensen, P Christiansen, J Cibor, R Debye, et al. Nuclear Stopping in Au+Au Collisions at  $\sqrt{s_{NN}}=200$  GeV. *Physical review letters*, 93(10):102301, 2004. (Cited on pages 88, 89, 96, 149, and 150.)
- [164] M Adamczyk, L Antvorskov, K Ashktorab, K Asselta, E Baker, IG Bearden, D Beavis, C Besliu, Y Blyakhman, J Brzychczyk, et al. The BRAHMS experiment at RHIC. *Nuclear Instruments and Methods in Physics Research Section A: Accelerators, Spectrometers, Detectors and Associated Equipment*, 499(2-3):437–468, 2003. (Cited on page 88.)
- [165] IG Bearden, D Beavis, C Besliu, Y Blyakhman, B Budick, H Bøggild, C Chasman, CH Christensen, P Christiansen, J Cibor, et al. Pseudorapidity distributions of charged particles from Au+Au collisions at the maximum RHIC energy,  $\sqrt{s_{NN}}=200$  GeV. *Physical Review Letters*, 88(20):202301, 2002. (Cited on pages 90, 91, and 149.)
- [166] Andrew Adare, S Afanasiev, C Aidala, NN Ajitanand, Yasuyuki Akiba, H Al-Bataineh, J Alexander, A Angerami, K Aoki, N Apadula, et al. Spectra and ratios of identified particles in Au+Au and d+ Au collisions at  $\sqrt{s_{NN}}=200$  GeV. *Physical Review C*, 88(2):024906, 2013. (Cited on pages 91, 92, and 149.)
- [167] K Adcox, SS Adler, M Aizama, NN Ajitanand, Y Akiba, H Akikawa, J Alexander, A Al-Jamel, M Allen, G Alley, et al. PHENIX detector overview. *Nuclear Instruments and Methods in Physics Research Section A: Accelerators, Spectrometers, Detectors and Associated Equipment*, 499(2-3):469–479, 2003. (Cited on page 91.)
- [168] Michael L Miller, Klaus Reygers, Stephen J Sanders, and Peter Steinberg. Glauber modeling in high-energy nuclear collisions. *Annu. Rev. Nucl. Part. Sci.*, 57:205–243, 2007. (Cited on page 91.)
- [169] Johann Rafelski and Berndt Müller. Strangeness production in the quark-gluon plasma. *Physical Review Letters*, 48(16):1066, 1982. (Cited on page 97.)

- [170] J Adams, MM Aggarwal, Z Ahammed, J Amonett, BD Anderson, M Anderson, D Arkhipkin, GS Averichev, Y Bai, J Balewski, et al. Scaling properties of hyperon production in Au+Au collisions at  $\sqrt{s_{NN}}=200$  GeV. *Physical review letters*, 98(6):062301, 2007. (Cited on pages 97, 98, and 150.)
- [171] M Anderson, J Berkovitz, W Betts, R Bossingham, F Bieser, R Brown, M Burks, M Calderón de la Barca Sánchez, D Cebra, M Cherney, et al. The STAR time projection chamber: a unique tool for studying high multiplicity events at RHIC. *Nuclear Instruments and Methods in Physics Research Section A: Accelerators, Spectrometers, Detectors and Associated Equipment*, 499(2-3):659–678, 2003. (Cited on page 97.)
- [172] BB Back, MD Baker, DS Barton, RR Betts, M Ballintijn, AA Bickley, R Bindel, A Budzanowski, W Busza, A Carroll, et al. Charged hadron transverse momentum distributions in Au+Au collisions at  $\sqrt{s_{NN}}=200$  GeV. *Physics Letters B*, 578(3-4):297–303, 2004. (Cited on pages 99 and 150.)
- [173] KHea Ackermann, N Adams, C Adler, Z Ahammed, S Ahmad, C Allgower, J Amsbaugh, M Anderson, E Anderssen, H Arnesen, et al. Elliptic Flow in Au+Au Collisions at  $\sqrt{s_{NN}}=130$  GeV. *Physical Review Letters*, 86(3):402, 2001. (Cited on pages 99 and 100.)
- [174] Thomas Schäfer and Derek Teaney. Nearly perfect fluidity: from cold atomic gases to hot quark gluon plasmas. *Reports on Progress in Physics*, 72(12):126001, 2009. (Cited on page 99.)
- [175] Ulrich W Heinz and Peter F Kolb. Early thermalization at RHIC. *arXiv preprint hep-ph/0111075*, 2001. (Cited on page 100.)
- [176] J Barrette, R Bellwied, S Bennett, P Braun-Munzinger, WE Cleland, M Clemen, J Cole, TM Cormier, G David, J Dee, et al. Observation of anisotropic event shapes and transverse flow in ultrarelativistic Au+Au collisions. *Physical review letters*, 73(19):2532, 1994. (Cited on page 100.)
- [177] H Appelshäuser, J Bächler, SJ Bailey, LS Barnby, J Bartke, RA Barton, H Bialkowska, CO Blyth, R Bock, C Bormann, et al. Directed and elliptic flow in 158 GeV/nucleon Pb+Pb collisions. *Physical Review Letters*, 80(19):4136, 1998. (Cited on page 100.)
- [178] K Adcox, SS Adler, NN Ajitanand, Y Akiba, J Alexander, Laurent Aphecetche, Y Arai, SH Aronson, R Averbeck, TC Awes, et al. Flow Measurements via Two-Particle Azimuthal Correlations in Au+Au Collisions at  $\sqrt{s_{NN}}=130$  GeV. *Physical Review Letters*, 89(21):212301, 2002. (Cited on page 100.)
- [179] BB Back, MD Baker, M Ballintijn, DS Barton, RR Betts, AA Bickley, R Bindel, A Budzanowski, W Busza, A Carroll, et al. Energy dependence of elliptic flow over a large pseudorapidity range in Au+Au collisions at the BNL relativistic heavy ion collider. *Physical review letters*, 94(12):122303, 2005. (Cited on page 100.)
- [180] Kenneth Aamodt, B Abelev, A Abrahantes Quintana, D Adamova, AM Adare, MM Aggarwal, G Aglieri Rinella, AG Agocs, S Aguilar Salazar, Z Ahammed, et al. Elliptic flow of charged particles in Pb-Pb collisions at  $\sqrt{s_{NN}}=2.76$  TeV. *Physical review letters*, 105(25):252302, 2010. (Cited on page 100.)

- [181] Serguei Chatrchyan, V Khachatryan, AM Sirunyan, A Tumasyan, W Adam, T Bergauer, M Dragicevic, J Erö, C Fabjan, M Friedl, et al. Measurement of the elliptic anisotropy of charged particles produced in PbPb collisions at  $\sqrt{s_{NN}}=2.76$  TeV. *Physical Review C*, 87(1):014902, 2013. (Cited on page 100.)
- [182] Ulrich Heinz, Chun Shen, and Huichao Song. The viscosity of quark-gluon plasma at RHIC and the LHC. In *AIP Conference Proceedings*, volume 1441, pages 766–770. American Institute of Physics, 2012. (Cited on page 100.)
- [183] A Peshier and W Cassing. The hot nonperturbative gluon plasma is an almost ideal colored liquid. *Physical review letters*, 94(17):172301, 2005. (Cited on page 100.)
- [184] Betty Abelev, J Adam, D Adamová, AM Adare, MM Aggarwal, G Aglieri Rinella, M Agnello, AG Agocs, A Agostinelli, Z Ahammed, et al. Directed flow of charged particles at midrapidity relative to the spectator plane in Pb-Pb collisions at  $\sqrt{s_{NN}}=2.76$  TeV. *Physical review letters*, 111(23):232302, 2013. (Cited on pages 101 and 150.)
- [185] Sergei A Voloshin, Arthur M Poskanzer, Aihong Tang, and Gang Wang. Elliptic flow in the Gaussian model of eccentricity fluctuations. *Physics Letters B*, 659(3):537–541, 2008. (Cited on page 100.)
- [186] Arthur M Poskanzer and Sergei A Voloshin. Methods for analyzing anisotropic flow in relativistic nuclear collisions. *Physical Review C*, 58(3):1671, 1998. (Cited on pages 100 and 102.)
- [187] Gabriel Sophys. *Formation of a Quark-Gluon-Plasma: understanding the energy and system size dependence*. PhD thesis, Nantes, 2018. (Cited on page 102.)
- [188] L Adamczyk, JK Adkins, G Agakishiev, MM Aggarwal, Z Ahammed, I Alekseev, J Alford, CD Anson, A Aparin, D Arkhipkin, et al. Elliptic flow of identified hadrons in Au+Au collisions at  $\sqrt{s_{NN}}=7.7\text{--}62.4$   $\sqrt{s_{NN}}$ . *Physical Review C*, 88(1):014902, 2013. (Cited on page 102.)
- [189] Andrew Adare, S Afanasiev, C Aidala, NN Ajitanand, Yasuyuki Akiba, H Al-Bataineh, J Alexander, K Aoki, Y Aramaki, ET Atomssa, et al. Measurement of the higher-order anisotropic flow coefficients for identified hadrons in Au+Au collisions at  $\sqrt{s_{NN}}=200$  GeV. *Physical Review C*, 93(5):051902, 2016. (Cited on pages 103, 104, 105, 106, and 150.)
- [190] Paul W Stankus, Milan Matos, and Collaboration Phenix. A reaction plane detector for PHENIX at RHIC. *Nuclear Instruments and Methods in Physics Research Section A: Accelerators, Spectrometers, Detectors and Associated Equipment*, 636(1), 2011. (Cited on page 103.)
- [191] Rajeev S Bhalerao, Jean-Paul Blaizot, Nicolas Borghini, and Jean-Yves Ollitrault. Elliptic flow and incomplete equilibration at RHIC. *Physics Letters B*, 627(1-4):49–54, 2005. (Cited on page 105.)
- [192] BB Back, MD Baker, DS Barton, S Basilev, R Baum, RR Betts, A Białas, R Bindel, W Bogucki, A Budzanowski, et al. The PHOBOS detector at RHIC. *Nuclear Instruments and Methods in Physics Research Section A: Accelerators, Spectrometers, Detectors and Associated Equipment*, 499(2-3):603–623, 2003. (Cited on page 107.)
- [193] Taesoo Song, Wolfgang Cassing, Pierre Moreau, and Elena Bratkovskaya. Discrepancy in low transverse momentum dileptons from relativistic heavy-ion collisions. *Physical Review C*, 98(4):041901, 2018. (Cited on page 111.)

- [194] Taesoo Song, Wolfgang Cassing, Pierre Moreau, and Elena Bratkovskaya. Open charm and dileptons from relativistic heavy-ion collisions. *Physical Review C*, 97(6):064907, 2018. (Cited on pages [111](#) and [112](#).)
- [195] Wolfgang Cassing and Elena Leontievna Bratkovskaya. Hadronic and electromagnetic probes of hot and dense nuclear matter. *Physics Reports*, 308(2-3):65–233, 1999. (Cited on page [111](#).)
- [196] EL Bratkovskaya and W Cassing. Dilepton production from ags to sps energies within a relativistic transport approach. *Nuclear Physics A*, 619(3-4):413–446, 1997. (Cited on page [111](#).)
- [197] EL Bratkovskaya and W Cassing. Dilepton production and off-shell transport dynamics at sis energies. *Nuclear Physics A*, 807(3-4):214–250, 2008. (Cited on page [111](#).)



- $\pi$ A** Collision between one pion and one nucleus. [47](#)
- AA** Collision between two nuclei. [13](#), [16](#), [18](#), [22](#), [23](#), [25](#), [26](#), [28](#), [31](#), [32](#), [38](#), [41](#), [47](#), [111](#)
- AMPT** A Multi-Phase Transport (AMPT) Model. AMPT is a Monte Carlo transport model for heavy ion collisions at relativistic energies.. [27](#), [28](#)
- Au-Au** Collision between two Gold nuclei. [14](#), [15](#), [17–21](#), [24](#), [26](#), [43](#), [62](#), [65](#), [70](#), [73–75](#), [77](#), [79](#), [80](#), [82](#), [84–99](#), [103–108](#), [113–115](#), [117–121](#), [125](#), [127](#), [129](#), [131](#), [141](#), [143](#), [145–151](#)
- $e^+e^-$**  Collision between one electron and one positron. [28](#)
- $e^-n$**  Collision between one electron and one neutron. [35](#)
- $e^-p$**  Collision between one electron and one proton. [33–35](#), [146](#)
- EPOS 1** The first version of EPOS without hydrodynamical evolution. [32](#)
- EPOS 2** The second version of EPOS with an event-by-event hydrodynamic implemented. [31](#), [45](#)
- EPOS 3** The third version of EPOS with a viscous hydrodynamic expansion and a parton saturation implemented. [23](#), [32](#), [45](#), [146](#)
- EPOS 4** The beta version of EPOS 3 (3.44d) with the new saturation scale. [32](#), [45](#), [61–63](#), [73](#), [76](#), [77](#), [79–82](#), [84–100](#), [103–109](#), [118](#), [125](#), [126](#), [129](#), [130](#), [143](#), [148–151](#)
- EPOS HQ** Studying the heavy flavors with the EPOS 3. [32](#), [45](#)
- EPOS LHC** Tuning EPOS 2 with LHC accelerator. [32](#), [45](#)
- EPOS $e$**  The evolution of matter in EPOS 4. [i](#), [42](#), [44](#), [45](#)
- EPOS $i$**  The initial condition in EPOS 4. [32](#), [45](#), [60](#), [61](#), [77](#), [79](#), [125](#), [129](#)
- EPOS $i$ +PHSD $e$**  Merging the initial condition from EPOS 4 and evolution of partonic and hadronic phases in PHSD. [32](#), [45](#), [61–63](#), [65–67](#), [73–77](#), [79–82](#), [84–100](#), [103–109](#), [111](#), [114–123](#), [125–127](#), [129–131](#), [141](#), [148–151](#)
- Herwig** A general purpose event generator coupled with ThePEG to be a complete event generator. [27](#), [28](#)

**hh** Collision between two hadrons. [28](#)

**HIJING** Heavy Ion Jet INteraction Generator. An Event Generator used for High Energy Collisions, and a Monte-Carlo program to study jets and particle production in High Energy Hadronic and Nuclear Collisions.. [27](#), [28](#)

**ISAJET** ISAJET is a Monte Carlo program which simulates  $pp$ ,  $p\bar{p}$ , and  $e^-e^+$  interactions at high energies.. [27](#), [28](#)

**NEXUS** The event generator based on Parton Based Grebov Regge Theory precursor of EPOS. [31](#)

**p  $\bar{p}$**  Collision between one proton and one anti-proton. [28](#)

**pA** Collision between one proton and one nucleus. [22](#), [25](#), [28](#), [31](#), [38](#), [41](#), [42](#), [47](#), [111](#)

**PHOBOS** Phobos is a moon of Mars, which was the name of the original proposed detector. Studies heavy-ion collisions at Brookhaven. [20](#), [99](#), [107](#), [108](#), [145](#), [150](#), [151](#)

**PHSDe** The evolution of partonic and hadronic phases in PHSD. [ii](#), [32](#), [55](#), [59–61](#), [77](#), [79](#), [125](#), [129](#)

**PHSDi** The initial condition in PHSD. [ii](#), [53](#), [54](#), [60](#)

**pp** Collision between two protons. [16](#), [18](#), [22](#), [25](#), [26](#), [28](#), [31–33](#), [35](#), [38](#), [41](#), [42](#), [127](#), [131](#)

**Pythia** A general purpose event generator and the Lund Monte Carlo generator based on the parton model. Pythia is the name of the high priestess of the Temple of Apollo at Delphi in the Greek Mythology. [27](#), [47](#), [54](#)

**VENUS** The event generator based on the Gribov Regge Theory and the precursor of NEXUS. [31](#)

- AGS** Alternating Gradient Synchrotron. [12](#), [31](#), [55](#), [100](#)
- ALICE** A Large Ion Collider Experiment. [16–18](#), [23](#), [145](#), [146](#)
- ATLAS** A Toroidal LHC ApparatuS. [7](#), [26](#)
- BNL** Brookhaven National Lab. [11](#), [12](#), [31](#)
- BRAHMS** Broad RAnge Hadron Magnetic Spectrometers. [88–91](#), [93–96](#), [149](#), [150](#)
- BSM** Beyond the Standard Model. [8](#)
- CERN** Conseil Européen pour la Recherche Nucléaire. [11](#), [12](#), [22](#), [31](#)
- CMS** Compact Muon Solenoid. [7](#), [16](#), [17](#), [26](#), [145](#)
- CTP** Closed Time Path. [49](#), [50](#)
- DGLAP** Dokshitzer Gribov Lipatov Altarelli Parisi. [38](#), [39](#)
- DQPM** Daynamical Quasiparticle Model. [53](#), [55](#), [57–60](#), [111](#), [112](#), [147](#)
- EoS** Equation of State. [12](#), [13](#), [20](#)
- EP** Event Plane. [100–103](#)
- EPOS** Energy conserving quantum mechanical approach, based on Partons, parton ladders, strings, Off-shell remnants, and Saturation of parton ladders. [13](#), [22](#), [27–29](#), [31](#), [32](#), [40–42](#), [44](#), [45](#), [55](#), [61–66](#), [68–74](#), [76](#), [77](#), [79](#), [102](#), [108](#), [125–127](#), [129–131](#), [141](#), [143](#), [146–148](#), [153](#)
- GRT** Gribov-Regge Theory. [32](#), [35–38](#), [45](#), [146](#)
- HICs** Heavy Ion Collisions. [5](#), [11–16](#), [18](#), [22](#), [25](#), [28](#), [47](#), [52](#), [53](#), [60](#), [61](#), [74](#), [76](#), [77](#), [79](#), [84](#), [96](#), [101](#), [111–114](#), [122](#), [125](#), [129](#), [150](#)
- HSD** Hadron String Dynamics. [111](#)
- LHC** Large Hadron Collider. [5](#), [7](#), [11](#), [12](#), [16](#), [22](#), [26](#), [28](#), [32](#), [100](#), [125](#), [127](#), [129](#), [131](#)
- IQCD** lattice Quantum ChromoDynamics. [10](#), [12](#), [53](#), [57](#), [58](#), [111](#), [147](#)

- MC** Monte Carlo. 5, 26, 28, 29, 31, 61, 68, 112
- PBGRT** Parton-Based-Gribov-Regge Theory. 28, 31, 32, 38–41, 45, 62, 77, 146
- PDFs** Parton Distribution Functions. 26, 33–35, 45
- PHENIX** Pioneering High Energy Nuclear Interaction eXperiment. 16, 17, 24, 91, 92, 103–106, 145, 146, 149, 150
- PHSD** Parton Hadron String Dynamics. 23–26, 28, 32, 45, 47, 52–55, 59–61, 66, 69–74, 76, 77, 79–82, 84–100, 103–109, 111–123, 125–127, 129–131, 141, 146, 148–151, 153
- PM** Parton Model. 32–35, 38, 45
- pQCD** perturbative Quantum ChromoDynamics. 16, 17, 23, 27, 28, 38
- QCD** Quantum ChromoDynamics. 7, 9, 28, 36, 54, 84, 145
- QED** Quantum ElectroDynamics. 6, 7, 9, 27, 35
- QFT** Quantum Field Theory. 6, 7, 9, 35, 45, 47
- QGP** Quark Gluon Plasma. 5, 7, 11–13, 15–18, 22, 23, 25, 28, 29, 53, 55, 57, 59, 60, 71, 74, 77, 84, 91, 97, 111–114, 122, 125, 129, 151
- RHIC** Relativistic Heavy Ion Collider. 11, 13, 16, 22, 28, 47, 61, 91, 99, 100, 107, 113, 125, 127, 129, 131
- RT** Regge Theory. 36–38, 45
- SIS** An Accelerator Facility for Relativistic Heavy Ions. 111
- SLAC** Stanford Linear Accelerator Center. 33, 35
- SM** Standard Model. 5–9, 28
- SPS** Super Proton Synchrotron. 11, 13, 17, 22, 31, 47, 55, 100, 111
- STAR** Solenoidal Tracker At RHIC. 15, 25, 26, 84–87, 97, 98, 102, 113–115, 145, 146, 148–151
- UrQMD** Ultrarelativistic Quantum Molecular Dynamics. 32, 45